Synthesis, Structure and Electrochemistry of Positive Electrode Materials for Rechargeable Magnesium and Lithium Ion Batteries: Mechanistic Investigations

by

Xiaoqi Sun

A thesis
presented to the University of Waterloo
in fulfillment of the
thesis requirement for the degree of
Doctor of Philosophy
in
Chemistry

Waterloo, Ontario, Canada, 2017

Examining Committee Membership

The following served on the Examining Committee for this thesis. The decision of the Examining Committee is by majority vote.

External Examiner	M. Stanley Whittingham Professor
Supervisor	Linda F. Nazar Professor
Internal Member	Holger Kleinke Professor
Internal-external Member	Kevin Musselman Assistant Professor
Other Members	Pavle Radovanovic Associate Professor Dmitriy Soldatov Associate Professor

AUTHOR'S DECLARATION

I hereby declare that I am the sole author of this thesis. This is a true copy of the thesis, including any required final revisions, as accepted by my examiners.

I understand that my thesis may be made electronically available to the public.

Abstract

To meet the requirements for high energy density storage systems, rechargeable batteries based on the "beyond lithium ion" technologies have been widely investigated. The magnesium battery is a promising candidate benefiting from the utilization of a Mg metal negative electrode. The discovery of potential positive electrode materials beyond the seminal Mo_6S_8 has been limited, however, mainly due to the sluggish mobility of a divalent Mg^{2+} ion in solid frameworks. Since the study of Mg batteries is still at the early stage, it is important to conduct research of both finding new materials and investigating mechanisms in order to move the field forward.

The strong interaction between Mg^{2+} and the solid framework, which is one of the key factors leading to the sluggish diffusion, can be reduced by using a lattice containing "soft" anions as already observed for the Mo_6S_8. Following this strategy, I test two titanium sulfide materials, namely spinel Ti_2S_4 (with trace Cu^+ in the structure which is omitted for simplicity) and layered TiS_2, as positive electrodes for Mg batteries, as discussed in Chapter 3. A fully reversible Mg^{2+} electrochemical cycling vs. a Mg negative electrode is demonstrated for the spinel Ti_2S_4. The capacity approaches 200 mAh g^{-1} at a practical rate of C/5 and yields an energy density of 230 Wh kg^{-1}, twice that of the Mo_6S_8 benchmark. The Mg^{2+} insertion process is then determined by X-ray diffraction and Rietveld refinement, which reveals a preferential Mg^{2+} occupation on the octahedral site of the spinel phase up to $Mg_{0.6}Ti_2S_4$ followed by a population on the tetrahedral site during further discharge. The layered polymorph of TiS_2 also shows a promising electrochemical performance with a stabilized capacity of 115 mAh g^{-1} in a Mg full cell. Unlike the sloping discharge and charge curves observed for the spinel phase, the layered material contains multiple voltage plateaus, corresponding to a change in lattice

parameter evolution as demonstrated by *in-situ* X-ray diffraction. These results suggest a more complicated cation siting and ordering behavior upon Mg^{2+} insertion into the layered structure. For both titanium sulfide materials, improved electrochemical performance is obtained by decreasing the particle sizes. Benefiting from the shorter ion diffusion length that results, the kinetics of Mg^{2+} de/intercalation is improved so that the overpotential becomes smaller. The cycle lives of both materials are also extended, with stable capacities of 70 cycles obtained for the nano-sized spinel Ti_2S_4 and 200 cycles for the nano-sized layered TiS_2.

In order to further increase the energy density of the electrodes, shifting from sulfides to oxides is a direct solution due to the lighter weight and higher electronegativity of the latter. However, such shifts have been hindered by the poor electrochemical performance of oxide materials in Mg cells. Thorough investigations of the limitations are required to guide the design and selection of new candidates. Chapter 4 presents the synthesis of the birnessite polymorph of MnO_2 as a nanostructured phase supported on conductive carbon cloth and the comparison of its electrochemistry and structural changes when cycled as a positive electrode material in a Mg-ion battery under aqueous and nonaqueous conditions. X-ray diffraction shows that intercalation of Mg^{2+} ions takes place when cycling in an aqueous electrolyte, accompanied by the expulsion of interlayer water and transformation to a spinel-like phase. In nonaqueous cells, on the other hand, a conversion mechanism takes place as evidenced by X-ray photoelectron spectroscopy and transmission electron microscopy studies, with the formation of MnOOH, MnO and $Mg(OH)_2$ at the end of discharge. The sharp contrast behavior in the two electrolytes points to the important role of Mg^{2+} desolvation in the overall electrochemical performance. The layered $Mg_2Mo_3O_8$ is also investigated as a potential positive electrode. While no electrochemical activity is observed – either in a nonaqueous or

in an aqueous electrolyte – chemical demagnesiation is achieved but leads to amorphization. This observation is in agreement with the subsequent first principles calculation which predicts a strong thermodynamic driving force for structure decomposition at low Mg^{2+} concentrations and high activation barriers for bulk Mg^{2+} diffusion. Further analysis of the Mg^{2+} diffusion pathway reveals an O-Mg-O dumbbell intermediate site that creates a high Mg^{2+} migration barrier. The study demonstrates the strong influence of transition states on setting the magnitude of migration barriers.

An alternative setup, which would also accomplish the advantages of a Mg negative electrode, is a Mg-Li hybrid system. By coupling with a Li^{+} insertion positive electrode through a dual salt electrolyte, the sluggish Mg^{2+} diffusion in solid is avoided. In Chapter 5, two "high voltage" Prussian blue analogues (average 2.3 V vs. Mg/Mg^{2+}) are investigated as positive electrode materials. Capacities of 125 mAh g^{-1} are obtained at a current density of 10 mA g^{-1} (~ C/10), while stable performance up to 300 cycles is demonstrated at 200 mA g^{-1} (~ 2C). Their electrochemical profiles, presenting two voltage plateaus, are explained based on the two unique Fe bonding environments. Structural water has a beneficial impact on the cell voltage but slightly harms the capacity retention. Overall, the hybrid cell design presents an alternative path towards building a safe and high energy density storage system.

Although much effort has been taken to develop "beyond Li-ion" systems, the Li-ion technology still governs the current rechargeable battery market and improvement is required. Chapter 6 demonstrates the possibility of stabilizing lithium transition-metal silicate in the olivine structure. Using $LiInSiO_4$ and $LiScSiO_4$ as the parent structures, transition metal (Mn, Fe, Co) substitutions on the In/Sc site are examined by atomistic scale simulation. The In-Co combination shows the highest probability of cation disorder. Subsequent solid state synthesis

reveals that a significant amount of cation substitution can be obtained only for the In-Co case, with Co in its +2 oxidation state at the end. The stabilization of the substituted structure is achieved by the additional entropy provided by cation disorder as well as the match of cation sizes in the lattice.

Acknowledgements

I would like to express my greatest gratitude to my supervisor Dr. Linda F. Nazar for her guidance and support during my doctoral study. Her intelligent ideas and scientific thinking have encouraged my research, and I have gained great experience on critical and independent thinking and planning in the past few years. I would like to thank my Ph. D. committee members Dr. Holger Kleinke, Dr. Pavle Radovanovic and Dr. Dmitriy Soldatov (University of Guelph) for their time and suggestions about my research. I would also like to thank Dr. Kevin Musselman and Dr. M. Stanley Whittingham for being my internal-external member and external examiner, respectively, and their time to participate in my thesis defence.

I would like to thank all the Research collaborators for their help and the great collaboration. Dr. Miao Liu from Dr. Kristin A. Persson group (Lawrence Berkeley National Laboratory) and Ziqin Rong from Dr. Gerbrand Ceder group (Massachusetts Institute of Technology, Lawrence Berkeley National Laboratory, University of California Berkeley) carried out theoretical calculation of spinel Ti_2S_4 (Chapter 3), and G. Sai Gautam from the Ceder group performed the calculation on $Mg_2Mo_3O_8$ (Chapter 4). I also appreciate the useful discussions with them. The HRTEM and EELS experiments as well as the data analysis of MnO_2 (Chapter 4) were done by Dr. B. Layla Mehdi and Dr. Nigel D. Browning (Pacific Northwest National Laboratory). The XANES measurements (Chapter 3 and 6) were performed by Dr. Mali Balasubramanian (Argonne National Laboratory). The neutron diffraction (Chapter 6) was carried out by Dr. Ashfia Huq (Oak Ridge National Laboratory). Herself and Dr. Guerman Popov helped with the data analysis.

I would also like to extend my appreciations to Dr. Rajesh Tripathi and Dr. Victor Duffort. Dr. Tripathi taught me the synthesis, characterization techniques and atomistic scale simulation as I first joined the Nazar group. The simulation in Chapter 6 was performed by him as well. I then worked with Dr. Duffort on the Mg project, which was a great experience as I learnt a lot from his brilliant ideas and ways of solving problems, as well as his comprehensive knowledge on solid state chemistry. My research would be much more difficult without their help. I would also like to thank Dr. Patrick Bonnick for the great discussions and collaborations on the Mg project. Also many thanks to the rest of the group for their help and construction of a nice working environment in the lab.

Finally, I would like to thank my parents who brought me the genes of studying chemistry and support me under all conditions. I would also like to thank my friends at Waterloo for bringing me joy outside the lab, as well as friends from Zaotuan and 1808 for their support.

Table of Contents

List of Figures

List of Tables

List of Abbreviations

3D	Three Dimension
ACN	Acetonitrile
AE	Auxiliary Electrode
APC	All-Phenyl Complex
BE	Binding Energy
BEC	Butyl Ethyl Complex
BM	Ball Mill
BSE	Backscattered Electron
C-Ti_2S_4	Cubic Titanium Sulfide
CE	Coulombic Efficiency
CP	Chevrel Phase
CV	Cyclic Voltammetry
DSC	Differential Scanning Calorimetry
EDX	Energy Dispersive X-Ray Spectroscopy
EELS	Electron Energy Loss Spectroscopy
EV	Electric Vehicle
f.u.	Formula Unit
FTIR	Fourier Transform Infrared Spectroscopy
FWHM	Full Width at Half Maximum
G4	Tetraglyme
HEV	Hybrid Electric Vehicle
HRTEM	High Resolution Transmission Electron Microscopy
ICE	Internal Combustion Engine
ICSD	Inorganic Crystal Structure Database
In-TM	Transition Metal Substituted $LiInSiO_4$
L-TiS_2	Layered Titanium Sulfide
Mg-bir/CC	MnO_2 Birnessite/Carbon Cloth Composite
MMC	Magnesium Monocarborane
ND	Neutron Diffraction
NMP	N-Methyl-2-Pyrrolidone
Occ.	Occupancy
PBA	Prussian Blue Analogue

PHEV	Plug-In Hybrid Electric Vehicle
PTFE	Polytetrafluoroethylene
PVDF	Polyvinylidene Fluoride
RE	Reference Electrode
S.H.E.	Standard Hydrogen Electrode
SE	Secondary Electron
SEM	Scanning Electron Microscopy
SXRD	Synchrotron X-Ray Diffraction
TEM	Transmission Electron Microscopy
$TFSI^-$	Bis(trifluoromethane)sulfonamide Anion
TGA	Thermogravimetric Analysis
THF	Tetrahydrofuran
TM	Transition Metal
TOF	Time-of-Flight
Wyck.	Wyckoff position
WE	Working Electrode
XANES	X-Ray Absorption Near Edge Structure
XRD	X-Ray Diffraction
XPS	X-Ray Photoelectron Spectroscopy

Chapter 1

Introduction

1.1 Energy Storage

The demand for energy storage systems has increased rapidly in the past decade. Fossil fuels are the primary energy sources nowadays; however, their limited reserves, as well as the environmental issues such as global warming caused by their massive production of CO_2 gas, have driven the search for new energy sources. Solar and wind are renewable energies and environmentally clean, making them competitive for grid energy storage. An energy storage system is then required for load leveling. Another large usage of fossil fuels is in internal combustion engine (ICE) vehicles, which have seen a great growth in demand in the past decade and are currently the dominant means of transportation. Today's dependence on fossil fuels can be reduced or eliminated by replacing ICE vehicles with electric powered ones, such as hybrid electric vehicles (HEVs), plug-in hybrid electric vehicles (PHEVs) and electric vehicles (EVs).

Rechargeable batteries have their potential applications in the above fields. Driven by the redox potential difference between positive and negative electrodes, electrons move along the external circuit of a battery, and energy is provided. A battery becomes rechargeable if this process can be reversed by applying an external power. In this way, energy is reversibly released and stored by switching between discharge and charge modes. Current state-of-the-art rechargeable batteries are based on lithium-ion technologies and widely used for small portable devices such as cell phones and laptops. However, their energy density needs to be further increased to be practical for vehicles. For example, a 50 km drive would require a

battery to provide at least 7.5 kWh energy assuming efficient energy conversion,[1] about 700 times the energy – thus size – of a typical cell phone battery. For a longer driving range on a single charge, even larger batteries are necessary. At the same time, the cost of batteries needs to be greatly reduced to be compatible with that of ICEs. A modification on the Li-ion batteries is undoubtedly necessary to meet the requirements. Alternatively, moving towards "beyond Li-ion" technologies provides a more fundamental solution to overcome the current limitations. Nevertheless, a thorough understanding of the Li-ion chemistry will provide insights to advance the research in other, related fields.

1.2 Rechargeable Lithium and Li-Ion Batteries

Lithium metal is one of the best choices as the negative electrode material for rechargeable batteries due to its light weight (6.941 g mol^{-1}) and low redox potential (-3.04 V vs. standard hydrogen electrode (S.H.E.)). In 1976, Whittingham *et al.* discovered reversible Li^+ de/intercalation into layered TiS_2, and constructed the first rechargeable Li battery, using a TiS_2 positive electrode and a lithium metal negative electrode.[2,3] V_2O_5 was identified as an alternative Li^+ intercalation positive electrode soon after,[4] and the focus of positive electrode materials has since then shifted to oxides due to their higher specific capacities and voltages than sulfides. In the 1980s, Goodenough *et al.* showed the excellent electrochemical performance of the layered $LiCoO_2$ (**Figure 1-1a**),[5] which still governs today's major class of positive electrodes. In parallel, it was realized that Li tends to form dendrite during electrochemical deposition, resulting in a short circuit between positive and negative electrodes upon cycling and causing safety issues.[6] Whereas an alloy negative electrode experiences large volume changes and results in limited cycle lives,[7] carbon-based materials that function on intercalation mechanism show superior properties.[8]

In 1991, Sony commercialized the first Li-ion battery using a $LiCoO_2$ positive electrode and graphite negative electrode.[9] The term "Li-ion" is a reflection of the fact that Li^+, rather than Li metal, is involved during electrochemical processes. In fact, the Li^+ de/intercalation mechanism takes place at both electrodes. Starting off from the initial fully discharged state, the cell is charged by an external power supply, forcing electrons to move from the positive to the negative electrodes through the outer circuit. This loss of electrons at the $LiCoO_2$ results in the oxidation of Co^{3+} to Co^{4+}, and Li^+ deintercalates from the structure to balance the charge. The Li^+ then migrates to the negative electrode through the electrolyte inside the cell, intercalates into the graphite layers, and carbon is reduced by the external electron. Energy is stored in this manner. The reverse process, on the other hand, takes place spontaneously due to the higher chemical potential of the positive electrode than the negative, so that the battery can be used as an energy supply for other devices. The two processes are summarized in the equations below (and in **Figure 1-2a** later in this chapter):

Charge process:

Positive electrode: $LiCoO_2 - xLi^+ - xe^- \rightarrow Li_{1-x}CoO_2$ **Equation 1-1**

Negative electrode: $C_6 + xLi^+ + xe^- \rightarrow Li_xC_6$ **Equation 1-2**

Discharge process:

Positive electrode: $Li_{1-x}CoO_2 + xLi^+ + xe^- \rightarrow LiCoO_2$ **Equation 1-3**

Negative electrode: $Li_xC_6 - xLi^+ - xe^- \rightarrow C_6$ **Equation 1-4**

The cell operates at an average voltage of 3.7 V, resulting from the ~ 4.0 V (vs. Li) voltage of $LiCoO_2$ and ~ 0.3 V (vs. Li) of graphite. The insertion of 1 Li^+ into a C_6 formula unit (f.u.) results in the typical specific capacity of 370 mAh g^{-1} of negative electrode material;

only half of the Li^+ should be taken out from $LiCoO_2$ to maintain structural stability, providing a specific capacity of 140 mAh g^{-1} of the positive electrode. A deeper charge on the $LiCoO_2$ would result in the removal of oxygen from the lattice, causing capacity fading and safety concerns.

Due to the structural instability of $LiCoO_2$ during deep charge as well as the high price and toxicity of cobalt, alternative positive electrode candidates have been proposed. Substitution of other transition metals on the Co site of the $LiCoO_2$ structure has led to the studies of a variety of compounds, one of the most extensively investigated being $LiMn_xCo_{1-2x}Ni_xO_2$.[10,11] In this material, Mn maintains its +4 oxidation state to provide additional structural stability, while Co decreases the cation mixing level that results from similar sizes between Li^+ and Ni^{2+}, ensuring a minimum amount of immobile Li^+ in the transition metal layer. Electron transfer takes place based on $Co^{3+/4+}$ and $Ni^{2+/4+}$ redox couples, resulting in a typical reversible capacity of ~ 180 mAh g^{-1}. Spinel $LiMn_2O_4$ is another compound of great interest owing to its three dimensional (3D) ion pathways in the structure (**Figure 1-1b**) and environmentally green composition.[12,13] However, it suffers from a limited cycle life caused by the dissolution of Mn^{2+}.[14]

Iron-based materials are more suitable for large-scale production due to the high availability, low price, and low toxicity of Fe. However, the $LiCoO_2$ iso-structured $LiFeO_2$ does not allow Li^+ extraction since it is generally difficult to access Fe^{4+}. The $Fe^{2+/3+}$ redox couple, on the other hand, processes too low a voltage for a positive electrode. These problems have led to the consequent research interest in polyanion-based materials that are composed of $(XO_4)^{y-}$ groups in the structure. The strong covalent X-O bond prevents O releasing from the lattice and provides further structural stability, while the high electronegativity of X levels up

the redox voltage of transition metal due to inductive effect.[15] In 1997, Goodenough *et al.* introduced the first polyanion-based positive electrode material, $LiFePO_4$.[16] It forms in an olivine structure with 1D Li^+ tunnels (**Figure 1-1c**). One Li^+/f.u. can be extracted from the structure at 3.4 V (vs. Li), resulting in a specific capacity of 170 mAh g^{-1}. Compounds based on alternative polyanion groups, such as BO_3^{3-}, SiO_4^{4-} and SO_4F^{3-}, have been extensively synthesized and examined for Li-ion intercalation since then.[17-20] Silicates, in particular, have received great attention due to the abundant and non-toxic properties of Si. Stable capacity has been obtained for the Li_3PO_4-type Li_2FeSiO_4 (**Figure 1-1d**) with 1 electron transfer/f.u.[21-24] However, the material undergoes irreversible phase transformation after the first cycle,

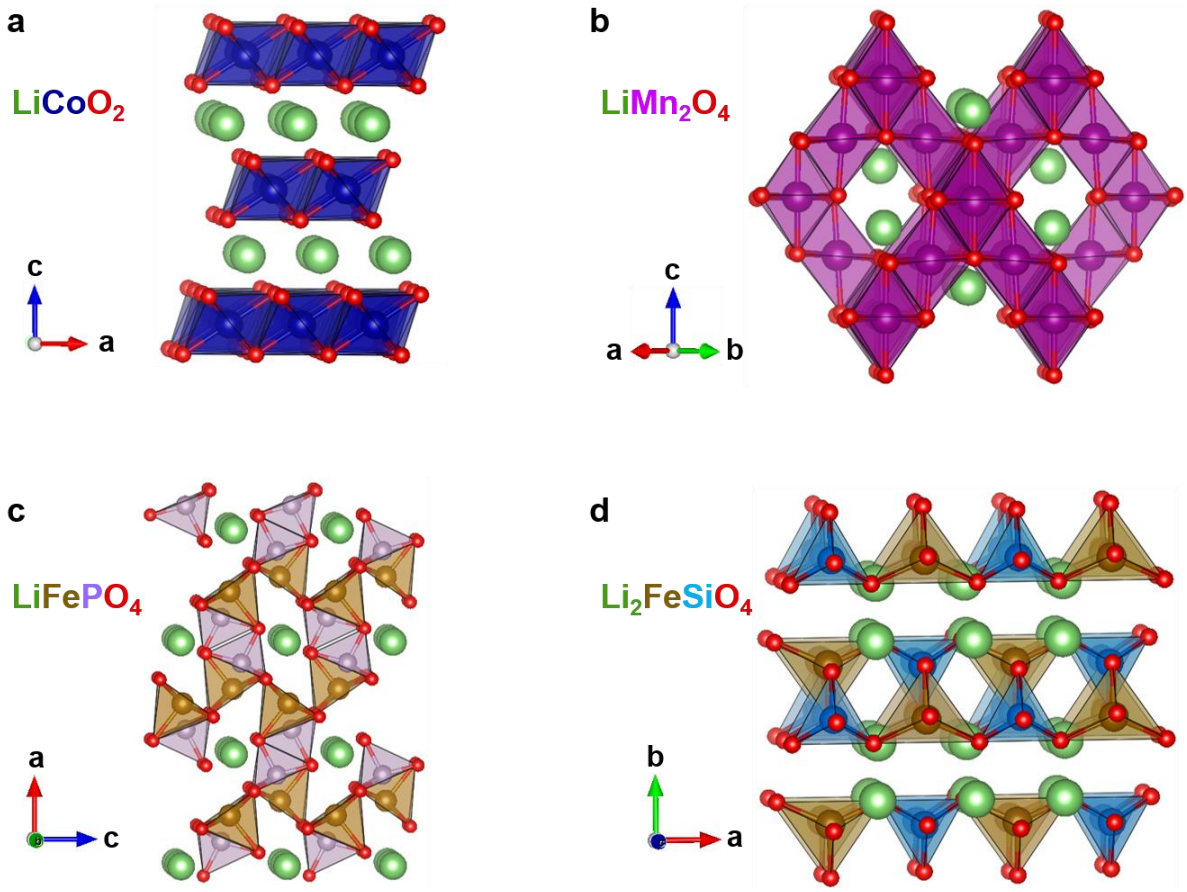

Figure 1-1. Crystal structures of (a) $LiCoO_2$, (b) $LiMn_2O_4$, (c) $LiFePO_4$ and (d) Li_2FeSiO_4. Color of each atom is indicated by the label beside the structure.

decreasing the discharge voltage from 3.1 V to 2.8 V.[25] A more robust structure has to be used for the silicates in order to achieve a stable long term cycling.

Despite the thorough investigation of electrode candidates for Li-ion batteries, the technology as yet provides limited energy density and at a relatively high price. Going beyond Li-ion is necessary to achieve practical usages for EVs or grid storage. Among the various technologies, including Li-S batteries, Li-O_2 batteries, all solid state Li batteries, Na-ion batteries, etc., magnesium batteries show great potential. Their history, current status, as well as difficulties will be discussed in detail in the following section.

1.3 Rechargeable Mg Batteries

1.3.1 Overview of Mg Batteries

Although the dendrite growth of Li metal hinders its application in a practical cell, the concept of the utilization of metal negative electrodes still holds true for achieving batteries with a high energy density and low cost. Among the various candidates, batteries that use Mg metal as the negative electrode are of special interest.[26] In addition to Mg's desirable electrochemical properties, including a high volumetric specific capacity of 3833 mAh mL^{-1}, low redox voltage of -2.37 V (vs. S.H.E.), and the absence of dendrite growth on electrochemical deposition,[27,28] Mg metal is already a material of broad industrial interest offering good availability and safe handling in the ambient atmosphere. Coupling with an appropriate positive electrode and electrolyte, a Mg battery system would offer high energy density, while maintaining satisfactory safety and low price.

Mg batteries function in a similar manner to Li-ion cells (**Figure 1-2**), except that reversible Mg stripping and plating, instead of ion de/intercalation, takes place at the negative electrode surface during discharge and charge. The first Mg battery prototype was proposed by Aurbach *et al.* in 2000.[29] Coupling a Mg negative electrode with a Chevrel phase (CP) Mo_6S_8 positive electrode and Mg organohaloaluminate type electrolyte, a specific capacity of ~ 75 mAh g^{-1} was obtained at an average voltage of 1.2 V (**Figure 1-3**). A variety of other positive electrodes and electrolytes have been tested in Mg cells since then; however, limited accomplishments have been achieved. Great challenges still remain in the Mg battery research due to the unique chemical properties of the divalent Mg^{2+} ion.

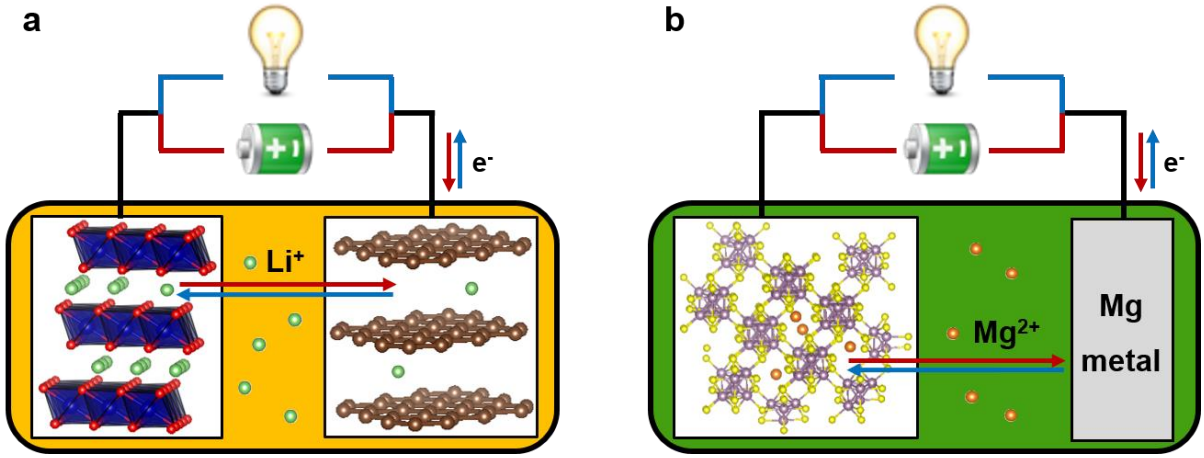

Figure 1-2. Schematic diagrams of the discharge (blue) and charge (red) processes in a (a) Li-ion and (b) Mg cell.

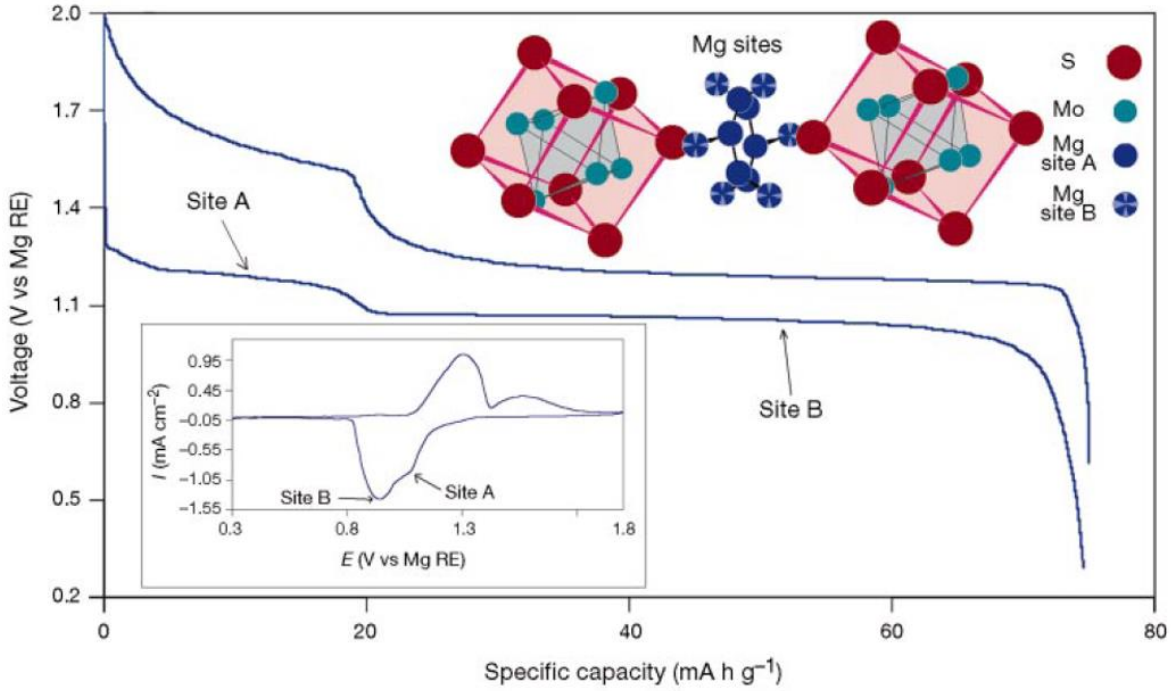

Figure 1-3. Electrochemistry of Mo_6S_8 positive electrode tested with a Mg negative electrode and 0.25 M $Mg(AlCl_2BuEt)_2$ in THF electrolyte. Reprinted with permissions from Ref. 29. Copyright 2000 Nature Publishing Group.

1.3.2 Positive Electrode Materials for Mg Batteries

The search for Mg^{2+} insertion positive electrode materials in fact started before Aurbach's work on the CP. Simple oxide materials were of more interest than sulfides due to their higher capacities and voltages, as is the case for Li-ion positive electrodes. However, sluggish Mg^{2+} diffusions were generally observed in solid lattices, leading to much poorer electrochemical performance of the electrodes compared to those based on Li^+ intercalation. In order to improve the kinetics, strategies including utilizing nano-sized materials to decrease the ion diffusion length, or involving solvent molecules in crystal structures to screen off the charge on Mg^{2+} are often applied.

The layered V_2O_5 presents a 2D ion pathway in its crystal structure and up to 3 Li^+/f.u can be inserted.[30] However, rather poor electrochemical performance was obtained with the bulk material in Mg non-aqueous electrolytes.[31] Only at a temperature as high as 150 ℃ could 0.5 Mg^{2+} be inserted into V_2O_5 at a slow rate, yet with limited reversibility and 300 mV higher overpotential than the Li case (**Figure 1-4**).[32] When the particle size decreased to the 20-50 nm range, around 180 mAh g^{-1} capacity was obtained, corresponding to the insertion of 0.6 Mg^{2+}/f.u.[33] Alternatively, a thin film electrode with around 100 nm thickness offered a capacity of 150 mAh g^{-1} at room temperature.[34] Nevertheless, the rather low current densities used in those works reflect the poor Mg^{2+} diffusion in the structure and hinder its practical application.

Introducing molecular water into the structure results in an xerogel V_2O_5, leading to an improvement in Mg^{2+} insertion kinetics compared to the "dry" material.[35-40] The larger interlayer spacing expended by structural water provides larger space for Mg^{2+} diffusion and

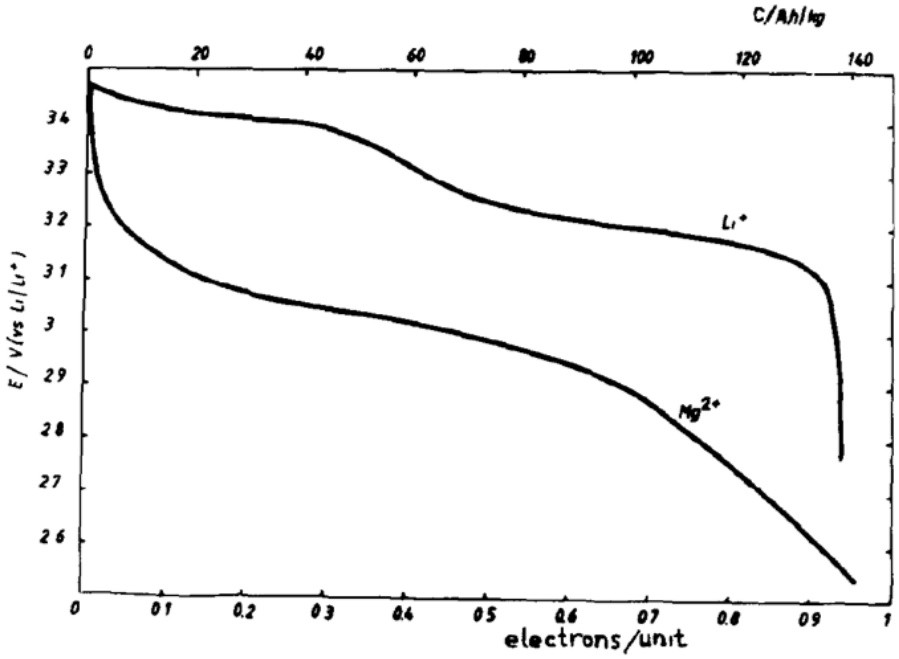

Figure 1-4. Comparison of the discharge curves of V_2O_5 tested in 1 mol kg^{-1} $LiClO_4$ or $Mg(ClO_4)_2$ in molten dimethyl sulfone electrolyte at 100 μA cm^{-2} current density at 150 ℃. Reprinted with permissions from Ref. 32. Copyright 1987 Elsevier B.V.

the multivalent charge is shielded by water molecules, leading to a weaker interaction with the oxygen ions in the lattice. Alternatively, adding water into the electrolyte also results in a better rate capability, as seen for V_2O_5[31,41,42] as well as other oxides such as MoO_3[43] and MnO_2.[44-47] However, careful evaluation of the insertion mechanism is necessary to identify the Mg^{2+} contribution. For example, it has been shown that proton intercalation into V_2O_5 contributes to the majority of the overall capacity with a high water level electrolyte.[48]

Mg^{2+} intercalation into the layered MnO_2 from water-containing electrolyte has been examined in detail.[46] The highest capacity of ~ 230 mAh g^{-1} was obtained at 100 mA g^{-1} current density with an aqueous or high water content electrolyte, showing superior insertion kinetics. The reversible change of interlayer distance and Mg^{2+} de/intercalation was proven by X-ray diffraction and scanning transmission electron microscopy. In the non-aqueous system, on the other hand, capacity dropped to below 60 mAh g^{-1} and not much change was shown in X-ray diffraction pattern. The results demonstrate that the charge on Mg^{2+} ions is effectively screened by the water in the electrolyte as well as in the MnO_2 crystal structure, facilitating the Mg^{2+} intercalation (**Figure 1-5a**). A separate work studied the Mg^{2+} insertion mechanism into the tunneled MnO_2 and observed a conversion mechanism in the non-aqueous electrolyte.[49] An oxide layer of (Mg,Mn)O was formed on the surface of MnO_2 during discharge (**Figure 1-5b**), resulting in a fast decay of capacity. Although the necessity of using water limits the usage of MnO_2 in a Mg full cell, such mechanism studies provide information on Mg^{2+} insertion behaviors and would guide future designs of the system.

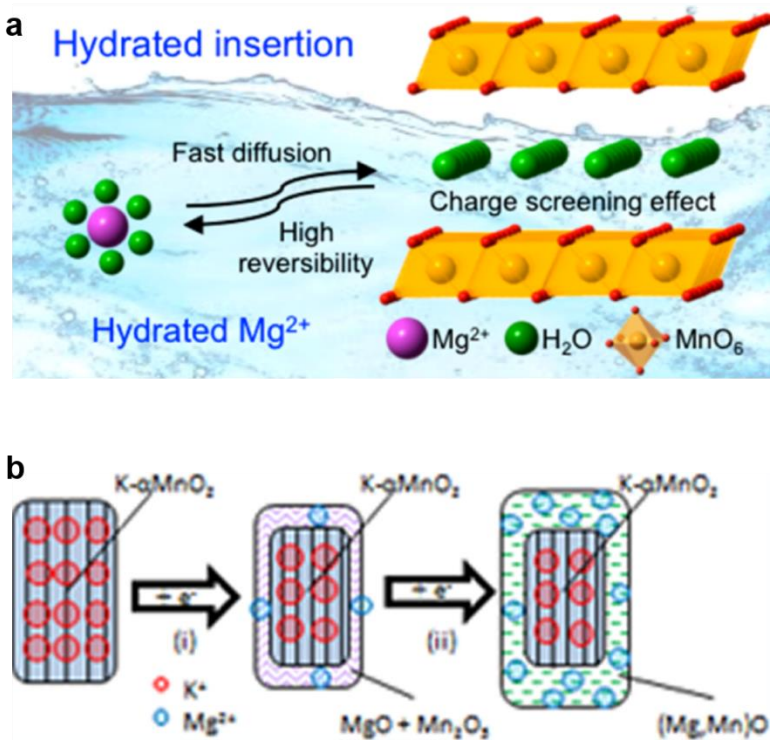

Figure 1-5. Schematic diagrams of (a) Mg^{2+} intercalation mechanism into layered MnO_2 from aqueous electrolyte and (b) conversion mechanism of tunneled MnO_2 from non-aqueous electrolyte. Reprinted with permissions from Refs. 46 and 49. Copyright 2015 American Chemical Society and Copyright 2014 American Chemical Society.

While limited success has been achieved with oxides, extensive work has been done to understand Mg^{2+} insertion into the CPs so as to guide the selection and design of potential candidates. In contrast to the strong ionic interaction that Mg^{2+} experiences in an oxide lattice, which results in a high diffusion barrier, the softer and more covalent characters of sulfide ions allow faster Mg^{2+} mobility in the structure. In addition, plenty of nearby empty sites, found in the cavities between Mo_6T_8 blocks in the Chevrel lattice (**Figure 1-6a**), are available for ion intercalation. The Mo_6 clusters, at the same time, promote facile local charge redistribution, which is especially critical for the diffusion of highly charged ions in solid structures.[50,51]

During the discharge of Mo_6S_8, the first Mg^{2+} inserts into the structure and occupies one of the six degenerate sites in cavity 1 (inner site) and gives rise to the first discharge plateau at 1.2 V. The next Mg^{2+} occupies one of the two degenerate sites in cavity 2 (outer site), resulting in the second discharge plateau at 1 V. During charge, the Mg^{2+} at the outer site can easily deintercalate due to the repulsion between the inserted ions. The removal of the other Mg^{2+} at cavity 1, however, is more difficult. Compared to jumping between the two cavities and diffusing through the structure, this Mg^{2+} prefers to hop between the inner sites, which is

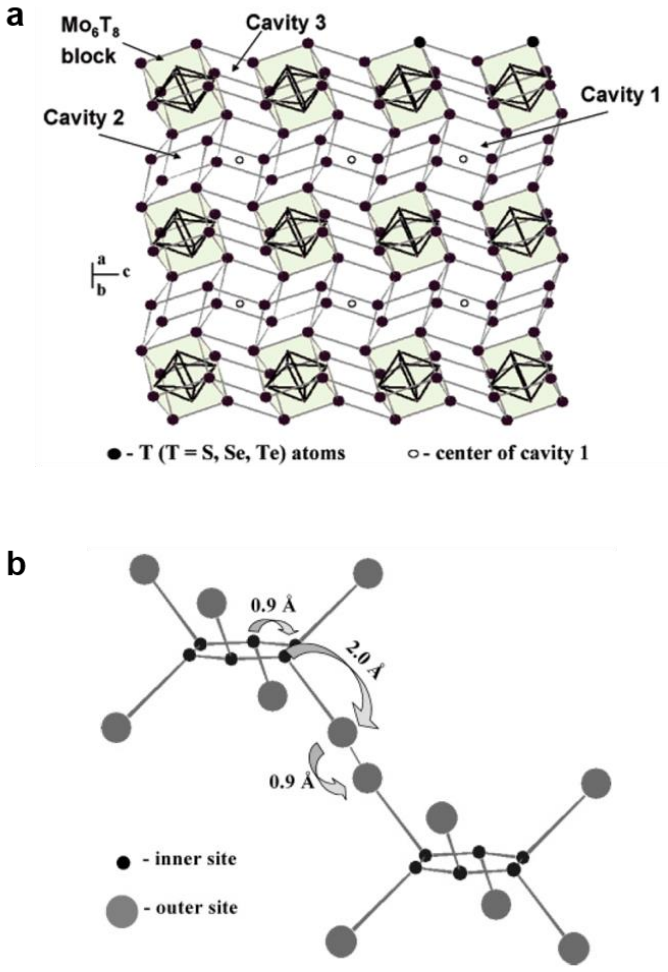

Figure 1-6. (a) Crystal structure of the CPs showing the Mo_6T_8 blocks and three cavities available for ion insertion; (b) Illustration of the inner site in cavity 1 and outer site in cavity 2 for Mg^{2+} diffusion in the CPs. Reprinted with permissions from Ref. 52. Copyright 2006 American Chemical Society.

only half a distance and experiences less repulsion from the Mo, leading to a circular motion within cavity 1 (**Figure 1-6b**).[52] As a result, Mg^{2+} trapping is often observed for the Mo_6S_8 positive electrode. Only at elevated temperatures can this effect be broken so that fully reversible Mg^{2+} de/intercalation is achieved.[53]

The iso-structured Mo_6Se_8, on the other hand, does not suffer from the cation trapping effect even at room temperature.[54] In addition to the larger unit cell and higher polarizability of the Mo_6Se_8 structure, the Mg^{2+} siting behavior in the two cavities is different from Mo_6S_8 so that the circular motion is no longer observed. Since the activation barrier for the hop between inner and outer sites is also low, a high Mg^{2+} mobility is observed in Mo_6Se_8.[55] Partially substituting S with Se, which forms a $Mo_6S_{8-x}Se_x$ solid solution, also benefits from the Se. Despite the lower theoretical capacity due to the heavier Se atom, the solid solution presents a higher practical capacity than Mo_6S_8 at room temperature.[56,57]

The concept of the utilization of soft anions in the lattice has then been applied to other materials. Certain electrochemical activities have been shown for TiS_2; however, a large overpotential between charge and discharge was present and the capacity decayed rapidly within the first few cycles (**Figure 1-7**).[58] CuS[59] and CoS[60] undergo conversion reactions in a Mg cell so that the cycle life tends to be limited, while the reaction mechanism of MoS_2 remains unclear.[61-64]

Overall, the accomplishment received in the research of positive electrode materials for Mg batteries has been limited. Clear proof of Mg^{2+} intercalation has only been shown for the CPs, while the factors hindering Mg^{2+} insertion into other structures have not been fully understood. The discovery of new positive electrodes and the investigation of mechanism are both important to promote the technology towards practical use.

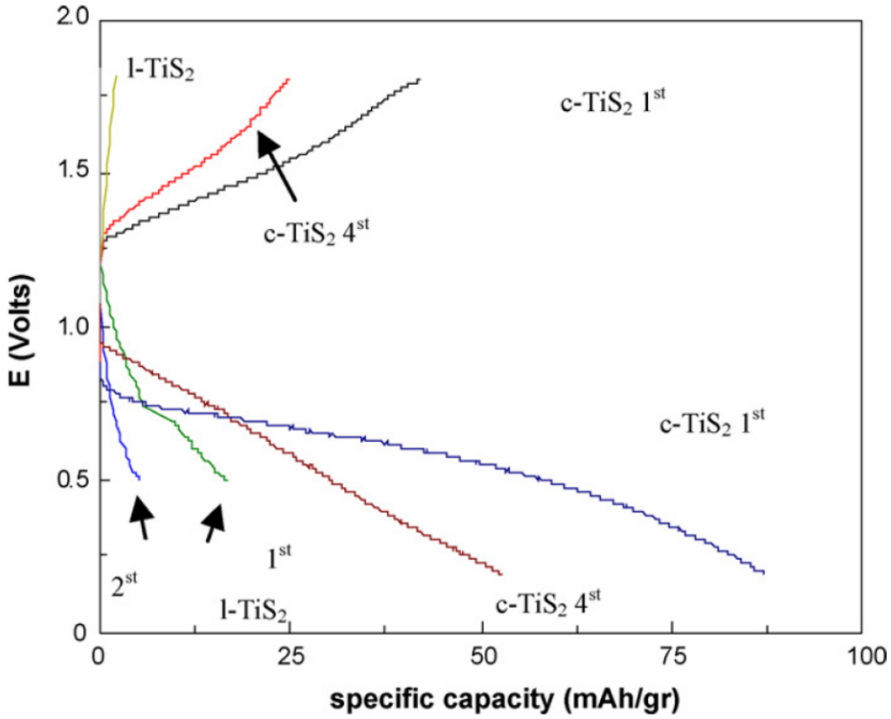

Figure 1-7. Voltage profiles of cubic TiS_2 (c-TiS_2) and layered TiS_2 (l-TiS_2) tested in BEC electrolyte at 0.1 mA cm^{-1} current density and 60 ℃. Reprinted with permissions from Ref. 58. Copyright 2007 Elsevier B.V.

1.3.3 Electrolytes for Mg Batteries

The low redox potential of Mg makes it prone to form an oxide layer on the surface by reacting with O_2, H_2O or certain electrolyte species. This layer, unlike the one for Li which is a good Li^+ conductor, is not permeable for Mg^{2+}, so that prevents facile Mg stripping and plating.[65] Thus, conventional solvents (carbonate, nitrile) and salts ($Mg(TFSI)_2$, $Mg(ClO_4)_2$) cannot be used for Mg electrolytes due to the passivation layer they would form on the Mg metal.[65,66] The functional electrolytes mostly use ethers that do not readily reduce on Mg as the solvent, while a variety of salts have been investigated.

Reversible Mg stripping/plating was first observed in the electrolyte composed of Grignard reagents,[67] which unfortunately suffers from low anodic stability and poor ionic conductivity. Introducing a Lewis acid into the solution, which reacts with the Grignard reagent through an acid-base reaction, improves the anodic stability of the electrolyte while maintaining effective Mg stripping/plating. Different combinations of the acid and base have been tested.[68] The Mg organohaloaluminate complex $Mg(AlCl_2EtBu)_2$ (butyl ethyl complex, BEC) generated from Bu_2Mg and $AlCl_2Et$ *in-situ* in THF showed a coulombic efficiency of almost 100% with > 2.1 V (vs. Mg) anodic stability (**Figure 1-8a**).[69,70] Further modification of the electrolyte resulted from the replacement of the alkyl group with phenyl so as to avoid β–elimination reaction which is the major limitation upon oxidation,[71] thus improving the stable window up to 3.3 V (vs. Mg) in the so-called all-phenyl complex (APC) electrolyte (**Figure 1-8a**).[72] At the same time, the synthesis reaction became milder with PhMgCl and $AlCl_3$ as the precursors. The dendrite-free Mg deposition from both BEC and APC was confirmed by SEM as shown in **Figure 1-8b**. By replacing the phenyl group with hexamethyldisilazide (HMDS), the nucleophilicity of the electrolyte can be reduced, allowing the utilization of a sulfur positive electrode for Mg batteries.[73]

Later on, an electrolyte made from inorganic salt only – $MgCl_2$ and $AlCl_3$ – showed reversible Mg stripping/plating at > 99% coulombic efficiency and provided an anodic stability of 3.1 V (vs. Mg).[74] The active species in MACC was identified to be $Mg_2(\mu\text{-}Cl)_3$ 6THF,[75] the same as in the Lewis acid-base electrolytes.[70] A conditioning process was required to initiate the electrolyte activity;[75,76] however, it was shown recently that $CrCl_3$ can be used as the promoter so that conditioning is not necessary.[77]

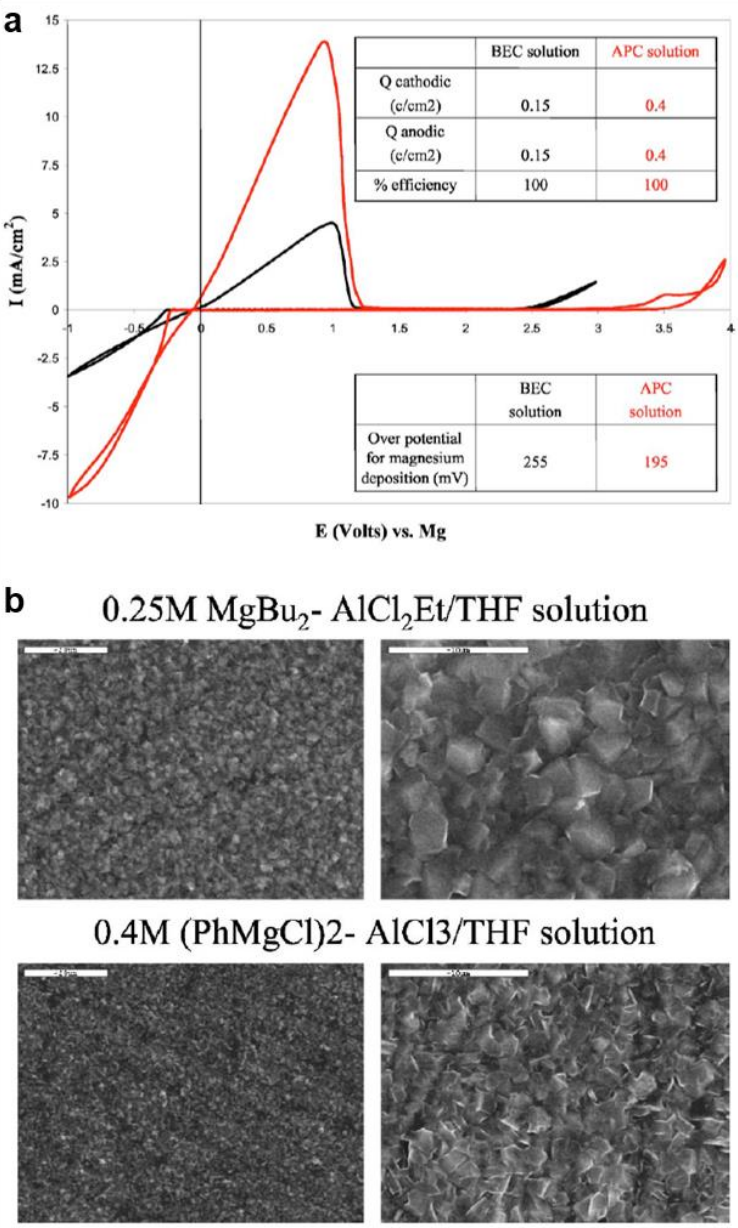

Figure 1-8. (a) Cyclic voltammograms of 0.25 M BEC and 0.4 M APC electrolytes measured with Pt electrodes at 25 mV s^{-1}. (b) SEM images of Mg deposited on Cu electrode at 2 mA cm^{-2} current density with a total charge of 2.8 Q cm^{-2}, showing dendrite free growth. Reprinted with permissions from Ref. 72. Copyright 2007 The Electrochemical Society.

In 2015, the Toyota group developed a halide-free single salt, $Mg(CB_{11}H_{12})_2$ (monocarborane, MMC), for Mg electrolyte.[78] The best electrochemistry was obtained with tetraglyme (G4) as the solvent, showing a superior anodic stability of 3.8 V (vs. Mg) with coulombic efficiency of > 99%. A unique feature of this electrolyte is its non-corrosive nature. MMC is stable with Al, Ni, stainless steel, glassy carbon and Pt above 3 V (**Figure 1-9**), on the contrary to most chlorine containing electrolytes which offer > 3 V anodic stability only with a Pt electrode but < 2 V against stainless steel or Al. This allows a convenient test for high voltage positive electrodes in coin cells made from stainless steel, or for practical use where the easily shaped Al commonly functions as the current collector. Other single salts, such $Mg(PF_6)_2$[79] and Mg bis(η^5-cyclopentadienyl),[80] have been studied later on, suggesting the promise of the utilization of simple salt in Mg battery electrolytes.

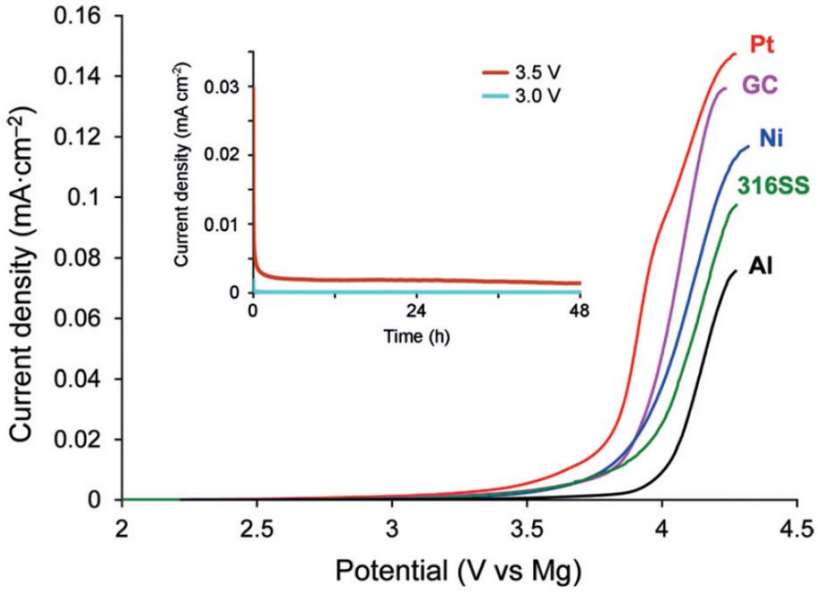

Figure 1-9. Linear seep voltammograms of 0.75 M MMC/G4 electrolyte with different electrodes at 5 mV s^{-1} (inset: chronoamaperometry of the electrolyte on a 316SS electrode at 3 V and 3.5 V). Reprinted with permissions from Ref. 78. Copyright 2015 WILEY-VCH Verlag GmbH & Co. KGaA, Weinheim.

1.3.4 Desolvation at Interphase

Although it has been observed that electrolytes affect the electrode electrochemistry, not much attention was paid to this influence until a recent calculation by Wan *et al.* showing the important role that Mg desolvation plays in the Mg intercalation into Mo_6S_8 from the APC electrolyte. During discharge, the Mg side of the $MgCl^+$ species from the electrolyte approaches the exposed S of the Mo_6S_8 surface, while the Cl is absorbed to a neighboring Mo center. Such interaction facilitates the Mg-Cl bond breaking procedure and allows the subsequent Mg diffusion into the bulk. The Cl left on the surface can interact with the next $MgCl^+$ to form $MgCl_2$, which would then return to the electrolyte and free up the Mo site for continuous stripping of Cl from Mg-Cl (**Figure 1-10**).[81] The overall process is critical for the facile Mg^{2+} intercalation into solid lattices from the APC electrolyte since the strong ionic Mg-Cl bond would prevent Mg^{2+} from desolvation. This could well be the reason for the poor electrochemical performance of many positive electrode materials in the APC type electrolyte. Even with non-APC electrolytes, the high charge on Mg ions would lead to a stronger interaction with the anion or solvent molecules in electrolyte compared to monovalent ions,

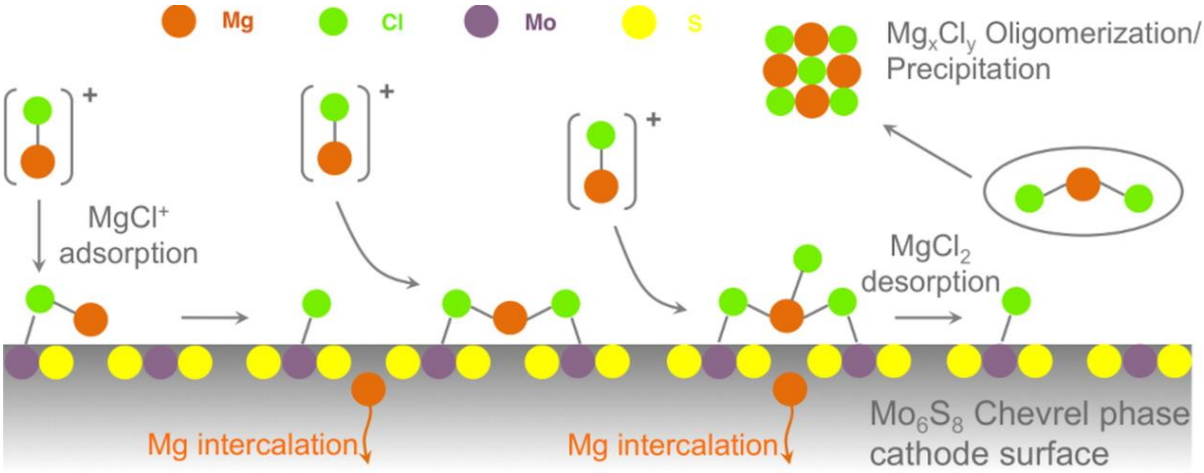

Figure 1-10. Schematic Diagram of APC desolvation process at Mo_6S_8 Surface. Reprinted with permissions from Ref. 81. Copyright 2015 American Chemical Society.

hindering the intercalation process. Thus, ion dissociation at the electrode/electrolyte interphase plays a role as important as bulk solid diffusion in determining the electrochemistry of a multivalent cell. Nevertheless, more experimental and theoretical investigations are still necessary to study further details.

1.3.5 Integration into a Full Cell

Up to date, the APC type electrolyte has been used as a standard electrolyte for testing new positive electrodes due to its excellent electrochemistry with a Mg negative electrode as well as the relatively low price and ease of synthesis. However, the chlorine ions make it highly corrosive towards oxide materials as well as the common current collectors such as stainless steel and Al at high voltages. As a result, for testing high voltage oxide materials, an electrolyte that could not strip/plate Mg has to be used in a half cell, usually with a high surface supercapacitive carbon counter electrode. This then raises the question of whether a similar result could be obtained with a different electrolyte that is hypothetically compatible with both high voltage oxide and Mg, considering the important role that desolvation plays at the interphase. In parallel, studies on new electrolytes mostly focus on the performance against the Mg electrode, while less care is taken on the positive electrode side. An integration of a full cell is difficult in the present circumstances due to the limited functional electrodes and electrolytes; nevertheless, such studies are necessary in order to move forward in this research field and achieve any practical usage of a Mg battery.

1.4 Rechargeable Mg-Li Hybrid Batteries

Since much difficulty has been experienced with the Mg^{2+} solid diffusion, a possible solution to completely avoid such process while maintaining the benefits of a Mg negative electrode is

the utilization of a Mg-Li hybrid battery. With a Mg-Li dual salt electrolyte used in the hybrid cell, a fast ionic transport is achieved in the positive electrode through reversible Li^+ intercalation owing to its superior mobility in solid structures compared to the divalent Mg^{2+}, while Mg stripping/plating takes place at the negative electrode due to its higher redox potential (-2.37 V vs. S.H.E.) than Li^+/Li^0 (-3.04 V vs. S.H.E.).[82] Although a recent study interestingly showed that a Mg rich Mg-Li alloy was produced at a similar voltage to Mg metal, suggesting that co-deposition occurred in their $Mg(BH_4)_2$-$LiBH_4$ dual salt electrolyte,[83] the main advantages of a Mg negative electrode is maintained as long as the electrodeposition is dendrite-free.

Owing to the limited electrochemical window imposed by the cell design (< 2 V vs. Mg in coin cells),[71] research on hybrid systems has been carried out using low voltage materials such as Mo_6S_8, TiS_2, TiO_2, $Li_4Ti_5O_{12}$, or FeS_2,[84-90] so that the energy density was limited. Nevertheless, a modification of the cell design, employing a molybdenum component on the positive side, increased the electrochemical window of the APC electrolyte above 2.8 V.[91] High voltage positive electrode materials able to survive highly chlorinated environments are thus needed, in order to exploit this breakthrough.

1.5 Summary

The Li-ion technology dominates the present commercial high energy density rechargeable batteries and provides a possible solution to minimize the society reliance on fossil fuels. However, further improvement is necessary for practical applications in EVs and grid storage. In addition to the modification on the current Li-ion system, the research of "beyond Li-ion" provides more possibilities towards a high energy storage system. The rechargeable Mg battery

is one of the promising candidates through the utilization of a Mg metal negative electrode. With the first prototype proposed in 2000, its development has not been as fast as the Li-ion technology, however, mainly due to the additional difficulties risen from a divalent Mg^{2+} ion. Sluggish solid diffusion is observed in many structures, limiting the available candidates for positive electrode materials, while facile stripping/plating can be realized only on a passivation film free Mg surface, eliminating the usage of many conventional salts and solvents that are readily reduced by Mg from electrolytes. The strong ion pairing of Mg^{2+} in electrolytes results in an additional factor of desolvation which must be overcome before its intercalation into positive electrodes.

While finding a practical rechargeable Mg battery is the final goal of the field, it is important currently to achieve a deeper understanding of the chemistry and electrochemistry of Mg. Detailed investigations of Mg solid diffusion behaviors should be carried out on the structures allowing facile Mg migration as well as those with high diffusion barriers, in order to provide information on the selection and design of solid structures for Mg positive electrodes. At the same time, examination of different electrolytes with a functional positive electrode would help to gain a deeper understanding of the desolvation process and to determine suitable electrode-electrolyte combinations. The knowledge obtained through those studies would provide an easier pathway towards the discovery of high energy density Mg battery systems. Alternative solutions, such as the utilization of Mg-Li hybrid cells in order to avoid the sluggish Mg^{2+} diffusion, also show potentials for high energy storage systems.

1.6 Scope of the Thesis

This thesis deals with the synthesis, characterization, electrochemical tests and mechanism studies of novel positive materials for rechargeable batteries, including Mg battery, Mg-Li hybrid battery, and Li-ion battery. Seven chapters are included. Chapter 1 gives a general introduction of the energy storage systems, including the state-of-the-art Li-ion technology and Mg battery as one of the promising "beyond Li-ion" candidates. The development and difficulties of the Mg research are discussed. Chapter 2 describes the synthesis and characterization techniques used during the studies of this thesis work. Part of this chapter is reproduced with permission from:

Talaie, E.; Bonnick, P.; Sun, X.; Pang, Q.; Liang, X.; Nazar, L. F. Methods and Protocols for Electrochemical Energy Storage Materials Research. *Chem. Mater.* **2017**, *29*, 90-105. DOI: 10.1021/acs.chemmater.6b02726. Copyright 2016: American Chemical Society.

Chapter 3 shows the spinel and layered structures of titanium sulfide as novel Mg intercalation positive electrodes. Even with the micron-sized material, both polymorphs show high capacities and good kinetics upon Mg insertion. The capacity retention could be further improved by applying nano-sized particles as the positive electrode materials. The detailed Mg de/intercalation mechanisms are investigated, suggesting the great influence of crystal structures on Mg^{2+} diffusions in solid lattices. While only the Chevrel family has been previously proven to allow Mg^{2+} intercalation, the two titanium sulfides constitute the available candidates for Mg battery positive electrode materials as well as the platforms for mechanism studies. The results have been published in the following studies and are reproduced with permission:

Sun, X.; Bonnick, P.; Duffort, V.; Liu, M.; Rong, Z.; Persson, K. A.; Ceder, G.; Nazar, L. F. A High Capacity Thiospinel Cathode for Mg Batteries. *Energy Environ. Sci.* **2016**, *9*, 2273-2277. DOI: 10.1039/c6ee00724d. Copyright 2016: The Royal Society of Chemistry.

Sun, X.; Bonnick, P.; Nazar, L. F. Layered TiS_2 Positive Electrode for Mg Batteries. *ACS Energy Lett.* **2016**, *1*, 297-301. DOI: 10.1021/acsenergylett.6b00145. Copyright 2016: American Chemical Society.

Chapter 4 investigates the limiting factors for Mg^{2+} intercalation into oxide materials. Using the layered MnO_2 positive electrode, the critical role of Mg^{2+} ion pairing in electrolyte and desolvation at the electrode/electrolyte interphase on the insertion mechanisms is identified. The work suggests that the electrolyte needs to be carefully selected in order to couple with the specific electrode. On the other hand, layered $Mg_2Mo_3O_8$ shows the importance of the transition state geometry on the energy barrier for Mg^{2+} diffusion in solid lattices, so that the investigation of ion pathways and intermediate states/coordinations would potentially help screen off high diffusion barrier structures. These results have been published in the following studies and are reproduced with permission:

Sun, X.; Duffort, V.; Mehdi, B. L.; Browning, N. D.; Nazar, L. F. Investigation of the Mechanism of Mg Insertion in Birnessite in Nonaqueous and Aqueous Rechargeable Mg-Ion Batteries. *Chem. Mater.* **2016**, *28*, 534-542. DOI: 10.1021/acs.chemmater.5b03983. Copyright 2015: American Chemical Society.

Gautam, G. S.; Sun, X.; Duffort, V.; Nazar, L. F.; Ceder, G. Impact of Intermediate Sites on Bulk Diffusion Barriers: Mg Intercalation in $Mg_2Mo_3O_8$. *J. Mater. Chem. A* **2016**, *4*, 17643-17648. DOI: 10.1039/c6ta07804d. Copyright 2016: The Royal Society of Chemistry.

Chapter 5 is a study on Mg-Li hybrid cells. The utilization of Mg-Li dual salt electrolytes allows facile Li^+ intercalation into the positive electrode structure while maintaining the advantages of a Mg negative electrode. Using the high voltage Prussian blue analogues as positive electrodes, the hybrid cells show stable capacity retention up to 300 cycles. The detailed Li^+ intercalation mechanism is studied and the influence of structural water is shown. The results have been published in the following study:

Sun, X.; Duffort, V.; Nazar, L. F. Prussian Blue Mg-Li Hybrid Batteries. *Adv. Sci.* **2016**, *3*, 201600044. DOI: 10.1002/advs.201600044. Copyright 2016: WILEY-VCH Verlag GmbH & Co. KGaA, Weinheim. Reproduced with permission.

Chapter 6 studies the possibility of stabilizing transition metal into an olivine silicate structure, which would be used as high capacity and low price positive electrode materials for Li-ion batteries. Using $LiInSiO_4$ and $LiScSiO_4$ olivines as the parent structures, combined atomistic scale simulation and solid state synthesis are used to evaluate the possibility of Mn, Fe and Co substitutions. A certain degree of Co substitution can be achieved into $LiInSiO_4$, induced by the additional entropy obtained by cation disordering and the formation of solid solutions.

The final chapter summarizes the work of the entire thesis and proposes potential further directions of the correlated research fields.

Chapter 2

Methods and Techniques

2.1 Overview

In the study of electrode materials in this thesis work, it is first necessary to synthesize the compound with the desired crystal structure and morphology. This was done by either following available synthesis procedure or testing out a new method. Various synthesis techniques, including solid state synthesis, wet synthesis and hydrothermal synthesis, were applied for different purposes. The materials obtained were then characterized to ensure they were the desired products. X-ray diffraction (XRD) and neutron diffraction (ND) were carried out in conjunction with Rietveld refinement[92] to study the crystal structure of the compound. Scanning electron microscopy (SEM) and transmission electron microscopy (TEM) yielded the morphology of the particles. The energy dispersive X-ray spectroscopy (EDX) was coupled with an SEM to perform elemental analysis for the particles within the microscope vision. X-ray photoelectron spectroscopy (XPS) and X-ray absorption near edge structure (XANES) were used to study the oxidation states of the elements near the surface or in the bulk of particles, respectively. Fourier transform infrared spectroscopy (FTIR) was applied to achieve the chemical bond information. Thermal gravimetric analysis (TGA) provided the thermal stability of a compound, and combustion analysis revealed the concentrations of hydrogen, carbon and nitrogen. Karl Fischer titration was taken to measure the water content in a solution with low water level.

Once the desired product was confirmed, its electrochemical properties were tested by galvanostatic cycling or cyclic voltammetry (CV). *In-situ* or *ex-situ* (post-cycling)

characterizations, using some of the above techniques, were sometimes carried out to study the mechanisms during electrochemical processes.

2.2 Synthesis Techniques

2.2.1 Solid State Synthesis

Solid state synthesis involves the mixing of precursors followed by a heat treatment. At high temperature, the atoms gain enough thermal energy to slowly re-arrange themselves and form the most thermodynamically stable products. The heat treatment can be carried out under atmosphere in a muffle furnace if the materials are not air-sensitive, or by applying a flow of gas in a tube furnace for air sensitive synthesis or if the gas itself is involved in the reaction. The precursors can also be sealed in a quartz tube under vacuum if no gas product is formed during the synthesis.

Since solid mixing creates only limited interaction surfaces between different precursors, the number of nucleation sites is low. Thus, solid state synthesis usually requires long reaction periods and results in large particles. One way to decrease the particle size of the product is to improve the mixing level of the precursors in order to generate more nucleation sites. This can be done by a sol-gel synthesis, which involves the dissolution of all precursors in a solution followed by the evaporation of the solvent, resulting in the mixing of precursors in a molecular level. However, it is important that the solvent provide similar solubility for all precursors so that they all precipitate out on a similar time scale.

A thorough mixing of the precursors can also be carried out by mechanical ball milling. The particle size of precursors is reduced and particles are pressed together at the same time as the mixing. Ball milling are also applied to the product to reduce the particle size. The ball

milling conditions, including time and speed, should be optimized to provide the most efficient milling. In addition, smaller grinding balls result in smaller sized particles. Increasing the ball to powder weight ratio also reduces the particle size; however, a minimum amount of powder is required so that the jar and balls do not grind against each other and introduce impurities. When milling hard compounds, the material of the jar and balls should be hard as well, for example ZrO_2 or stainless steel. On the contrary, soft materials such as polytetrafluoroethylene (PTFE) are used for ball milling soft particles. A solvent is sometimes added to the mixture for wet milling.

2.2.2 Wet Synthesis

In contrast to solid state synthesis, a solvent is used as reaction mediator for wet synthesis, where the precursors are dissolved and mixed at a molecular/ionic level. A special type of wet synthesis is the hydrothermal/solvothermal reaction.[93] By sealing the solution in an autoclave, the temperature of the reaction can be raised above the boiling point of the solvent, providing a high-pressure condition for the synthesis. Since the ion diffusions in liquid phases are much faster than solid phases, wet synthesis can be carried out at a much lower temperature and shorter period than solid state reactions typically. This results in a smaller particle size. The specific morphology of the product can even be controlled by modifying the synthesis conditions such as solvent, concentration and temperature. In addition, the wet synthesis undergoes a more kinetic driven pathway, allowing to obtain meta-stable phases that cannot be synthesized via the thermodynamics driven solid state reactions.

After the reaction is finished, the solid product is collected by filtration and subsequent washing with solvents to remove any side products.

2.2.3 Chemical Oxidation

A mobile cation can be removed from a solid structure while another ion is oxidized to balance the charge, with the lattice framework maintained. This is a similar process to charging a positive electrode material, but the electron is released to an oxidizing agent instead of an outer circuit. Such method allows the synthesis of meta-stable phases or the examination of cation mobility in solid structures in order to study their potential usages as electrode materials. Conventional oxidizing agents include NO_2BF_4, Br_2 and I_2, with a decrease of oxidizing strength in the order. A suitable agent should be chosen so as not to over-oxidize the material. Acetonitrile is usually used as the solvent due to its high anodic stability.

A chemical oxidation reaction is carried out by adding the starting material to a solution with an excess of oxidizing agent to ensure complete oxidation. After stirring for a few days at room or elevated temperatures, the oxidized product is recovered by filtration. All procedures should be carried out under inert atmosphere if any component of the reaction is air sensitive.

2.3 Diffraction Techniques

2.3.1 Powder X-Ray Diffraction

X-ray is a part of the electromagnetic radiation. The wavelength of X-ray, 0.01 to 10 nm, is in the same range as the atomic distance in a crystal, so that it will be diffracted by the repeated atom planes. A constructive interference will happen if the diffracted beams are in-phase. As illustrated in **Figure 2-1**, such diffraction requires the incident beam angle (θ), wavelength (λ) and crystal plane spacing (d) to satisfy the following relationship:

$n\lambda = 2d\cdot\sin\theta$ (n = integer) **Equation 2-1**

which is known as Bragg's law. This gives rise to a peak in the diffraction pattern.

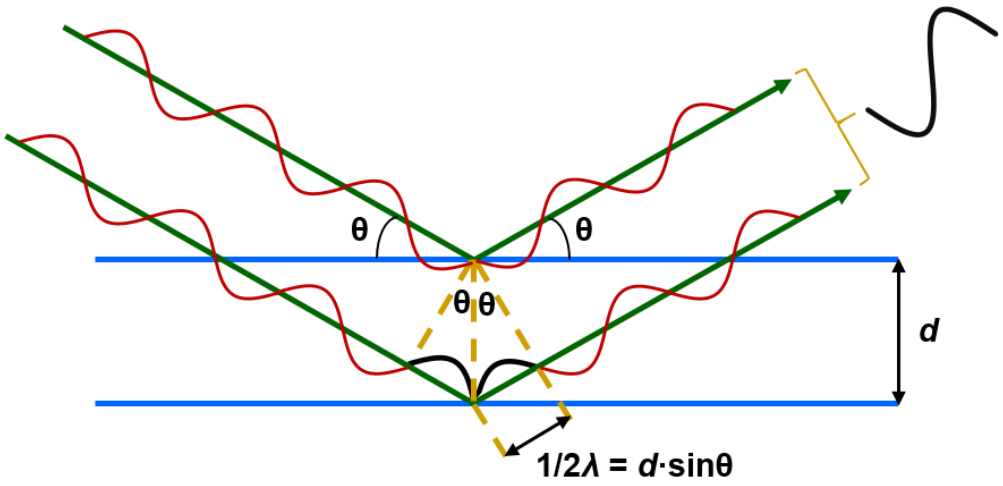

Figure 2-1. Schematic diagram of Bragg's law.

Since X-ray is actually scattered by the electron clouds around the atoms, the intensity of the diffraction beam directly correlates to the number and position of electrons, thus the specific atoms. In fact, the structure factor (F) of a reflection can be calculated by

$$F_{hkl} = \sum f_j \exp[2\pi i(hx_j + ky_j + lz_j)] \qquad \textbf{Equation 2-2}$$

where (hkl) is the Miller index of the plane, (x,y,z) is the coordinates of the atom and f is the atomic scattering factor that is dependent on the atom type as well as the scattering angle. The intensity of the peak is related to the structure factor via the following equation

$$I = A \cdot F^2 \qquad \textbf{Equation 2-3}$$

where A includes other factors such as polarization, absorption and temperature. As a result, the XRD pattern could be used to evaluate the crystal structure information.

Since the directions of crystal planes are 3D, the diffraction beams they result in are going towards all the directions obeying Bragg's law. In order to collect the diffraction pattern

of a single crystal, the crystal has to be rotated if the detector only moves in 2D. This is not necessary for a powder sample, however, since the powder contains millions of single crystals that are randomly oriented and can be regarded as "rotating" themselves already.

Figure 2-2a shows the scheme of the Bragg-Brentano geometry, which is the most commonly used setup for a laboratory diffractometer. The powder sample is mounted on a flat holder, with the X-ray source and detector moving -θ and θ degrees with respect to the sample stage plane. In this circumstance, the diffractions from the crystal planes parallel to the sample stage will reach the detector and result in a diffraction signal. If the sample is randomly oriented, which is true in general cases, the possibility of being parallel is the same for all the crystal planes. However, crystals with special shapes would result in a preferred orientation during sample preparation. For example, platelet crystals tend to lay on the sample stage instead of standing perpendicularly. As a result, the detector will obtain more diffraction signal from certain planes than the rest, which affects the intensities. This effect should be taken care of when refining the crystal structure.

An alternative geometry that would remove the preferred orientation issue is the Debye-Scherrer geometry (**Figure 2-2b**). In this case, the powder sample is mounted into a glass capillary which is rotated while the X-ray source and detector move -θ and θ degrees. Such setup also benefits the measurements for air sensitive samples by sealing the powder in a capillary under inert atmosphere. The Debye-Scherrer is a type of transmission geometry, so that X-ray has to go through the sample and the signal it obtains is normally lower than the Bragg-Brentano which works on reflection. In the conventional XRDs carried out in this thesis work, the Bragg-Brentano geometry was used for air stable samples while the Debye-Scherrer

was used for air sensitive samples. Measurements were performed with a PANalytical Empyrean diffractometer with Cu-Kα radiation.

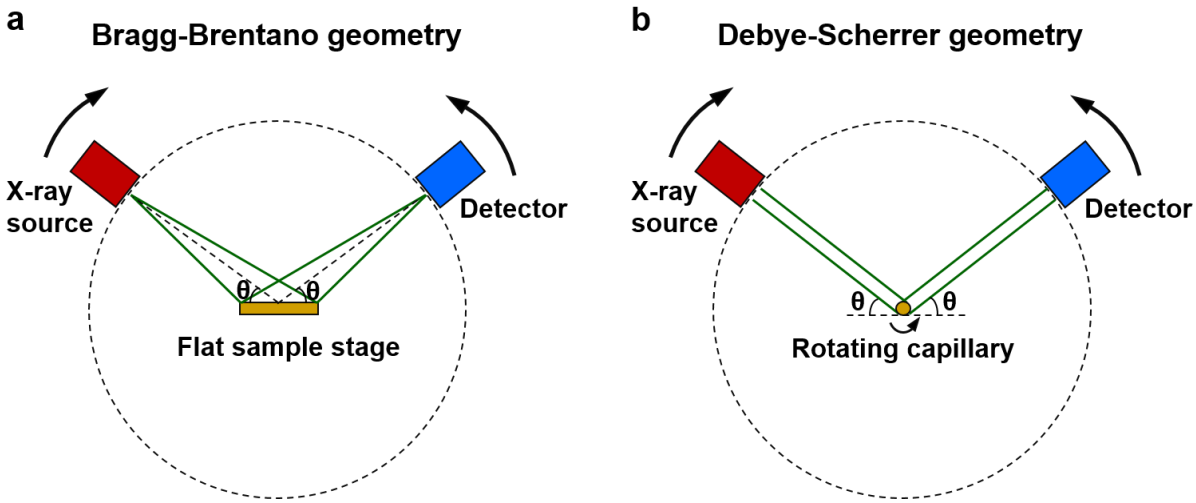

Figure 2-2. Schematic diagrams of (a) Bragg-Brentano and (b) Debye-Scherrer geometries.

In addition to steady-state measurements, *in-situ* XRD can also be carried out with laboratory diffractometer. With the sample mounted to a sealed chamber, thermodiffraction can be performed by heating up the sample stage while scans are taken simultaneously. It provides a faster clue on the reactions that happens at certain temperatures. Alternatively, *in-situ* XRD can also be coupled with electrochemical measurements, showing the real-time information of the electrode material during cycling. The *in-situ* cell used in this thesis work was made by Dr. Victor Duffort.

Synchrotron radiation comes from the electromagnetic field given out by the centripetal accelerated high energy electrons. This results in a much more intense and collimated signal compared to laboratory X-ray sources which generate X-ray by the photoelectron effect of a metal target hit by electrons. Thus, synchrotron XRD (SXRD) gives a better resolution and signal to noise ratio, revealing more details of crystal structure information. The SXRD

measurements in this thesis work were carried out at the Advanced Photon Source (APS) at Argonne National Laboratory (ANL).

2.3.2 Time-of-Flight Neutron Diffraction

Due to the wave-particle duality of elementary particles, a beam of neutrons has the character of wave and can also be diffracted by atomic planes, obeying Bragg's law. Unlike X-rays, neutrons interact with the nucleus instead of the electrons of the atom, resulting in different scattering factors. Thus, ND and XRD can be used together to obtain more complete atomic information. For example, XRD cannot distinguish between Fe and Co since they only differ by one electron, but their neutron scattering lengths are 9.45 fm and 2.78 fm, respectively, so that they can be easily resolved by ND. ND is also better for light elements whose XRD scattering factors are low due to the small amount of electrons, while XRD has to be used for studying vanadium which is almost transparent to neutrons. In addition, the peak intensity decay at high scattering angles in ND is much smaller than in XRD due to the smaller volume of a nucleus than an electron cloud. Thus, ND provides clearer information on small d-spacing planes.

The Time-of-Flight (TOF) method is one of the conventional approaches for ND. Instead of fixing λ and changing θ as in XRD, the diffraction angle is fixed while neutrons with various wavelengths are applied to the sample in TOF ND. The time (t) a neutron takes to reach the detector is recorded and converted to its speed (v) by L/t, where L is the distance the neutron travels. The speed is related to wavelength, as stated in de Broglie equation:

$\lambda = h/mv$ **Equation 2-4**

where h is the Planck's constant and m is the mass of the neutron. Combining with Bragg's law, this results in

$\lambda = h/mv = ht/mL = 2d \cdot \sin\theta$ **Equation 2-5**

so that *d*-spacing is obtained. The resolution and signal to noise ratio of the pattern can be optimized by changing the scattering angle.

The TOF ND measurements in this thesis work were performed in Oak Ridge National Laboratory (ORNL) by Dr. Ashfia Huq.

2.3.3 Rietveld Refinement

Rietveld refinement, identified by its name, is used to refine instead of to solve a structure. A starting module should be given to start with, which is subsequently refined to minimize the least-squares between experimental and calculated data:

$\sum w_i[y_i(obs) - y_i(calc)]^2$ **Equation 2-6**

Each data point of the diffraction pattern is calculated individually to extract the maximum information. Although peak overlap happens frequently for powder diffractions, the contribution from each peak can still be separated due to their specific profiles.

For practical refinements, it is convenient to apply a Le Bail fit[94] on the pattern first. This method assigns intensities to all the peaks automatically in order to obtain the best fit. It allows a focus on lattice parameters and peak profiles while atomic information is left behind. Background, sample displacement, lattice parameters and peak broadening are refined in order. Once a satisfactory fit is obtained, those parameters are fixed and the refinement is switched to the Rietveld mode. Scale factors, atomic positions, occupancies, thermal parameters, and

preferred orientation if any are refined subsequently. All the parameters are relaxed in the end to perform a complete refinement. If more than one phase is present, Rietveld refinement also results in a ratio between different components.

A simple judgement on how well the refined result matches with the actual structure is to look at the actual fit of the pattern. While this method is rather arbitrary, a few agreement factors are used:

$$R_{wp} = \{\sum w_i[y_i(obs) - y_i(calc)]^2 / \sum w_i y_i(obs)^2\}^{1/2} \times 100\% \quad \textbf{Equation 2-7}$$

$$R_{exp} = \{(N\text{-}P+C) / \sum w_i y_i(obs)^2\}^{1/2} \times 100\% \quad \textbf{Equation 2-8}$$

(N = number of observations, P = parameter refined, C = number of constraints)

$$\chi^2 = (R_{wp}/R_{exp})^2 \quad \textbf{Equation 2-9}$$

$$R_{Bragg} = \sum \left| I_{obs} - I_{cal} \right| / \sum \left| I_{obs} \right| \quad \textbf{Equation 2-10}$$

The χ^2 factor is often reported as a weighted-profile factor, and the R_{Bragg} (Bragg factor) reflects the fit of structural parameters with profile parameters omitted.

The refinements in this thesis work were carried out with the FullProf suite[95] (Chapter 3, Chapter 4, Chapter 5) or GSAS and EXPGUI (Chapter 6).[96, 97]

2.4 Electron Microscopy

Electron microscopy provides the high-resolution images of a specimen. Electrons are produced at the top of the microscope and accelerated by the potential drop along the pathway towards the specimen. A typical accelerating voltage of 5~20 kV used in SEM results in electron beams with 5 ~ 20 keV energy, or 0.06 ~ 0.25 nm wavelength. The much shorter wavelength of such electron beam compared with visible light (400 ~ 700 nm), as well as the

improved probe focus that results, allows SEM to achieve a much better resolution than optical microscopes. TEM uses even larger accelerating voltages of 100 ~ 400 kV, further improving the resolution.

When electron beam illustrates on a specimen, the interaction volume forms a teardrop shape (**Figure 2-3a**). A few events would take place. Loosely bound electrons are ejected by collisions with incoming electrons and form secondary electrons (SE, **Figure 2-3b**). Their energies are typically low, so that only those near the surface of the specimen (~ 10 nm depth) are able to reach the detector on top (SEM case) while deeper ones are absorbed on their way out. Thus, the volume width of SE is close to the spot size of the beam, providing good spatial resolution and is commonly used for image formation.

At the same time, the incident electrons are elastically scattered by the specimen. Those with a scattering angle > 90 ° are called backscattered electrons (BSE, **Figure 2-3b**). Heavier elements scatter more strongly than lighter ones; thus, the BSE provide information about

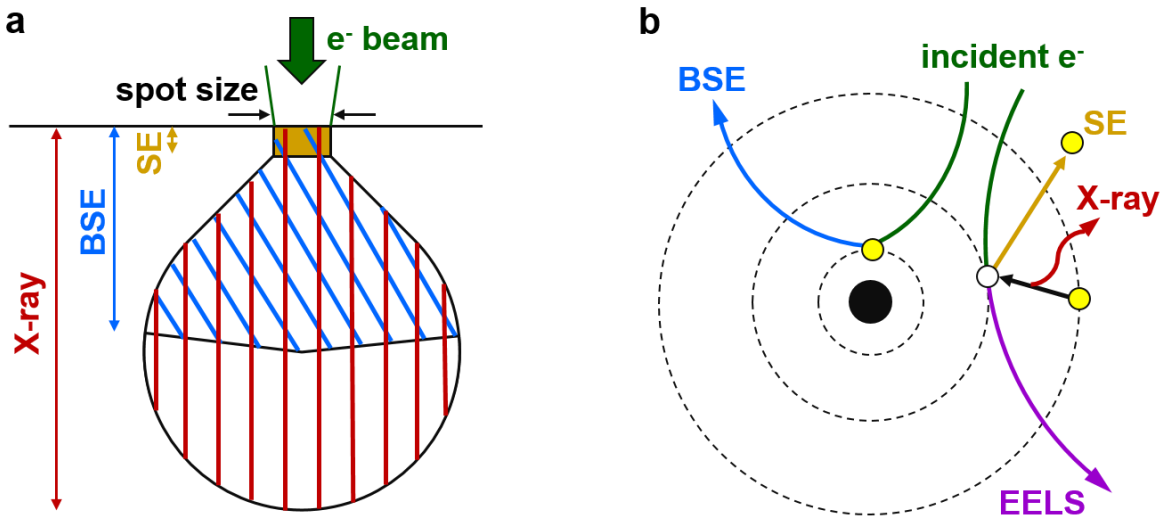

Figure 2-3. Schematic diagrams of (a) teardrop shape of the interaction volume in SEM and (b) different types of interaction between the incident electron beam and specimen.

chemical contrast (Z-contrast). With larger energies than SE, deeper BSE (1 ~ 3 μm depth) can be measured by the detector as well. However, due to the teardrop shape of the interaction volume, the spatial resolution of the image formed by BSE is worse.

When a core electron is ejected, an electron from the outer shell will fill its orbital and X-ray is emitted (**Figure 2-3b**). The energy of this X-ray is related to the orbital energy difference and can be used to identify the specific element. Thus, EDX is normally coupled with an SEM to study the chemical composition of the specimen. The X-ray emitted from the entire interaction volume will be detected, so that its spatial resolution is similar to BSE.

The incident electrons would also interact with the sample to form photons and Auger electrons, which find their usages in cathodoluminescence and Auger electron spectroscopy, respectively.

If the conductivity of the specimen is not good, electrons will accumulate and the surface becomes charged (bright in the image). This further repels the incident beam and causes image distortion. As a result, a conductive coating, normally Au, is required for non-conductive samples.

With thin samples and high energy electron beams, the incident electrons will pass through the specimen. This is the case for TEM. In addition to the higher resolution image, TEM also provides higher resolution for EDX since the interaction volume is only the neck part of the teardrop in a thin specimen. The electrons would also be diffracted by the lattice planes, which finds use in the electron diffraction technique. Besides, the electrons would lose energy by colliding and ejecting bonded electrons (**Figure 2-3b**). This energy loss, collected

by EELS, can be used to study the ionization energy, bonding state, oxidation state, etc. of the elements in the specimen.

In this thesis work, the morphological and elemental analysis of the materials was examined with Zeiss Ultra or LEO 1530 field emission SEM equipped with an EDX. TEM images were obtained on a Zeiss Libra 200MC TEM by Dr. Yan Wang-Duffort. High-resolution TEM (HRTEM) images and EELS were obtained with FEI TITAN 80-300 eV TEM/STEM operated at 300 kV at Pacific Northwest National Laboratory (PNNL). The microscope was outfitted with a spherical aberration corrector for the probe-forming lens, enabling sub-Angstrom resolution in the TEM and STEM mode. The electron energy loss spectra were acquired with a monochromated electron gun, providing chemical and electronic structure analysis with atomic level resolution measurements. The experiments and data analysis were carried out by Drs. B. Layla Mehdi and Nigel D. Browning.

2.5 X-Ray Photoelectron Spectroscopy

XPS is a surface sensitive technique and characterizes the oxidation states of elements in the specimen. By illustrating X-ray on the specimen, electrons are emitted due to photoelectric effect. The binding energy of such photoelectrons, related to the energy of the origin orbital thus the bonding environment of the element, can be calculated from their kinetic energy that is measured by the detector:

$$E_{binding} = E_{photon} - E_{kinetic} - \phi \qquad \textbf{Equation 2-11}$$

where ϕ is the work function. Once photoelectrons are produced, they would interact with the surrounding material and get absorbed. Only those near the surface are able to escape from the sample and reach the detector in spite that X-ray beam can penetrate ~ 1 mm down in the

specimen to produce photoelectrons. Thus, XPS provides information on the elements at 1 ~ 10 nm depth of the specimen.

When a photoelectron is emitted from the p orbital of an element containing unpaired d electrons, the unpaired electrons from either orbital will couple with each other, resulting in multiple final states. This gives rise to multiplets in the XPS spectrum and allows to distinguish among the compounds with elements at the same oxidation state. Using this principle, the Mn 2p spectra were used to identify the manganese species in Chapter 4.

The XPS measurements were carried out on a Thermo VG Scientific ESCALab 250 instrument. Spectra were processed using Gaussian-Lorentzian functions and a Shirley-type background with CasaXPS software and referenced to adventitious carbon at 285.0 eV.

2.6 X-Ray Absorption Near Edge Spectroscopy

XANES also studies the oxidation states of elements but it provides information of the bulk material. When a specimen is illustrated by X-ray, a core electron would absorb the X-ray and get excited to an unoccupied orbital, leaving a hole on the core orbital. This is a highly unstable state, so that electron from higher energy level is relaxed to fill the hole right after, together with a fluorescence of X-ray. The energies of both the absorbed and the fluorescent X-ray reveal the orbital energies and can be measured by a transmission mode or a fluorescence mode of XANES, respectively. The spectra are then used to study the oxidation states and bonding environments of the elements.

In this thesis work, XANES measurements were performed at the sector 9-BM-B at the APS using a Si(111) crystal monochromator. The spectra were normalized to unity absorption well above the edge after a linear background subtraction with Demeter software.[98] Data

acquisition and analysis were carried out with the help of Drs. Mahalingam Balasubramanian, Marine Cuisinier, and Guerman Popov.

2.7 Fourier Transform Infrared Spectroscopy

FTIR determines the vibration energies of chemical bonds in the material, allowing the identification of bond types. Samples in the forms of solid, liquid or gas can all be measured. In this thesis work, solid FTIR was carried out. The sample was ground with 100 ℃ vacuum dried KBr and pressed into a pellet in an Ar-filled glovebox. The spectra were recorded in a Bruker Tensor infrared spectrometer under a dry N_2 flow. The background scan was performed with bare KBr, the signal of which was subtracted from the spectra with the samples.

2.8 Thermal Analysis

TGA is carried out by heating up a small amount of sample at certain rates and recording the weight change with temperature. It is often coupled with a differential scanning calorimetry (DSC) that measures the heat flow in the system. They result in the thermal stability as well as the phase transformation temperatures of the material and are also used to track the reacting temperatures of a mixture. In this thesis work, TGA and DSC were performed with TA Instruments SDT Q600 under a flow of dry air or N_2.

2.9 Combustion Analysis

When a material contains C, N or H, it will produce CO_2, N_2 and H_2O upon combustion. By measuring the weight of initial material and the amount of evolving gases, the percentages of the corresponding elements can be calculated, providing a clue to the unknown composition.

In this thesis work, combustion analysis was carried out on a 4010 Elemental Analyzer with the assistance of William Mark.

2.10 Karl Fischer Titration

In nonaqueous battery systems, the amount of water in electrolyte is critical to the electrochemical performance so that should be carefully evaluated. With coulometric Karl Fischer analysis, water content between 1 ppm to 5% can be accurately determined. The titrator constructs of an electrolytic cell. The working principle is based on the following reaction:

$$ROH + SO_2 + 3\,RN + I_2 + H_2O = (RNH)\,SO_4R + 2(RNH)I \qquad \textbf{Equation 2-12}$$

During the measurement, I_2 generated from the electrochemical oxidation of I^- at the anode reacts with water, while RNH^+ is reduced to form RN and H_2 at the cathode. The amount of water is calculated from the electrons passing through the electrolytic cell.

In the thesis work, the water contents in non-APC based nonaqueous electrolytes were determined by Karl Fischer titration with Mettler Toledo Coulometric Karl Fischer Titrator C30. The as-prepared electrolyte was added to the titrator directly for the measurement, while that after cycling was extracted using dry acetonitrile. Two to three measurements were taken for each sample.

2.11 Electrochemical Techniques

In order to carry out electrochemical tests, the material is cast into electrodes first. The active material is often mixed with carbon to improve the electric conductivity and binder additives to increase the elasticity and viscidity. The mixture is ground in solvent and cast onto a metal or carbon foil, and the solvent is allowed to evaporate afterwards. The electrode, which is

normally cut into a circular shape, is assembled in a battery cell in the order of positive electrode, separators with electrolyte, negative electrode, spacer and spring (**Figure 2-4**). The spring is necessary to maintain a constant pressure among each component in the cell. Steps should be carried out in an inert atmosphere whenever air sensitive component is involved; however, the air-tight seal of the cell allows to carry out electrochemical measure in the ambient atmosphere.

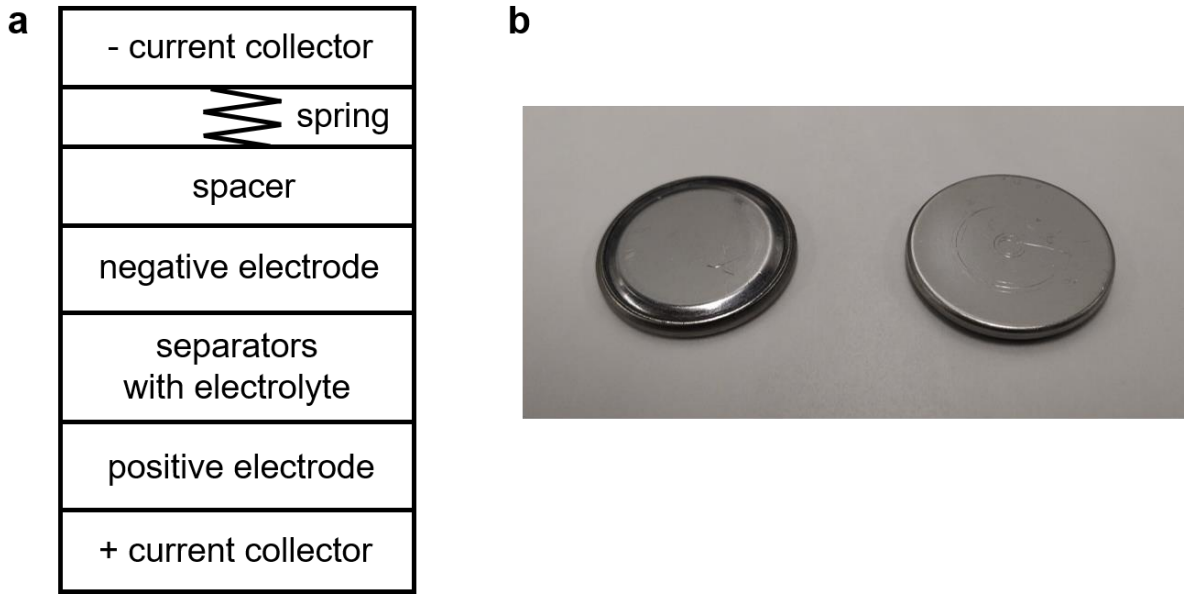

Figure 2-4. (a) Schematic diagram of internal components and (b) picture of coin cells.

Galvanostatic charge and discharge is usually used to study the capacity, rate capability and capacity retention of an electrode. By applying a constant current, the electrode is oxidized/reduced while cations (Mg^{2+}, Li^{+}, etc.) are de/inserted, resulting in a change in the capacity and cell voltage. The voltage response could be either a linear increase/decrease with respect to capacity, corresponding to a solid solution de/insertion mechanism, or a flat plateau resulting from a two-phase reaction. When approaching the capacity limit, a faster increase/drop of voltage would be observed. A voltage limit is often set to terminate a half

cycle for galvanostatic measurements. For measurements at elevated temperatures, the cells are placed in a thermostatted oven.

The “C-rate” is a common way to define the current applied for cycling. The “C” is the specific capacity obtained with the de/insertion of one ion or electron per formula unit, while C/x equals the current that allows to reach such capacity within x hours theoretically. In most cases, however, the theoretical capacity cannot be obtained and the actual time for a half cycle is less than x hours. Alternatively, current densities with the unit of mA g^{-1} are also used to define the current used to charge and discharge a cell. The actual current is calculated by multiplying the current density by the mass of active material. Note that the “C-rate” and current density are effectively the same and can be converted back and forth.

Taking the derivative of capacity against voltage results in a differential capacity (dQ/dV) curve. The peaks correspond to the different electrochemical steps. The information given by a dQ/dV plot is similar to CV where a constant potential sweep rate is applied to the cell and current responses are recorded; however, CV forces the system beyond its kinetic limit so that some capacity cannot be accessed. On the other hand, CV contains rate capability information and is often used for testing electrolytes.

The electrochemical measurement can be carried out with two electrode or three electrode configurations. In the two electrode setup, the material of interest is assigned as the working electrode (WE), while the other electrode serves as both the auxiliary electrode (AE, also called counter electrode) and the reference electrode (RE). In order to be a good RE in addition to an AE, the AE should have a small overpotential and a stable voltage during electrochemical processes. Lithium and sodium metals in rechargeable Li and Na cells are good such examples, so that their positive electrode materials can be studied in two electrode

configurations with the corresponding metal as the AE/RE. The readily available two-electrode cell designs include coin cells and Swagelok cells. Due to the easy assembly and low price of two electrode cells, they are preferred if a separate reference electrode is not necessary.

Since the result given in the two electrode setup is a combination of WE and AE signals, an approximation is taken here that the electrochemical response at AE is small enough so that the overall result represents the properties of the WE. However, sometimes the WE signal needs to be well separated in order to study the mechanisms in detail, or there is no suitable material to serve as both the AE and RE. In those cases, an individual RE is required and this can be accomplished in the three electrode setup. A good RE material should provide a stable and accurate voltage. Examples include the silver/silver chloride electrode, saturated calomel electrode, and mercury/mercury oxide electrode for aqueous systems, as well as silver/silver nitrate and ferrocene for non-aqueous systems. A simple setup is obtained by immersing the three electrodes in a beaker cell. There are also other available three-electrode cell designs, such as the Conflat cell,[99] T-shaped Swagelok cell,[100] and modified coin cell,[101] where the cells are airtight and only a small amount of electrolyte is required.

In this thesis work, the positive electrodes were prepared by grinding the active material with Super P and polyvinylidene fluoride (PVDF, average Mw ~ 534,000) in an 8:1:1 weight ratio in N-methyl-2-pyrrolidone (NMP) and casting the slurry onto Mo foil or carbon paper. Magnesium metal was polished with carbide paper (Mastercraft ®, 180 grit SiC) and cleaned prior to use. Coin cells (2325) with Mg counter electrodes were used for two electrode studies, while Conflat cells with Mg reference electrodes or T-shaped Swagelok cells with Ag/AgCl reference electrodes were assembled for three electrode measurement. All electrochemical measurements were performed with a VMP3 potentiostat/galvanostat cycler. (Bio-logic).

Chapter 3

Synthesis, Electrochemistry and Mechanism Investigation of Spinel and Layered Titanium Sulfides as Positive Electrode Materials for Mg Batteries

3.1 Overview of Titanium Sulfide

The search for positive electrode materials able to reversibly intercalate Mg^{2+} and which present a higher energy density than Mo_6S_8 has been generally unrewarding and the Chevrel phase has remained the benchmark for magnesium batteries. It has been realized that magnesium electrochemistry is more difficult than that of its monovalent alkali cation cousins such as lithium and sodium. The lower mobility of Mg^{2+} ions within solid oxide hosts[33,50,102-104] and a probable higher energy penalty for the desolvation of Mg^{2+},[81] are among the limiting factors identified so far. To date, oxide positive electrode materials exhibit extremely sluggish kinetics,[105] and conversion materials lack the required cycle life.[26] On the contrary, solid frameworks with softer anions, such as sulfur and selenium, offer better opportunity for facile multivalent ion diffusion due to the weaker coulombic attraction between the guest ions and host lattice. Among the various candidates, sulfide based compounds are lighter and more electronegative, offering a higher specific capacity and voltage, thus higher energy density, when used as positive electrode materials.

Titanium sulfides, in particular, are of great interest. They could form a layered or spinel structure (a second cation normally presents in the latter). The layered polymorph is constructed of hexagonal close packed (hcp) sulfur, with titanium occupying all the octahedral sites every other layer, resulting in 2D ion pathways through the empty layers (**Figure 3-1**).

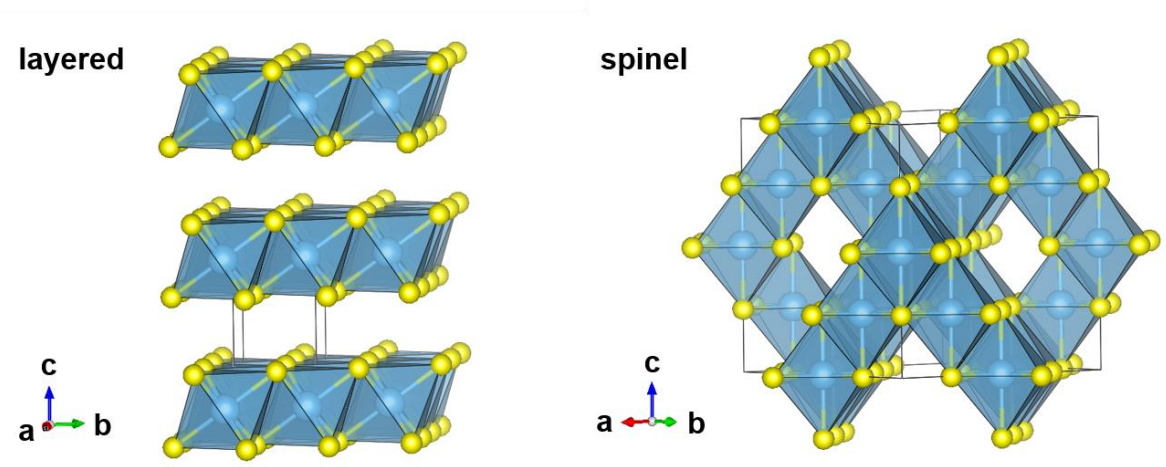

Figure 3-1. Crystal Structure of layered (left) and spinel (right) titanium sulfide. Ti atoms are shown in blue and S atoms are in yellow. The TiS_6 octahedra are drawn to demonstrate ion migration tunnels. Cu ions are not shown for simplicity.

The spinel phase, on the other hand, has cubic close packed sulfur, and titanium occupies every other octahedral sites in all directions. This forms 3D ion tunnels in the structure (**Figure 3-1**). The layered structure is a stable phase while the spinel is metastable at room temperature. It will transform to the former as temperature increases above 700 K.[106] Thus, solid state synthesis from the elements forms the more stable layered compound,[107] whereas the spinel phase needs to be obtained by electrochemical[106] or chemical[108-110] removal of Cu from spinel $CuTi_2S_4$ and trace Cu normally remains in the structure (~ $0.1Cu/Ti_2S_4$, Cu^+ is omitted in describing the compound in this thesis for simplicity).

No electrochemistry studies on Mg^{2+} intercalation into either of the titanium sulfide compound have been demonstrated; nevertheless, they are promising Mg positive electrodes as suggested by related studies. Highly reversible and facile Li^+ de/intercalation has been observed into both structures[2,108] – in fact, the layered polymorph is the first Li battery positive electrode (Chapter 1). Although this could not be derived to the Mg case directly, the success of chemical magnesiation into both structures suggests some Mg^{2+} mobility in the lattice. A

maximum of 0.25Mg/TiS_2 can be inserted into the spinel phase through chemical method and gives rise to an expansion of unit cell. On the other hand, inhomogeneous Mg^{2+} insertion is observed for the layered material, resulting in a two phase mixture with cell expansion shown in one of the them. An in-depth theoretical study predicts a ~ 550 meV Mg^{2+} diffusion barrier in both lattices when allowing 10% volume expansion,[111] which would provide reasonable Mg^{2+} diffusivity, at least at elevated temperature.

This chapter describes the first utilization of spinel and layered titanium sulfides as positive electrode materials for Mg batteries. The reversible Mg^{2+} de/intercalation is proven, and corresponding mechanism is investigated in details.

3.2 Spinel Ti_2S_4

3.2.1 Synthesis and Characterization of Spinel Ti_2S_4

The spinel Ti_2S_4 (labeled as C-Ti_2S_4) was synthesized following Bruce's method.[110] Typically, $CuTi_2S_4$ was first obtained by grinding the stoichiometric mixture of Cu, Ti and S elements, pressing into pellets in an Ar-filled glovebox, and sealing in an evacuated quartz tube. Subsequent sintering was carried out at 700 ˚C for 2 weeks with an intermediate grinding. The product was then added to 1 M Br_2 in acetonitrile (ACN) solution with molar ratio 1:2 between $CuTi_2S_4$ and Br_2, and stirred for 3 days at room temperature under Ar for chemical de-copperation. The mixture was filtered, washed with ACN and CS_2 to retrieve the C-Ti_2S_4 solid.

To reduce the particle size, ball milling was carried out with a Pulverisette 23 mini-miller. 1 g C-Ti_2S_4 solid and 1.5 mL ACN were added to a 15 mL ZrO_2 jar containing 12 g of 5 mm ZrO_2 balls, and ball milled for different periods at 30 Hz in an Ar-filled glovebox. The solid was collected after evaporation of ACN solvent.

The crystal structure of C-Ti_2S_4 was confirmed by Rietveld refinement[92] of the XRD pattern (**Figure 3-2** and **Table 3-1**), showing a single cubic *Fd*-3*m* phase with a stoichiometry of $Cu_{0.1}$Ti2S4 and a lattice parameter of 9.776 Å. Such results indicate that some residual copper remains in the thiospinel, as also suggested by EDX analysis (see later). This is in

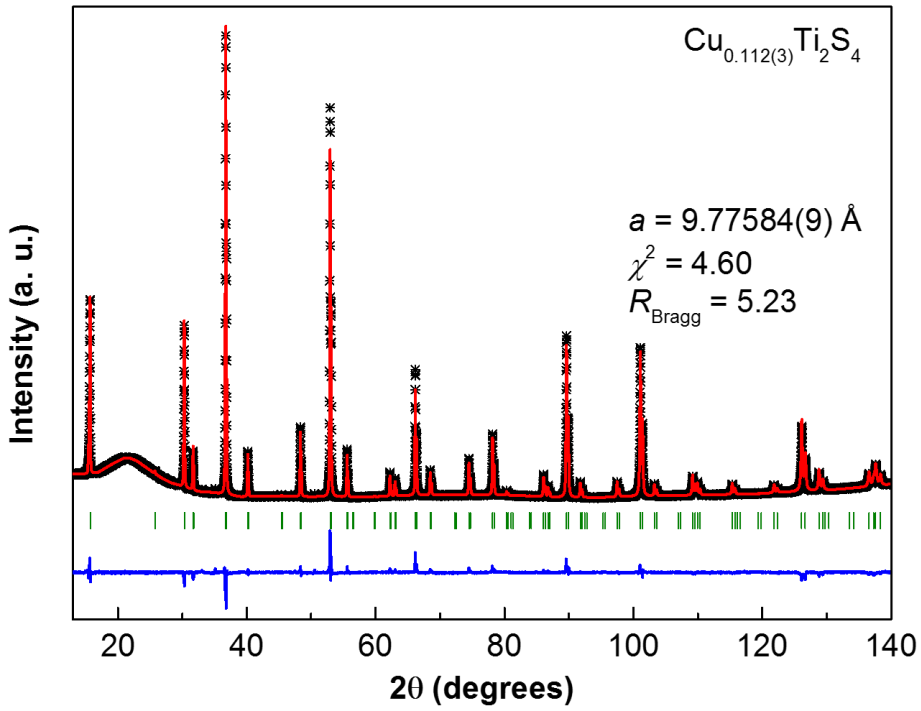

Figure 3-2. Rietveld refinement fit of C-Ti_2S_4. XRD was taken with Debye-Scherrer geometry. Black crosses – experimental data, red lines – fitted data, blue line – difference curve between observed and calculated data, green ticks – the Bragg peak positions. The broad hump is a background signal from the X-ray capillary.

Table 3-1. Refined parameters for de-copperiated C-Ti_2S_4 (space group = *Fd*-3*m*, *a* = 9.77584(9) Å, χ^2 = 4.60, Bragg *R*-factor = 5.23).

Atom	**Wyck.**	***x***	***y***	***z***	**Occ.**	B_{iso} **(Å^2)**
Cu	8a	0.125	0.125	0.125	0.112(3)	1.0
Ti	16d	0.5	0.5	0.5	1.00	1.05(2)
S	32e	0.25161(5)	0.25161(5)	0.25161(5)	1.00	0.80(2)

agreement with previous results where the incomplete extraction of Cu^{+} observed.[108,109] The particle size of the as synthesized C-Ti_2S_4 ranged from 1 to 10 μm, and was reduced to around 1 μm after ball milling (**Figure 3-3**).

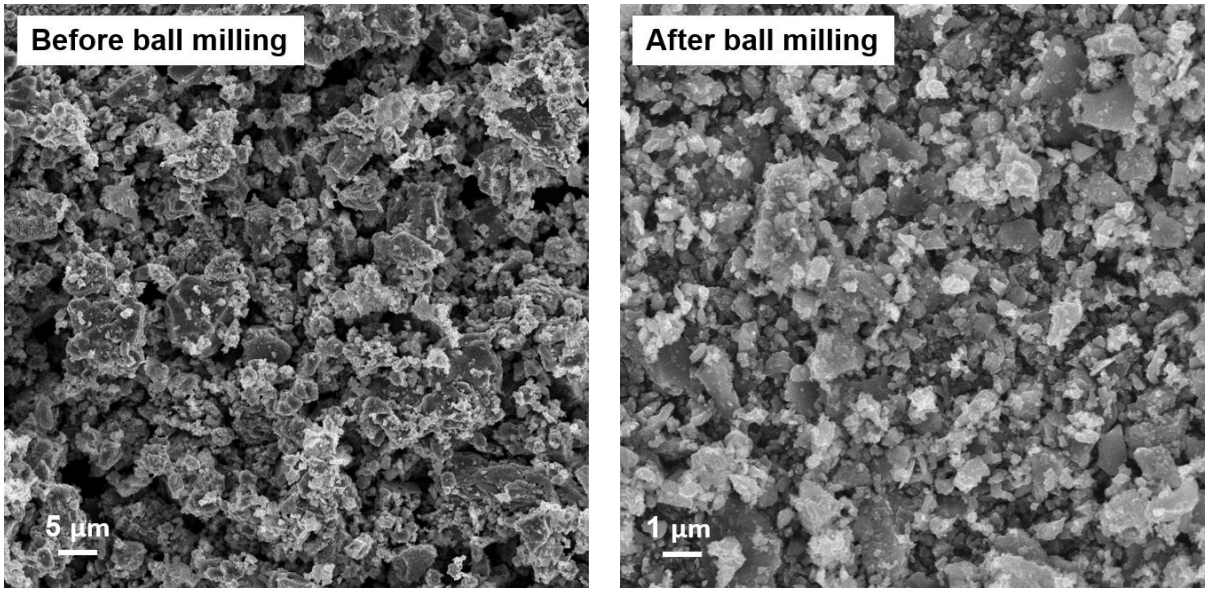

Figure 3-3. SEM images of C-Ti_2S_4 before (left) and after (right) 4h ball milling.

3.2.2 Electrochemistry of Spinel Ti_2S_4

APC based electrolyte was used for electrochemical studies of titanium sulfides. The APC in tetrahydrofuran (APC/THF) electrolyte was synthesized by a slow addition of 0.5334 g $AlCl_3$ into 6 mL distilled THF and stirred for 1 h. 4 mL of 2 M phenylmagnesium chloride in THF was then added to the above solution, and the mixture was stirred overnight.[72] Such electrolyte shows low overpotential for Mg stripping/plating and high reversibility (**Figure 3-4**), which makes it desirable to study the voltage profiles of positive electrode material in a 2 electrode cell. However, THF has a low boiling point of 66 ˚C and tends to evaporate through the gasket of coin cells slowly. Thus, tetraglyme with a 275 ˚C boiling point (electrolyte labeled as APC/G4[59]) was used instead for long term cycling tests at evaluated temperature.

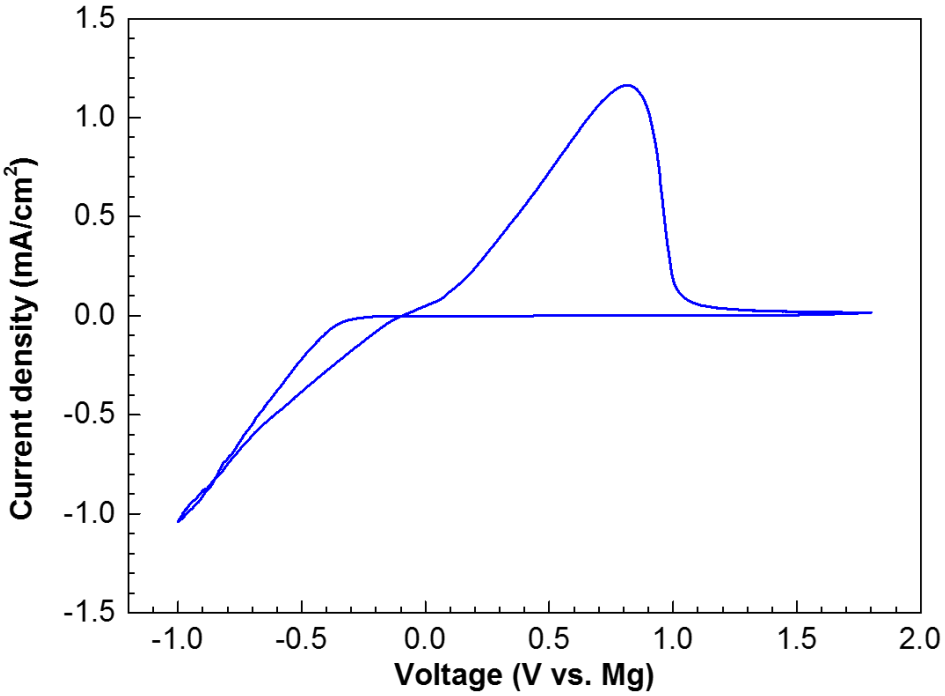

Figure 3-4. CV of APC/THF electrolyte tested in 2 electrode coin cell at 10 mV s^{-1} and room temperature.

Titanium sulfide positive electrode materials were tested in galvanostatic mode with 2 electrode coin cells using Mg as the negative electrode and APC as the electrolyte. The electrochemistry of C-Ti_2S_4 was firstly investigated at room temperature in APC/THF electrolyte. At a C/50 rate (1C = 1 Mg^{2+}/C-Ti_2S_4 in 1 h, **Figure 3-5**), initial discharge capacity reaches 130 mAh g^{-1} which is already the theoretical value for the CP. The performance is further enhanced with cells running at 60 ˚C. As shown in **Figure 3-6**, an initial discharge capacity of 200 mAh g^{-1} – corresponding to $Mg_{0.84}Ti_2S_4$ – is achieved at C/20 (black curve), with an overpotential as low as 50 mV from equilibrium. The sloping curve between 1.5 V to 1 V demonstrates a solid-solution Mg^{2+} insertion mechanism, in agreement with the previous prediction by theory.[111] Such values yields 240 Wh kg^{-1} specific energy, which doubles the CP

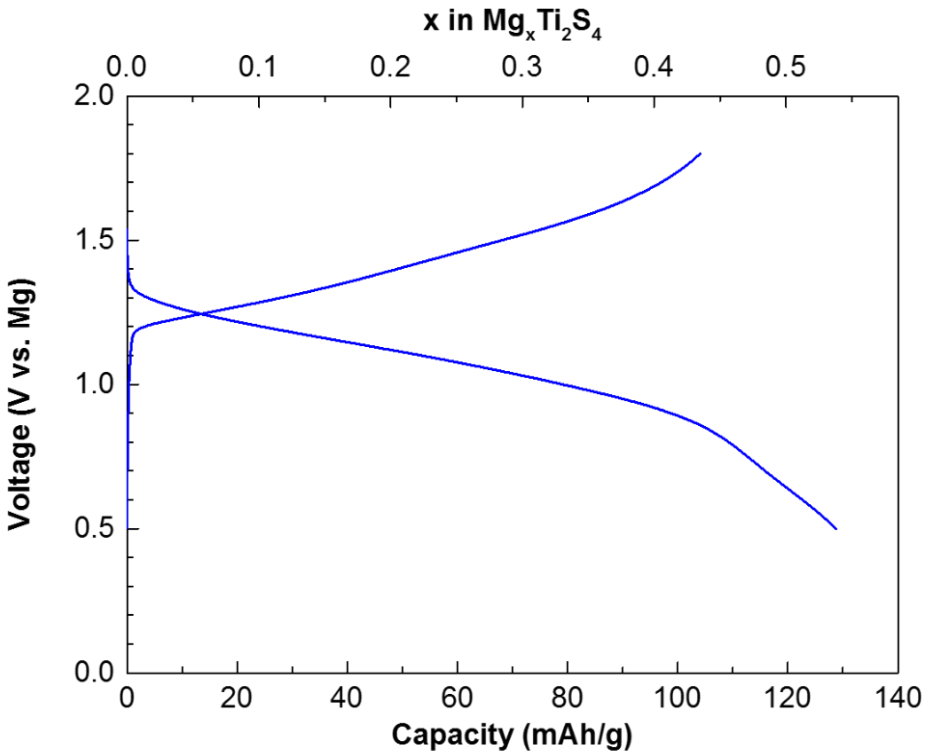

Figure 3-5. Discharge and charge curves of C-Ti_2S_4 tested in coin cells with APC/THF electrolyte and a Mg negative electrode at 60 ˚C and C/50

benchmark. As the cycling rates increase to C/10 and C/5, the discharge capacity slightly drops to 195 mAh g^{-1} and 190 mAh g^{-1}, respectively, demonstrating the surprisingly good rate capability of the material. At all three rates, the first charge shows minor irreversible capacity (10% at C/5), which disappears on the 2nd cycle (**Figure 3-6** inset).

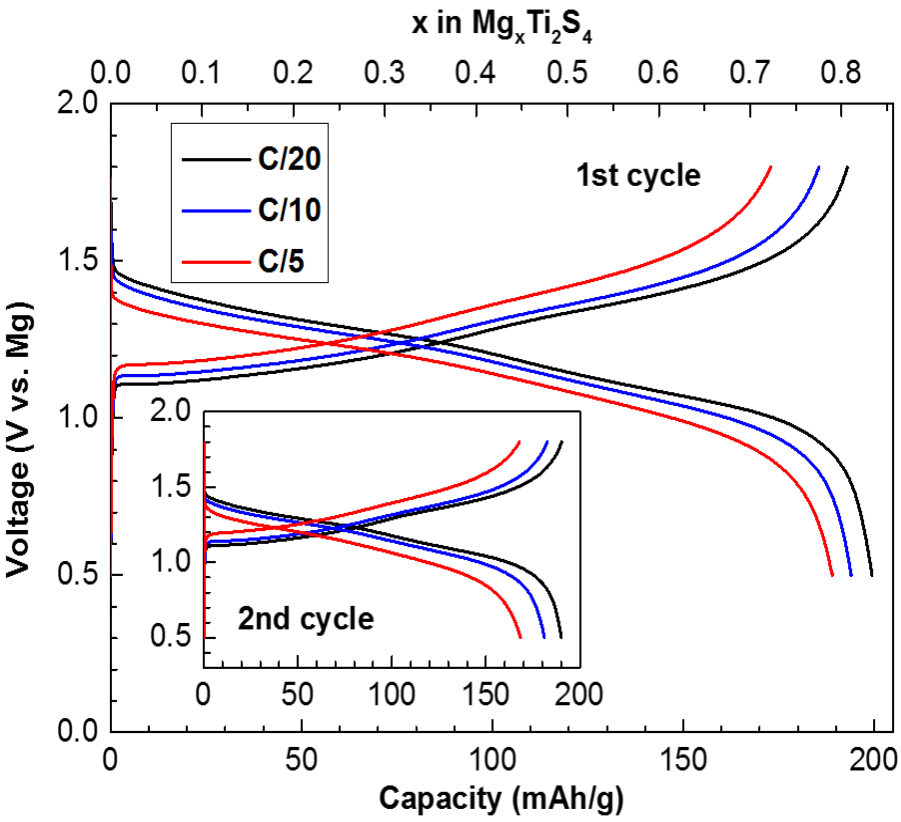

Figure 3-6. Discharge and charge curves of the first and second (inset) cycles of C-Ti_2S_4 tested in coin cells with APC/THF electrolyte and a Mg negative electrode at 60 ˚C and various rates.

Long term cycling was examined in APC/G4 electrolyte at 60 ˚C. Similar capacities of 195 mAh g^{-1} at C/20, dropping to 175 mAh g^{-1} at C/5, are observed in such electrolyte (**Figure 3-7**). The slightly larger polarization comparing to APC/THF data is a result of the higher Mg stripping/plating overpotential at the negative electrode. From cycle 2 onward (**Figure 3-9**), the drop levels off, and a capacity of 140 mAh g^{-1} is attained after 40 cycles at C/10. The origin of the cycling fade might be due to the micron-sized active material particles that would kinetically trap Mg^{2+} during charge. By reducing the particle size through ball milling (**Figure 3-3**), hence the ion diffusion length, an improved retention is obtained with capacity stabilized at 130 mAh g^{-1} up to 70 cycles after the initial formation cycles (**Figure 3-8**). Note the initial lower capacity of ball milled material is due to the fact that a small amount of ZrO_2 scratched from ball mill jar was counted for active material mass as well.

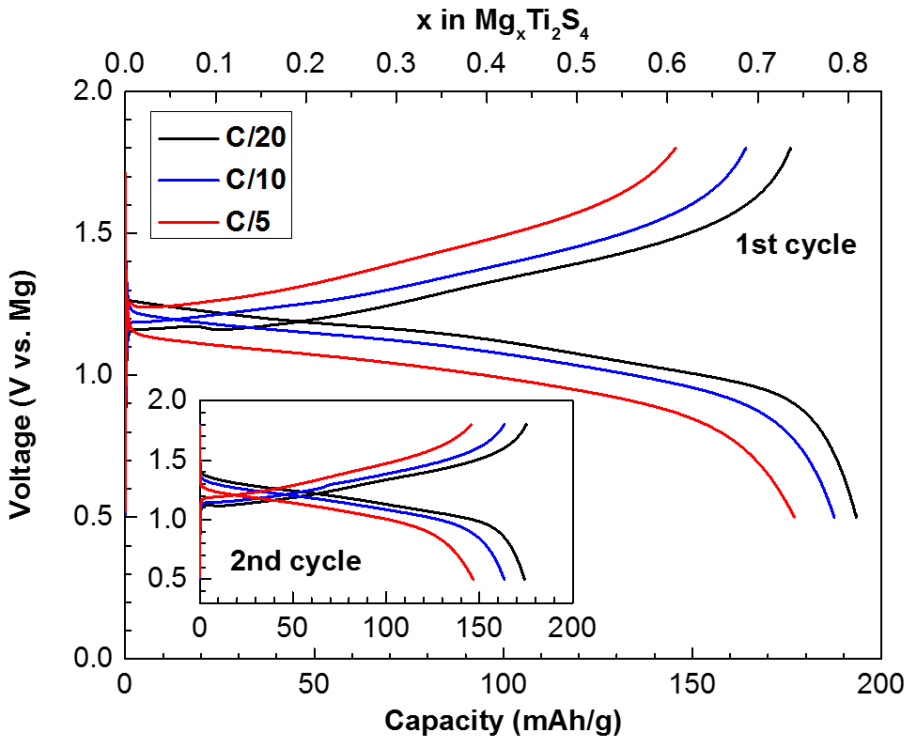

Figure 3-7. Discharge and charge curves of the first and second (inset) cycles of C-Ti_2S_4 tested in coin cells with APC/G4 electrolyte and a Mg negative electrode at 60 ˚C and various rates.

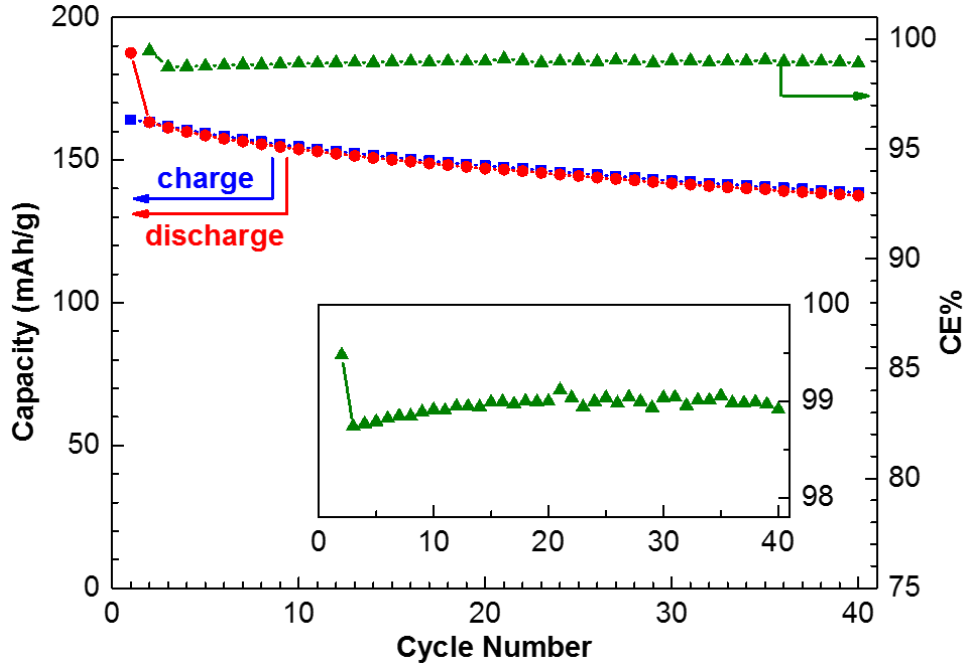

Figure 3-9. Capacity and coulombic efficiency (CE) evolution of C-Ti_2S_4 at a C/10 rate in APC/G4 electrolyte (inset showing 99% CE).

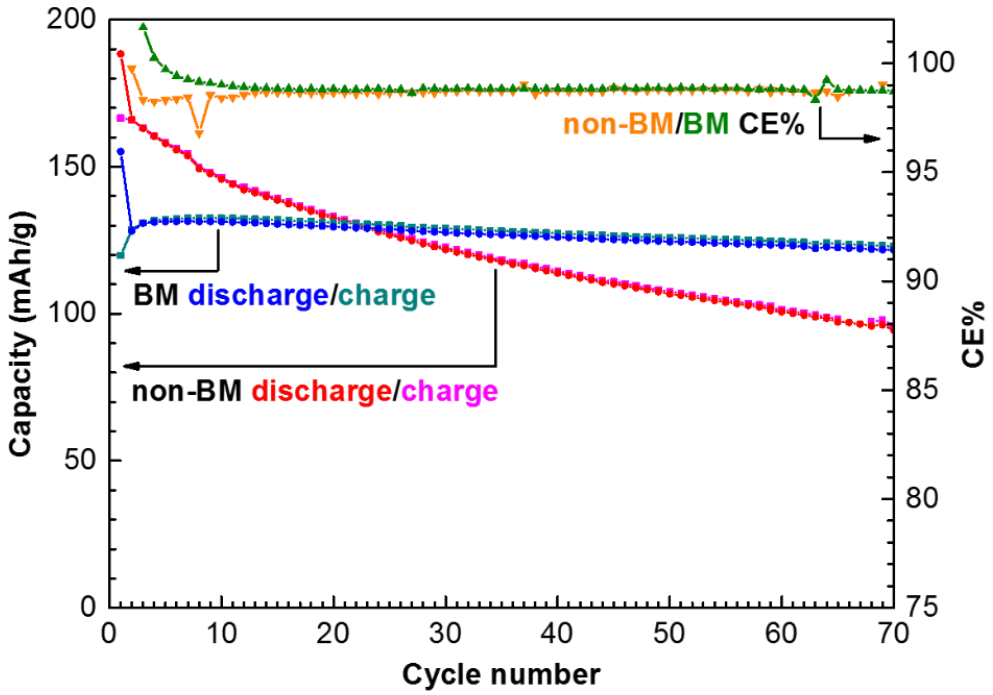

Figure 3-8. Capacity and coulombic efficiency (CE) evolution comparison of non-ball milled (non-BM) and ball milled (BM) C-Ti_2S_4 at a C/5 rate in APC/G4 electrolyte.

3.2.3 Investigation of Mg^{2+} De/Intercalation Mechanism into Spinel Ti_2S_4 by XRD, EDX and XANES

The reversible intercalation of Mg^{2+} into C-Ti_2S_4 is confirmed by XRD as shown in **Figure 3-10**, and by energy EDX (**Table 3-2**). Rietveld refinement[92] of the discharged XRD pattern (**Figure 3-12**) demonstrates the preservation of the *Fd*-3*m* cubic spinel phase, with lattice parameters expanded to 10.097 Å from their pristine values (9.776 Å) on electrochemical magnesiation of 0.8 Mg^{2+}. Fourier mapping carried out with Cu, Ti, and S occupying their normal sites reveals electron density on both the tetrahedral (8a) and octahedral (16c) sites

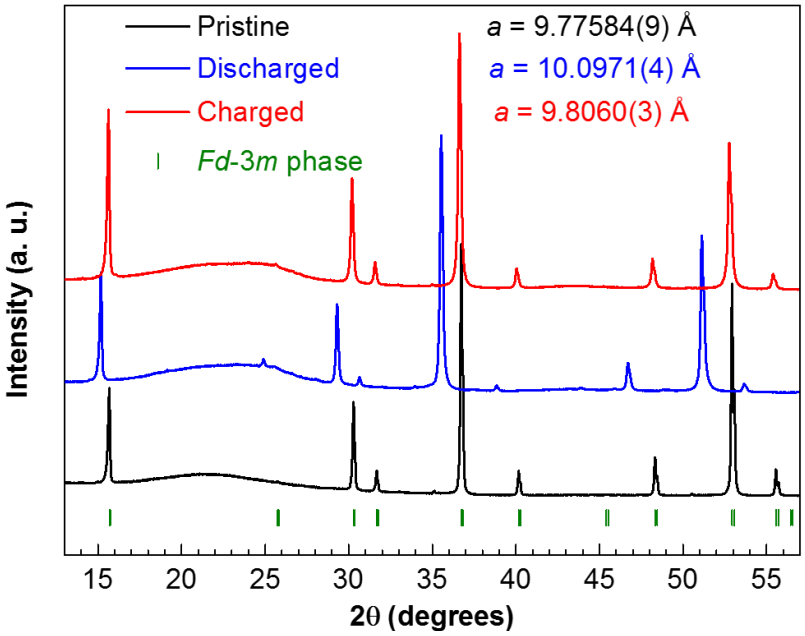

Figure 3-10. Comparison of the XRD pattern of the initial C-Ti_2S_4 spinel (black), with the discharged (blue) and charged (red) states. The electrodes were cycled in APC/THF electrolyte with a Mg negative electrode at 60 ˚C and C/20.

Table 3-2. EDX results for C-Ti_2S_4 (electrodes cycled in APC/THF electrolyte with a Mg negative electrode at 60 ˚C and C/20).

Sample	**Pristine**	**Discharged**	**Charged**
EDX	$Cu_{0.09(2)}Ti_2S_{3.57(8)}$	$Mg_{0.79(7)}Cu_{0.10(2)}Ti_2S_{3.69(9)}$	$Mg_{0.084(4)}Cu_{0.127(9)}Ti_2S_{3.91(6)}$

(**Figure 3-11**). Mg is placed on both these sites in the subsequent refinements of Mg occupancy, resulting in ~ 30% occupation of the octahedral 16c site and ~ 20% on the

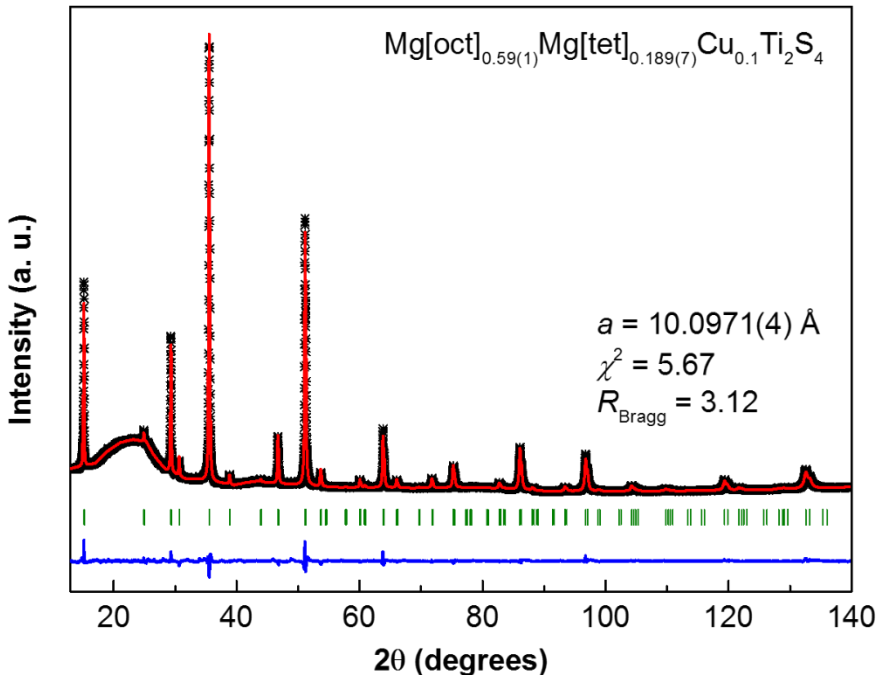

Figure 3-12. Rietveld refinement fit of the discharged sample, $Mg_{0.8}Ti_2S_4$. Black crosses – experimental data, red lines – fitted data, blue line – difference curve between observed and calculated data, green ticks – the Bragg peak positions. The broad hump is a background signal from the X-ray capillary.

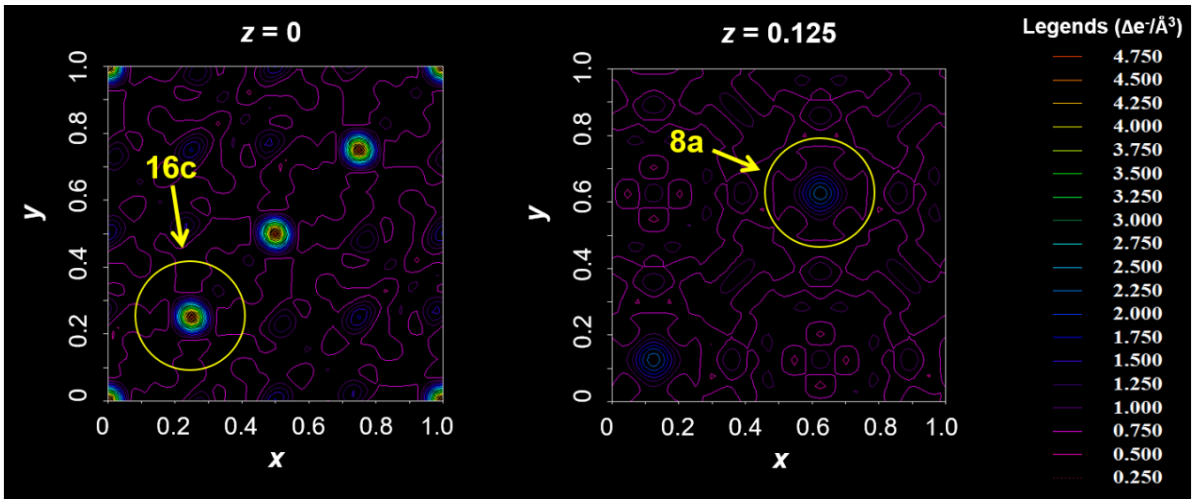

Figure 3-11. Fourier maps of the discharged XRD pattern with only Cu, Ti, S in the structure, showing the missing electron density on the (a) 16c and (b) 8a site in the absence of Mg occupation.

tetrahedral 8a site (**Table 3-3**). The corresponding composition $Mg[oct]_{0.59(1)}Mg[tet]_{0.189(7)}Cu_{0.1}Ti_2S_4$ is in excellent agreement with the electrochemical capacity ($Mg_{0.84}Ti_2S_4$) and the EDX data (**Table 3-2**). Only relatively minor shifts in the atomic positions occur upon magnesiation (**Table 3-1** and **Table 3-3**). Along with the moderate volume expansion on full insertion (10%), this confirms that the structure of the C-Ti_2S_4 thiospinel exhibits little distortion on Mg cycling, which promotes good capacity retention. Upon charging the material, the XRD pattern (red) reverts to the pristine composition with a lattice parameter of a = 9.806 Å. EDX and XRD confirm that Mg^{2+} is essentially removed from the C-Ti_2S_4. The composition of $Mg_{0.08}Ti_2S_4$ determined by EDX (**Table 3-2**) and the tiny increase in the lattice parameter (vis à vis 9.776 Å) are in accord with a trace of Mg remaining on the 16c site (**Table 3-4** and **Figure 3-13**). Overall, the data unequivocally show that the electrochemical activity of the material is due to reversible (de)intercalation of Mg^{2+} into the spinel structure.

Table 3-3. Refined parameters for **discharged** C-Ti_2S_4 (Echem = $Mg_{0.84}$/C-Ti_2S_4, refined = $Mg[oct]_{0.59(1)}Mg[tet]_{0.189(7)}Cu_{0.1}Ti_2S_4$, space group = *Fd*-3*m*, a = 10.0971(4) Å, χ^2 = 5.67, Bragg *R*-factor = 3.12).

Atom	**Wyck.**	***x***	***y***	***z***	**Occ.**	B_{iso} **(Å^2)**
Cu	8a	0.125	0.125	0.125	0.112	1.0
Ti	16d	0.5	0.5	0.5	1.00	1.05
S	32e	0.2551(1)	0.2551(1)	0.2551(1)	1.00	0.80
Mg1	8a	0.125	0.125	0.125	0.189(7)	1.0
Mg2	16c	0	0	0	0.296(5)	1.0

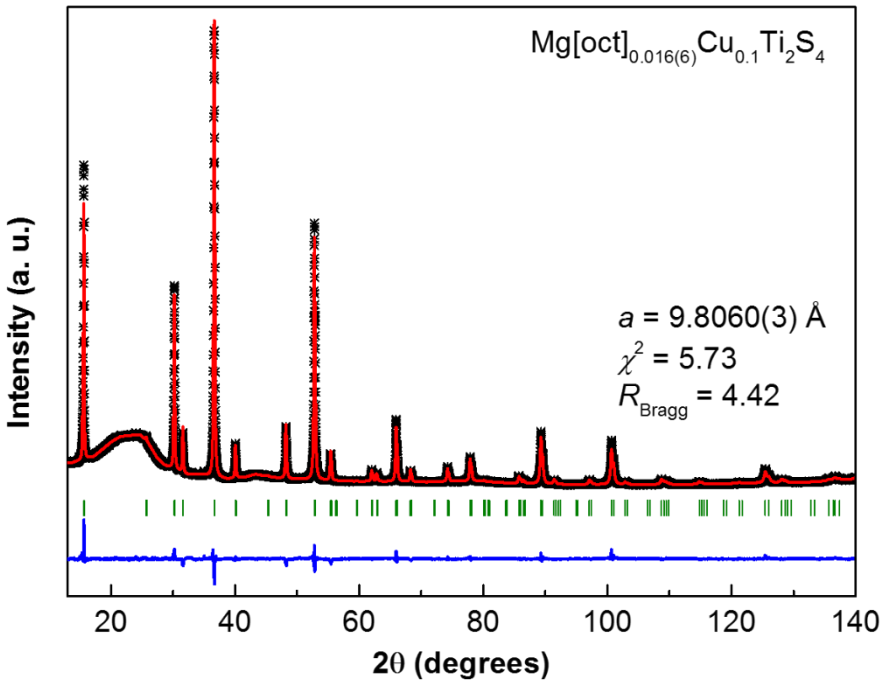

Figure 3-13. Rietveld refinement fit of the charged sample. Black crosses – experimental data, red lines – fitted data, blue line – difference curve between observed and calculated data, green ticks – the Bragg peak positions. The broad hump is a background signal from the X-ray capillary.

Table 3-4. Refined parameters for **charged** C-Ti_2S_4 (Echem = $Mg_{0.03}$/C-Ti_2S_4, refined = $Mg[oct]_{0.016(6)}Cu_{0.1}Ti_2S_4$, space group = *Fd*-3*m*, *a* = 9.8060(3) Å, χ^2 = 5.73, Bragg *R*-factor = 4.42).

Atom	**Wyck.**	***x***	***y***	***z***	**Occ.**	B_{iso} **(Å^2)**
Cu	8a	0.125	0.125	0.125	0.112	1.0
Ti	16d	0.5	0.5	0.5	1.00	1.05
S	32e	0.25296(5)	0.25296(5)	0.25296(5)	1.00	0.80
Mg	16c	0	0	0	0.008(3)	1.0

Since Mg^{2+} occupation on the tetrahedral site was not identified in early studies of chemical magnesiation (albeit limited to $Mg_xTi_2S_4$ where $x < 0.5$),[112] we took a closer look on partially discharged C-Ti_2S_4 materials. At 0.4 and 0.6 Mg/C-Ti_2S_4, refinement reveals that Mg^{2+} on octahedral sites only (**Figure 3-14**, **Table 3-5** and **Table 3-6**), in agreement with the preferential Mg^{2+} occupation on the octahedral site at low content observed by Bruce *et al.* in the entire range of their studies (0.07 – 0.5 Mg/Ti_2S_4).[112] Thus, a somewhat stepwise Mg^{2+} insertion behavior is therefore demonstrated, with the 16c site being filled first, followed by population of the 8a site that is driven by subtle thermodynamic and kinetic factors. The solid solution-like nature of the discharge/charge curves suggests that at the cross-over point, the energetics for occupation of either site are similar and the system lowers its (electrostatic) energy by distributing Mg^{2+} over both tetrahedral and octahedral sites. In fact, first principles calculations (in collaboration with Drs. Ceder and Persson groups at LBNL) shows a rather small energy difference for Mg^{2+} occupation on the octahedral, tetrahedral or mixed states, indicating the disorder across octahedral and tetrahedral sites is quite likely.[113] I propose that upon Mg^{2+} insertion beyond $x = 0.5$, energetics that result in coulombic repulsion favor redistribution amongst the possible sites. Kinetic condition might also change due to the local switchover from the tri-vacancy to di-vacancy diffusion mechanism[114] and affect Mg^{2+} siting. Based on the experimental results, this limitation occurs at about 0.6 Mg^{2+}/ $Cu_{0.1}Ti_2S_4$, upon which point a change on Mg^{2+} occupation behavior takes place so that tetrahedral Mg is present at the end of full discharge.

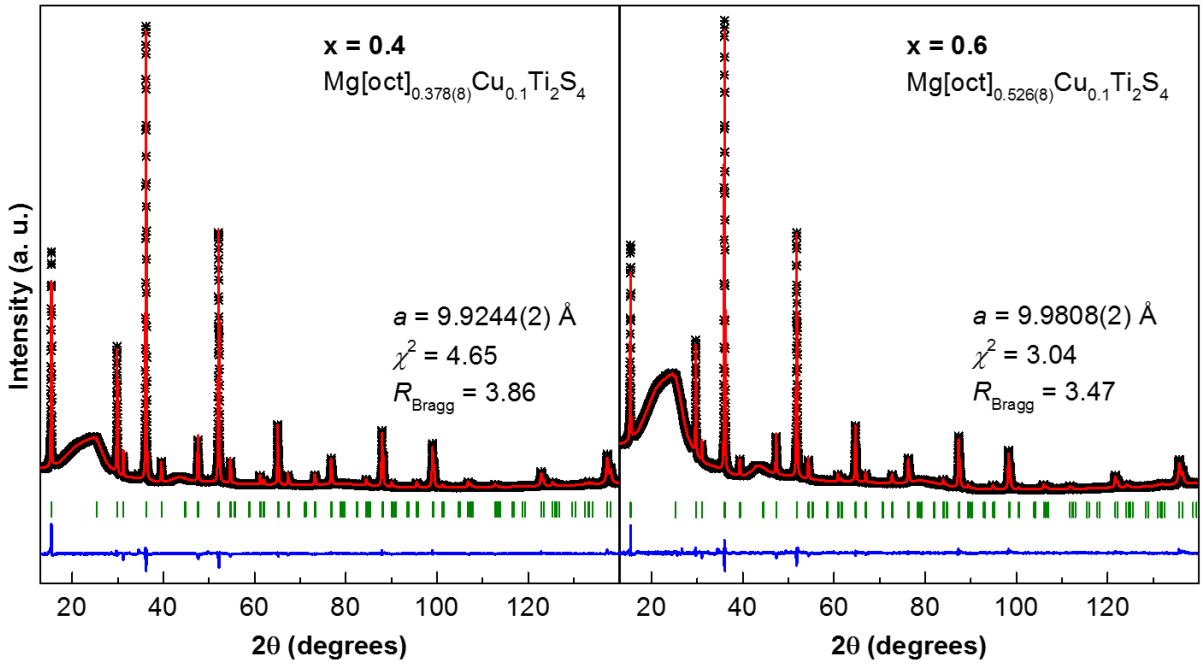

Figure 3-14. Rietveld refinement fit of partially discharged samples, $Mg_{0.4}Ti_2S_4$ (left) and $Mg_{0.6}Ti_2S_4$ (right). Black crosses – experimental data, red lines – fitted data, blue line – difference curve between observed and calculated data, green ticks – the Bragg peak positions. The broad hump is a background signal from the X-ray capillary.

Table 3-5. Refined parameters for **partially discharged** C-Ti_2S_4 (Echem = $Mg_{0.43}$/C-Ti_2S_4, refined = $Mg[oct]_{0.378(8)}Cu_{0.1}Ti_2S_4$, space group = *Fd*-3*m*, *a* = 9.9244(2) Å, χ^2 = 4.65, Bragg *R*-factor = 3.86).

Atom	**Wyck.**	***x***	***y***	***z***	**Occ.**	B_{iso} **(Å^2)**
Cu	8a	0.125	0.125	0.125	0.112	1.0
Ti	16d	0.5	0.5	0.5	1.00	1.05
S	32e	0.25389(5)	0.25389(5)	0.25389(5)	1.00	0.80
Mg	16c	0	0	0	0.189(4)	1.0

Table 3-6. Refined parameters for **partially discharged** C-Ti_2S_4 (Echem = $Mg_{0.6}$/C-Ti_2S_4, refined = Mg[oct]$_{0.526(8)}Cu_{0.1}Ti_2S_4$, space group = *Fd*-3*m*, *a* = 9.9808(2) Å, χ^2 = 3.04, Bragg *R*-factor = 3.47).

Atom	**Wyck.**	***x***	***y***	***z***	**Occ.**	B_{iso} **(Å^2)**
Cu	8a	0.125	0.125	0.125	0.112	1.0
Ti	16d	0.5	0.5	0.5	1.00	1.05
S	32e	0.25411(5)	0.25411(5)	0.25411(5)	1.00	0.80
Mg	16c	0	0	0	0.263(4)	1.0

The oxidation state change during electrochemistry process was investigated by Ti K-edge XANES (**Figure 3-15**). The $CuTi_2S_4$ was measured as a standard point (purple). Upon chemical de-copperation, the Ti edge of C-Ti_2S_4 moves to a higher energy (blue), indicating a loss of electron on the Ti center during oxidation. At the end of discharge (red), Ti is reduced and the energy of the edge drops below $CuTi_2S_4$. This agrees with the lower average oxidation state of Ti in $Mg_{0.84}Cu_{0.1}Ti_2S_4$ ($Ti^{3.1+}$) than in $CuTi_2S_4$ ($Ti^{3.5+}$). Upon charge (green), the Ti edge almost shifts back to the C-Ti_2S_4 position with slightly lower energy, which is due to the trace Mg^{2+} trapping during the first cycle.

Such results demonstrate that Ti is the major redox center during Mg^{2+} de/intercalation. Since Ti 3d band lies slightly above the S 3p band,[115] valence electrons are mostly from the former. This is on the contrary to latter transition metals whose 3d bands start to fall below the S 3p band. For those compounds, holes have to be generated on the S band during oxidation, which, however, is a difficult process due to the high electronegativity of sulfur.[116] In fact, when a similar chemical oxidation procedure was tested for CuV_2S_4 and $CuCr_2S_4$, low or no Cu^+ extraction happened. As a result, the band structure would also be essential for the

excellent electrochemical activity of C-Ti_2S_4. Such information should be taken care of when testing other transition metal sulfides.

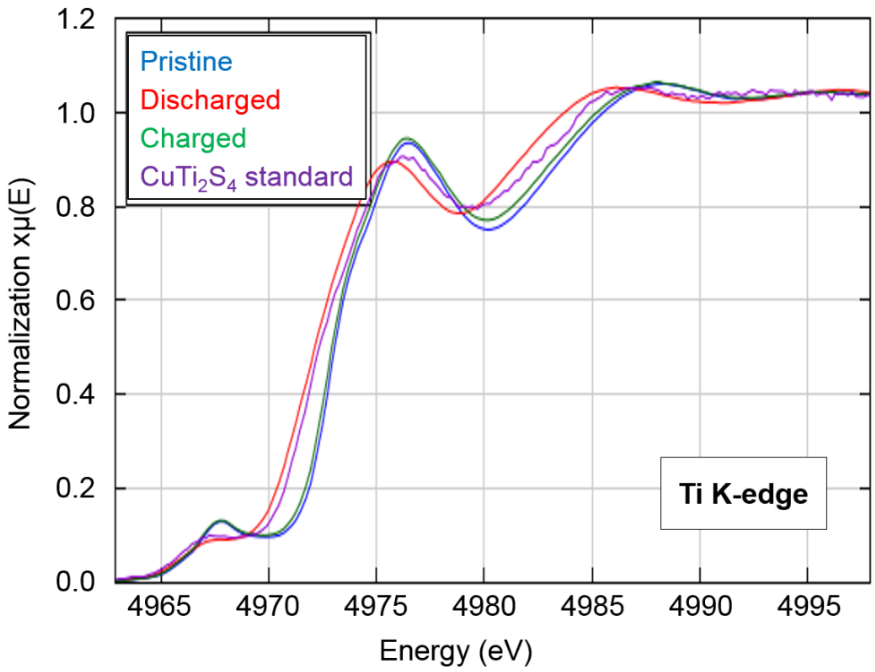

Figure 3-15. Comparison of the Ti K-edge XANES of the C-Ti_2S_4 spinel (blue), discharged (red), charged (green) states and $CuTi_2S_4$ (purple). The electrodes were cycled in APC/THF electrolyte with a Mg negative electrode at 60 ˚C and C/20.

3.2.4 Summary of Spinel Ti_2S_4

The thiospinel Ti_2S_4 shows promise as a new positive electrode material for Mg batteries, yielding a high capacity of 200 mAh g^{-1} at an average voltage of 1.2 V vs. Mg (corresponding to a volumetric energy density of about 350 Wh L^{-1} for a full Ti_2S_4 – Mg cell). On subsequent cycles with a capacity of 150 mAh g^{-1}, the specific energy is 180 Wh kg^{-1}, almost twice that of the Chevrel phase at 100 Wh kg^{-1}. Despite the moderate Mg^{2+} diffusion barrier, spinel Ti_2S_4 exhibits excellent rate capabilities at 60 ˚C. The small volume change during cycling ensures the good capacity retention. Reducing particle size promotes the retention even better by

minimizing cation trapping effect with the shorter ion diffusion length. Rietveld refinement reveals stepwise Mg^{2+} insertion process, with the octahedral site occupied first followed by the tetrahedral. Titanium is identified as the major redox center, which would benefit electrochemistry by avoiding hole formation on sulfur.

3.3 Layered TiS_2

3.3.1 Synthesis and Characterization of Layered TiS_2

The bulk L-TiS_2 (bL-TiS_2) was obtained by solid state synthesis.[107] In an Ar-filled glovebox, Ti powder was ground with 10% excess S and sealed in an evacuated quartz tube. Sintering temperature was initially held at 450 ˚C for 1 day, which was then ramped to 550 ˚C in a 2-day period and held for 46 hours. The mixture was quenched in water, reground with additional 5% S, sealed under vacuum in a quartz ampule, heated at 1 ˚C/min to 550 ˚C for 36 hours and quenched in water.

Nano platelets L-TiS_2 (nL-TiS_2) was obtained via wet synthesis as proposed by Jeong *et al.*[117] In a 100 mL round bottom flask, 880 μL $TiCl_4$ was added to 12 g oleylamine and heated up to 300 ˚C under magnetic stirring and N_2 flow. 1.56 mL CS_2 was then added to the mixture, which was observed to turn black right away. The temperature was held at 300 ˚C for 15 min to allow the completion of the reaction. The flask was transferred to an Ar-filled glovebox after naturally cooling down to room temperature, and the product was collected by filtration and washed with butanol and 3:1 volume ratio of methanol:hexane.

The XRD patterns of both L-TiS_2 were indexed in the standard *P*-3*m*1 space group (**Figure 3-16**). Platelet morphology, which is a result of the layered crystal structure, was

observed for both materials (**Figure 3-17**). The solid state synthesized compound showed micron-sized facial section, while that for the wet synthesis was below 200 nm.

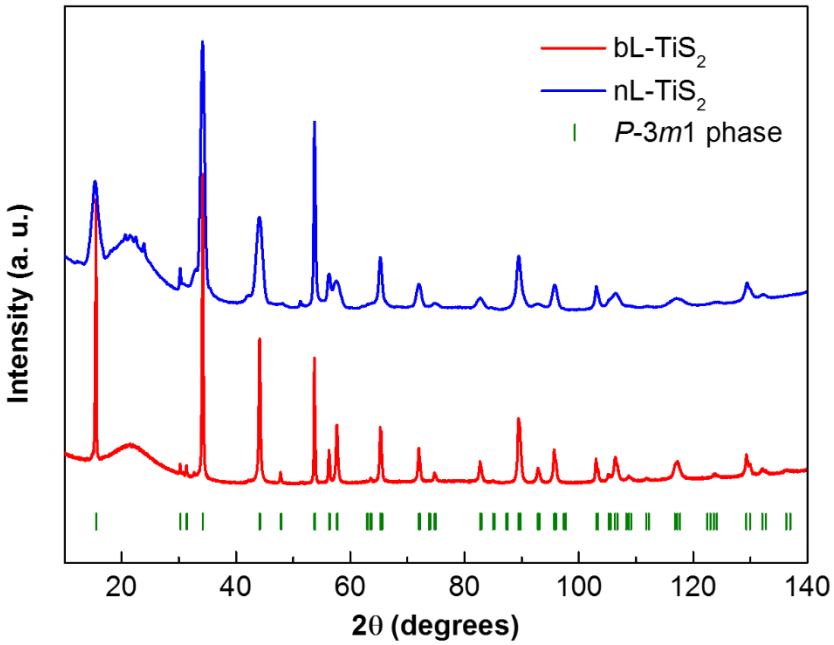

Figure 3-16. XRD (Debye-Scherrer geometry) of bL-TiS_2 (red) and nL-TiS_2. The *P*-3*m*1 phase marks are shown in green ticks. The broad hump is a background signal from the X-ray capillary

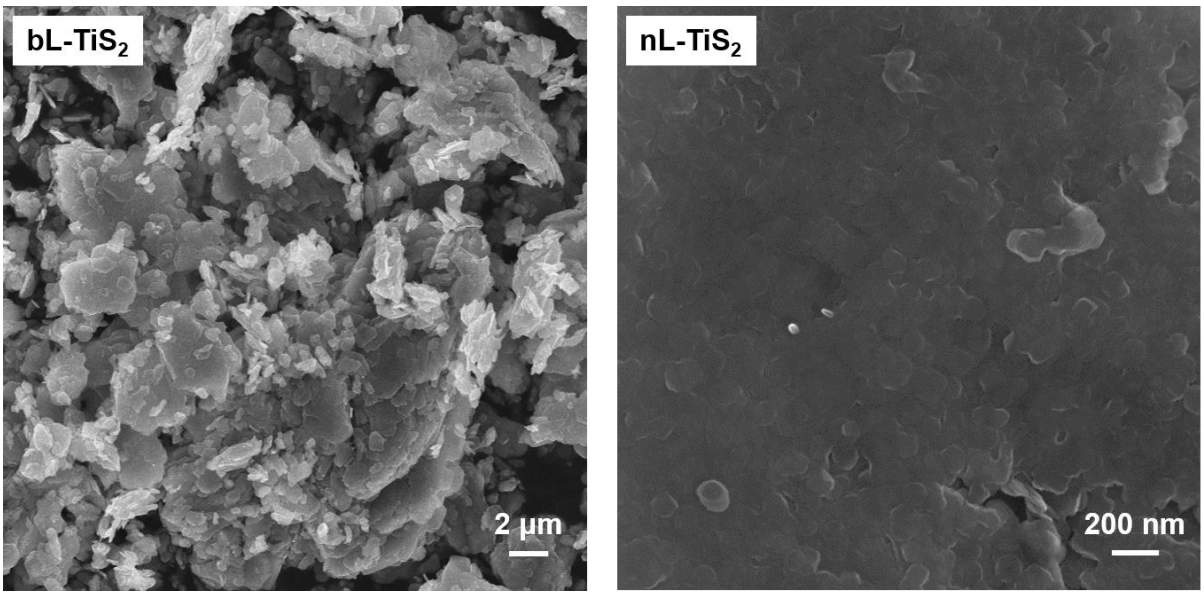

Figure 3-17. SEM images of bL-TiS_2 (left) and nL-TiS_2 (right)

3.3.2 Electrochemistry of Layered TiS_2

Similar to the strategy used for C-Ti_2S_4, electrochemistry test on bL-TiS_2 was also first tested in the APC/THF electrolyte. **Figure 3-18** shows the voltage profiles at various rates at 60 ˚C. At C/20 (1C = 1 e^-/L-TiS2 in 1 h, equivalent to 1C for 1 Mg^{2+}/C-Ti_2S_4, black curve), an initial discharge capacity of 270 mAh g^{-1} ($Mg_{0.56}TiS_2$) is obtained (**Figure 3-18** inset), twice that of the CP phase, at a similar voltage. A larger irreversible capacity is present in bL-TiS_2 compared to C-Ti_2S_4 during the first cycle, indicating a stronger cation trapping effect in the layered structure. Nevertheless, the reversibility improves dramatically from the second cycle onward, and the capacity stabilizes at around 160 mAh g^{-1} (0.33Mg/TiS_2). Thus, cation entrapment does not continue upon cycling; instead, reversible Mg^{2+} de/intercalation is achieved with the partially magnesiated L-TiS_2 ($Mg_{0.26}TiS_2$) formed on the first cycle. Unlike the solid solution

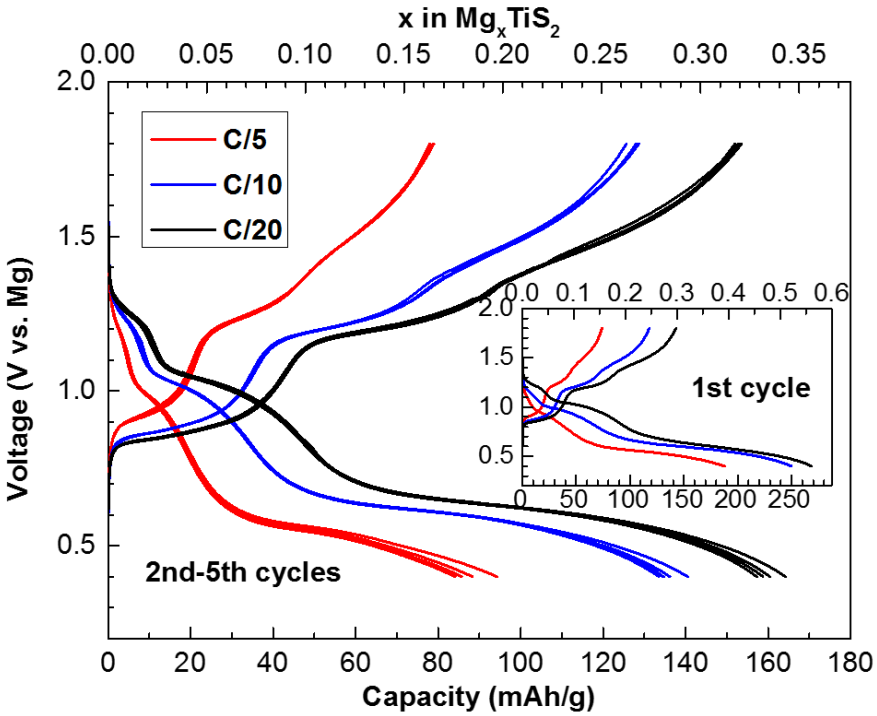

Figure 3-18. Discharge and charge curves of the first 5 cycles of bL-TiS_2 tested in coin cells with APC/THF electrolyte and a Mg negative electrode at 60 ˚C and various rates.

behavior in the thiospinel, three distinct processes are observed in the voltage profile of the layered compound and its associated differential capacity curve (**Figure 3-19**), indicating a multistep Mg^{2+} insertion mechanism that will be discussed in more detail later.

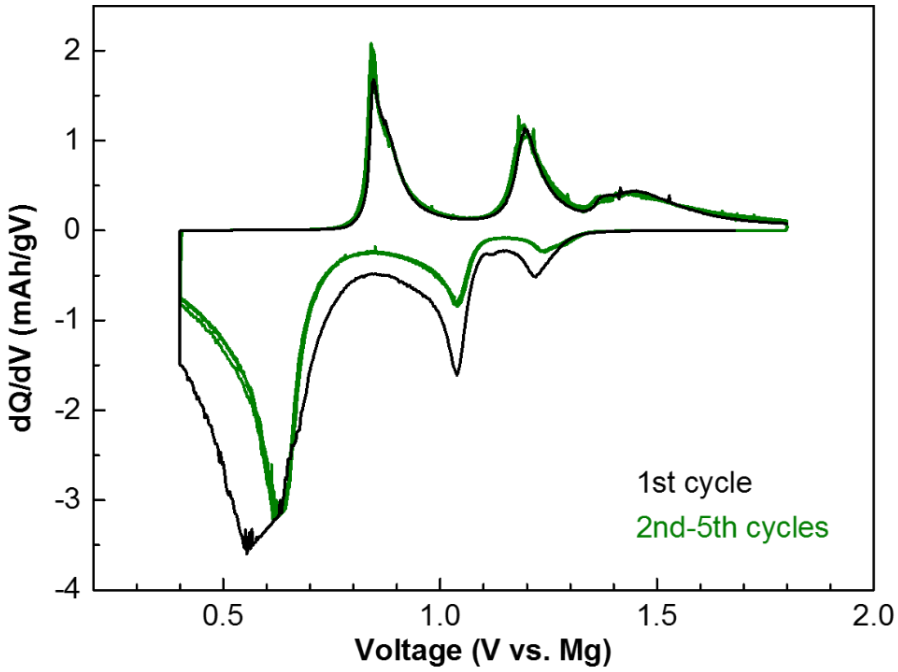

Figure 3-19. Differential capacity curve of bL-TiS_2 at C/20 and 60 ˚C.

As the cycling rates increase to C/10 and C/5, the capacities drop to 250 mAh g^{-1} and 140 mAh g^{-1} during the initial discharge, and stabilize at 140 mAh g^{-1} and 90 mAh g^{-1}, respectively, during subsequent cycles. Long-term cycling of the material examined in APC/G4 electrolyte is shown in **Figure 3-20**. A relatively stable capacity of 115 mAh g^{-1} is obtained after a few cycles of stabilization.

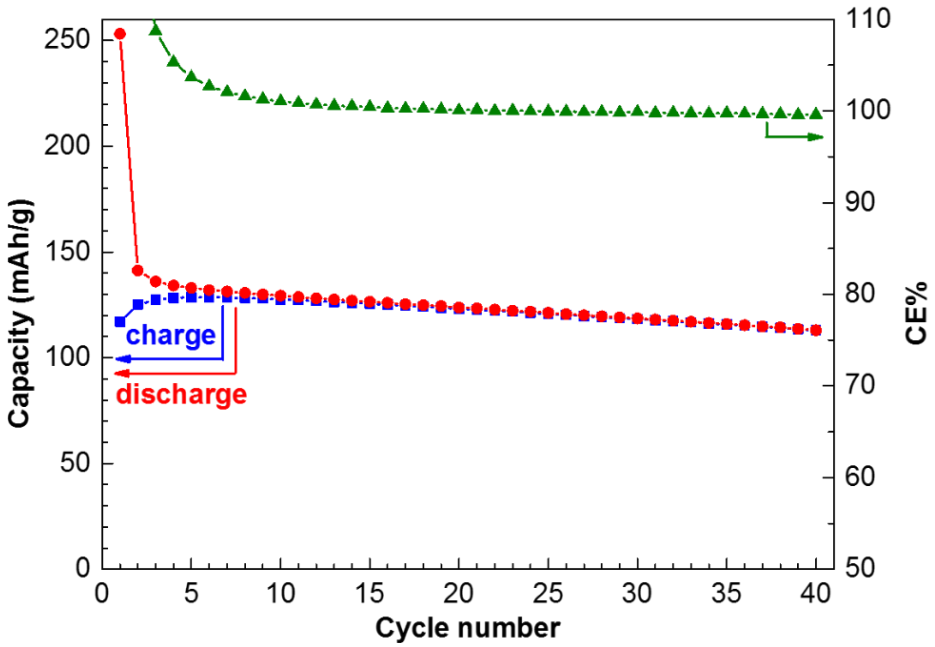

Figure 3-20. Capacity and coulombic efficiency (CE) evolution of bL-TiS_2 at a C/10 rate and 60 ℃ in APC/G4 electrolyte.

As with the thiospinel, reducing particle size – thus ion diffusion length – also improves the electrochemistry of L-TiS_2. **Figure 3-22** shows the discharge and charge curves of the nL-TiS_2 at 60 ˚C. The stepwise voltage profiles indicate a similar Mg^{2+} insertion mechanism as the micron-sized material. At a C/20 rate, the initial discharge capacity increases to 300 mAh g^{-1}, and the irreversible capacity is largely decreased during the first charge, demonstrating a reduced Mg^{2+} trapping effect. The capacity only drops slightly to 270 mAh g^{-1} on the second discharge. The rate capability is also better for the nano-sized material, with 270 mAh g^{-1} and 260 mAh g^{-1} capacities obtained at C/10 and C/5 for the initial discharge, respectively, and 230 mAh g^{-1} and 200 mAh g^{-1} during the second. Furthermore, the nL-TiS_2 shows an excellent capacity retention during long term cycling (**Figure 3-21**). At 60 ˚C and C/5, the capacity stabilizes at 170 mAh g^{-1} from the 2^{nd} to 50^{th} cycle, at which point a slight drop to 150 mAh g^{-1} capacity is observed. Up to the 200^{th} cycle, 120 mAh g^{-1} capacity is preserved. Even at room temperature, a stable capacity at 70 mAh g^{-1} is obtained up to 200 cycles.

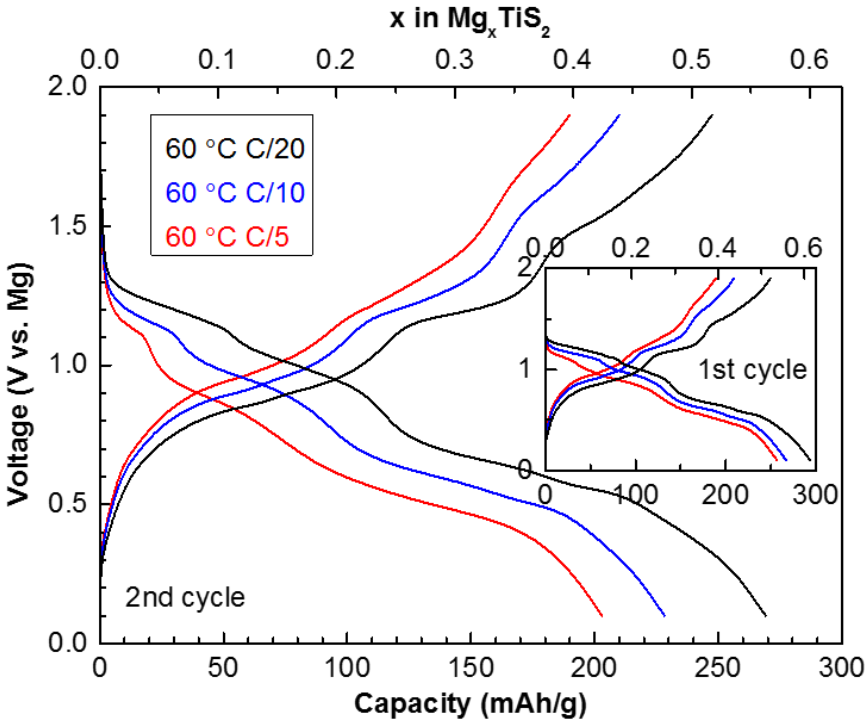

Figure 3-22. Discharge and charge curves of the first two cycles of nL-TiS_2 tested in coin cells with APC/THF electrolyte and a Mg negative electrode at 60 ˚C and various rates.

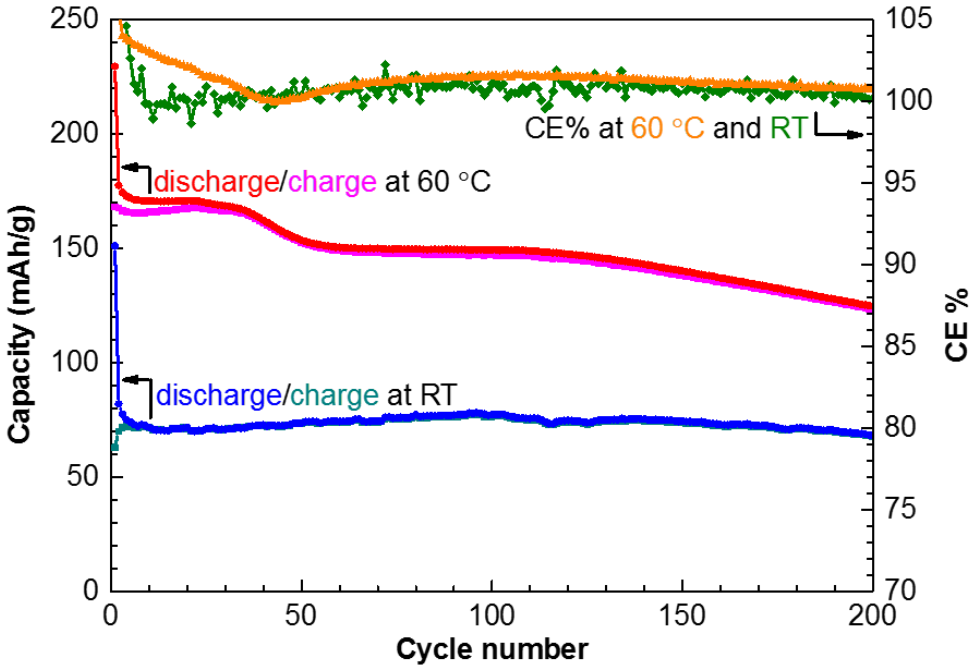

Figure 3-21. Capacity and coulombic efficiency (CE) evolution of nL-TiS_2 with a C/5 rate at 60 ℃ (APC/G4 electrolyte) and room temperature (APC/THF electrolyte).

3.3.3 Investigation of Mg^{2+} De/Intercalation Mechanism into Layered TiS_2 by EDX and *In-Situ* XRD

Reversible Mg^{2+} intercalation into bL-TiS_2 is first confirmed by EDX (**Table 3-7**), revealing Mg contents in good agreement with the electrochemistry capacity. Detailed Mg insertion mechanism into bL-TiS_2 is the investigated by *in-situ* XRD, with scans taken at the end of each pronounced electrochemical step (**Figure 3-23a**). The first three intense peaks of the *P*-3*m*1 phase – (001), (011), and (012) – are used to extract the *a* and *c* lattice parameters by Le Bail[94] full-profile fitting (**Figure 3-24**). Owing to preferred orientation, limited positive electrode thickness in the *in-situ* cell and multiple phases, Rietveld analysis could not be readily carried out. **Figure 3-23b** shows the evolution of those three peaks; the corresponding *a* and *c* values are summarized in **Figure 3-23c,d** and **Table 3-8**. In the pristine material (point A, phase 1), lattice parameters for L-TiS_2, a = 3.4058(2) Å and c = 5.6987(4) Å, are obtained. Preventing nonstoichiometry in TiS_2 (where typical lattice parameters are as high as a = 3.419 Å and c = 5.713 Å), due to excess Ti atoms occupying interlayer sites and pinning the layers, is crucial for good Li^+ intercalation properties.[118,119] Similar logic likely applies to Mg^{2+} intercalation. During the discharge process, the peak intensities of phase 1 decrease, while a new set of peaks evolve. At the end of the first discharge plateau (point B, 0.05Mg/TiS_2), a second phase (phase 2) appears, denoted by weak shoulders at lower angle to the phase 1 reflections. Phase 2 exhibits a notably increased *c* parameter (5.903(7) Å), but only a small increase in *a* (3.416(3) Å). Upon further discharge to point C, 0.17Mg/TiS_2, a third phase (phase 3) appears with sharper reflections. Again, the *c* parameter increases greatly (6.112(3) Å), while *a* remains almost constant (3.431(2) Å). At point C, the asymmetric peak shapes indicate a small amount of phase 2 persists. At the end of discharge (point D, 0.56Mg/TiS_2), the (011) and (012) peaks

of phase 3 shift further but the (001) reflection remains at the same position. This results from a major increase in *a* to 3.4934(5) Å and a minor increase in *c* (6.123(1) Å) of the new phase (phase 4) by comparison with phase 3. The lattice parameters of phase 4 are in agreement with those obtained by chemical Mg^{2+} insertion into layered TiS_2 reported by Bruce *et al.*[120,121] Structural analysis of that material was not provided. At this state of discharge, we also note that some phase 1 still remains. Because the TiS_2 electrode particles are micrometer-sized, diffusion lengths between the surface and the interior of individual TiS_2 particles are large enough that presumably phase 1 remains within the particle core. The fraction of phase 1 to phase 4, estimated by comparison of the intensity of the well-resolved (012) reflections of phase 1 and phase 4, is about 15%.

Table 3-7. EDX results for bL-TiS_2 (electrodes cycled in APC/THF electrolyte with a Mg negative electrode at 60 ˚C and C/20).

Sample	**Pristine**	**Discharged**	**Charged**
EDX	$Ti_{1.09(3)}S_2$	$Mg_{0.54(2)}Ti_{1.10(4)}S_2$	$Mg_{0.30(2)}$ $Ti_{1.02(5)}S_2$

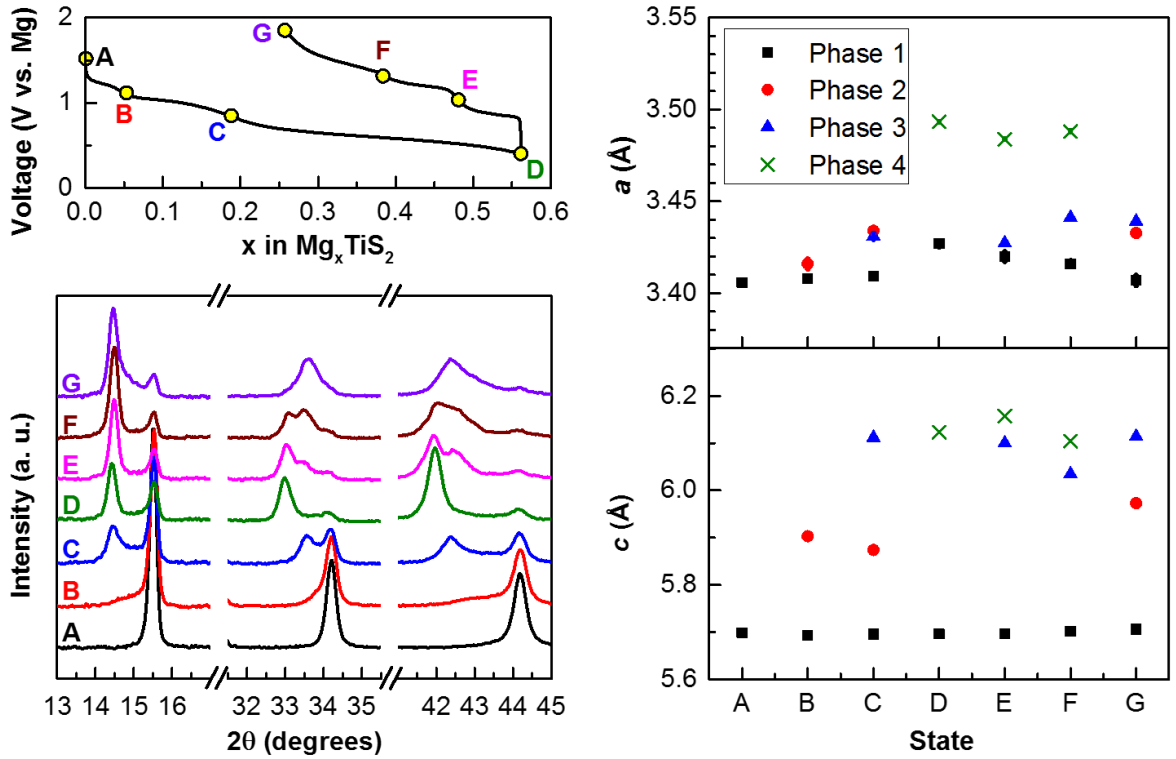

Figure 3-23. XRD studies of TiS_2 structure evolution during cycling. (a) Electrochemical discharge−charge profile at C/20 on the first cycle showing labeling of the points at which diffraction patterns were collected. (b) XRD profiles. Note that a trace of the pristine material remains throughout cycling. (c) Extracted lattice parameters for *a* at each state. (d) Extracted lattice parameters for *c* at each state.

Table 3-8. Lattice parameter evolution of layered TiS_2 during electrochemical cycling.

Point	Phase 1		Phase 2		Phase 3		Phase 4	
	***a* (Å)**	***c* (Å)**	***a* (Å)**	***c* (Å)**	***a* (Å)**	***c* (Å)**	***a* (Å)**	***c* (Å)**
A	3.4058(2)	5.6987(4)	-	-	-	-	-	-
B	3.4079(3)	5.6925(4)	3.416(3)	5.903(7)	-	-	-	-
C	3.4091(5)	5.6955(6)	3.434(2)	5.874(6)	3.431(2)	6.112(3)	-	-
D	3.427(2)	5.696(3)	-	-	-	-	3.4934(5)	6.123(1)
E	3.420(3)	5.696(2)	-	-	3.4273(7)	6.1001(9)	3.4838(5)	6.158(2)
F	3.416(2)	5.702(2)	-	-	3.4412(8)	6.035(3)	3.4881(7)	6.1041(5)
G	3.407(3)	5.706(3)	3.4328(6)	5.973(2)	3.4391(6)	6.1144(6)	-	-

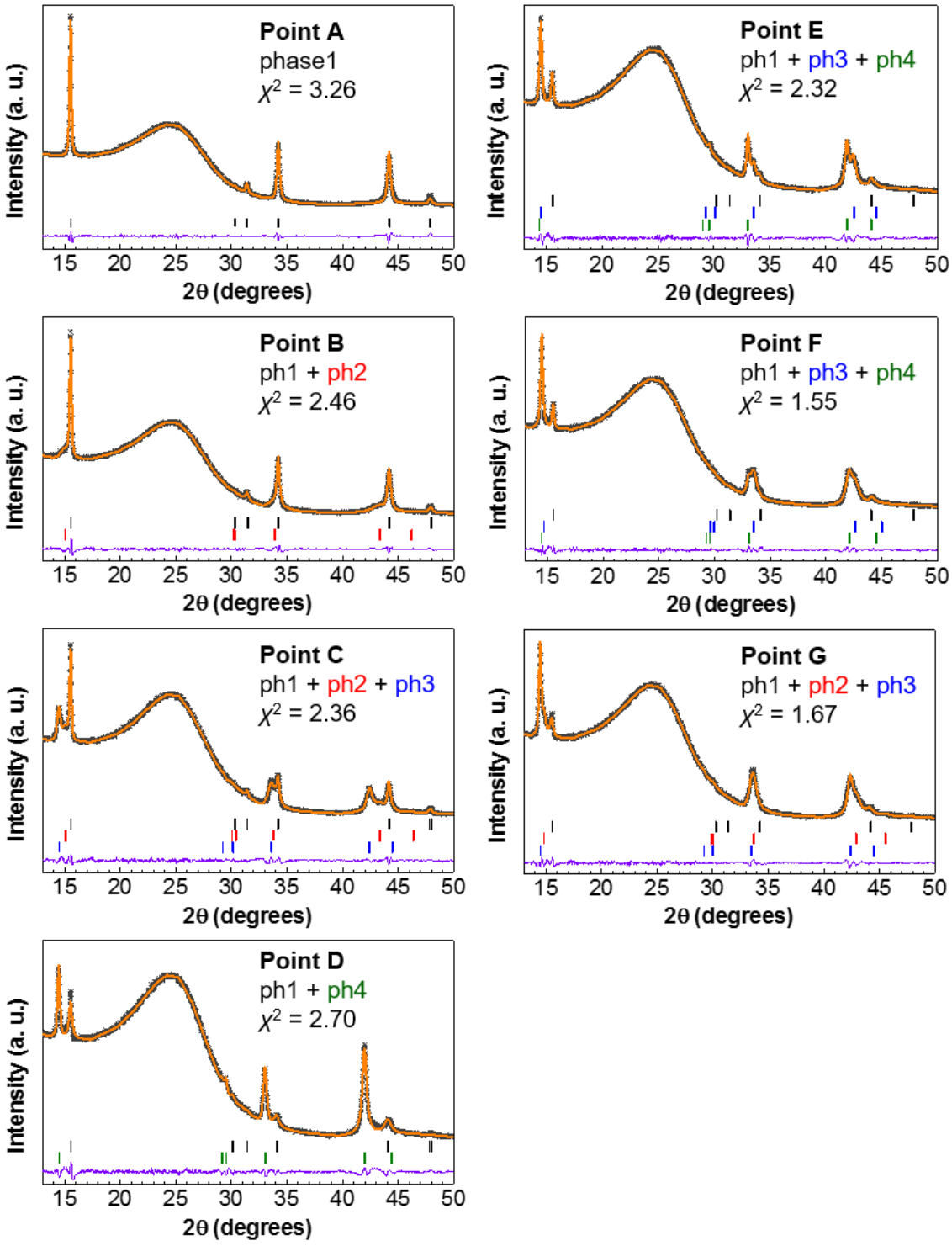

Figure 3-24. XRD Le Bail (full profile) fitting of TiS_2 at different electrochemical stages (grey crosses – experimental data, orange lines – fitted data, violet lines – difference map between observed and calculated data, ticks – the *P*-3*m*1 phases (black – phase 1, red – phase 2, blue – phase 3 and green – phase 4)). The broad hump is a background signal from the glassy carbon window on the *in-situ* cell.

The overall discharge process thus involves an initial expansion of the *c* parameter from point A to point C, followed by an increase in the *a* parameter during the final step (point D). Based on previous computational results, the octahedral site energy for Mg^{2+} occupation is much lower than the tetrahedral site during the initial stages of intercalation.[111] This suggests preferred Mg^{2+} insertion onto the octahedral sites during early discharge (A to C). In fact, at point C the Mg stoichiometry in phase 3 is likely larger than the overall x = 0.17. When the intensities of the (012) reflections at this intermediate point are compared, phase 3 comprises about 50% of the material. As such, the Mg content of the outer shell of the active material is more likely $x = 2 \times 0.17 = 0.34$, corresponding to the ordered composition $Mg_{1/3}TiS_2$ where Mg^{2+} occupies octahedral sites and whose existence was suggested by first principles calculations.[111] These calculations also showed that as the unit cell increases in size with increasing Mg^{2+}/e^- content, the Mg^{2+} preference for the octahedral site over the tetrahedral site is lessened,[111] suggesting an increased likelihood of tetrahedral occupation at high x values. Meanwhile, there is a possible parallel with lithium insertion in TiS_2 where a switchover in siting as a function of depth of intercalation occurs. On the insertion of between 0~1 Li/TiS_2,[122] Li^+ occupies octahedral sites (causing an increase in only the *c* parameter).[123-126] Subsequent insertion of 1~2 Li/TiS_2 populates the tetrahedral sites, accompanied by an increase in the *a* parameter.[126] These changes in lattice parameters match those in our study, namely, an increase of the *c* parameter in phase 1 to 3, followed by an increase in the *a* parameter from phase 3 to 4. Thus, the increase in *a* may also result from additional Mg^{2+} occupation on the tetrahedral sites (i.e., mixed occupation driven by subtle thermodynamic and kinetic factors).

Upon charging, at the end of the first plateau (point E), the intensities of phase 4 reflections decrease and those of phase 3 start to appear. This trend continues on the next plateau (E to F), while the *c* parameters of both phases decrease. Upon final charge (G), phase 4 disappears completely and phase 3 is the major phase along with a minor contribution of phase 2. The intensity of the residual phase 1 reflections remains constant on charging; thus, the pristine structure is not regenerated. The lack of conversion of phase 2/3 back to phase 1 indicates some Mg^{2+} is trapped (presumably on octahedral sites), accounting for some of the capacity loss during the first cycle. The overall process is summarized in **Figure 3-25**. Such cation entrapment is potentially due to an increase of the Mg^{2+} diffusion barrier as lattice parameters decrease during Mg^{2+} extraction, effects of Mg^{2+}/vacancy ordering, and/or kinetic constraints imposed by the need for the migration of octahedral Mg^{2+} to pass through adjacent tetrahedral sites[111] (partially populated on discharge). The behavior contrasts sharply with the highly reversible solid solution Li^{+} de/insertion process in TiS_2[2] where the mobility is less affected by the Li^{+} concentration.[127,128] The higher charge on the divalent Mg^{2+} cations leads both to a stronger coulombic attraction to the anions in the lattice and greater cation repulsion. These interactions retard diffusion and lead to the complex ordering observed in the voltage profile as predicted by first principles calculations.[111]

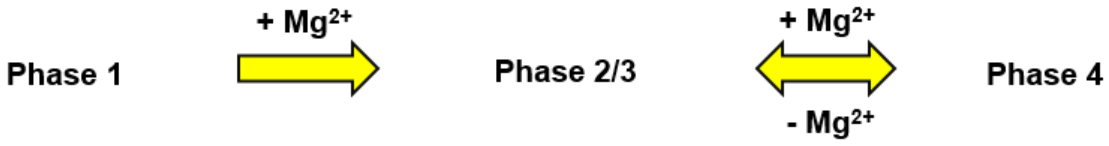

Figure 3-25. Proposed Mg^{2+} (de)insertion mechanism based on XRD data. This involves a multistep Mg insertion mechanism into TiS_2, with initial occupation of primarily the octahedral sites (phases 2/3) followed by occupation of the octahedral and tetrahedral sites (conversion of phases 2/3 to phase 4). The latter process is electrochemically reversible, but the first is not.

3.3.4 Summary on Layered TiS_2

Layered TiS_2 is a promising insertion positive electrode material for nonaqueous Mg batteries. With micron-sized material, a stabilized capacity of 115 mAh g^{-1} is obtained at C/10 rate and 60 ℃ for 40 cycles. Nano-sized material provides improved properties, with capacities of 170 ~ 120 mAh g^{-1} up to 200 cycles at C/5 and 60 ℃, or 70 mAh g^{-1} at room temperature. A capacity drop after the first cycle appears to be due to partial Mg^{2+} entrapment within the structure owing to complex ordering and kinetic effects. The drop is much smaller with nano-material owing to the decreased ion diffusion length it provides. XRD analysis on the micron-sized TiS_2 and a comparison with previous computation and Li^+ insertion results suggest that the multistep Mg^{2+} insertion observed during cycling can be assigned to progressive changes in Mg^{2+} siting. The multiple phases shown by XRD indicate an inhomogeneous Mg^{2+} distribution throughout the micron-sized particles but also suggest the capability of the material to accept more Mg^{2+} than the average value presented. By decreasing the particle size, an improved capacity is obtained, suggesting an easier homogenization of Mg^{2+} within nano-sized TiS_2.

3.4 Discussion and Conclusions on the Two Titanium Sulfides

Lattices containing softer anions potentially allow faster cation diffusion due to a weaker coulombic interaction. This is more critical for the higher charged multivalent ions. Benefit from the soft sulfide frameworks, two titanium sulfides – the spinel and layered – allow facile reversible Mg^{2+} de/intercalation and show promising electrochemistry results as positive electrode materials for Mg batteries. Reducing particle size further promotes the performance by decreasing ion migration length and allowing easier diffusion.

Despite the similarity in the composition of the two materials, different Mg^{2+} insertion processes are identified. The thiospinel phase follows a solid solution pathway, with a switchover from octahedral to tetrahedral occupation of Mg^{2+} at about $0.6Mg^{2+}/Ti_2S_4$. No pronounced inflection is shown in the electrochemical curve due to the similar site energies. However, subtle distribution of Mg^{2+} on the two sites of the lattice at high Mg^{2+} concentrations would result in complex behavior such as a modified Mg^{2+} diffusion path. This situation is further complicated with the trace Cu^{+} left in the structure which occupies the same tetrahedral site as Mg^{2+}. Those factors, in combination, defines the current Mg^{2+} insertion limit into the thiospinel structure. Unlike the C-Ti_2S_4, distinct plateaus are present for the Mg^{2+} insertion into the layered TiS_2. In addition to a change of occupation on sites that have larger energy difference, cation ordering would introduce additional metastable intermediate phases and result in a change in cell voltage as well. In a layered structure, the inserted Mg^{2+} would experience more influence from each other in the otherwise empty layer, than in a spinel structure which has Ti^{4+} in the way blocking the effect. Thus, Mg^{2+} is more likely to order themselves in a layered structure to reduce the entropy.

A lower overpotential is observed for Mg^{2+} insertion into spinel structure than the layered. Other than the different bulk Mg^{2+} diffusion mechanisms, the Mg^{2+} desolvation at the electrode/electrolyte interphase would also play an important role, as already shown for the CP where the atom arrangement on the surface of Mo_6S_8 shows critical effect in breaking the Mg-Cl interaction and promoting further intercalation.[81] Unique desolvation process would be present in the two titanium sulfides as well. Due to the distinct sites allowing Mg^{2+} insertion as well as their surrounding atoms in either crystal structure, a change in desolvation energy is

expected, which would finally contribute to the overall electrochemistry profiles. More discussions on the desolvation effect will be presented in next chapter.

The two titanium sulfides described in this chapter are a large step forward from the semi-functional CP that has been the only positive electrode family for Mg batteries for 15 years. The titanium sulfides not only provide improved electrochemical performance, but also add additional menus of options (apart from the CP) which should accelerate the fundamental understanding of Mg^{2+} intercalation behavior in solid structures. Benefitting from the same elemental composition, the effect from crystal structure could be more emphasized. This will provide direct guidance in the search for more Mg positive electrode candidates.

Chapter 4

Investigation of Factors for the Sluggish Mg^{2+} Insertion into Oxide Materials

4.1 Overview of Oxides as Positive Electrode Materials for Mg Batteries

While sulfide materials show great promise for facile and reversible Mg^{2+} de/intercalation as discussed in Chapter 3, the energy density they could offer is limited. Replacing sulfur with the more electronegative oxygen would increase the redox potential of transition metal in the lattice due to a stronger ionic character in the metal-oxygen bond. At the same time, the lighter weight of oxygen results in a higher theoretical specific capacity of the positive electrode material by increasing the amount of electron transfer per unit weight. Thus, oxide positive electrodes hold great potential for high energy density Mg batteries.

However, sluggish multivalent ion diffusion is generally observed in oxides, hindering their electrochemical performance. At the same time, there is a lack of systematic analysis on the detailed Mg^{2+} insertion mechanism into oxides. The limited understanding on such processes makes it difficult to design and discover new functional materials. This chapter thus focuses on the mechanism studies of Mg^{2+} insertion into oxide materials. Inspired by the work of Wan *et al*. that shows the essential role of facile Mg desolvation at the CP/APC interphase for its excellent electrochemistry by first principles calculations,[81] I emphasized my focus on the experimental investigation of such process for an oxide positive electrode, MnO_2, which would explain the dramatically different behavior in aqueous and nonaqueous electrolytes. In parallel, Rong *et al.* has identified the preferential site occupation of inserted cation as one of the factors leading to sluggish ion diffusion in lattice.[129] Following this principle, I examine

$Mg_2Mo_3O_8$ as a Mg positive electrode and establish additional circumstance that would affect diffusion barrier.

4.2 Birnessite MnO_2

Manganese oxide have been extensively investigated in the battery literature owing to their rich crystal chemistry.[130-141] The edge sharing MnO_6 octahedra can form ribbons of finite width that interconnect to generate tunnel structures such as hollandite (α-MnO_2) or todorokite: these consist of tunnels spanned by (2 × 2) or (3 × 3) octahedra, respectively. Alternatively, bidimensional structures consisting of stacked MnO_2 planes crystallize either without water in the interlayer space (i.e., O′3-$NaMnO_2$) or insert structural water. The latter are exemplified by the minerals birnessite (**Figure 4-1**)[142] and buserite, structures that are characterized by interlayer distances of ~7 Å and ~10 Å, respectively.[143] Studies of these materials as positive electrodes for Mg-ion batteries are rather limited. It has been shown that magnesium cells using α-MnO_2 positive electrodes undergo a conversion mechanism, resulting in poor cyclability.[49]

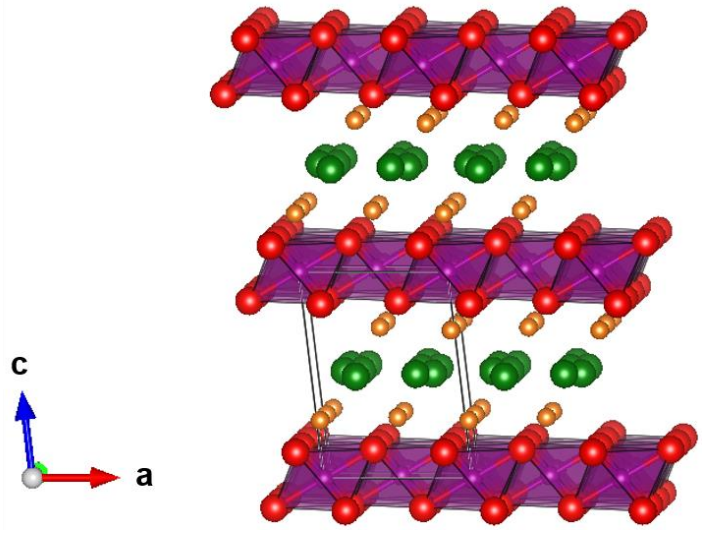

Figure 4-1. Birnessite crystal structure showing a water monolayer (green) between the MnO_2 sheets (purple). Mg ions are shown in orange.

Comprehensive analysis demonstrates that the Mg^{2+} intercalation barrier into such structures at an early stage is comparable with Li^+, but thermodynamics drive the transformation of the highly unstable product into the rock salt oxide ($Mg_{1-x}Mn_xO$) on the outer particle surface.[49,144] This conversion mechanism is also applicable to other MnO_2 oxides in nonaqueous Mg cells according to experimental studies that show the surface area is the largest factor influencing their electrochemistry.[145] On the other hand, two recent studies have emphasized the beneficial role of a high water content in the electrolyte in facilitating Mg^{2+} intercalation using anhydrous layered MnO_2[146] and spinel $MgMn_2O_4$[46] positive electrode materials. These studies parallel my interest in exploring the behavior of birnessite in both aqueous and nonaqueous electrolytes to identify the main factors that trigger intercalation or a conversion mechanism.

4.2.1 Synthesis and Characterization

The birnessite $Mg_{0.15}MnO_2 \cdot 0.9H_2O$/carbon cloth composite (labeled as Mg-bir/CC) was prepared by a hydrothermal method. Typically, 150 mg of $Mg(MnO_4)_2 \cdot xH_2O$ was dissolved in 36 mL of deionized water and transferred to a Teflon® lined stainless steel autoclave. A square piece of carbon cloth (7×7 cm^2) was placed in the autoclave to serve as the conductive substrate. The mixture was heated at 160 ℃ for 2 h. After being cooled to room temperature, the product was washed with water and dried in air.

The diffractogram of the pristine sample of Mg-bir/CC (**Figure 4-2a**) is composed of the amorphous carbon cloth scattering and the diffraction peaks of the birnessite phase (space group = *C*2/*m*, ICSD-068917).[142] The (001) peak at 12.5 °is characteristic of the ~7 Å spacing of the MnO_2 sheets in birnessite due to its monolayer of structural water (**Figure 4-1**). It allows clear differentiation from the parent buserite structure that features a double layer of structural water and a interplanar distance of ~10 Å. The large breadth of the diffraction peaks is in good

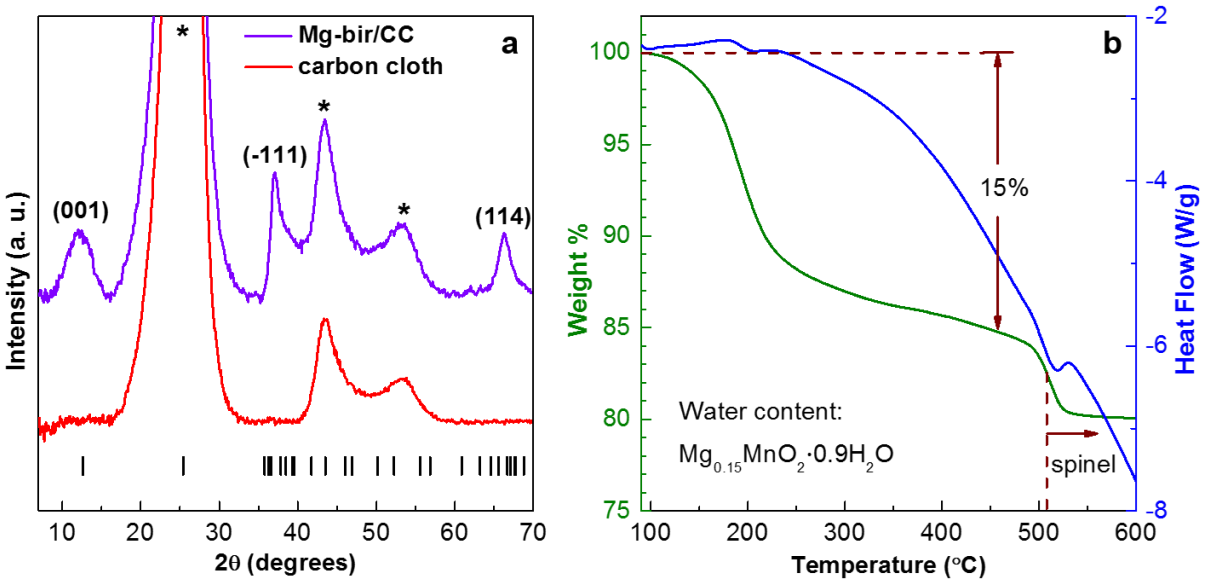

Figure 4-2. (a) XRD comparison of Mg-bir/CC composite (violet; only the index for the peak with highest intensity of the clump is shown for the purpose of clarity) and bare carbon cloth (red). Bragg peak positions for birnessite are noted by the black tick marks, and reflections from the carbon cloth are indicated by asterisks; (b) TGA of a standard sample of birnessite without carbon cloth substrate at a heating rate of 5 ˚C min^{-1} under a N_2 flow. The temperature was held at 90 ˚C for an hour prior to the scan to remove physisorbed water.

agreement with the birnessite nano-morphology observed by electron microscopy (**Figure 4-3a**). The structural water content in birnessite was determined to be 0.9 by TGA (**Figure 4-2b**), in agreement with previously reported values of 0.85.[142]

The composite morphology consists of a homogeneous ~ 1 μm thick coating of birnessite MnO_2 wrapped around the ~ 7.5 μm m diameter fibers of the carbon cloth (**Figure 4-3b** inset). The mineral coating is composed of thin platelets radially arranged around the carbon fiber surface, with the platelet plane (of Mg^{2+} mobility) perpendicular to the fibers (**Figure 4-3b**). This assembly offers an optimal configuration that can be used directly as a positive electrode material for magnesium cells owing to the underlying electronically conductive substrate and the nanometric morphology of the active material that benefits the typically low mobility of Mg^{2+} by providing short diffusion pathways.

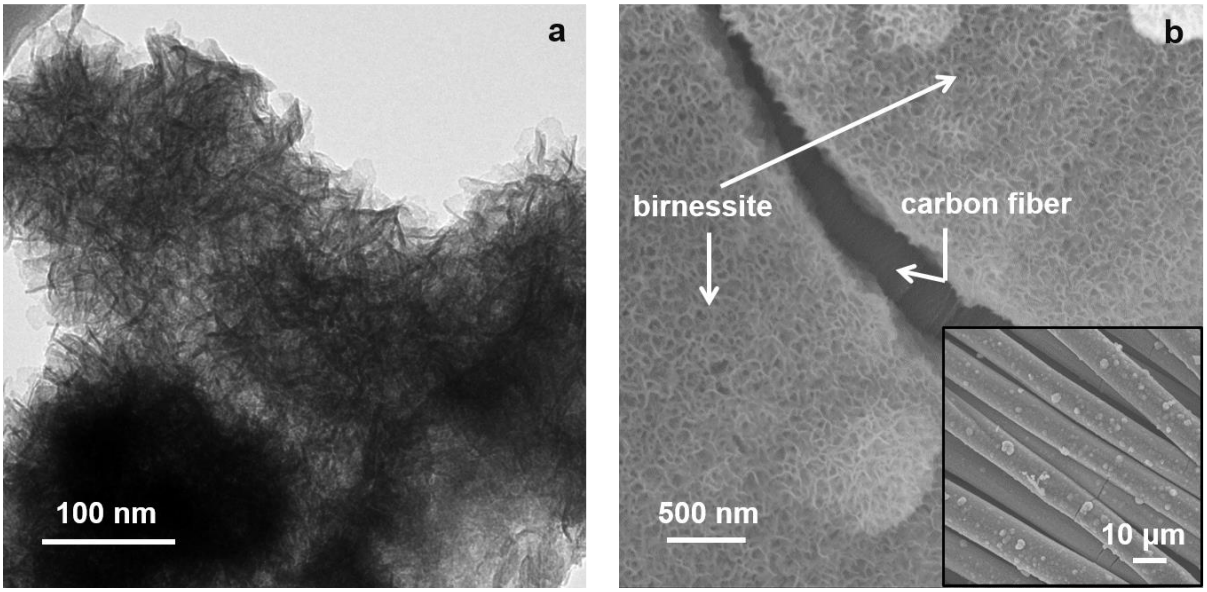

Figure 4-3. (a) TEM and (b) SEM images of Mg-bir/CC.

4.2.2 Electrochemistry and *Ex-Situ* XRD Studies in Aqueous Electrolyte

The good performance of birnessite positive electrodes in Mg aqueous cells or in an organic solvent with a significant amount of water (i.e., 5−20% wt.) has been previously established.[46,146] However, in those studies, the birnessite structure was obtained through the electrochemical conditioning of a nonhydrated manganese oxide, either MnO_2[146] or $MgMn_2O_4$.[46] Owing to the disordered nature of the birnessite framework, detailed structural information is not readily accessible using XRD. Therefore, substantial differences in the local arrangement of the different materials, induced by the conditioning process, could lead to significant differences in the electrochemical mechanism that are not observable by XRD. For this reason, the behavior of the Mg-bir/CC composite electrodes was first verified in aqueous media.

The material was examined in an electrolyte composed of 0.5 M $Mg(ClO_4)_2$ in deionized water using Pt gauze as the counter electrode and Ag/AgCl (saturated) as the reference electrode in T-shape Swagelok three-electrode cells. Sloping curves are observed for the discharge and charge voltage profiles (**Figure 4-4**), consistent with previous studies. [46,146] As expected from its low surface area, the capacitive response of carbon cloth (~ 0.05 mAh g^{-1} of active material, **Figure 4-4** inset) is negligible compared to the initial capacity of 150 mAh g^{-1}, i.e., insertion of 0.3 Mg^{2+}, as observed here and by others. [46146] The expected reversible "theoretical" capacity is 0.5 Mg^{2+} based on a one electron transfer (since deep reduction of Mn^{3+} to Mn^{2+} is typically not very reversible). However, different from previous reports, capacity fading is observed over the first 20 cycles (**Figure 4-5**). This is due to the

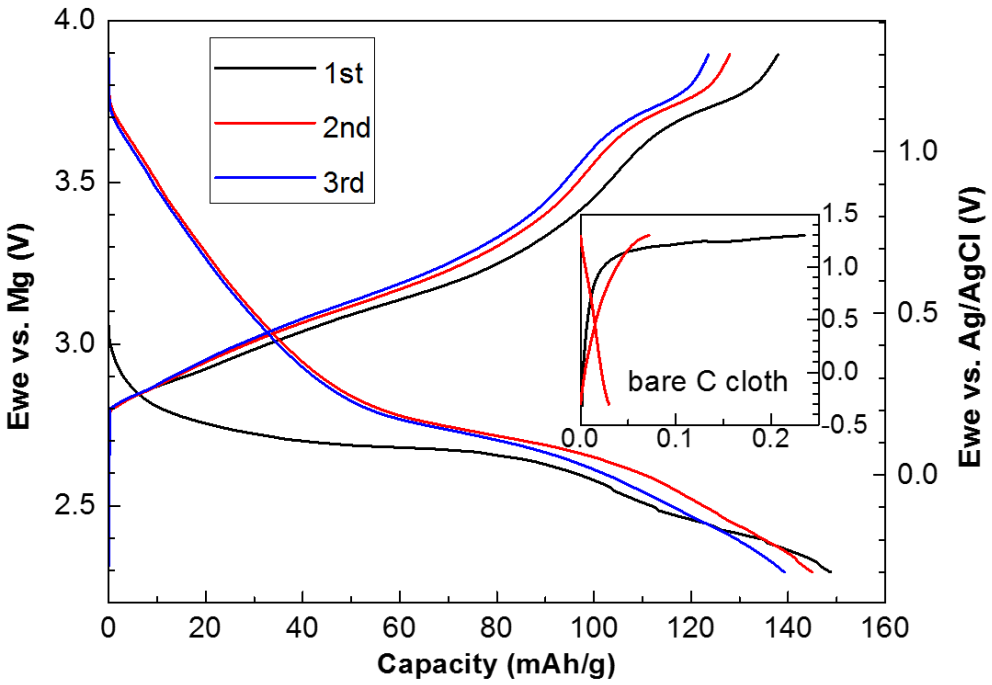

Figure 4-4. Discharge and charge profiles of Mg-bir/CC positive electrode in 0.5 M $Mg(ClO_4)_2$/water electrolyte at 2C rate. Inset shows negligible capacity of the bare carbon cloth (specific capacity calculated with respect to the loading of birnessite in the actual Mg-bir/CC cell).

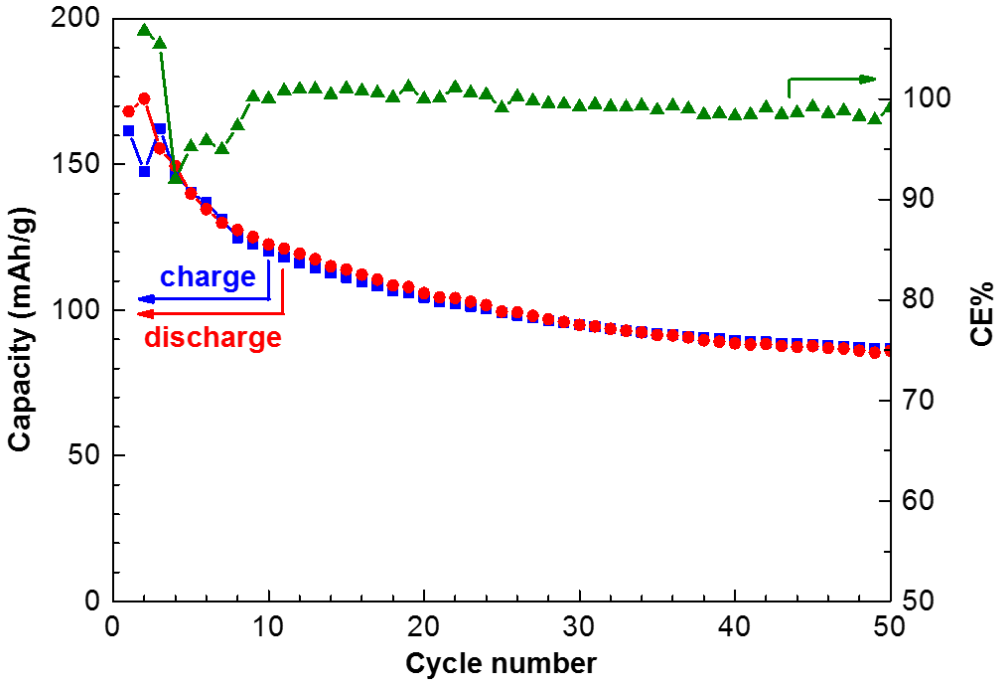

Figure 4-5. Capacity and coulombic efficiency evolution of Mg-bir/CC positive electrode in 0.5 M $Mg(ClO_4)_2$/water electrolyte at 2C rate.

enhancement of Mn^{2+} dissolution due to the nanometric size of the active material as well as the low loading used in this study. Further evidence of this is found by post-mortem SEM imaging of the dried separator facing the negative electrode, showing the precipitation of large manganese containing particles (**Figure 4-6**).

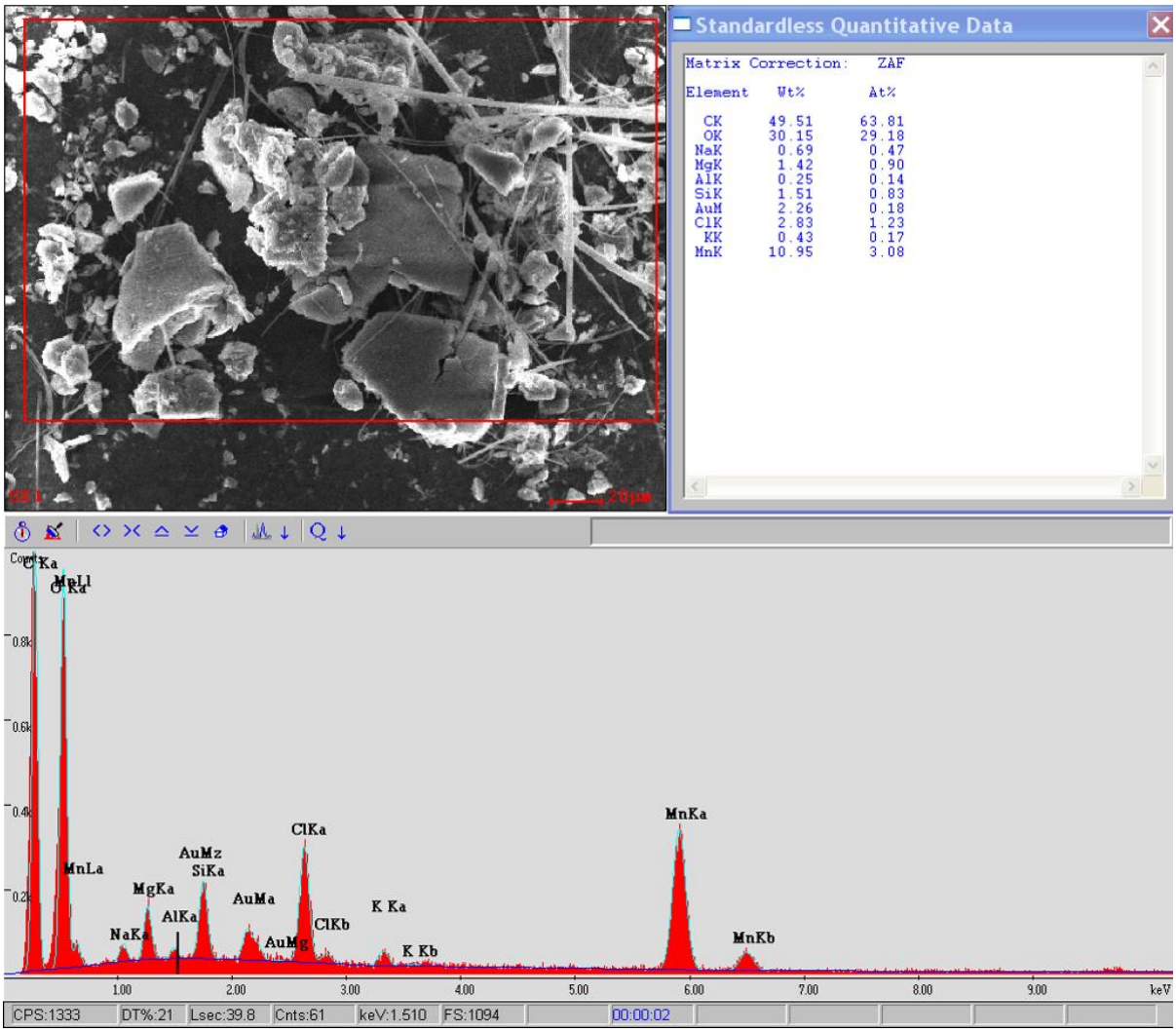

Figure 4-6. SEM and accompanying EDX of a piece of separator after Mg-bir/CC is discharged in 0.5 M $Mg(ClO_4)_2$/water electrolyte. Two separaters were used in the cell, and the one facing the negative electrode side was used to ensure that no birnessite contamination occurred.

XRD analysis of the composite electrode in the discharge (magnesiated) and charge (demagnesiated) states (**Figure 4-7**) confirms the magnesium intercalation process in aqueous cells. However, modification of the intercalate concentration changes the electrostatic interaction responsible for the layered arrangement, resulting in a major topotactical transformation of the structure. Upon discharge, the intercalated Mg^{2+} allows for more efficient screening of the interslab electrostatic repulsion. This triggers a contraction of the interlayer spacing from 7 Å to 4.86 Å, as evidenced by the shift of the first diffraction peak from 12.5 ° (2θ) to 18.6°. Conversely, the removal of Mg^{2+} upon charge induces an expansion of the interlayer distance to the 10 Å spacing characteristic of a double layer of water between the MnO_2 layers in the buserite structure. The (001) and (002) buserite reflections are clearly visible at 9.2 ° and 18.4 °.

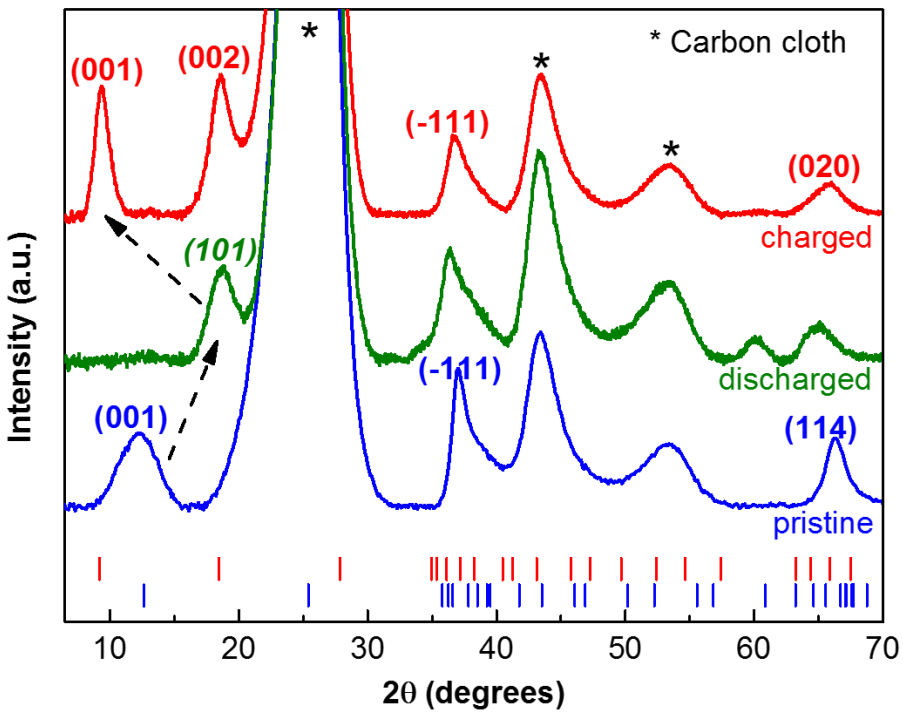

Figure 4-7. XRD patterns of cycled birnessite electrodes in the aqueous cell: blue, pristine; green, discharged; red, charged. The tickmarks represent the Bragg peak position of the birnessite (blue) and buserite (red).

The structural evolution in the discharged material implies not only a contraction of the interlayer spacing, but also a glide of the MnO_2 planes. Owing to the poor crystallinity of the phases, full structure determination was not possible. Nonetheless, the interlayer distance of the magnesiated phase (4.86 Å) corresponds exactly to the distance between the octahedral slabs in the $MgMn_2O_4$ spinel structure (**Figure 4-8**). Comparison of the diffractogramms of the discharged phase and $MgMn_2O_4$ clearly shows the strong relationship between the two structures. Some of the reflections of the spinel structure are extinct in the discharged phase,

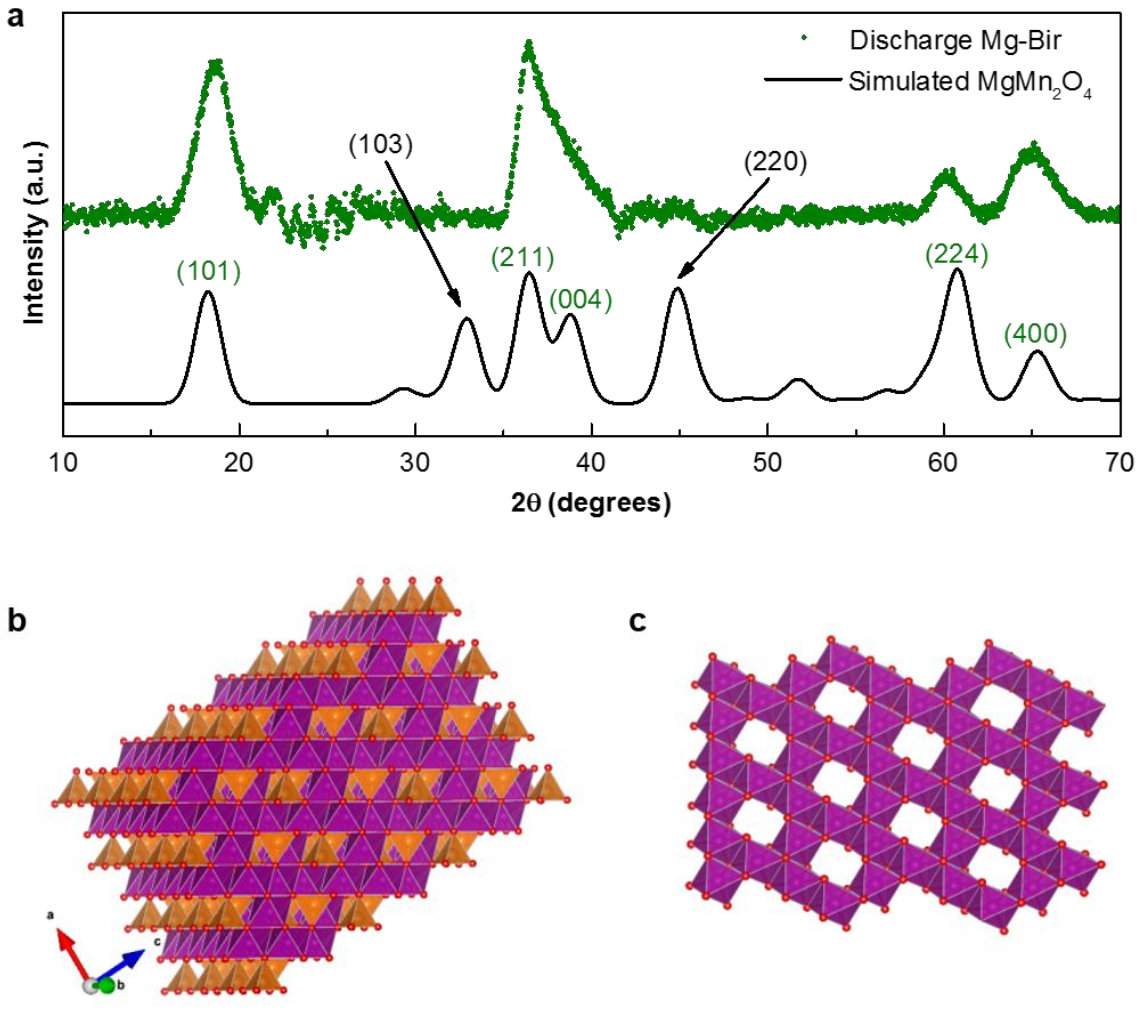

Figure 4-8. (a) Comparison of the XRD patterns of discharged Mg-bir/CC in aqueous cell and the spinel $MgMn_2O_4$; (b) Representation of the spinel $MgMn_2O_4$ showing the stacking of (c) the kagome layers.

the most evident being the (103) reflection at 33 °(**Figure 4-8a**). Thus, it is proposed here that the structure of the discharged phase is based on the same layer arrangement as the spinel phase; i.e., Jahn-Teller distorted, partially occupied triangular slabs of MnO_6 octahedra interconnected by tetrahedral MgO_4 and octahedral MnO_6 moieties. The appearance of a new translational symmetry element, as evidenced by the disappearance of the (103) spinel reflection, suggests a slightly different stacking scheme that does not exactly reproduce the tridimensional structure of $MgMn_2O_4$ (**Figure 4-8c**). Attempts to manually determine the precise stacking sequence using the FAULTS software[147] were unsuccessful.

The hypothesis of a local structure similar to the spinel phase is further supported by a previous study that clearly shows the formation of spinel in the discharged state,[46] although it was not reported as such. In the latter study, the birnessite phase was obtained through a conditioning of the spinel phase where the original kagome layers are probably preserved in the birnessite phase, thus favoring the reformation of the spinel structure upon remagnesiation. On the other hand, in the present study, there is no reason to presume a similar arrangement of manganese vacancies in the triangular lattice of the pristine birnessite phase. Therefore, it is likely that the creation of the manganese vacancies occurs during the contraction of the interlayer spacing: the stabilization of Mg^{2+} in the tetrahedral interlayer site generates a very short (1.84 Å) Mn−Mg distance, forcing Mn out of the triangular lattice and into the interlayer space. The arrangement of the created vacancies would induce a different stacking scheme than in the spinel structure.

The formation of such a small interlayer spacing raises the question of the fate of the water. There is no available site to accommodate water in the interlayer space of the discharged phase. The formation of hydroxl groups, as observed in layered MnOOH, would imply the

reorganization of the entire close packed oxygen framework and therefore is unlikely. Hence, water is most likely expelled from the structure. This conversion of the layered structure to the spinel is reminiscent of the conversion of metastable layered $Li_{0.5}MnO_2$ to the more thermodynamically stable spinel $LiMn_2O_4$ on cycling in nonaqueous media,[148] where similar driving forces are undoubtedly responsible.

4.2.3 Electrochemistry and *Ex-Situ* Karl Fischer, XPS, TEM Studies in Nonaqueous Electrolyte

Traditional Mg-electrolytes based on Grignard compounds (RMgCl in association with $AlCl_3$) are considered highly corrosive to oxide materials, and their sensitivity to moisture could interfere with the structural water contained in birnessite. The electrochemical behavior of Mg-bir/CC in nonaqueous solvents was therefore investigated using the electrolyte 0.25 M $Mg(TFSI)_2$/diglyme (water content below 50 ppm). This electrolyte, reported for the first time by Ha et al.,[149] exhibits, in my experience, a large overpotential (> 2 V) when significant current flows through a Mg negative electrode. However, magnesium metal can still be used as a reference electrode owing to the extremely low current passed in this case. The electrochemistry of Mg-bir/CC was investigated in a three-electrode cell obtained from DPM Solutions Inc,[99] with a Mg reference and a capacitive-carbon counter (3:2 weight ratio of Black Pearls 2000, surface area ~ 1500 $m^2\ g^{-1}$: PVDF).[150]

Figure 4-9 shows the representative voltage profiles for the eighth cycle at a current density of C/10. The working electrode exhibits a voltage plateau at ~ 1.4 V during discharge and ~ 1.7 V during charge. Such flat plateaus suggest a two-phase reaction mechanism.[114] The almost linear voltage evolution of the carbon electrode with respect to capacity proves its double layer capacitor behavior,[151] validating the use of Mg metal as a reference electrode in

this system. However, the three-electrode cells showed limited lifetime. Owing to the gradual increase of the water content in the electrolyte (see later), the surface of the reference electrode is progressively passivated by a film of magnesium hydroxide.

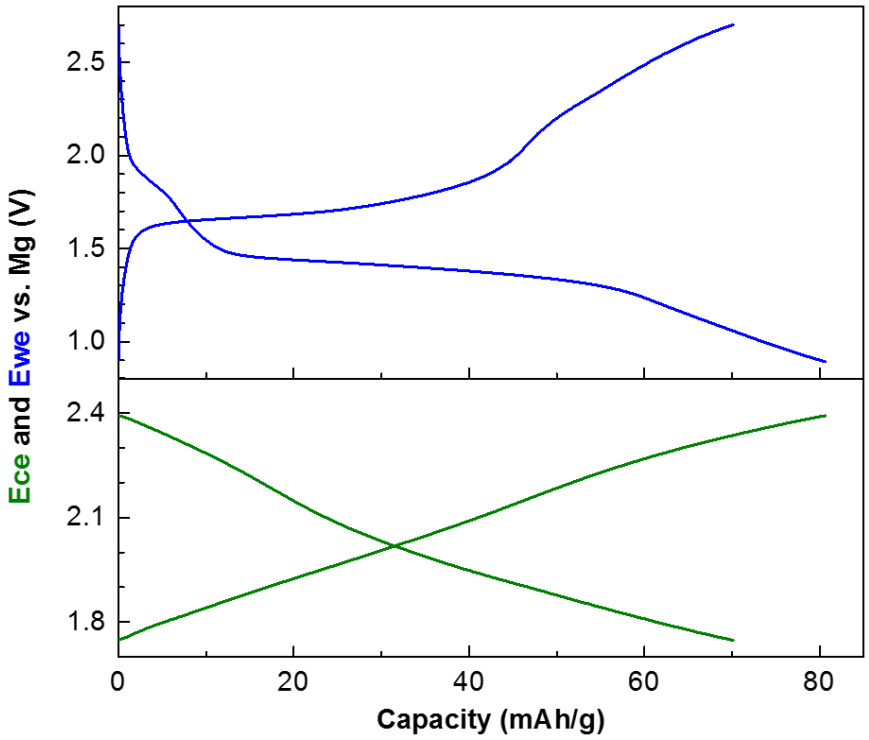

Figure 4-9. Voltage profiles of the working (top) and counter (bottom) electrode of Mg-bir/CC tested in a three-electrode cell with 0.25 M $Mg(TFIS)_2$/diglyme electrolyte and a Mg reference at C/10.

Thus, typical two-electrode coin cells were used to study long-term cycling performance and water content evolution (**Figure 4-10**). At both C/5 and C/10 rates, a long conditioning process is observed before the Mg-bir/CC electrodes achieve their maximum reversible capacity (**Figure 4-10b**). A capacity of about 135 mAh g^{-1} is obtained after 20 cycles at C/10 before the capacity slowly decays, whereas at a C/5 rate, about 50 cycles are necessary to achieve a capacity of 90 mAh g^{-1} that is maintained over 100 cycles. The higher capacity

sustained at a C/10 rate compared to a C/5 rate indicates slow kinetics of the electrochemistry process, in complete contrast to the aqueous case where Mg^{2+} ions show good solid state diffusion at a 2C rate, and where the attendant phase transformation to the spinel is accompanied by water egress.

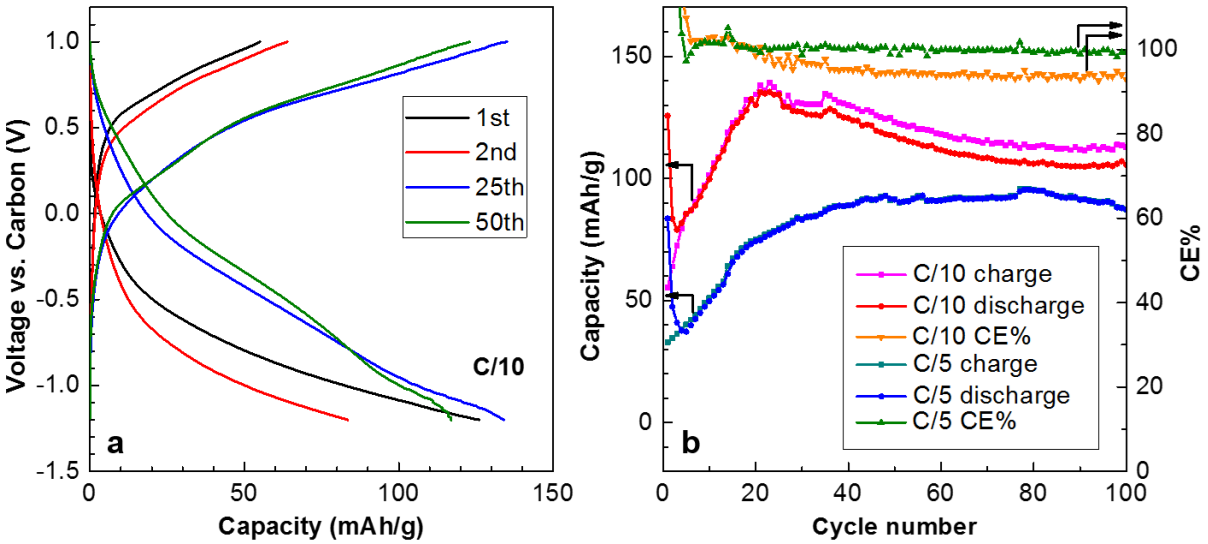

Figure 4-10. (a) Voltage profile, (b) capacity and coulombic efficiency evolution of Mg-bir/CC tested in coin cells with 0.25 M $Mg(TFSI)_2$/diglyme electrolyte.

No significant changes were observed in the diffractograms of the charged and discharged samples, showing that owing to the intrinsic disorder of the birnessite structure and the extremely small particle size, XRD is not an ideal probe of the changes involved upon cycling. However, a progressive broadening of the (001) peak is present as a function of the cycle number; after 20 cycles, this feature is barely visible, whereas the other peaks remain (**Figure 4-12a**). A similar evolution is observed by thermodiffraction upon dehydration of Mg-bir/CC (**Figure 4-11**), suggesting the release of structural water into the electrolyte. This is confirmed by the continuous increase in the water content of the electrolyte (**Figure 4-12b**) up to the 20th cycle, as monitored by Karl Fischer titration. Interestingly, the number of cycles

required to release all of the structural water into the electrolyte corresponds to the number of cycles of the conditioning process (**Figure 4-10b**). Addition of a small fraction of water (0.3% wt. (3,000 ppm)) to the electrolyte shows the same conditioning process (**Figure 4-13**),

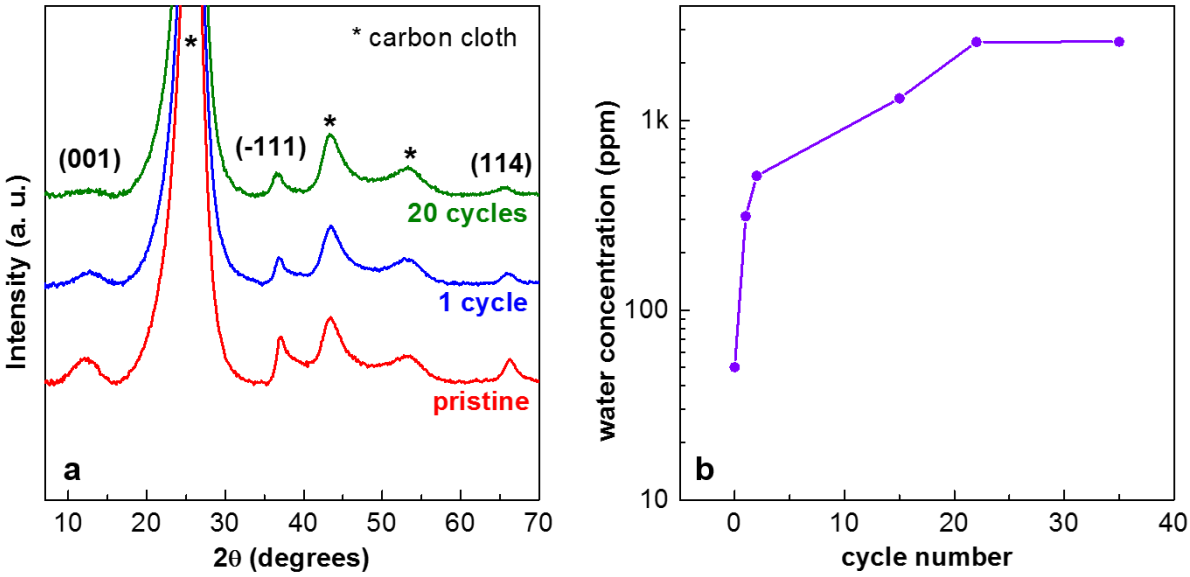

Figure 4-12. (a) XRD patterns of cycled electrodes (charged states) in the nonaqueous cell; (b) water content of the electrolyte as determined by Karl Fischer titration.

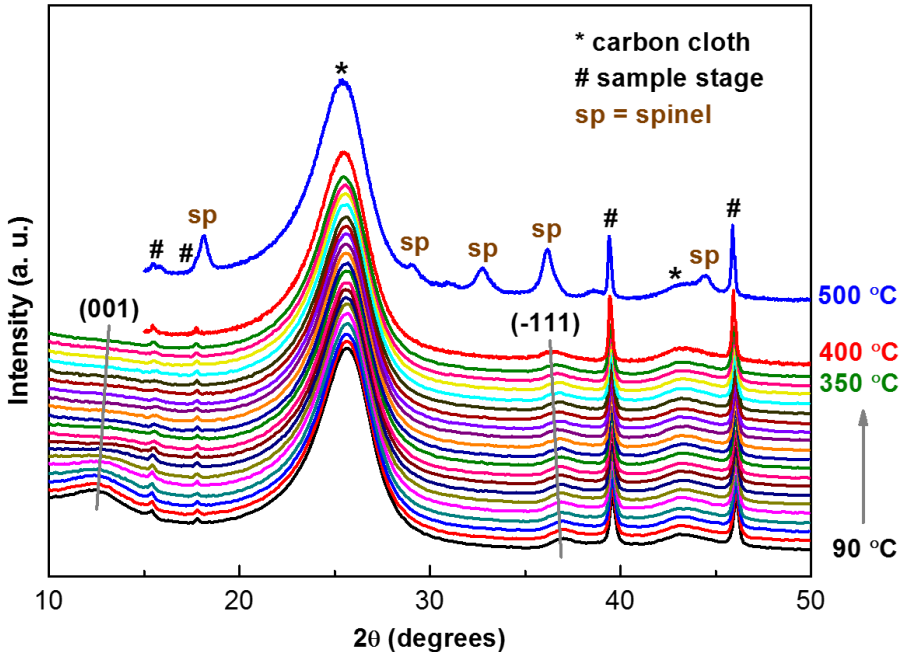

Figure 4-11. Thermodiffraction of Mg-bir/CC under a helium flow.

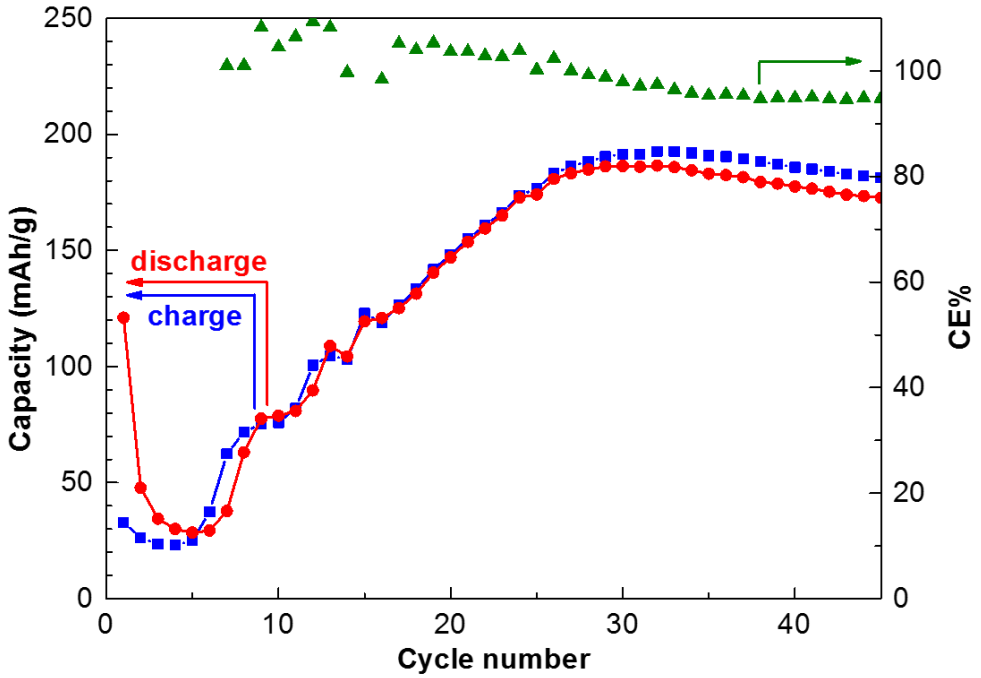

Figure 4-13. Capacity and coulombic efficiency evolution of Mg-bir/CC in 0.25M $Mg(TFSI)_2$/ diglyme electrolyte with 0.3 wt% ppm water at C/10.

suggesting that the increase in reversible capacity comes from the modification of the active material structure rather than the overall water concentration.

The evolution of the chemical speciation upon cycling is studied by *ex-situ* XPS, showing semi-reversible shift of Mn 2p spectra and change in O 1s spectra are obtained (**Figure 4-14**). An in-depth fitting is then carried out to study the detailed mechanism, and the results are summarized in **Figure 4-15** and **Table 4-1**~**Table 4-4**. The Mn $2p_{3/2}$ spectra are fit by sextuplets using parameters previously established for each oxidation number and chemical environment (**Table 4-1**~**Table 4-3**).[152-154] Note that the multiplets result from the multiple final states that are generated by coupling the unpaired d electrons with the unpaired 2p electron. The peak shapes can be different even with the same oxidation state. Thus, in the fitting procedure the peak separation, ratio and width are constrained among the multiplets in

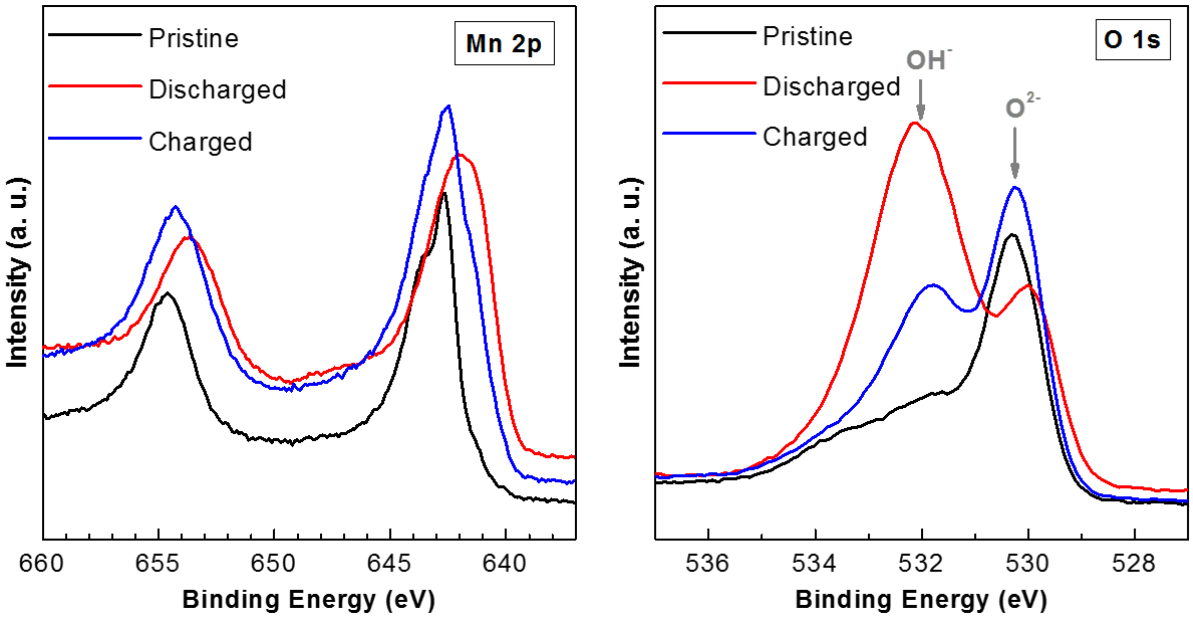

Figure 4-14. Mn 2p and O 1s XPS spectra comparing the pristine, discharged and charged samples cycled in nonaqueous electrolyte.

accord with the previously reported values for specific species. Such splitting does not happen for O 1s spectra, and they are fit by singlets of M-O, M−OH and H_2O (**Table 4-4**).

The pristine sample shows results consistent with previously reported values.[152] The manganese in birnessite exhibits mixed valence states composed of about 77% Mn^{4+}, 20% Mn^{3+}, and 3% Mn^{2+} (**Figure 4-15a**) in good agreement with the chemical formula $Mg_{0.15}MnO_2$ $0.9H_2O$. The oxygen spectrum (**Figure 4-15d**) is fit with a oxide component (54%) and two hydrogenated oxygen environments; hydroxide (30%) and structural water (16%).

Upon discharge, the shift to lower binding energy in the Mn $2p_{3/2}$ spectrum (**Figure 4-15b**) is characteristic of the reduction of the manganese ions. The shoulder at 647 eV represents a highly characteristic satellite of MnO,[154] clearly proving the existence of this oxide at the surface of the discharged sample. The remaining part of the Mn $2p_{3/2}$ spectrum is well

fit using a component typical of MnOOH.[154] Consistent with this, the O 1s spectrum of the discharged sample (**Figure 4-15e**) shows an increase of hydroxide species (up to 62%), whereas the oxide content decreases to 21%. The large excess of hydroxide with respect to the oxide component suggests the formation of $Mg(OH)_2$. A small fraction of the O 1s signal (3%) is assigned to water; however, its nearly 0.7 eV higher binding energy with respect to the pristine sample suggests that the remaining water is physisorbed rather than chemically bonded.[155] The additional peak at 533 eV corresponds to the oxygen in the $TFSI^-$ anion,[156] which is supported by the presence of corresponding signals in the C 1s (**Figure 4-16a**) and N 1s, F 1s, and S 2p regions (**Figure 4-16b**). The O 1s spectrum could not be fit without this contribution. Furthermore, significant signal from the $TFSI^-$ is found only in the case of the discharged, i.e. magnesiated sample, despite extensive washing of the electrode. This indicates, importantly, that $TFSI^-$ anions are chemically bonded to the surface of the cathode since the same washing procedure efficiently removed contamination from the electrolyte on the charged cathodes.

In the charged sample, the Mn $2p_{3/2}$ peak shifts back to higher binding energy (**Figure 4-15c**), implying reoxidation of the Mn species. The lower Mn^{4+} concentration (44%) than in the pristine sample (77%) is consistent with the irreversible capacity observed in the first discharge. The remainder of the Mn $2p_{3/2}$ spectrum is fit by 42% Mn^{3+}, corresponding to a birnessite environment, and 14% MnO. Similarly, the "oxygen speciation" evolves from a hydroxide environment to an oxide environment close to that observed in the pristine sample.

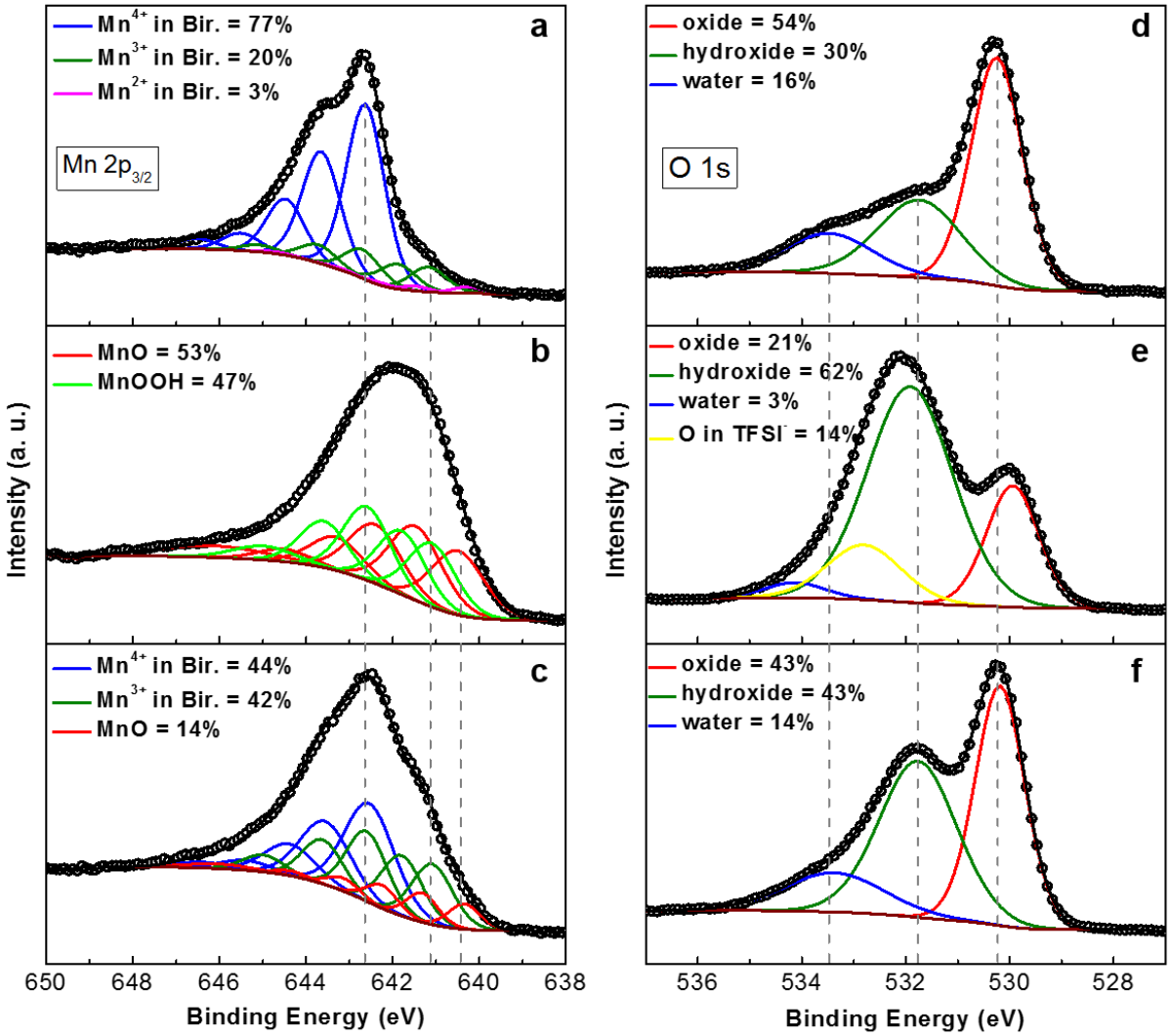

Figure 4-15. (a-c) Mn 2p3/2 and (d-f) O 1s XPS spectra of (a, d) pristine, (b, e) discharged, and (c, f) charged Mg-bir/CC electrodes cycled in nonaqueous electrolyte; fits are shown in color as labeled.

Table 4-1. Mn $2p_{3/2}$ multiplet peak parameters for the pristine electrode

Peak	**B. E. (eV)**	**FWHM (eV)**	**Percent (%)**	**Comments**
Mn^{2+} ($2p_{3/2}$) parameters: Mn^{2+} (total) = 2.83%				
Mn^{2+}-birnessite	640.27	0.784	1.04	Multiplet no. 1
Mn^{2+}-birnessite	641.47	0.784	0.74	Multiplet no. 2
Mn^{2+}-birnessite	642.27	0.784	0.43	Multiplet no. 3
Mn^{2+}-birnessite	643.17	0.784	0.31	Multiplet no. 4
Mn^{2+}-birnessite	644.67	0.784	0.31	Multiplet no. 5
Mn^{3+} ($2p_{3/2}$) parameters: Mn^{3+} (total) = 20.56%				
Mn^{3+}-birnessite	641.18	0.987	4.93	Multiplet no. 1
Mn^{3+}-birnessite	641.88	0.987	4.93	Multiplet no. 2
Mn^{3+}-birnessite	642.69	0.987	5.72	Multiplet no. 3
Mn^{3+}-birnessite	643.71	0.987	3.60	Multiplet no. 4
Mn^{3+}-birnessite	645.08	0.987	1.38	Multiplet no. 5
Mn^{4+} ($2p_{3/2}$) parameters: Mn^{4+} (total) = 76.60%				
Mn^{4+}-birnessite	642.63	1.030	36.15	Multiplet no. 1
Mn^{4+}-birnessite	643.65	1.030	23.12	Multiplet no. 2
Mn^{4+}-birnessite	644.48	1.030	11.56	Multiplet no. 3
Mn^{4+}-birnessite	645.51	1.030	3.61	Multiplet no. 4
Mn^{4+}-birnessite	646.53	1.030	2.16	Multiplet no. 5

Table 4-2. Mn $2p_{3/2}$ multiplet peak parameters for the **discharged** electrode

Peak	**B. E. (eV)**	**FWHM (eV)**	**Percent (%)**	**Comments**
Mn^{2+} ($2p_{3/2}$) parameters: Mn^{2+} (total) = 52.52%				
Mn^{2+}-MnO	640.50	1.419	12.59	Multiplet no. 1
Mn^{2+}-MnO	641.47	1.419	14.58	Multiplet no. 2
Mn^{2+}-MnO	642.40	1.419	11.58	Multiplet no. 3
Mn^{2+}-MnO	643.30	1.419	6.55	Multiplet no. 4

Mn^{2+}-MnO	644.50	1.419	2.46	Multiplet no. 5
Mn^{2+}-MnO	646.20	2.923	4.76	Satellite
Mn^{3+} ($2p_{3/2}$) parameters: Mn^{3+} (total) = 47.48%				
Mn^{3+}-MnOOH	641.09	1.294	11.41	Multiplet no. 1
Mn^{3+}-MnOOH	641.79	1.294	11.40	Multiplet no. 2
Mn^{3+}-MnOOH	642.59	1.294	13.18	Multiplet no. 3
Mn^{3+}-MnOOH	643.59	1.294	8.31	Multiplet no. 4
Mn^{3+}-MnOOH	644.99	1.294	3.18	Multiplet no. 5

Table 4-3. Mn $2p_{3/2}$ multiplet peak parameters for the **charged** electrode

Peak	**B. E. (eV)**	**FWHM (eV)**	**Percent (%)**	**Comments**
Mn^{2+} ($2p_{3/2}$) parameters: Mn^{2+} (total) = 13.92%				
Mn^{2+}-MnO	640.35	0.863	3.34	Multiplet no. 1
Mn^{2+}-MnO	641.32	0.863	3.86	Multiplet no. 2
Mn^{2+}-MnO	642.25	0.863	3.07	Multiplet no. 3
Mn^{2+}-MnO	643.15	0.863	1.74	Multiplet no. 4
Mn^{2+}-MnO	644.35	0.863	0.65	Multiplet no. 5
Mn^{2+}-MnO	646.05	1.779	1.26	Satellite
Mn^{3+} ($2p_{3/2}$) parameters: Mn^{3+} (total) = 42.44%				
Mn^{3+}-birnessite	641.09	1.101	10.18	Multiplet no. 1
Mn^{3+}-birnessite	641.79	1.101	10.18	Multiplet no. 2
Mn^{3+}-birnessite	642.60	1.101	11.80	Multiplet no. 3
Mn^{3+}-birnessite	643.62	1.101	7.43	Multiplet no. 4
Mn^{3+}-birnessite	644.99	1.101	2.85	Multiplet no. 5
Mn^{4+} ($2p_{3/2}$) parameters: Mn^{4+} (total) = 43.63%				
Mn^{4+}-birnessite	642.54	1.363	20.59	Multiplet no. 1
Mn^{4+}-birnessite	643.56	1.363	13.17	Multiplet no. 2
Mn^{4+}-birnessite	644.39	1.363	6.58	Multiplet no. 3

Mn^{4+}-birnessite	645.42	1.363	2.06	Multiplet no. 4
Mn^{4+}-birnessite	646.44	1.363	1.23	Multiplet no. 5

Table 4-4. O 1s multiplet peak parameters

Peak	**B. E. (eV)**	**FWHM (eV)**	**Percent (%)**
Pristine			
oxide	530.25	1.164	54.12
hydroxide	531.74	1.887	29.82
water	533.47	1.974	16.06
Discharged			
oxide	529.94	1.196	21.51
hydroxide	531.91	1.936	61.79
water	534.13	1.349	3.04
O in $TFSI^-$	532.80	1.689	13.67
Charged			
oxide	530.18	1.122	42.60
hydroxide	531.76	1.759	43.46
water	533.37	2.251	13.94

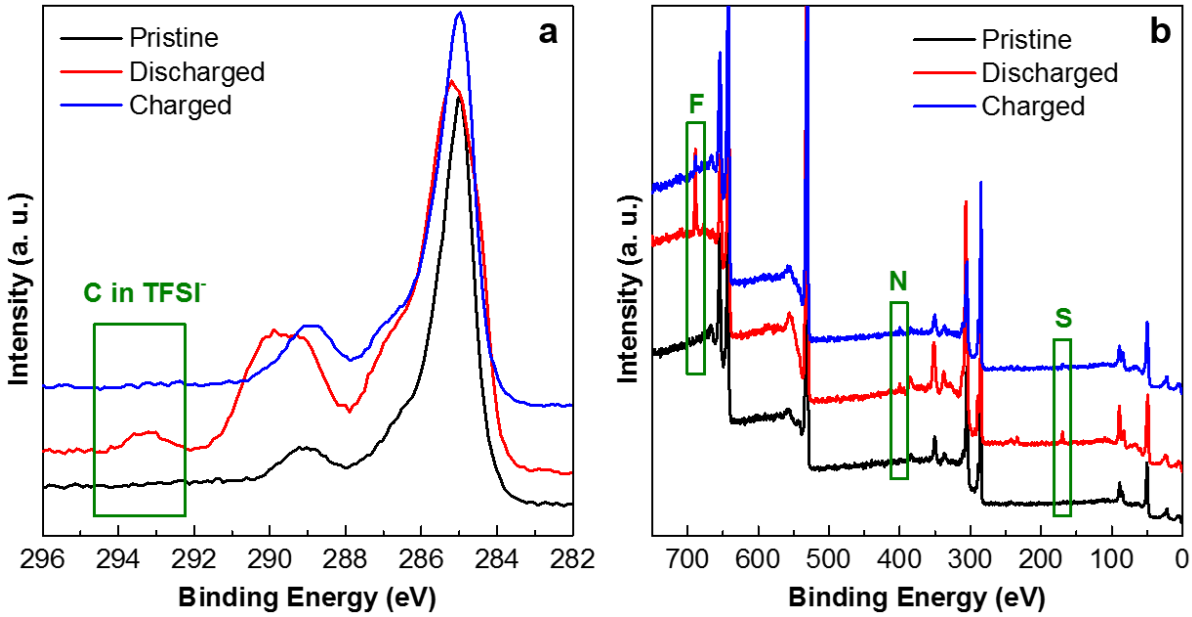

Figure 4-16. (a) C 1s and (b) typical survey XPS spectra comparing the pristine, discharged and charged samples cycled in nonaqueous electrolyte, showing contributions from the $TFSI^-$ anion on discharge.

The evolution of the nature of the surface species upon magnesiation, as resolved by XPS, points at a conversion mechanism involving the formation of manganese oxyhydroxide (MnOOH) and manganese oxide (MnO) as well as magnesium hydroxide ($Mg(OH)_2$), summarized by the following equation:

$$Mg_{0.15}MnO_2 + H_2O \text{ (structural or from electrolyte)} + xMg^{2+} + 2xe^- \Leftrightarrow (2x - 0.70)MnO + (1.70 - 2x)MnOOH + (x + 0.15)Mg(OH)_2 \quad \textbf{Equation 4-1}$$

The voltage plateau observed in the first section of the discharge in the three electrode cell (**Figure 4-9**) agrees with this proposed multiphase process. The reversible capacity (135 mAh g^{-1}) obtained after conditioning of the electrode at a C/10 rate corresponds to about a 0.5 electron transfer per Mn atom. However, the change in the mean oxidation state (as measured by XPS) between the discharged and charged sample, + 2.5 and +3.3, respectively (i.e., a 0.8

e^- transfer), is larger than expected showing that the reaction occurs predominantly at the surface of the material. This behavior is typical of conversion reactions, where nucleation and growth of the conversion products take place at the interphase between electrode and electrolyte. Propagation of the reaction to the bulk is hindered if the conversion product does not allow for facile Mg^{2+} diffusion. Assuming a simplistic two-phase model, about 60% of the active material is estimated to involve in the electrochemical process. Despite the nanoscopic morphology of the active material, the reaction cannot proceed to the core of the particles, implying the formation of an interphase that does not conduct Mg^{2+} ions. The gradual decrease of the ionic conductivity of the solid interphase gives rise to the sloping voltage curve observed in the second part of the discharge.

HRTEM analysis was carried out to further characterize the species at the discharged and charged states. The positive electrodes used were cycled at 90 ℃ at C/10 with a carbon counter electrode and nonaqueous electrolyte. A higher temperature was employed here to push the reaction further to completion so that the products would be easier to track by TEM where only small area could be sampled each time. As shown in **Figure 4-17a**, capacities of ~ 210 mAh g^{-1} are obtained under these conditions, which approximates to a 0.8 electron transfer. A conditioning process is also required for the cell to achieve maximum capacity (**Figure 4-17b**), indicating the same conversion mechanism as observed at room temperature. However, fewer cycles are required to reach maximum capacity (i.e., two cycles at 90 ℃ as opposed to 20 cycles at room temperature) because of the high temperature, which allows the electrode and electrolyte to reach an equilibrium state more quickly.

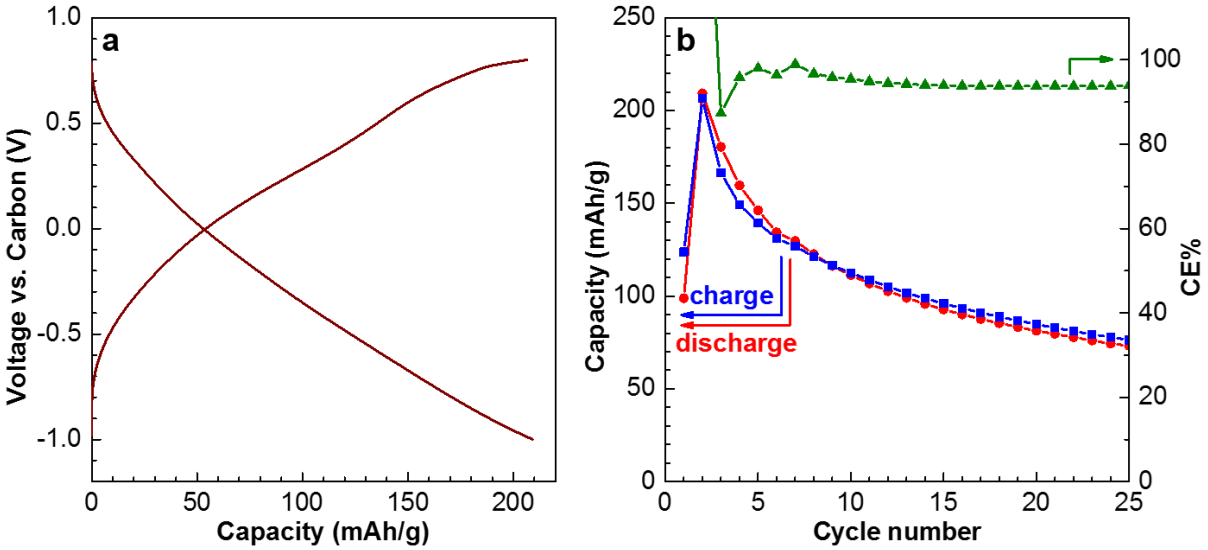

Figure 4-17. (a) Voltage profile and (b) capacity evolution of Mg-bir/CC cycled in 0.25M $Mg(TFSI)_2$/ diglyme electrolyte at C/10 and 90 ℃.

The EELS spectra shown in **Figure 4-18**, panels a and b are consistent with a conversion reaction. The small changes in the oxygen K-edge indicate that new oxide species are formed on discharge, which agrees with the XPS result where the transformation from the layered oxide and structural water matrix to the hydroxide, oxyhydroxide, and oxide mixture is observed. The reversible change of the Mg K-edge intensity and its energy indicate that Mg-oxide is formed at the positive electrode during discharge and consumed on charge, with the positive charges on Mg^{2+} compensated by the reduction or oxidation of Mn. The corresponding change in the Mn valence can be evaluated by the Mn-L2,3 ratio (**Figure 4-18a**). To a first approximation, in the absence of a detailed calibration curve, the observed Mn valence is scaled in the pristine birnessite, which is known to be +3.7 based on chemical analysis. The Mn valence decreases to +3.2 upon discharge and increases to +3.5 upon charge (**Figure 4-18c**). The difference in these values between the Mn valence calculated from the electrochemical capacities on discharge and charge of +2.9 and +3.7, respectively (**Figure 4-17a**), indicates an

inhomogeneous reaction within the positive electrode matrix. A spatially resolved EELS spectra of only the surface could not be achieved owing to the very highly divided nature of the birnessite. It is expected that the core remains as unreacted birnessite, and reduction of manganese proceeds on the shell of the particles as previously confirmed for α-MnO_2.[49] Thus,

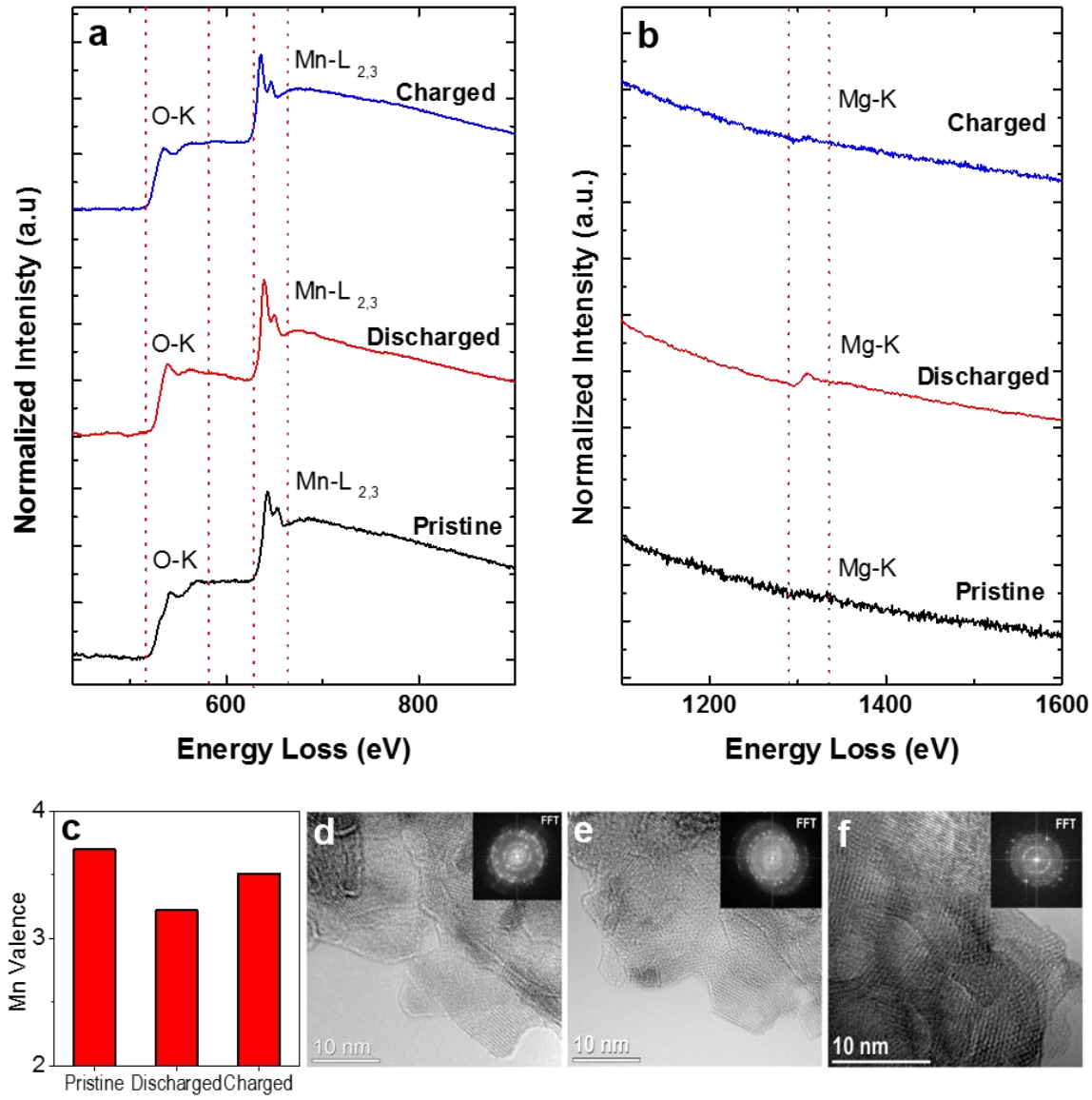

Figure 4-18. EELS spectra of the pristine, discharged and charged cathode material: (a) O−K edge and Mn L-edge; (b) Mg K-edge. (c) Bar plot showing the quantification of the Mn valence state determined from the L3/L2 ratio. HRTEM images of the (d) pristine, (e) discharged, and (f) charged cathode materials show their polycrystalline nature.

the Mn valence derived from EELS is the expected average. Finally, the HRTEM images shown in **Figure 4-18**, panels d−f demonstrate that there is no major change in the overall morphology of the electrode materials during cycling.

4.2.4 Key Factor Determining Mg^{2+} Insertion Mechanisms

Figure 4-19 summaries the electrolyte influence on the Mg^{2+} insertion into birnessite. While facile Mg^{2+} intercalation takes place in aqueous system, a conversion mechanism prominently at the surface of the particles despite their small size is identified in nonaqueous media. Such difference can not only result from the slow diffusion kinetics of Mg^{2+} ions. Indeed, the XPS results show clear evidence of the presence of $TFSI^-$ anions strongly bonded to the surface of the discharged sample, which suggests that in addition to the formation of thermodynamically favorable oxides,[144] a limiting factor is also the disruption of the ion pairing of the electrolyte salt. The high energy of ion pairing in $Mg(TFSI)_2$ in diglyme was recently calculated and measured, showing a well-defined Mg-O(TFSI) distance of 2.08 Å, which is smaller than the distance observed in solids such as MgO (2.11 Å).[157] Moreover, the importance of the H_2O/Mg ratio in the electrolyte rather than the overall water concentration showed by this study and others[46,146] clearly links the improvement of performance to the full solvation of Mg^{2+} by water molecules when H_2O/Mg > 6. These findings, together with the APC dissociation process proposed by calculation,[81] show that solid-state diffusion of Mg^{2+} might not be the only penalizing factor when moving from a singly charged ion (Li^+, Na^+) battery to a multivalent battery. Mg^{2+} desolvation at the electrode/electrolyte interphase is equally critical in determining the Mg^{2+} insertion kinetics, which would furthermore modify the specific mechanism. The development of new electrode materials for Mg batteries, therefore, should also focus on parameters leading to efficient disruption of the ion pairing at the interphase.

Strategies such as employing easily dissociated salt in electrolyte and coupling with solvent molecules or surface atoms of positive electrode would be applied to accelerate the desolvation process.

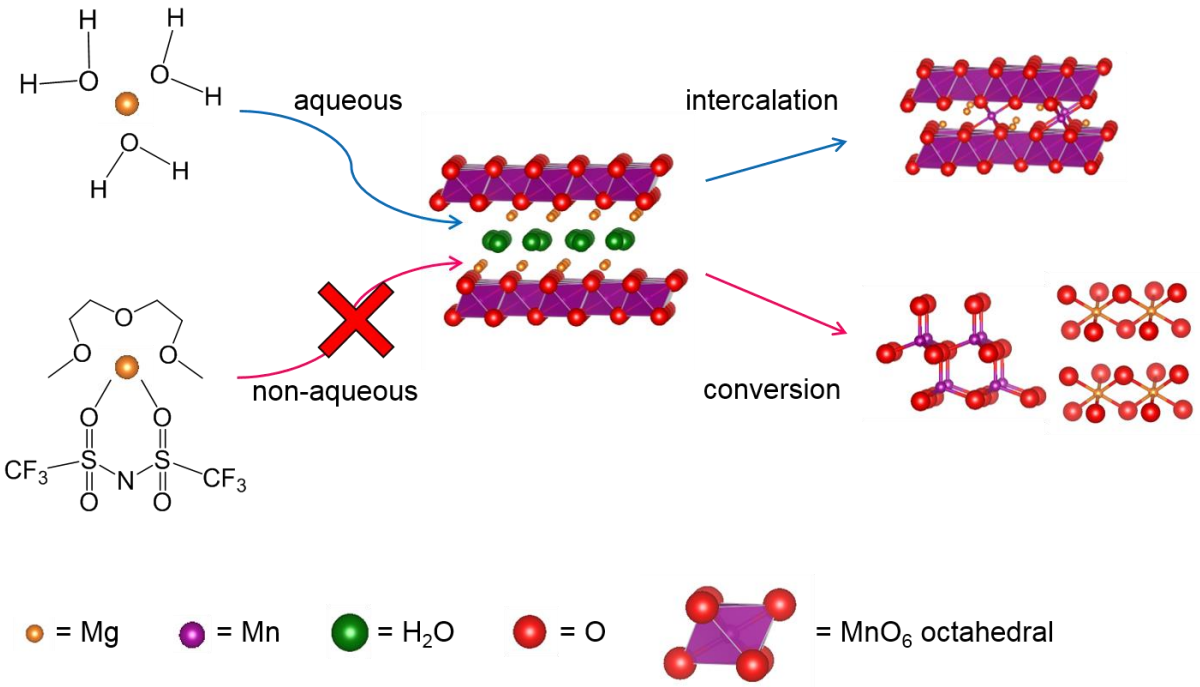

Figure 4-19. Schematic diagram showing the electrolyte influence on Mg^{2+} insertion mechanism into birnessite.

4.3 Layered $Mg_2Mo_3O_8$

The layered $Mg_2Mo_3O_8$ compound consists of Mo_3O_8 layers with Mg^{2+} occupying both octahedral and tetrahedral interlayer sites (**Figure 4-20a**), thus potentially provides good Mg^{2+} mobility due to the non-preferred Mg^{2+} coordination.[129] Additionally, the Mo_3 clusters existed in the Mo_3O_8 layers (**Figure 4-20b**)[158,159] would help with charge redistribution and further promote Mg^{2+} diffusion, as suggested for the effect of the Mo_6 clusters in the Chevrel lattices.[50] The Li analogue ($Li_4Mo_3O_8$) has previously been examined in a Li cell, offering an initial

specific capacity of 218 mAh g^{-1}.[160] Other materials with similar structures containing Mo_3 clusters, such as $LiMoO_2$ and Li_2MoO_3, also function well as Li-ion positive electrodes.[160-162] However, only limited work has been done on Mg^{2+} intercalation in Mo-oxides,[34,163,164] motivating the examination of the Mg^{2+} diffusion properties in $Mg_2Mo_3O_8$ and its potential as a positive electrode material for Mg batteries.

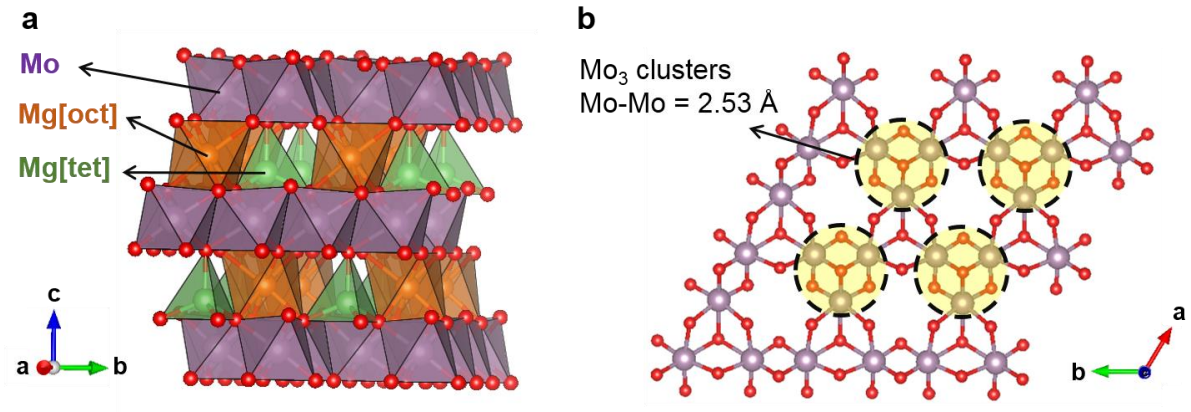

Figure 4-20. (a) Crystal structure of $Mg_2Mo_3O_8$. (b) MoO_6 octahedra layer showing Mo_3 clusters.

4.3.1 Synthesis and Characterization

$Mg_2Mo_3O_8$ was synthesized by heating the wet ball milled (ethanol as solvent) 1:1 mixture of MgO and MoO_2 at 1000 ℃ for 12 hours under Ar flow. The small amount of MgO impurity was washed away with 1M HCl. The structure of the product was confirmed by the Rietveld refinement[92] of the XRD pattern (**Figure 4-21a** and **Table 4-5**). The obtained particles have well-defined edges and are around 2 μm in size (**Figure 4-21b**).

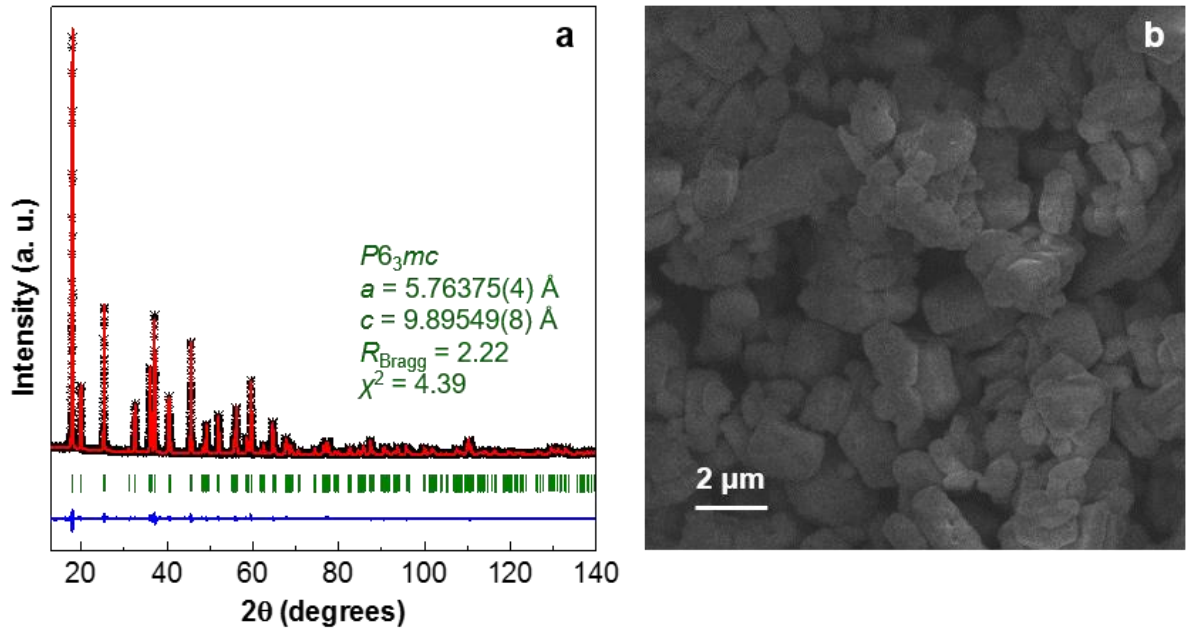

Figure 4-21. (a) Rietveld refinement fit and (b) SEM image of pristine $Mg_2Mo_3O_8$ (Bragg-Brentano geometry, black crosses – experimental data, red lines – fitted data, blue line – difference curve between observed and calculated data, green ticks – the Bragg peak positions of the $Mg_2Mo_3O_8$ phase).

Table 4-5. Refined parameters for pristine $Mg_2Mo_3O_8$ (space group = $P6_3mc$, a = 5.76375(4) Å, c = 9.89549(8) Å, χ^2 = 4.39, Bragg R-factor = 2.22).

Atom	**Wyck.**	***x***	***y***	***z***	**Occ.**	**B_{iso} (Å^2)**
Mo	6c	0.14639(4)	0.85361(4)	0.250(5)	1	0.050(4)
Mg1	2b	0.33333	0.66667	0.948(5)	1	0.43(4)
Mg2	2b	0.33333	0.66667	0.513(5)	1	0.43(4)
O1	2a	0	0	0.397(5)	1	0.13(3)
O2	2b	0.33333	0.66667	0.142(5)	1	0.13(3)
O3	6c	0.4881(4)	0.5119(4)	0.371(5)	1	0.13(3)
O4	6c	0.1682(6)	0.8318(6)	0.632(5)	1	0.13(3)

4.3.2 Chemical De-Magnesiation

In order to study the possibility of Mg removal from such a structure, chemical demagnesiation was carried out using NO_2BF_4, a commonly used oxidizing agent for chemical delithiation.[165] $Mg_2Mo_3O_8$ were added to 0.2 M NO_2BF_4 in ACN solution at a 1:4 ratio and stirred for 1 day in an Ar-filled glovebox at room temperature, which would allow complete Mg de-intercalation with each NO_2BF_4 sustained a one electron reduction as anticipated. The product was filtered and washed with ACN.

EDX reveals that the majority of the Mg was removed from the structure (**Table 4-6**). At the same time, the particles become smaller after demagnesiation (**Figure 4-22b**), suggesting some changes in the material. Despite these differences, the XRD results show no shift of the peaks (**Figure 4-22a**). The atomic positions obtained by Rietveld refinement[92] are almost the same as those of the pristine and no change on the Mg occupancies is observed (**Table 4-7** and **Table 4-5**), suggesting that a two-phase reaction takes place, with the demagnesiated phase being amorphous. During this process, Mg is presumably first removed from the outer shell, leading to the destabilization of the parent lattice and eventual amorphization.

The amount of the amorphous phase in the demagnesiated product is then estimated using silicon as an external standard. XRD was carried out on a mixture of 0.9:0.1 weight ratio of th demagnesiated material and Si, and refinement results in a weight ratio of 0.54:0.46 between the crystalline $Mg_2Mo_3O_8$ and Si (**Table 4-7**). This corresponds to about 87 wt% amorphous phase in the product, giving an overall composition of $Mg_{0.24}Mo_3O_8$ assuming no Mg present in the amorphous phase. Such value is similar to the cationic ratio determined by EDX (**Table 4-6**) and indicates complete demagnesiation of the amorphous component. The ~

13 wt% unreacted $Mg_2Mo_3O_8$ results from the reduced oxidizing strength of NO_2BF_4 exhibited near the end of the reaction due to low oxidizer concentration, or other side reactions that consumed the oxidizer.

Table 4-6. EDX results for chemical demagnesiation of $Mg_2Mo_3O_8$

Sample	Pristine	Partially demagnesiated	Fully demagnesiated
Mg/Mo	1.59(4)/3	0.53(4)/3	0.13(6)/3

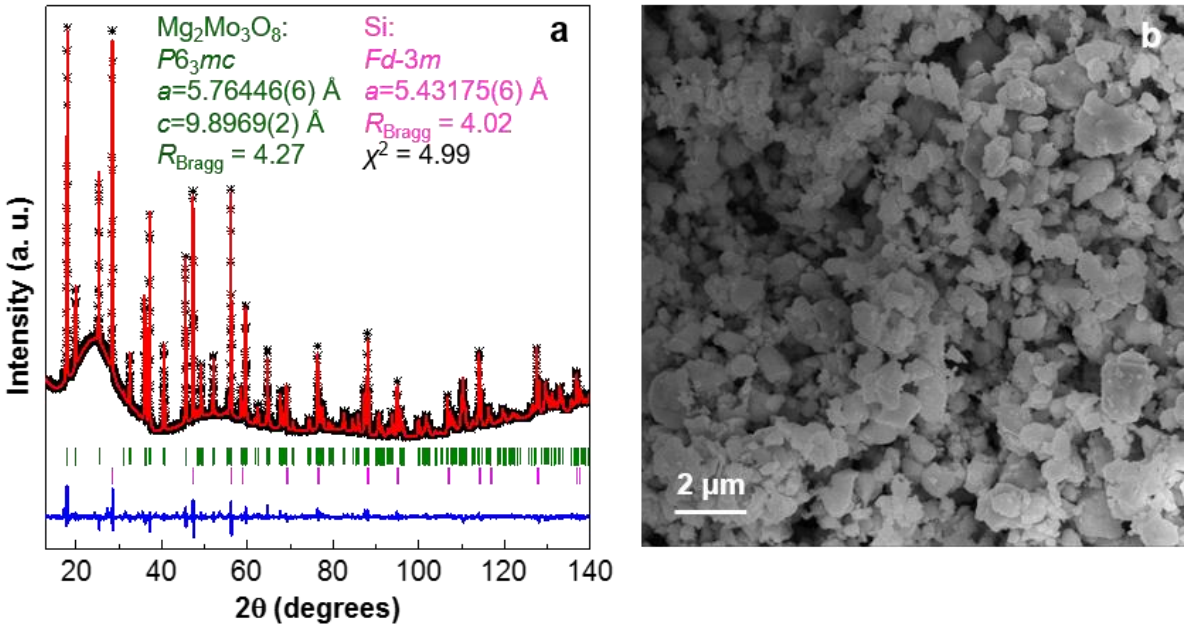

Figure 4-22. (a) Rietveld refinement fit and (b) SEM image of fully demagnesiated $Mg_2Mo_3O_8$ (Debye-Scherrer geometry, black crosses – experimental data, red lines – fitted data, blue line – difference curve between observed and calculated data, ticks – the Bragg peak positions of $Mg_2Mo_3O_8$ (green) and standard silicon (pink). The broad hump is a background signal from the X-ray capillary).

Table 4-7. Refined parameters for a mixture of 90 wt% fully demagnesiated $Mg_2Mo_3O_8$ and 10 wt% silicon standard (χ^2 = 4.99).

Atom	**Wyck.**	***x***	***y***	***z***	**Occ.**	**B_{iso} (Å^2)**
$Mg_2Mo_3O_8$, S.G. = *P6$_3$mc*, *a* = 5.76446(6) Å, *c* = 9.8969(2) Å, 54.0(6) wt%, Bragg *R*-factor = 4.27						
Mo	6c	0.14632(8)	0.85368(8)	0.250(6)	1	0.071(6)
Mg1	2b	0.33333	0.66667	0.949(6)	1	0.50(6)
Mg2	2b	0.33333	0.66667	0.513(6)	1	0.50(6)
O1	2a	0	0	0.397(6)	1	0.21(4)
O2	2b	0.33333	0.66667	0.143(6)	1	0.21(4)
O3	6c	0.4880(9)	0.51204(9)	0.371(6)	1	0.21(4)
O4	6c	0.172(1)	0.828(1)	0.632(6)	1	0.21(4)
Silicon, S.G. = *Fd*-3*m*, *a* = 5.43175(6) Å, 46.0(6) wt%, Bragg *R*-factor = 4.02						
Si	8a	0.875	0.875	0.875	1	0.527(6)

Partial demagnesiation from the $Mg_2Mo_3O_8$ structure was not achieved by reducing the amount of oxidizing agent ($Mg_2Mo_3O_8$:NO_2BF_4 = 1:2), as indicated by the preservation of the initial phase obtained by XRD refinement (**Figure 4-23a** and **Table 4-8**). Together with the decrease of the overall Mg/Mo ratio to ~ 0.53(4)/3 (**Table 4-6**) and the co-existence of different morphologies (**Figure 4-23b**), the results suggest that part of $Mg_2Mo_3O_8$ undergoes complete demagnesiation and becomes amorphous while the rest fraction of material does not participate in the reaction.

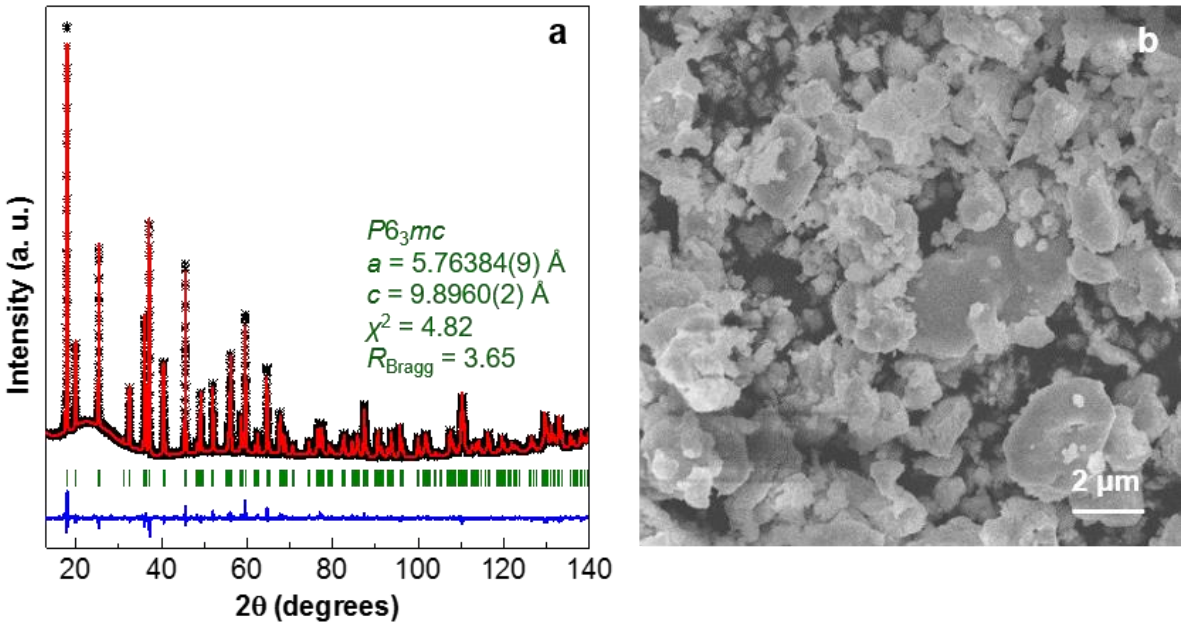

Figure 4-23. (a) Rietveld refinement fit and (b) SEM image of fully demagnesiated $Mg_2Mo_3O_8$ (Debye-Scherrer geometry, black crosses – experimental data, red lines – fitted data, blue line – difference curve between observed and calculated data, green ticks – the Bragg peak positions. The broad hump is a background signal from the X-ray capillary).

Table 4-8. Refined parameters for partially demagnesiated $Mg_2Mo_3O_8$ (space group = $P6_3mc$, a = 5.76384(9) Å, c = 9.8960(2) Å, χ^2 = 4.82, Bragg R-factor = 3.65).

Atom	**Wyck.**	***x***	***y***	***z***	**Occ.**	B_{iso} **(Å²)**
Mo	6c	0.14626(5)	0.85374(5)	0.250(8)	1	0.059(4)
Mg1	2b	0.33333	0.66667	0.950(8)	1	0.42(4)
Mg2	2b	0.33333	0.66667	0.512(8)	1	0.42(4)
O1	2a	0	0	0.396(8)	1	0.27(3)
O2	2b	0.33333	0.66667	0.146(8)	1	0.27(3)
O3	6c	0.4886(6)	0.5114(6)	0.369(8)	1	0.27(3)
O4	6c	0.1747(8)	0.8253(8)	0.633(8)	1	0.27(3)

First principles calculation was then carried out to explain the amorphization (in collaboration with Dr. Ceder group in LBNL).[166] The energy above the convex ground state hull (E^{hull}) of the $Mg_xMo_3O_8$ structures was calculated with respect to the stable compounds in the Mg-Mo-O ternary phase diagram, so as to evaluate the thermodynamic stability of demagnesiated materials.[102,103] Typically, a thermodynamically stable structure will have an E^{hull} of 0 meV per atom, while more positive E^{hull} values indicate a greater driving force to form other phases. Note that E^{hull} values are evaluated at 0 K and entropic contributions can stabilize a structure at higher temperatures. Based on available compounds in the Materials Project database,[167] increasing E^{hull} values are obtained with more Mg removal from $Mg_2Mo_3O_8$ (**Table 4-9**), demonstrating an increase in the thermodynamic driving force for decomposition. The high E^{hull} values at lower Mg concentrations would be responsible for the amorphization during chemical Mg extraction from $Mg_2Mo_3O_8$, which is also in consistent with the naturally amorphous occurrence of Mo_3O_8.[168,169]

Table 4-9. The E^{hull} values (in meV per atom) and the corresponding decomposition products are listed as a function of the Mg content in the Mo_3O_8 structure, as obtained from the Materials Project database. The comments column indicates available experimental observations.

Composition	**E^{hull}**	**Decomposition products**	**Comments**
$Mg_2Mo_3O_8$	51	MoO_2 + MgO	Chemically synthesizable
$MgMo_3O_8$	180	MoO_2 + $MgMoO_4$	-
Mo_3O_8	330	MoO_2 + Mo_8O_{23}	Natrually amorphous

4.3.3 Electrochemical De-Magnesiation

Since the degree of chemical oxidation is hard to control, the stepwise demagnesiation behavior was attempted to evaluate by an electrochemical method. As it has been suggested that the Mg desolvation process depends on the solvent [170, 171] and is critical for the electrochemical mechanism at the positive electrode (Section 4.2),[47,81] $Mg_2Mo_3O_8$ was examined in both non-aqueous (APC) and aqueous ($Mg(ClO_4)_2$ in water) systems. A demagnesiation voltage similar to the delithiation voltage of $Li_4Mo_3O_8$ (average of ~ 2.4 V vs. Mg) [160] or at ~ 2.6 V as predicted by first principles calculation[166] would be expected, which could be stably offered by both electrolytes. However, no electrochemical activity is observed in either system (**Figure 4-24**). Such results potentially indicate the existence of a high Mg^{2+} diffusion barrier in the structure, hence kinetics being the main limitation. Chemical oxidation, on the other hand, might involve a mechanism other than simple cation diffusion, such as a partial dissolution/re-precipitation process. This helps in lowering the kinetic barrier and establishes successful Mg removal.

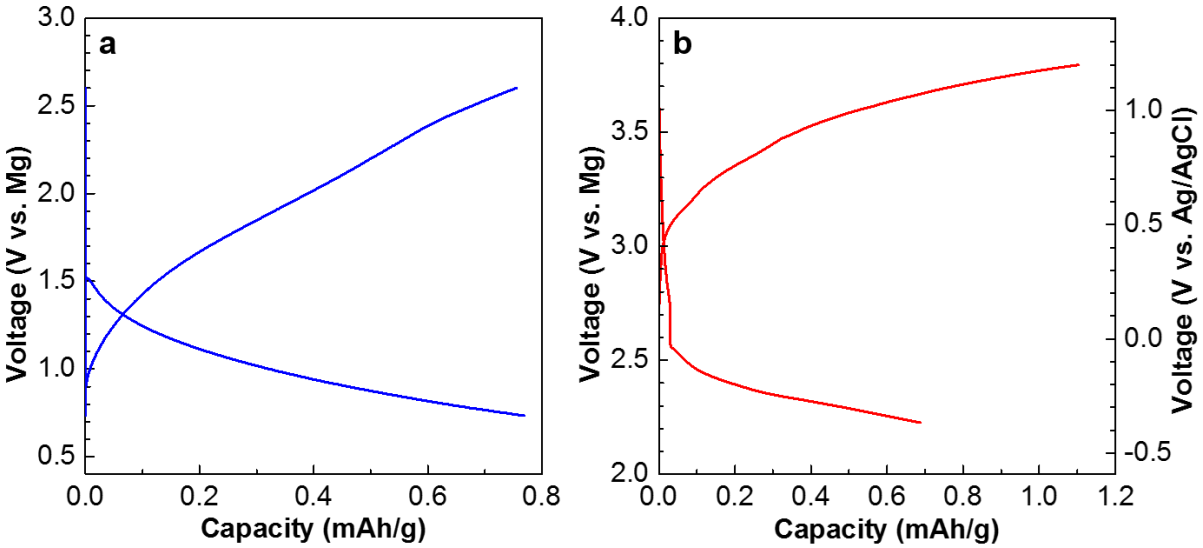

Figure 4-24. Electrochemistry of $Mg_2Mo_3O_8$ (a) casted on Mo current collector and tested in 0.4M APC, and (b) casted on Ti current collector and tested 0.5M $Mg(ClO_4)_2$ in water at C/20 rate ($1Mg^{2+}/Mg_2Mo_3O_8$ in 20 hours) and room temperature, showing no activity.

4.3.4 High Barrier Dumbbell Transition State

To evaluate the Mg^{2+} mobility in the $Mg_2Mo_3O_8$ structure, the activation barriers of possible Mg diffusion hops were investigated by first principles calculation (in collaboration with Dr. Ceder group at LBNL). The shortest hop (hop 1) involves Mg migration from a tetrahedral site to an octahedral site (or *vice versa*) within the same Mg-plane (**Figure 4-25b**), constructing 2D Mg^{2+} pathways between the Mo_3O_8 layers. Alternative hop (hop 2) requires Mg going across the Mo-plane to the adjacent Mg-plane. **Figure 4-25a** shows the calculated Mg migration barriers (at $x_{Mg} \sim 2$ with a dilute vacancy limit) along the pathway. A small energy difference of around 250 meV is obtained between the tetrahedral (starting) and octahedral (ending) site, in agreement with the non-preference Mg occupation in the structure. However, it is notable that relatively high activation energies are obtained for both hops (~ 1200 and 2000 meV, respectively), considering a diffusion barrier of 525 ~ 650 meV is normally required for bulk Mg mobility at reasonable rates.[129] The above 1 eV barriers would readily lead to sluggish Mg^{2+} diffusion in the $Mg_2Mo_3O_8$ structure, explaining the poor electrochemical performance.

While the high barrier for the cross-plane hop is due to the strong electrostatic repulsion that Mg experiences from Mo atoms as it passes through a triangular face of oxygen atoms across the Mo_3O_8 layer, a closer look to hop 1 is required to understand the large barriers. **Figure 4-25b** shows the representative intermediate sites with the corresponding energies labeled in **Figure 4-25a**. Although site 3 (triangular face) has an energy of ~ 685 meV with respect to the tetrahedral site (similar to ~ 600–800 meV observed in oxide spinels[102]), the magnitude of the barrier is determined by site 1 where Mg is situated along an O–O bond (edge of the stable tetrahedron), in a dumbbell configuration. Significant increase of the distance

between two oxygens is required to fit in a Mg; however, this is difficult in a rigid solid structure. Previous evaluations of Mg migration through an O–O dumbbell hop for layered NiO_2 have reported high barriers (~ 1400 meV),[129] similar to the present result. An alternative pathway (**Figure 4-25c**) which would avoid the O-Mg-O intermediate state does not result in a decrease of energy barrier, either. The new intermediate tetrahedron site (yellow) that generates is face-shared with a MoO_6 octahedron (light blue) and experiences strong repulsion. Indeed, calculations relax to a pathway similar to the O-Mg-O hop with a similar barrier (~ 1150 meV). Such absence of low energy pathways for Mg diffusion in the $Mg_2Mo_3O_8$ structure is responsible for its poor electrochemistry. The results suggest the importance of intermediate sites along a diffusion path, which is determined by the specific topology of cation sites in the lattice, in addition to the occurrence of the mobile cation with a non-preferred coordination and a preferentially coordinated metastable site.[129]

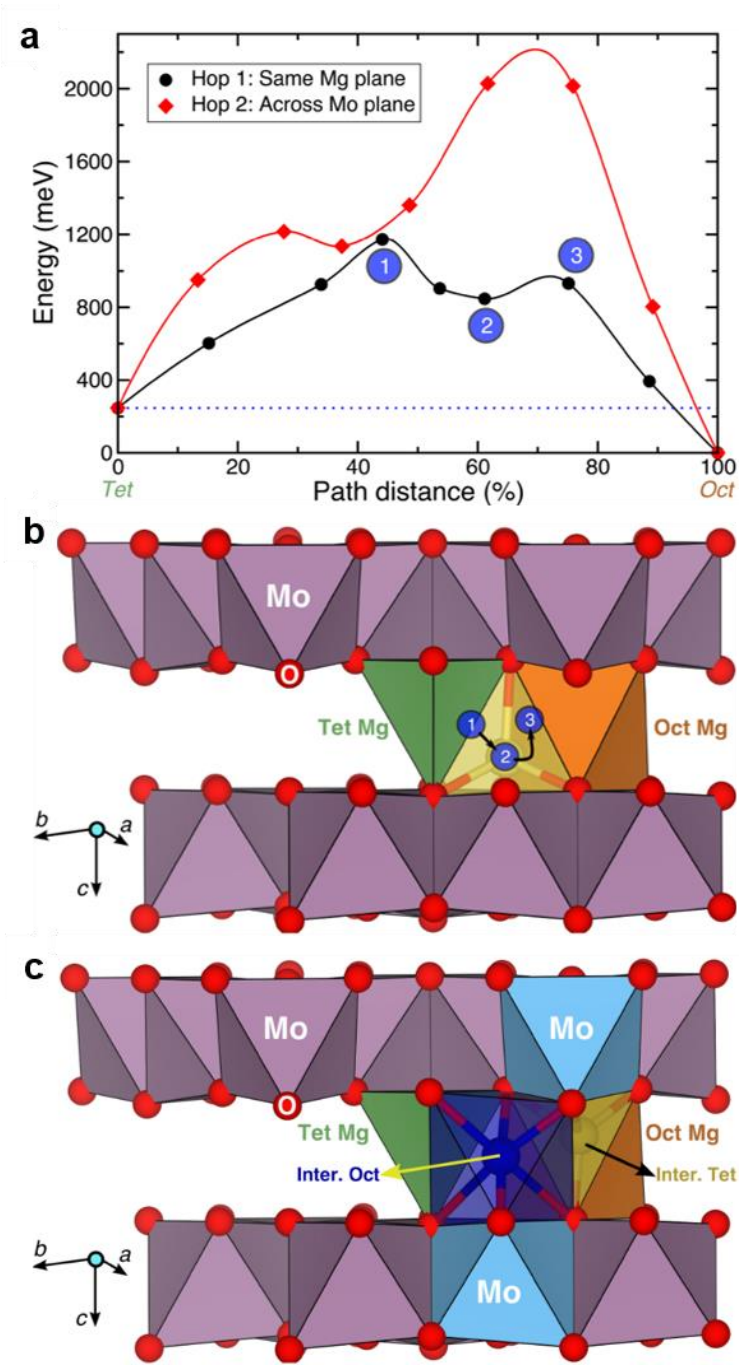

Figure 4-25. (a) The activation barrier for Mg diffusion along hops 1 and 2 in the $Mg_2Mo_3O_8$ structure, with the normalized path distance on the x-axis. (b) A closer view of hop 1, where the numbered circles correspond to various intermediate sites along the hop as labeled in (a). The intermediate tetrahedral site, which is edge-sharing with the stable tetrahedral site (green), is indicated in yellow. (c) An alternate pathway for hop 1 that involves intermediate octahedral (dark blue) and tetrahedral (yellow) sites, which are face-sharing with the stable tetrahedral (green) and octahedral (orange) sites, respectively. The intermediate sites in (c) also share a face with the MoO_6 octahedra (light blue).

4.4 Conclusions

In this chapter the limiting factors for Mg^{2+} insertion into oxide lattices are investigated. A case study of birnessite MnO_2 shows that in addition to the cation diffusion in solid structures, desolvation process at the electrode/electrolyte interphase is another rate determining step for Mg^{2+} insertion. Due to the high Mg^{2+} desolvation energy in non-aqueous electrolyte, the positive electrode undergoes a conversion mechanism instead which does not require complete desolvation beforehand and lowers the barrier. Similar principle would be applied to other materials as well. When an alternative low barrier mechanism is not available, however, poor electrochemistry would be expected. This explains the general observation of the superior electrochemistry of a Mg positive electrode in aqueous electrolyte than non-aqueous and suggests the importance of coupling appropriate electrolyte for a Mg positive electrode to improve the battery performance.

The $Mg_2Mo_3O_8$ is then used as a sample compound to study Mg^{2+} diffusion in solid. While non-preferential Mg^{2+} occupation has been suggested as one requirement for its facile diffusion, the present study reveals the specific topology of cation sites along the diffusion pathway as another key factor. The highly unstable O-Mg-O dumbbell intermediate configuration is identified in the $Mg_2Mo_3O_8$ structure and hinders Mg^{2+} diffusion. A similar logic allows a rough examination on the possible Mg^{2+} diffusion pathways in other crystal structures for non-theoretical researchers. Intermediate sites involving low Mg^{2+} coordination number or strong repulsion from an adjacent high valence cation would likely imply a high diffusion barrier and might not be suitable for Mg positive electrode structures.

Chapter 5

Prussian Blue Positive Electrode Materials for Rechargeable Mg-Li Hybrid Batteries

5.1 Overview

As discussed in Chapter 1, a hybrid Mg-Li battery is an alternative setup which would fully utilize the advantages provided by a Mg negative material, while the sluggish Mg^{2+} diffusion in solid is avoided. Previous work mostly focused on relatively low voltage (< 2 V) positive electrodes due to the corrosive nature of the APC electrolyte. In order to improve the energy density of the cell, components that are stable against chlorine attack are required. The molybdenum has shown to offer good anodic stability against APC electrolyte[91] and thus can be used as the current collector for positive electrode. The positive electrode itself should also contain robust framework. The Prussian blue analogues (PBA) are good such choices.

The crystal structure of PBA (**Figure 5-1**) – $ATM[TM'(CN)_6]_{1-x} \cdot yH_2O$ (A = alkali; TM = transition metal) – is similar to the ReO_3 and perovskite structure types, being comprised of cubes with TM residing on the corners and bridged by cyano groups along the edges, and thus generating a large central cavity (the A site in the perovskite structure).[172] The cyano (CN^-) ligands are highly covalently bonded to the transition metal ions ($TM^{2+/3+}$) owing to strong π-backbonding, gaining much better chlorination resistance than oxo (O^{2-}) ligands and providing the possibility of electrochemistry test with an APC electrolyte at high voltage. Additionally, the structure constructs clear 3D pathways for ion migration. It has recently received attention as positive electrode materials for rechargeable non-aqueous Li-ion,[173-175] Na-ion,[176-182] Ca-ion,[183] aqueous divalent-ion,[184] and Al-ion batteries.[185] The vacancies resulting from the

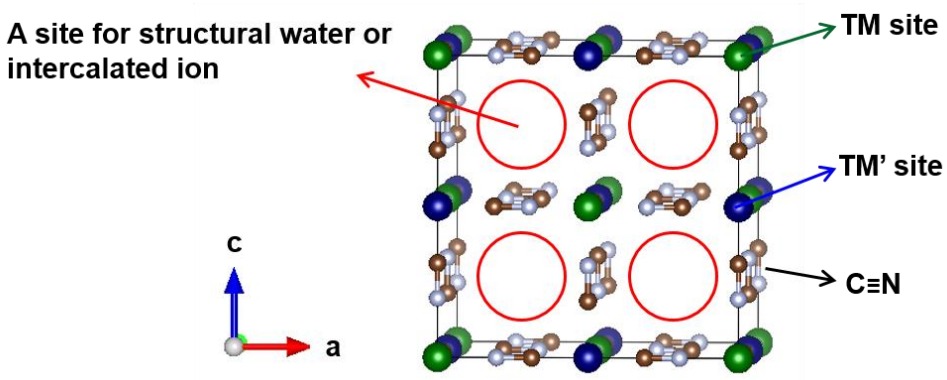

Figure 5-1. Idealized crystal structure of a Prussian blue analogue (PBA).

absence of complete $[TM'(CN)_6]^{3-/4-}$ units (x in the above formula) are filled by structural water with the O atoms occupying the empty sites and coordinated to the adjacent TM. Water molecules can also be found within the central cavity (A site), either in the exact center of the cavity or slightly shifted due to hydrogen bonding interaction with water molecules coordinated to the transition metal ions.[186] Those structural waters have shown effect on the electrochemistry. For example, it was demonstrated that the transition metal coordinated to carbon had a slightly higher redox voltage in Na cells when structural water is present; however, this water was removed on Na^+ de-intercalation.[181]

This chapter describes the utilization of both hydrated ($Fe[Fe(CN)_6]_{0.95}$ $2.3H_2O$, 23-PBA) and vacuum dried ($Fe[Fe(CN)_6]_{0.95}$ $0.7H_2O$, 07-PBA) PBA in hybrid Mg-Li full cells. The influence of structural water and Li salt concentration on the electrochemistry, as well as the detailed Li^+ intercalation mechanism at the positive electrode and metal deposition at negative electrode will be discussed.

5.2 Synthesis and Characterization

$Na_xFe[Fe(CN)_6]_{0.94}$ was first obtained following a previously reported procedure.[178] Typically, 5 mL of 37% HCl was mixed with 500 mL deionized water, followed by the addition of 4.84 g $Na_4Fe(CN)_6 \cdot 10H_2O$. The mixture was heated to 60 ˚C and kept for 4 hours. The solid product was collected by filtration and washed with water and ethanol. De-sodiation of $Na_xFe[Fe(CN)_6]_{0.94}$ was carried out subsequently by stirring the material in an excess of 0.25 M NO_2BF_4 in ACN at room temperature for 24 h in an Ar-filled glovebox. The 23-PBA product was collected by filtration and washed with ACN. 07-PBA, with lower structural water content, was obtained by heating the material before and after de-sodiation at 160 ˚C under vacuum overnight.

Complete removal of Na^+ was confirmed by EDX. Both PBA materials are produced in the same morphology, namely, homogenous ~ 1 μm cubes as revealed by SEM (**Figure 5-2a**). TGA (**Figure 5-2b**) demonstrates that the release of structural water commences around 130 ˚C, with 07-PBA losing less mass (5%) than 23-PBA (14%). The release/combustion of the cyanide group begins at ~ 300 ˚C that yields Fe_2O_3 upon completion of the reaction. This allows us to accurately measure the iron content of the sample. In order to avoid inaccuracy arising from the difficulty in precisely deconvoluting the two mass losses, the carbon and nitrogen contents were determined separately by combustion analysis. The remainder of the mass was attributed to water which is in good agreement with the TGA (**Table 5-1**). The obtained stoichiometries, $Fe[Fe(CN)_6]_{0.95} \cdot 2.3H_2O$ for 23-PBA and $Fe[Fe(CN)_6]_{0.95} \cdot 0.7H_2O$ for 07-PBA, show that the vacancy concentration is low and unaffected by the drying process.

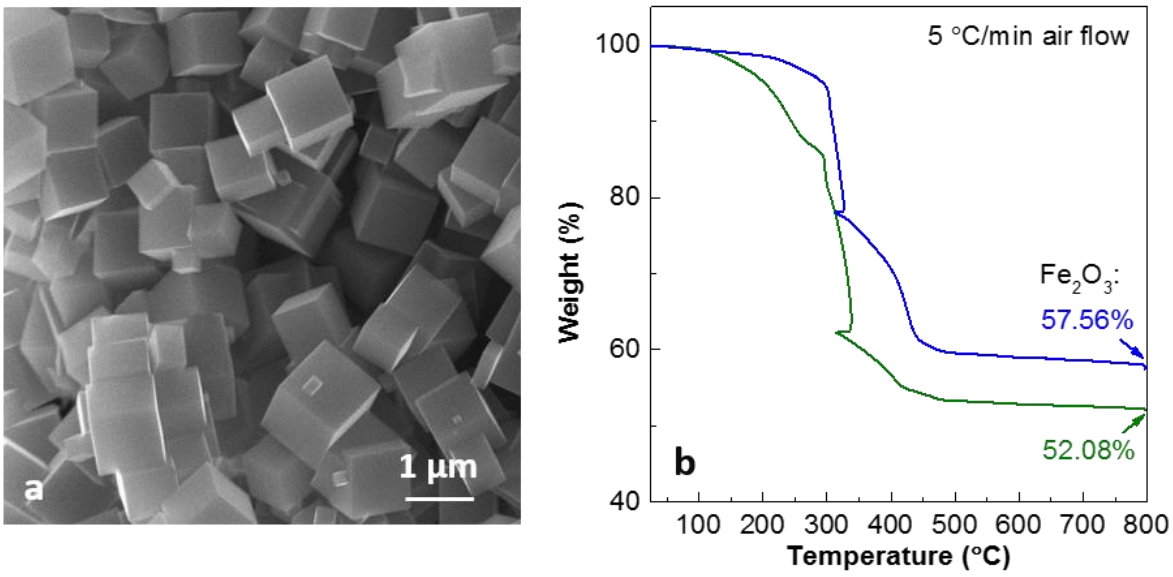

Figure 5-2. (a) SEM image of PBA crystallites and (b) TGA of 23-PBA (green) and 07-PBA (blue).

Table 5-1. Percentages (wt% represents weight percent and at% represents atomic percent) of each element in both PBAs. C wt% and N wt% are obtained from combustion analysis; Fe wt% is calculated from the Fe_2O_3 wt% given by TGA; the remainder of the mass is assigned to H_2O. Chemical formulae are calculated to be $Fe[Fe(CN)_6]_{0.95} \cdot 2.3H_2O$ for 23-PBA and $Fe[Fe(CN)_6]_{0.95} \cdot 0.7H_2O$ for 07-PBA, respectively.

Sample	**C**	**N**	**Fe**	**H_2O**
23-PBA	22.780 wt%	26.735 wt%	36.430 wt%	14.055 wt%
	36.2 at%	36.4 at%	12.5 at%	14.9 at%
07-PBA	25.345 wt%	29.535 wt%	40.260 wt%	4.860 wt%
	40.5 at%	40.5 at%	13.8 at%	5.2 at%

The powder XRD patterns of both materials were indexed in the *Fm*-3*m* space group, the typical cubic unit cell of PBAs.[172] Their structures were investigated by Rietveld refinement[92] (**Figure 5-3**), using compositions constrained by the chemical analysis and TGA measurements, i.e., 5% $[Fe(CN)_6]^{n-}$ vacancies, and 14.05 wt% water for 23-PBA or 4.86 wt% water for 07-PBA (**Table 5-1**). The empty N site of the $[Fe(CN)_6]^{n-}$ vacancy is occupied by water, fulfilling the octahedral environment of Fe.[186] The refined structures are reported in **Table 5-2** and **Table 5-3**. Both H-bonded (O2, *x*,*x*,*x*) and non-H-bonded (O3, 0.25,0.25,0.25) water molecules are present in the 23-PBA structure, whereas only the former exists in 07-PBA. All of the cavities are occupied by water molecules in 23-PBA, with 64% H-bonded and 36% non-H-bonded to the coordinated water, whereas only 20% of the cavities are occupied by H-bonded water in the 07-PBA structure.

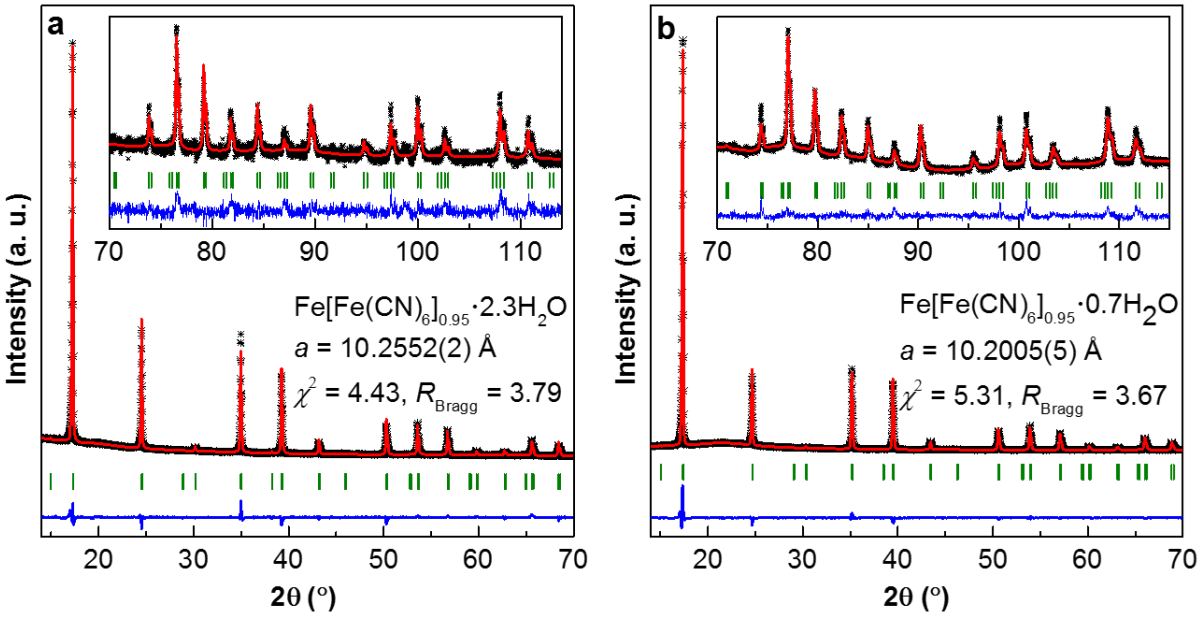

Figure 5-3. Rietveld refinement results for (a) 23-PBA and b) 07-PBA (black crosses represent experimental data; red solid lines show fitted data; blue lines show the difference map between observed and calculated data; and green ticks indicate the reflections of the *Fm*-3*m* PBA phase). Insets show the fit at high angle.

Table 5-2. Refined parameters for 23-PBA ($Fe[Fe(CN)_6]_{0.95}\cdot 2.3H_2O$), space group = *Fm*-3*m*, *a* = 10.2552(2) Å, χ^2 = 4.43, Bragg *R*-factor = 3.79).

Atom	**Wyck.**	***x***	***y***	***z***	**Occ.**	B_{iso} **(Å^2)**
Fe1	4a	0	0	0	1	1.90(1)
Fe2	4b	0.5	0.5	0.5	0.95	1.90(1)
C	24e	0.3059(3)	0	0	0.95	1.90(1)
N	24e	0.1950(2)	0	0	0.95	1.90(1)
O1	24e	0.1950(2)	0	0	0.05	1.90(1)
O2	32f	0.3364(2)	0.3364(2)	0.3364(2)	0.1606(4)	1.90(1)
O3	8c	0.25	0.25	0.25	0.357(2)	1.90(1)

Table 5-3. Refined parameters for 07-PBA ($Fe[Fe(CN)_6]_{0.95}\cdot 0.7H_2O$), space group = *Fm*-3*m*, *a* = 10.2005(5) Å, χ^2 = 5.31, Bragg *R*-factor = 3.67).

Atom	**Wyck.**	***x***	***y***	***z***	**Occ.**	B_{iso} **(Å^2)**
Fe1	4a	0	0	0	1	2.04(2)
Fe2	4b	0.5	0.5	0.5	0.95	2.04(2)
C	24e	0.3102(2)	0	0	0.95	2.04(2)
N	24e	0.1965(2)	0	0	0.95	2.04(2)
O1	24e	0.1965(2)	0	0	0.05	2.04(2)
O2	32f	0.3109(6)	0.3109(6)	0.3109(6)	0.05	2.04(2)

Table 5-4. Bond lengths in 23-PBA and 07 PBA.

Bond	**23-PBA**	**07-PBA**
Fe–C	1.991(4) Å	1.936(3) Å
Fe–N	2.000(3) Å	2.004(3) Å
C–N	1.137(6) Å	1.160(5) Å

Removing the structural water results in a shrinkage of the lattice parameter from a = 10.255 Å in 23-PBA to a = 10.201 Å in 07-PBA. Analysis of the evolution of the bond distance (**Table 5-4**) shows that the contraction is absorbed by the shrinkage of the Fe-C bond. Owing to the hybridization of the π^* orbital of the ligand, the shrinkage of this bond implies a weakening of the C≡N bond and should affect the cell voltage. This is in agreement with the FTIR spectra of the two PBAs (**Figure 5-4**). The peaks at 2080 and 2170 cm^{-1} correspond to the cyanide group with C bonded to Fe^{2+} and Fe^{3+}, respectively.[187,188] The presence of 0.15 Fe^{2+}/f.u. is expected to compensate for the $[Fe(CN)_6]^{n-}$ vacancies. The C≡N vibration in ferricyanide (Fe^{3+}) gives a much weaker signal than in ferrocyanide (Fe^{2+}) at the same concentration;[189] however, without a standard for the bulk material, an accurate estimation of the concentration of each oxidation state is not possible by FTIR. The cyanide bands of 07-PBA are more complex than those of the hydrated phase. This could either mean a perturbation

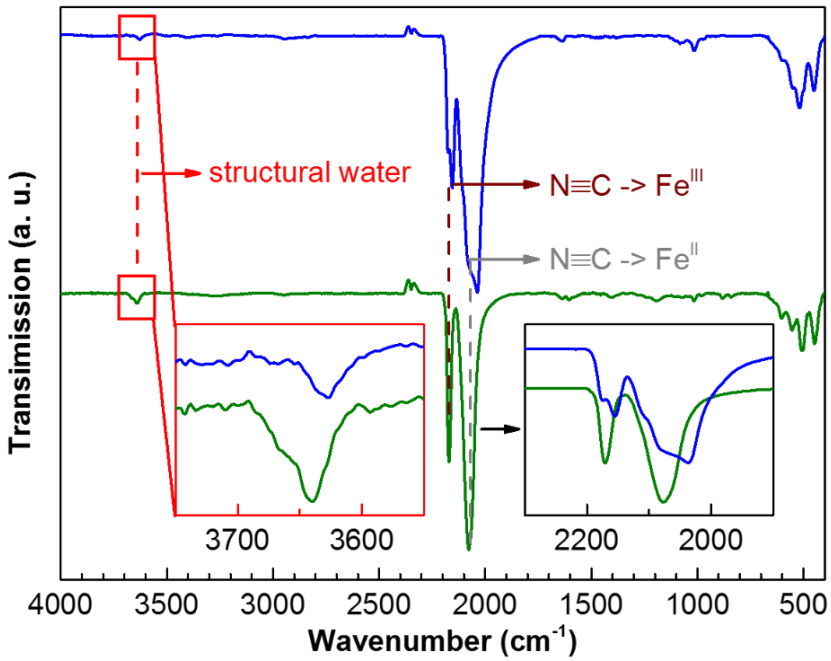

Figure 5-4. FTIR spectra of 23-PBA (green) and 07-PBA (blue) (insets showing the OH stretch of structural water and C≡N stretch).

of the local symmetry or an inhomogeneous chemical environment due to the lower number of water molecules present in the structure. Moreover, the redshift induced by drying is a direct consequence of the elongation of C≡N bond observed by XRD. The lower content of structural water in 07-PBA is also confirmed by FTIR (**Figure 5-4**).

5.3 Electrochemistry

APC in THF was used as the basis for the electrolyte in our study. The positive side of the cell was protected by a Mo disc to improve the anodic stability of the electrolyte. The electrochemical activity of both PBAs in a Mg cell was first evaluated. However, very low capacities (~ 3 mAh g^{-1}) are obtained (**Figure 5-5**), showing that Mg^{2+} does not readily intercalate into PBA either with or without the aid of structural water. On the other hand, no corrosion is observed up to 3 V vs. Mg for a PBA positive electrode supported on Mo foil. This proves that metal hexacyanates exhibit good resistance to chlorine attack, presumably

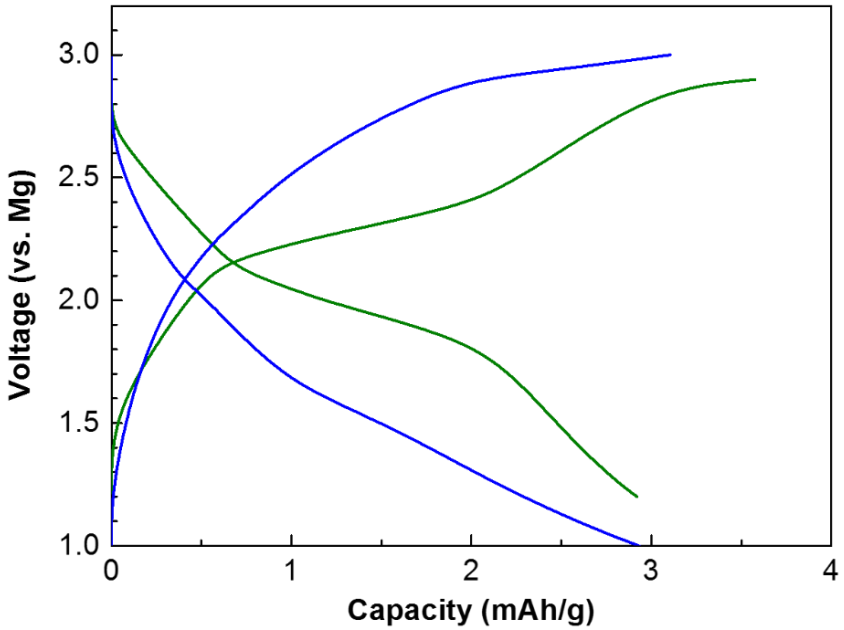

Figure 5-5. Discharge and charge profiles of 23-PBA (green) and 07-PBA (blue) in APC/ THF without Li-salt addition at a current density of 10 mA g^{-1} at room temperature.

owing to their structure comprised of robust M-CN bonds. In contrast, metals such as stainless steel or aluminum exhibit corrosion because of the poor stability of their oxide-passivated surfaces.[190-192] The fact that 23-PBA does not insert Mg^{2+} in APC is in sharp contrast with the behavior in aqueous electrolytes.[184] Similar to what was observed with layered hydrated manganese oxide, sluggish surface reactions are observed in the nonaqueous electrolyte whereas rapid Mg^{2+} insertion is observed in aqueous electrolytes, as discussed in Chapter 4.[46,47] This difference points once more at a specific mechanism through which the Mg^{2+} ions are delivered to the surface of the Mo_6S_8 positive electrode material,[81] suggesting that multivalent ion desolvation must be activated on the surface of the positive electrode material.

Since Mg^{2+} does not intercalate into the PBA structures, a monovalent cation, Li^+, was introduced into the electrolyte by adding LiCl. Similar to APC, the dual salt electrolyte also shows reversible metal stripping/plating at the Mg negative electrode and an anodic stability up to 3.2 V with a Mo positive electrode current collector (**Figure 5-6**). A series of Mg-Li dual

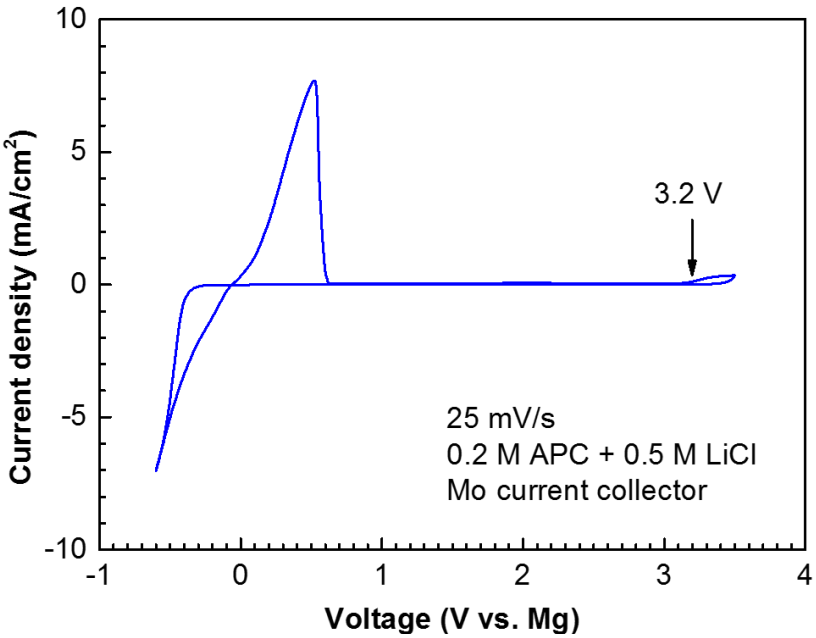

Figure 5-6. CV of the dual salt electrolyte showing reversible metal stripping/plating on Mo current collector and an anodic stability of 3.2V**.**

salt electrolytes with fixed 0.2 M APC concentration and different LiCl concentrations were examined with both PBA materials in three-electrode cells[99] at a current density of 10 mA g^{-1} (~ C/10, where 1C corresponds to a 1 e^-/PBA f.u.). As the LiCl concentration increases up to 0.5 M, the capacity also increases until it reaches the maximum value achieved in this study of 125 mAh g^{-1} for both 23-PBA (**Figure 5-7a**) and 07-PBA (**Figure 5-7c**). Note that considering the mass loading of the positive electrode material and the volume of electrolyte used, about 0.1 M LiCl is required to fill up the PBA structures with the maximum theoretical intercalate content of 1.8 Li per $Fe[Fe(CN)_6]_{0.95}$ $2.3H_2O$ or $Fe[Fe(CN)_6]_{0.95}$ $0.7H_2O$ (162 and 179 mAh g^{-1}, respectively). The fivefold lithium excess required to achieve maximum capacity might be due to the complex speciation equilibria of the different ionic species observed in chloride-based electrolytes,[76] which yields higher conductivity in electrolyte upon LiCl addition[71] or traps part of the lithium ions in non-electrochemically active complexes. Finally, the ± 0.1 V overpotential (**Figure 5-7b,d**) for metal stripping and plating in the dual salt electrolyte is similar to what is observed in the pure magnesium APC electrolyte.[72] The slight deviation among different cells with different LiCl content may arise from unavoidable variation in the sanding procedure used to clean the Mg negative electrode. We note that the plating potential does not reach -0.7 V vs. Mg which is normally required to plate Li metal.

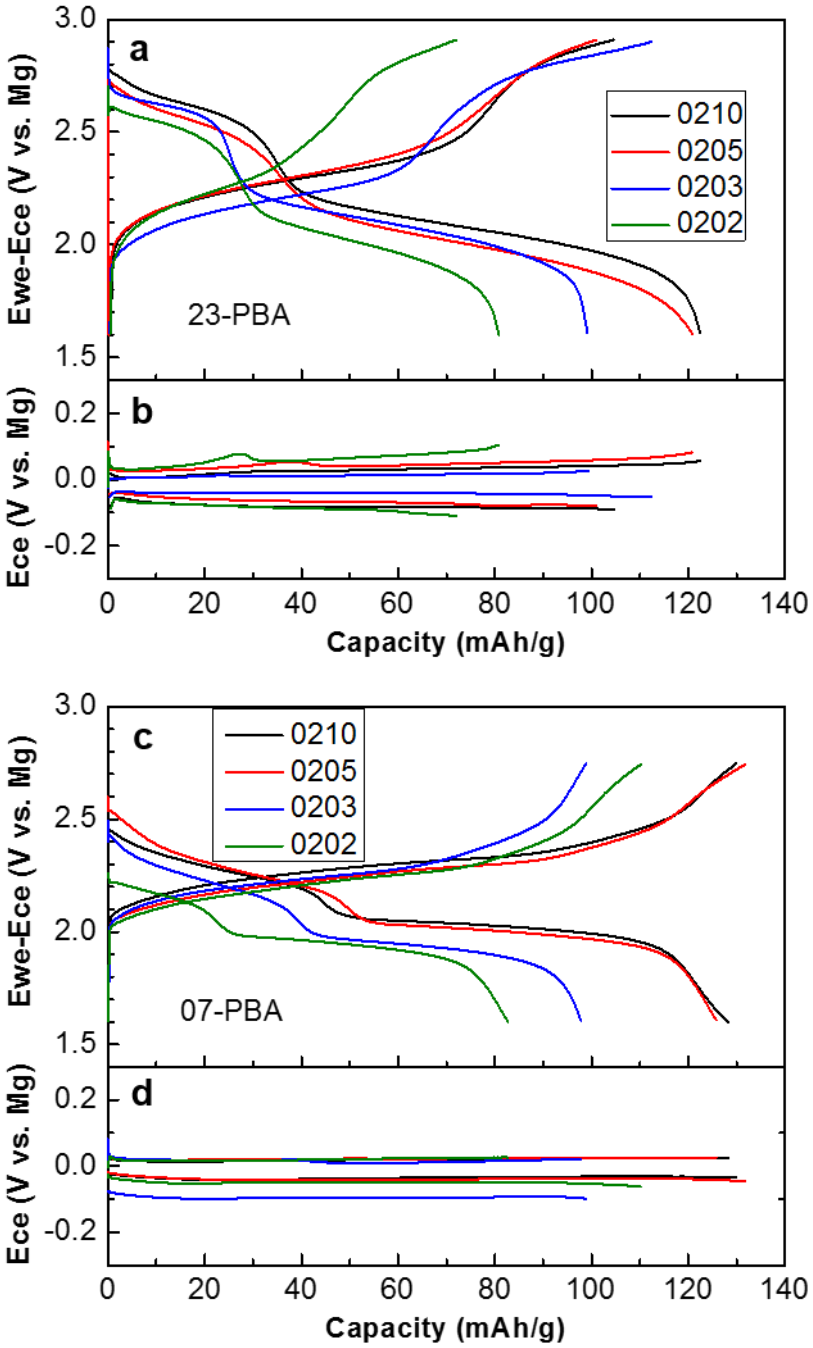

Figure 5-7. Voltage profiles and metal stripping/plating behavior on Mg negative electrode of (a)(b) 23-PBA and (c)(d) 07-PBA in Mg-Li hybrid cells with different salt concentrations ("0205" represents [0.2 M APC + 0.5 M LiCl in THF], as an example) in the electrolyte at a current density of 10 mA g^{-1} (~ C/10) at room temperature. (we = working electrode; ce = counter electrode)

Long-term cycling of both materials was studied with [0.2 M APC + 0.5 M LiCl] in coin cells at 200 mA g^{-1} (~ 2C, **Figure 5-8**). The cell with 07-PBA shows a drop of capacity in the first ten cycles, and rapidly stabilizes at 65 mAh g^{-1} up to 300 cycles with 99% coulombic efficiency, whereas 23-PBA displays a slow drop in capacity from 70 mAh g^{-1} at the tenth cycle to 55 mAh g^{-1} at the 300th cycle as well as a slightly lower coulombic efficiency (98%). The higher voltage of 23-PBA would allow for higher energy density; however, not all Li^+ could be extracted simply due to electrolyte anodic decomposition at the end of charge. Although structural water remains in 23-PBA during the first cycle, it does not persist until the end of 300 cycles according to FTIR (see next section). This release of structural water into the electrolyte on long-term cycling also affects the overall cell performance.

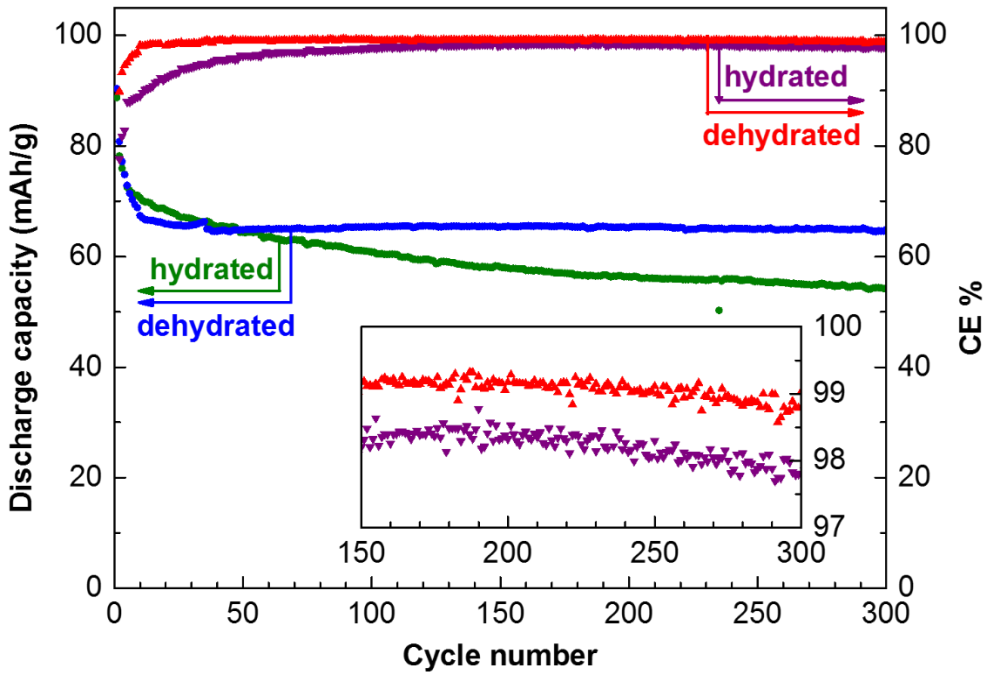

Figure 5-8. Capacity evolution of 23-PBA and 07-PBA in a [0.2 M APC + 0.5 M LiCl in THF] electrolyte. The cells were cycled at 200 mA g^{-1} (~ 2C) at room temperature.

5.4 Li^+ Insertion Mechanism and Structural Water Influence for PBA Positive Electrodes

5.4.1 *Operando* XRD

In contrast to the Chevrel phase performance in a dual salt electrolyte where co-intercalation of Li^+ and Mg^{2+} readily takes place,[84] no Mg is observed in the discharged PBA electrodes by EDX investigation (**Figure 5-9**). Thus all electrochemical capacities represent Li^+ de/intercalation only, as expected based on the results without LiCl addition (vide supra). Structural evolution of both PBAs during electrochemical cycling was examined by *operando* XRD in an electrolyte comprised of [0.2 M APC + 0.5 M LiCl]. The cubic lattice parameter evolution extracted by a Le Bail fit[94] of the full patterns is summarized in **Figure 5-10** along with the electrochemical profile.

The process is similar for both materials and only 23-PBA is described in detail. The diffraction data are presented here for the fourth cycle, after the formation cycles. The lattice

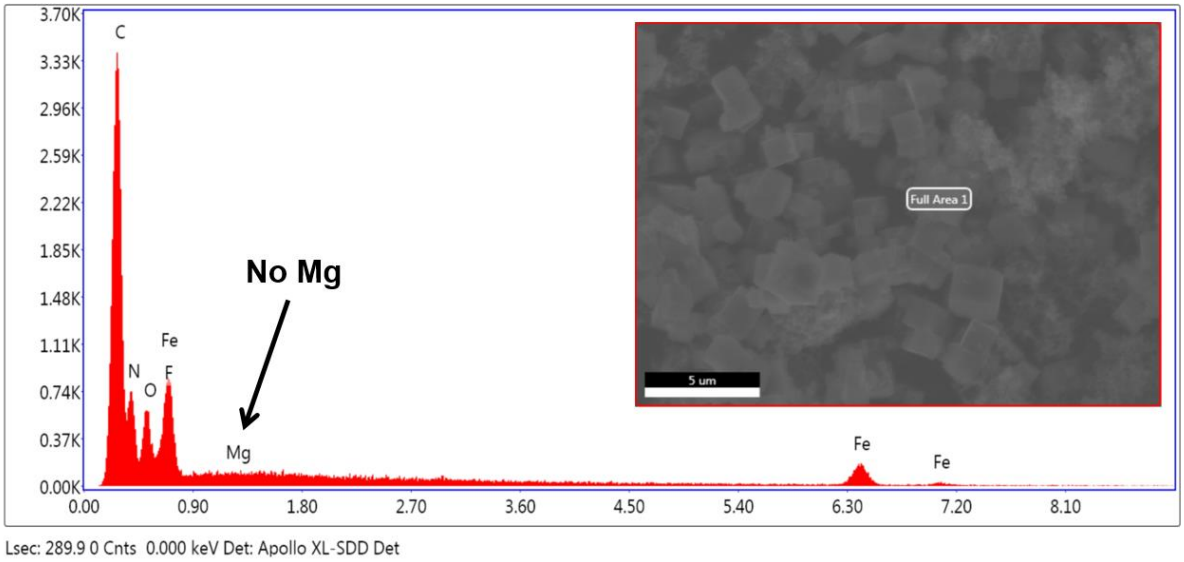

Figure 5-9. EDX showing the absence of Mg in PBA when discharged in the dual-salt electrolyte (F is due to the PVDF binder).

parameter decreases upon Li^+ insertion during the high voltage process, whereas on the low voltage plateau the XRD pattern is clearly indexed with two different cubic phases (**Figure 5-10c,f**), one showing very little lattice parameter evolution upon Li^+ insertion and the second presenting a large increase as the lithium content increases. Such behavior is similar to a two-phase reaction, with a constant Li-poor phase and an evolving Li-rich phase. The fraction of the Li-poor phase continually decreases upon discharge; however not all of it converts at the end, which prevents the material from achieving full capacity (a 1.8 e^- transfer with the insertion of 1.8 Li ions). Similar phase separation has been observed during Na^+ insertion into $Fe[Fe(CN)]_6]_{1-x}$ yH_2O, where part of the material does not uptake Na^+ at all.[193] Interestingly, in 23-PBA, the majority phase exhibits the major change in lattice parameter; conversely, in the case of the dried sample, the majority phase maintains an almost constant lattice parameter. This suggests that the phase segregation is due to inhomogeneity in the water content of the positive electrode material; water-rich phases being more prone to correlation between intercalate content and lattice parameter than a water-poor phase. The charge process follows a reverse mechanism showing the good reversibility of Li^+ interaction.

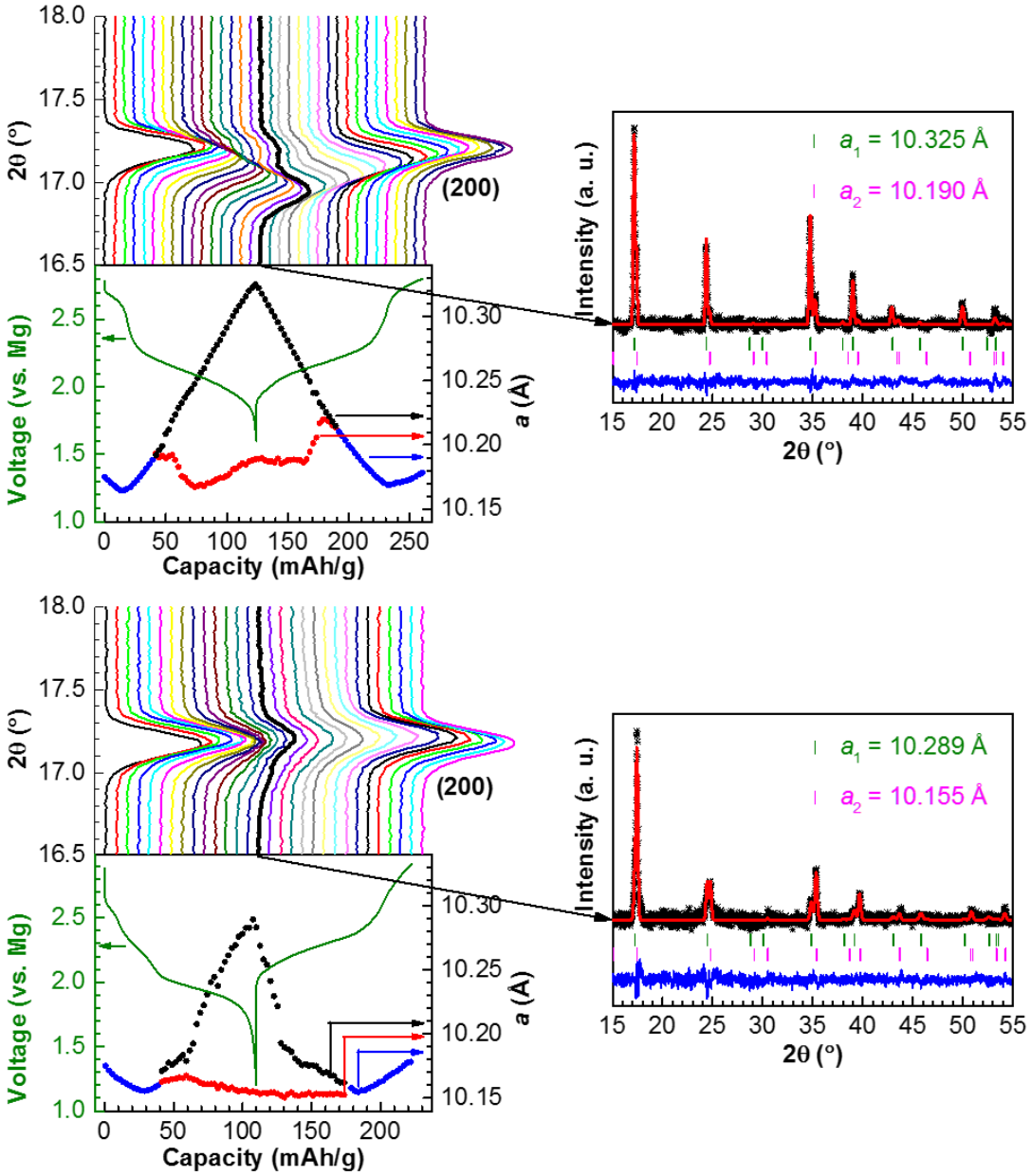

Figure 5-10. Diffraction data for (a)(b)(c) 23-PBA and (d)(e)(f) 07-PBA cycled in an electrolyte comprised of [0.2 M APC + 0.5 M LiCl in THF] at a current density of 10 mA g^{-1} at room temperature. (a)(d) *Operando* XRD patterns showing only the evolution of the (200) peak in the expanded range from 16.5° to 18° 2θ for simplicity (the pattern at full discharge is indicated in bold black); (b)(e) lattice parameter evolution at points along the electrochemical cycle (blue: single phase during the high voltage plateau; black: Li^+ de/intercalation phase; red: Li-poor phase corresponding to phase separation during the low voltage plateau; green: voltage profile); (c)(f) Le Bail fitting showing two cubic phases obtained at the end of discharge (black crosses: experimental data; red solid lines: fitted data; blue lines: the difference map between observed and calculated data; green and pink ticks: the reflections of the two *Fm*-3*m* phases).

5.4.2 *Ex-Situ* FTIR

Two voltage plateaus are observed in both cases, resulting from the existence of two different $Fe^{2+/3+}$ redox centers. Due to the strong coordination between Fe and C, the oxidation state of such iron would influence the C≡N stretch and can be tracked by FTIR. In contrast, less effect is expected from the Fe coordinated to N with a weaker orbital overlap. FTIR is thus carried out to investigate the stepwise redox process, and results are shown in **Figure 5-11**. At the beginning, two C≡N stretches are present, corresponding a mixture of $Fe^{2+/3+}$-C≡N species as discussed in Section 5.2. As the voltage drops to 2.1 V, the peak for the C≡N stretch with C bonded to Fe^{3+} disappears, demonstrating such iron is reduced to Fe^{2+} and is responsible for the high voltage plateau. This is in agreement with the crystal field theory which suggests a stabilization of the Fe-C bond owing to the strong hybridization of the π* orbitals of the CN^- ligand (**Figure 5-12a**). Upon further discharge, no significant change is shown by FTIR,

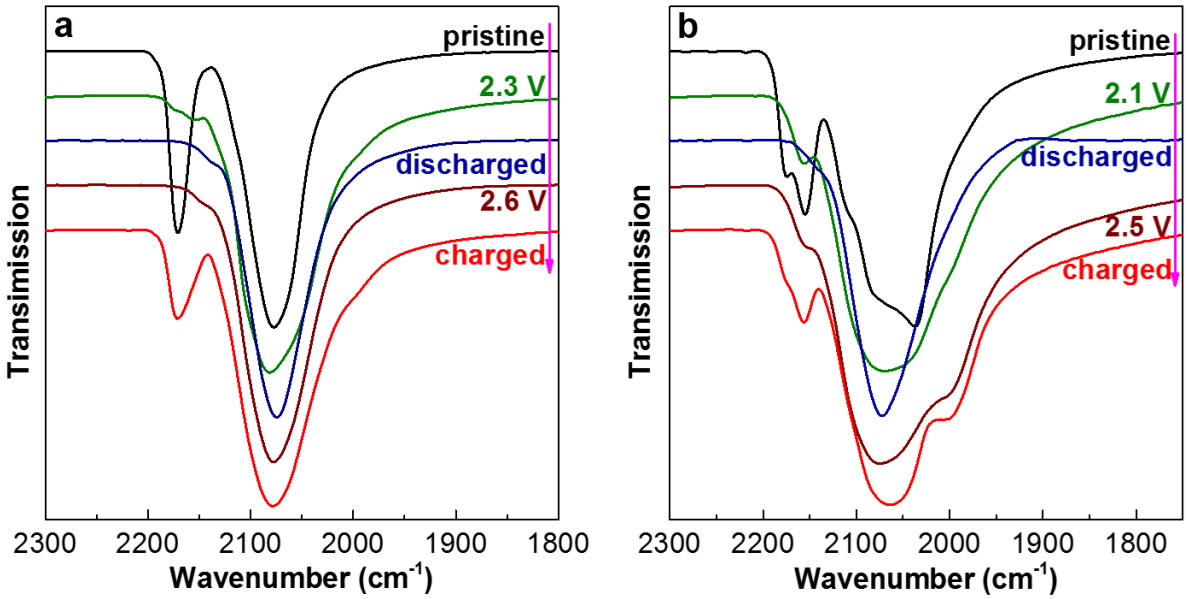

Figure 5-11. CN stretching band evolution probed by *ex-situ* FTIR spectroscopy on (a) 23-PBA and (b) 07-PBA (Black: pristine; green: end of first discharge plateau; blue: end of second discharge plateau; brown: end of first charge plateau; red: end of second charge plateau).

indicating the lower plateau corresponds to the redox of the nitrogen coordinated iron. This result in turn explains the evolution of lattice parameters. The initial contraction of unit cell is a result of the addition of electron to the Fe-C bonding orbital (**Figure 5-12a**) and shrink of the bond. Subsequent reduction of the other metallic center populates the nonbonding orbitals (**Figure 5-12b**) and has little effect on the bond length. The increase of lattice parameter is believed to be due to pure steric effects.

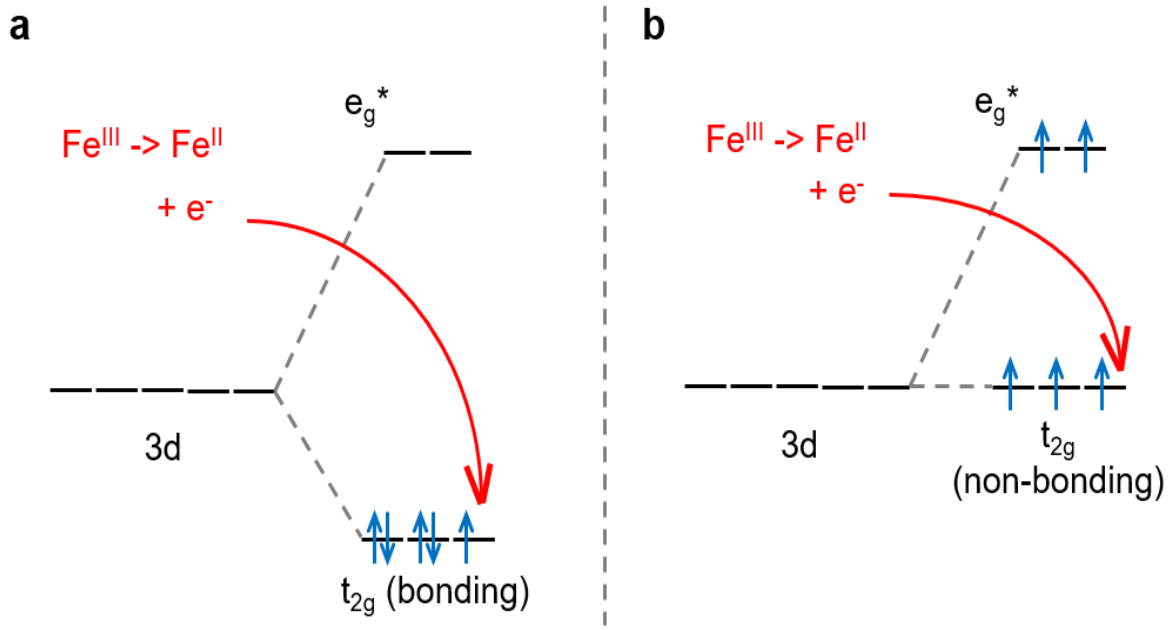

Figure 5-12. Fe 3d orbital energy splitting when bonded to the (a) C (-C≡N as π-acceptor) and (b) N (-N≡C as σ-donor) center of cyanide group.

The water content significantly impacts the oxidation potential of the $Fe^{2+/3+}$-CN centers while having very little influence on the potential of $Fe^{2+/3+}$-NC (**Figure 5-7**). This is surprising since the shorter Fe-C bond in 07-PBA, 1.936(3) Å vs. 1.991(4) Å (**Table 5-4**), generates a higher crystal field stabilization, indicating that the structural water molecules play an active role in the stabilization of Li^+. Unlike the Na^+ de/intercalation into PBA, where structural water is extracted together with Na^+ during the first cycle,[181] Li^+ extraction here does not modify the water content as evidenced by the sharp crystalline water peak[194] in the 3550–3700 cm^{-1} region of the discharged 23-PBA FTIR spectrum (**Figure 5-13**). A slight shift in frequency results from the water interaction with the inserted Li ions. Nevertheless, the decrease of peak intensity after 300 cycles (violet curve) indicates water is still slowly released from PBA structure during the repeated Li^+ de/intercalation process.

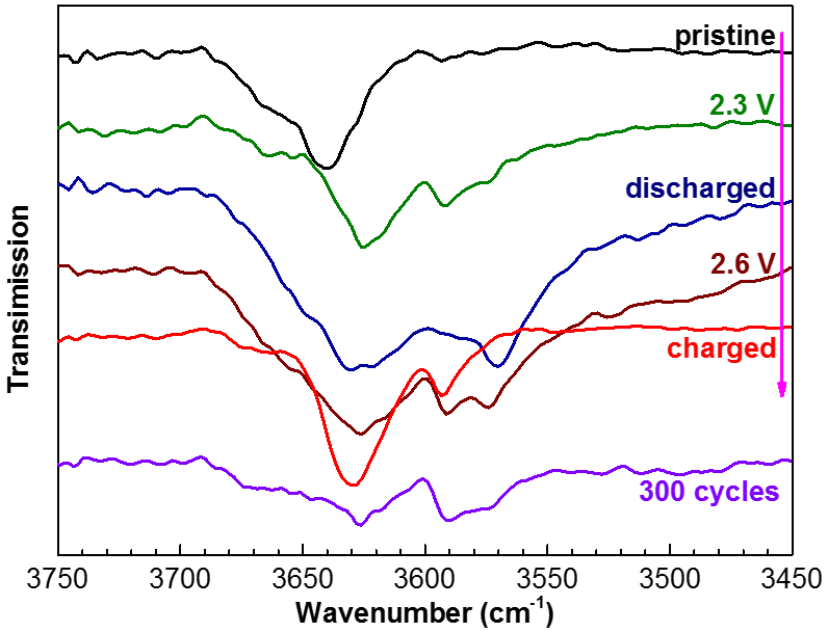

Figure 5-13. OH stretching band evolution probed by *ex-situ* FTIR spectroscopy on 23-PBA (Black: pristine; green: end of first discharge plateau; blue: end of second discharge plateau; brown: end of first charge plateau; red: end of second charge plateau; violet: after 300 cycles).

5.5 Characterization of the Mg Negative Electrode

The morphology of the Mg negative electrode after long-term cycling was characterized by SEM, showing a dense and dendrite-free surface (**Figure 5-14a**) and demonstrating that electrodeposition resembles that of Mg metal rather than Li. Multiple XPS analyses of the electrode surface indicate only the presence of Mg (**Figure 5-14b**), suggesting that Li co-deposition does not occur in this system. Such behavior is expected considering the voltage for metal plating on the negative electrode is at −0.1 V vs. Mg (**Figure 5-7b,d**), which is 0.6 V above Li^+/Li^0. This is different from that of the $Mg(BH_4)_2$-$LiBH_4$ dual salt electrolyte in diglyme where a magnesium-rich Mg-Li alloy was formed at a potential close to the magnesium metal theoretical deposition potential.[83] The nature of the electrodeposition process was further investigated at high rates in Mg/Mg symmetric cells (5 mA cm^{-2}), which also results in a non-dendritic growth (**Figure 5-15**). The stability of the deposited species in

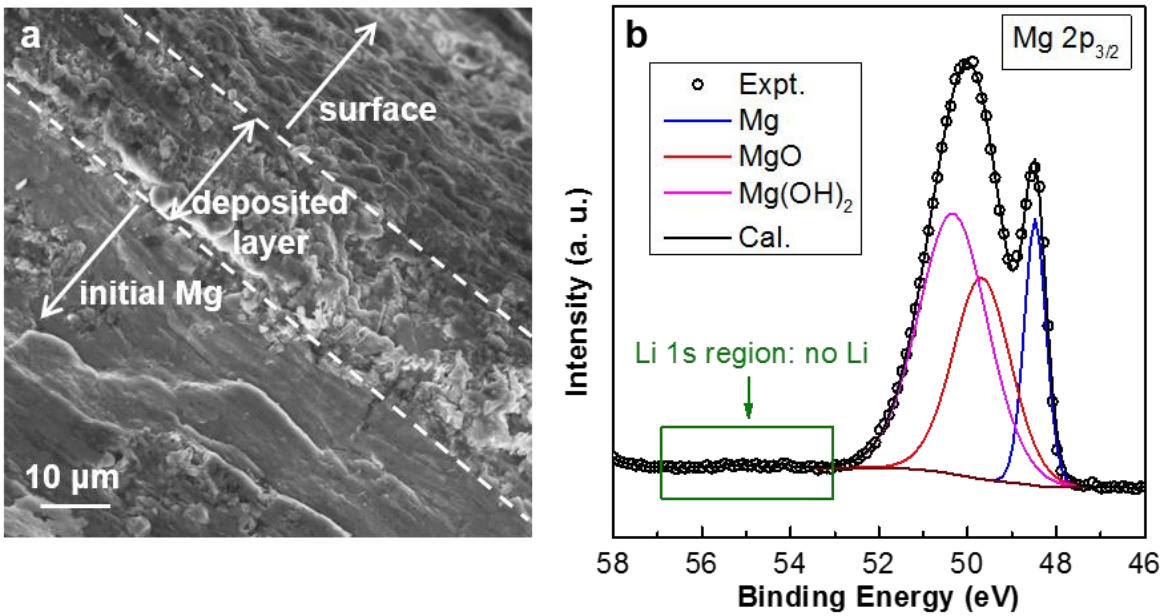

Figure 5-14. (a) SEM image showing the surface and cross section, and (b) XPS spectrum of the Mg negative electrode after 300 cycles in a hybrid cell at a current density of 200 mA g^{-1}, showing the absence of dendrite and Li signal.

the atmosphere was confirmed by placing an electrode strip into water. It was observed to react very slowly, unlike Li metal. Thus, the primary advantages of using an Mg negative electrode – including dendrite-free deposition and quasi-stability in ambient atmosphere – are preserved in this hybrid cell.

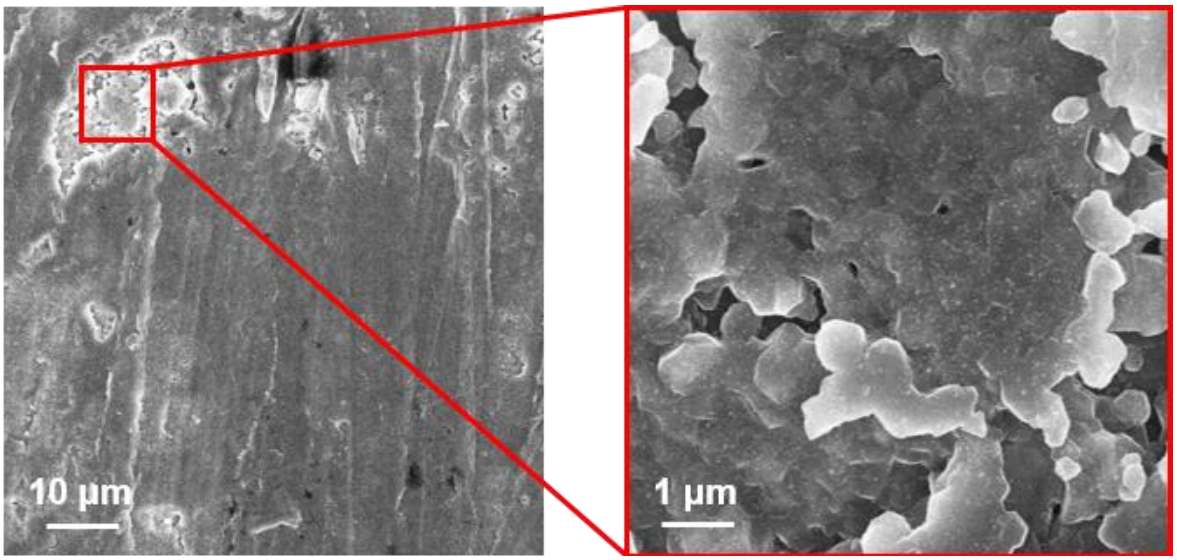

Figure 5-15. SEM images of electrodeposited layer on Mg at a 5 mA cm^{-2} current density in a [0.2 M APC + 0.5 M LiCl in THF] electrolyte (the layer was peeled off together with the separator).

5.6 Conclusions

Examination of the Li^+ insertion mechanism into two iron Prussian blue analogue positive electrode materials with different water contents – 23-PBA and 07-PBA – shows that the electrochemical profile, consisting of two voltage plateaus, can be explained based on the basis of two unique Fe bonding environments. The full cell with a Mg negative electrode reaches ~ 125 mAh g^{-1} capacity at an average voltage of 2.3 V with a moderate 10 mA g^{-1} rate (~ C/10), resulting in an energy density of 290 Wh kg^{-1}. Such results represent improved performance compared to the state-of-the-art hybrid cell with a Chevrel Mo_6S_8 positive electrode that

operates at an average voltage of 1.4 V and yields 170 Wh kg^{-1} energy density.[84,85] At a higher current density (2C rate), the Prussian blue cell still delivers 150 Wh kg^{-1}, which is comparable, albeit a little lower, to the Chevrel that is reported to provide an energy density of 165 Wh kg^{-1}. The unique combination of a metal negative electrode and a very robust high voltage insertion material offers an alternative to designs based on Mg^{2+} insertion positive electrodes. Although hybrid cells are limited by the Li^{+} cation content in the electrolyte, and hence present lower volumetric capacity compared to a hypothetical Mg^{2+} ion intercalation battery, they function with greatly extended cycling. The absence of corrosion at high voltage in this system offers very good life span and a capacity fade of less than 0.011% $cycle^{-1}$ over 300 cycles after initial conditioning of the electrode. Given the vast number of PBAs reported in the literature, these findings encouragingly open new doors for implementation of these materials in such cells. Moreover, dendrite-free metal deposition at the negative electrode is auspicious for the practical use of such devices.

Chapter 6

Stabilization of Transition Metal in Olivine Silicates

6.1 Overview of the Olivine Structure

Although much research has been carried out for "beyond Li-ion" technologies, the Li-ion cells still dominate the present commercialized high energy density rechargeable batteries. For Li-ion battery positive electrodes, polyanion-based materials[195-197] are of great interest due to the good structure stability and higher transition metal redox voltage offered by the covalent X-O bond. The olivine $LiFePO_4$ shows one of the best performance among these,[16] and owing to one dimensional channels of facile Li-ion conduction[198-200] it displays superior rate capability in a Li-ion battery.[201 - 203] However, the specific energy density is quite modest. The electrochemical de/intercalation of Li takes place at 3.45 V (vs. Li) and the maximum specific capacity is only 170 mAh g^{-1}. Replacing the phosphate group with a silicate would double the theoretical capacity owing to the higher charge to weight ratio offered by the four negative charges on the SiO_4^{4-} anion. Previous work mostly focused on the Li_3PO_4-type Li_2FeSiO_4 which unfortunately only cycles one Li^+/f.u. (166 mAh g^{-1} capacity) due to the difficulty in accessing Fe^{4+}. Additionally, the structure instability during cycling leads to a phase transformation and decrease of voltage from 3.1 V to 2.8 V.[204] Clearly, these compounds must be synthesized in more robust frameworks in order to be used as high capacity electrodes for long term applications.

Since the olivine structure has already shown desirable properties for reversible Li^+ ion diffusion in $LiFePO_4$, similar circumstances would be applied to the silicate as well. In fact, many natural silicate minerals also adopt the olivine structure with a general formula of

$M_IM_{II}SiO_4$ (M_I, M_{II}: cations). It has hexagonal closed packed oxygen with the two characteristic cation sites octahedral coordinated and Si occupying 1/8 of the tetrahedral sites (**Figure 1-1c**). Examples include materials where both cations are in their +2 state, such as $MgFeSiO_4$ (where Mg and Fe are fully disordered over site 1 and site 2) and Mn_2SiO_4.[205,206] Where the cations either have +1 or +3 charges as in $LiScSiO_4$ and $LiInSiO_4$, the charge difference results in the cations being ordered over the two sites.[207,208] This makes these materials a good choice as potential Li-ion positive electrodes if a transition metal can be substituted for Sc or In. The voltage for Li extraction from $LiMSiO_4$ (M = Mn, Fe, Co, Ni) was predicted to be around 5V[209] which approaches the upper voltage limit of typical electrolytes, potentially allowing two electron transfer/f.u. According to a computational study by Tarascon *et al.*, olivine type $LiFeSiO_4$ has a lower free energy than the material arising from the extraction of one Li ion from Li_2FeSiO_4. However, their attempts to directly synthesize olivine $LiMSiO_4$ (M=Fe, Mn) resulted in the formation of many other products with the pyroxene ($LiMSi_2O_6$) as the major phase.[210] Alternative attempts to partially replace P by Si in the cation ordered olivine $LiFePO_4$ resulted in a solid solution between $LiFePO_4$ and Fe_2SiO_4 in which Fe^{2+} partially occupies both sites M_I and M_{II}.[211] The immobile and disordered Fe^{2+} cations in the structure blocks the characteristic Li-ion pathways in olivine and renders the material electrochemically inactive.

In this thesis work, I investigate the possibility of using $LiInSiO_4$ and $LiScSiO_4$ as the parent structures to stabilize two series of the olivine silicate compounds of general formula $LiIn_{1-x}M_xSiO_4$ and $LiSc_{1-x}M_xSiO_4$ (M= Mn^{3+}, Fe^{3+} or Co^{3+}). Atomistic scale simulation is used to explore the energetics of transition metal cation substitution behavior. Based on simulation

results, solid state synthesis is carried out and combined neutron and synchrotron refinements are performed to study the cation occupancies in the two cation sites of olivine structure.

6.2 Atomistic Scale Simulation

Atomistic scale simulation methods have been successfully used to calculate relative substitution energies of different dopants in a given structure for olivine $LiFePO_4$ and many other technologically important compounds.[212,213] The interaction between ions are separated to a long-range Coulombic term and a short-range component representing electron-electron repulsion and van der Waals interactions. The short-range interactions are modeled using the two-body Buckingham potential, while an additional three-body term is used for the SiO_4^{4-} unit to account for the angle dependent nature of the O-Si-O bonds. A shell model is employed for the polarizability effects of the charged defects on the electronic charge clouds.[214] The lattice relaxation about defects (such as Li vacancies) and migrating ions can be calculated by an implementation of the Mott-Littleton scheme incorporated in the GULP code.[215] This method partitions a crystal lattice into two regions, where ions in the inner region immediately surrounding the defect (on the order of >700 ions) are relaxed explicitly. Relaxations of such a large number of ions are important for charge defects that introduce long-range electrostatic perturbations and are not easily treated by electronic structure methods. The outer region extends to infinity, with the outer lattice relaxations treated by quasi-continuum methods.

In the present work, simulations were first used to reproduce the crystal structures of olivine $LiInSiO_4$ and $LiScSiO_4$ based on the interatomic potential parameters that have been previously reported (**Table 6-1**).[213,216-221] **Table 6-2** compares the values obtained by these calculations to those reported experimentally using diffraction based methods,[207,208] showing

a maximum difference for any lattice parameter of only 0.9%. Similar differences are also found in calculated and experimentally obtained In-O, Sc-O and Si-O bond lengths (**Table 6-3**). Such small deviations between calculated and experimental results confirm the validity of interatomic potentials to be used for further calculations in this work.

Table 6-1. Short range potential parameters for $LiInSiO_4$ and $LiScSiO_4$.

a. Two-body			
Bond	**A (eV)**	**ρ (Å)**	**C (eV·Å^6)**
Li-O	632.1018	0.2906	0
Si-O	1612.46	0.29988	0
O-O	22764.3	0.149	44.53
In-O	1495.6	0.331	4.325
Sc-O	1389.4	0.3312	0
Mn-O	1686.13	0.2962	0
Fe-O	1342.754	0.3969	0
Co-O	1007.1	0.3069	0
b. Three-body			
Bond type	**k (eV·rad^{-2})**	**Θ_0 (deg)**	
O-Si-O	2.09724	109.47	
c.			
Species	**Y (e)**	**k (eV·Å^{-2})**	
Li	1	99999.0	
Si	4	99999.0	
O	-3.22	65.0	
In	9.1	1680.0	
Sc	3	99999.0	
Mn	1.971	148.0	
Fe	1.971	10082.0	
Co	1.971	10082.0	

Table 6-2. Comparison of calculated and experimentally obtained lattice parameters of $LiInSiO_4$ and $LiScSiO_4$ olivine silicates.

Lattice Parameters	**$LiInSiO_4$**			**$LiScSiO_4$**		
	Calc.	**Expt.**	**% Diff.**	**Calc.**	**Expt.**	**% Diff.**
a (Å)	4.8073	4.8448	-0.77	4.7905	4.8168	-0.55
b (Å)	10.5683	10.5043	0.61	10.5250	10.4317	0.89
c (Å)	6.0323	6.0634	-0.51	5.9621	5.9650	-0.05

Table 6-3. Comparison between calculated and experimental obtained bond lengths of $LiInSiO_4$ and $LiScSiO_4$.

Bond	**Average bond length**					
	$LiInSiO_4$			**$LiScSiO_4$**		
	Calc. (Å)	**Expt. (Å)**	**% Diff.**	**Calc. (Å)**	**Expt. (Å)**	**% Diff.**
Li-O	2.1451	2.1764	-1.4	2.1388	2.1835	-2.0
Si-O	1.6944	1.6354	3.6	1.6944	1.6311	3.9
In-O	2.1434	2.1649	-0.99	-		
Sc-O	-			2.1189	2.1182	0.033

Since the purpose of the current study is to substitute a transition metal into $LiMSiO_4$ (M= In, Sc), the following two formulations, similar to the scheme used by Islam *et al.* previously for calculating substitution energies in $LiMPO_4$,[213] were used to calculate the energy required for doping Mn^{3+}, Fe^{3+} and Co^{3+} into $LiInSiO_4$ and $LiScSiO_4$ (equations in Kröger Vink notation):

1. Dopant occupies M_{II} site in the olivine structure:

a) M^{3+} (M=Mn, Fe, Co) in $LiInSiO_4$

$$2In_{In}^{x} + M_2O_3 \rightarrow 2M_{In}^{x} + In_2O_3$$ **Equation 6-1**

b) M^{3+} (M=Mn, Fe, Co) in $LiScSiO_4$

$$2Sc_{Sc}^{x} + M_2O_3 \rightarrow 2M_{Sc}^{x} + Sc_2O_3$$ **Equation 6-2**

2. Dopant occupies M_I site in the olivine structure (formation of an antisite defect):

a) M^{3+} (M=Mn, Fe, Co) in $LiInSiO_4$

$$2In_{In}^{x} + 2Li_{Li}^{x} + M_2O_3 \rightarrow 2M_{Li}^{\bullet\bullet} + 2Li_{In}^{/\!/} + In_2O_3$$ **Equation 6-3**

b) M^{3+} (M=Mn, Fe, Co) in $LiScSiO_4$

$$2Sc_{Sc}^{x} + 2Li_{Li}^{x} + M_2O_3 \rightarrow 2M_{Li}^{\bullet\bullet} + 2Li_{Sc}^{/\!/} + Sc_2O_3$$ **Equation 6-4**

Equations 6-1 and **6-3** (or **6-2** and **6-4**) represent two extreme cases of the dopant ion completely occupying either site M_I or site M_{II} in the olivine structure. Energy of formation of the defect represented by **Equation 6-1** can be calculated as follows:

$$E_{1a} = E_{In_2O_3} + 2E_{M_{In}^{x}} - E_{M_2O_3}$$ **Equation 6-5**

and that represented by **Equation 6-3**:

$$E_{2a} = E_{In_2O_3} + 2E_{M_{Li}^{\bullet\bullet}} + 2E_{Li_{In}^{/\!/}} - E_{M_2O_3}$$ **Equation 6-6**

where E_{M2O3} and E_{In2O3} represent respective lattice energies and E_{defect} represents energy of formation of the isolated defect. Antisite defects are created together and tend to associate themselves, and this tendency was taken into account in present simulation methods by introducing these two defects in the structure simultaneously. Such strategy of calculating the

energy of formation of associated defects was previously reported for olivine $LiMPO_4$ type compounds as well.

The difference in energy of formation of defects represented by these equations (**6-1** and **6-3**) denotes the tendency of the substituted ion to be disordered over the two cationic sites in the olivine structure. Less difference in the energy will lead to equal distribution of cations over the two sites and therefore higher cationic disorder. This energy can be calculated as:

$$E_{order} = E_{2a} - E_{1a} = E_{M_{Li}^{\bullet\bullet}} + E_{Li_{In}^{//}} - E_{M_{In}^{x}} \qquad \textbf{Equation 6-7}$$

Table 6-4 presents values of E_{order} for Mn^{3+}, Fe^{3+} and Co^{3+} substitution in olivine $LiInSiO_4$ and $LiScSiO_4$. Positive values of the E_{order} indicate all substituents prefer site M_{II} over site M_I. More interestingly, E_{order} decreases as it moves across from Mn to Fe to Co. This trend is valid for both parent compounds but the value for Co^{3+} substitution in $LiInSiO_4$ is the smallest which means that Co^{3+} is the most cation disordered in $LiIn_{1-x}M_xSiO_4$. Although values calculated here apply only when a rather insignificant amount of substituents is used (assumption of non-interacting defects), these comparative trends in E_{order} are expected to hold true even for large concentrations of substitution.

Table 6-4. E_{order} for various substituents in olivine type $LiInSiO_4$ and $LiScSiO_4$.

Energy (eV)	**$LiInSiO_4$**			**$LiScSiO_4$**		
	Mn^{3+}	**Fe^{3+}**	**Co^{3+}**	**Mn^{3+}**	**Fe^{3+}**	**Co^{3+}**
E (M on M_{II})	-7.2040	-7.1056	-10.8549	-6.7010	-6.6066	-10.3824
E (M on M_I)	-6.2218	-6.1685	-10.4045	-4.5218	-4.4654	-8.9013
E (order)	0.9822	0.9371	0.4504	2.1792	2.1412	1.4811

6.3 Experimental Examination of Transition Metal Substitution

Cation substitution behavior was experimentally examined by solid state synthesis. A starting molar ratio of 1:1 between the M_I (Mn/Fe/Co) and M_{II} (In/Sc) precursors (Mn_2O_3, Fe_2O_3, $Co(C_5H_7O_2)_3$, $In(C_2H_3O_2)_3$, Sc_2O_3) were mixed with stoichiometric Li_2CO_3 and SiO_2 and heated at 900 ˚C. While the XRD peaks of $LiScSiO_4$ remained unaffected after mixing with any transition metal, the In-TM substitution revealed some interesting results. **Figure 6-1** compares the XRD patterns of the products. The non-substituted material is shown in black. Although certain amount of In_2O_3 impurity presents in the product, which should be removable by optimizing the synthesis condition, the olivine serves as the main phase and provides enough information for the lattice parameter comparisons with the substituted samples. Upon

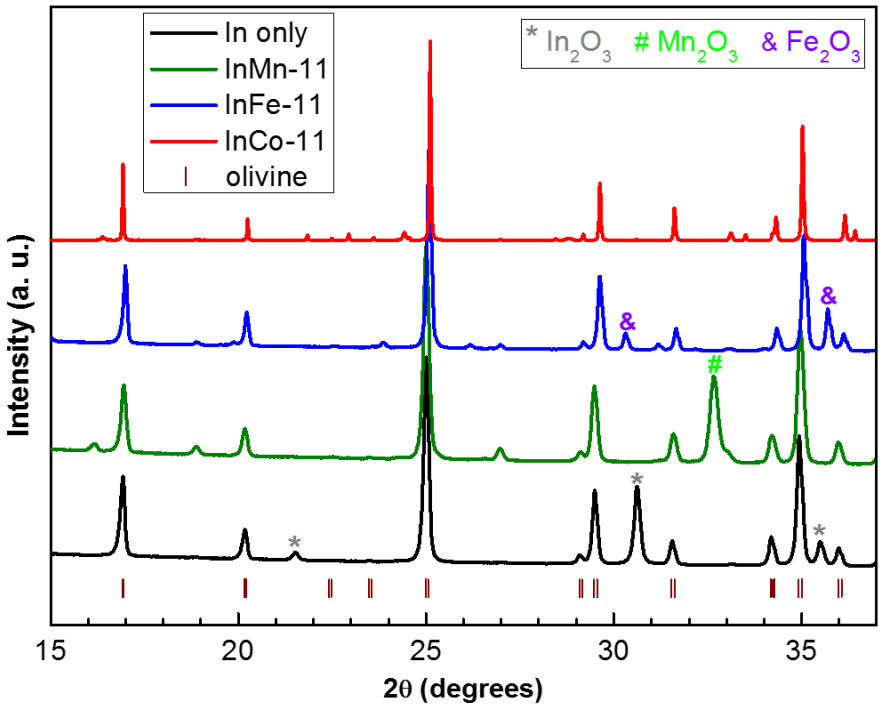

Figure 6-1. XRD comparison of transition metal substituted and non-substituted samples (laboratory diffractometer, Cu Kα radiation for In only, InMn-11 and InFe-11, and synchrotron, λ = 0.413738 Å for InCo-11 with 2θ adjusted to the Cu Kα radiation wavelength). The impurity peaks are marked and labelled in the figure.

the addition of Mn in the precursors (InMn-11), little change is observed in the olivine phase of the product and significant amount of Mn_2O_3 is present, indicating the substitution was not successful. The olivine peaks of the In-Fe sample (InFe-11), on the other hand, shift slightly to the right of the non-substituted $LiInSiO_4$. This decrease of lattice parameters would be well from the partial substitution of In^{3+} by the smaller Fe^{3+}. Nevertheless, the relatively high intensities of the Fe_2O_3 impurity peaks imply a rather low substitution level.

The XRD pattern of the In-Co product (InCo-11) shows an obvious shift of the olivine peaks (**Figure 6-1**), indicating a change of lattice parameters caused by cation substitution. In addition to the materials prepared at a 1:1 ratio, two other In/Co ratios were also synthesized, namely 3:1 (InCo-31) and 1:3 (InCo-13). By comparison to the non-substituted sample, the three patterns show a continuous shift to higher two-theta values, i.e. smaller lattice parameters, with increasing Co concentration (**Figure 6-2a**). Although minor impurities are observed in each case, overall the results demonstrate a higher level of substitution is obtained by increasing the Co ratio.

To elucidate information on the cobalt oxidation state in the targeted olivine, cobalt K-edge XANES measurements were carried out, with CoO and Li_2CoSiO_4 as the standards for Co^{2+}, Co_3O_4 for mixed Co^{2+}/Co^{3+}, and $LiCoO_2$ for Co^{3+}. Surprisingly, the main cobalt edges of all three samples are close to those of CoO and Li_2CoSiO_4 whereas the Co^{3+} in the standards (Co_3O_4 and $LiCoO_2$) is clearly at higher energy (**Figure 6-2b**). This suggests that Co^{2+} is mainly present in the final products, despite the use of a Co^{3+} precursor under an oxidizing atmosphere (O_2) in the reaction. This reduction could be due to the presence of the acetylacetonate and acetate anions in the precursors, providing a slightly reductive atmosphere

during the reaction. The cation size of Co^{2+} is comparable to Li^{+} and In^{3+} and hence it has a good solubility in the olivine structure .

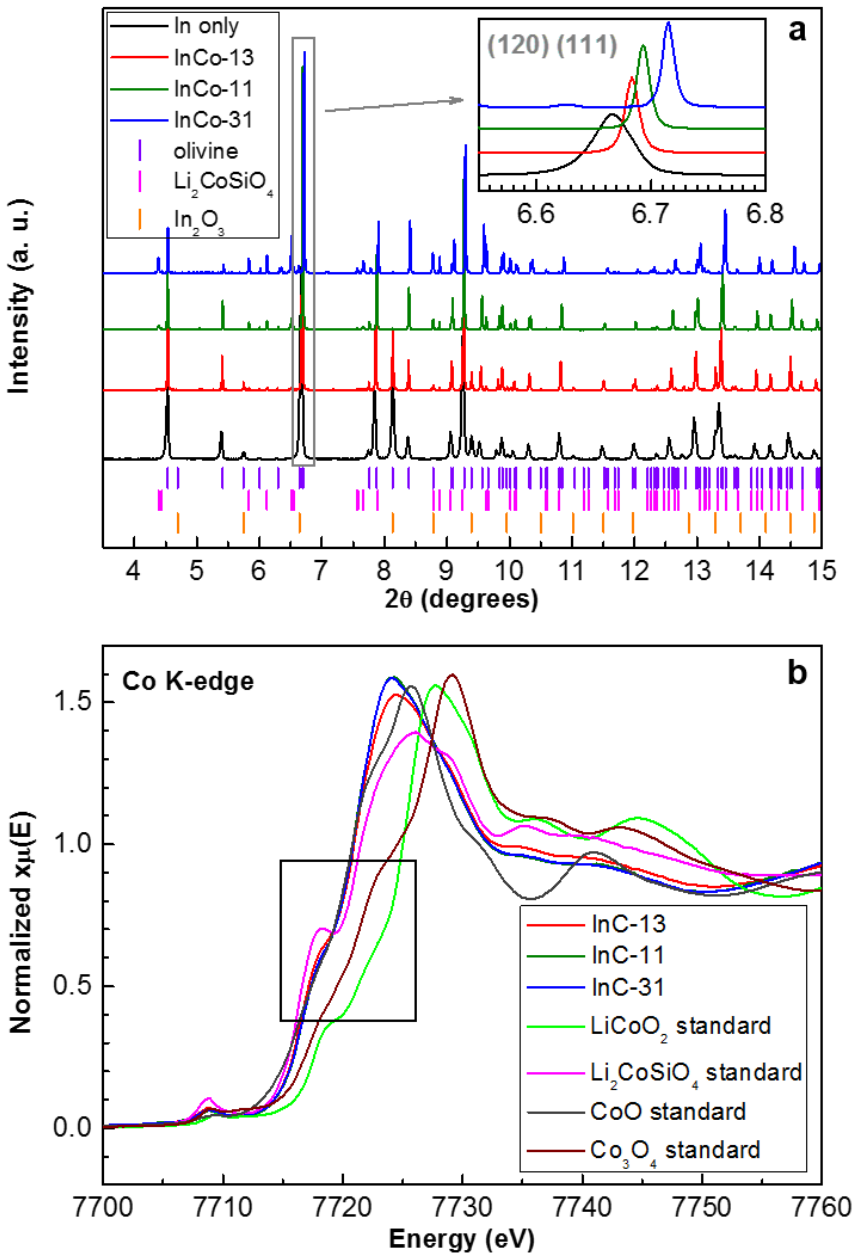

Figure 6-2. (a) XRD comparison of the cobalt substituted (synchrotron, λ = 0.413738 Å) and non-substituted (laboratory diffractometer, Cu Kα radiation, 2θ adjusted to synchrotron wavelength) samples, showing a right shift of olivine peaks with an increase of cobalt concentration as well as minor impurities. (b) The Co K edge XANES of cobalt substituted samples together with a few standards, demonstrating the Co oxidation state in InCo samples close to +2.

The cation arrangement in the Co substituted olivine phase was further examined by combined Rietveld refinement[92] of the SXRD and ND patterns. The InCo-11 sample was studied in detail because of the relatively large XRD peak shift and small impurity fraction. The stoichiometry of olivine phase in such sample was determined to be $Li_{0.8}In_{0.8}Co_{0.4}SiO_4$ (from charge balance and assuming fully occupied sites), indicating similar amount of lithium and indium were substituted by cobalt. The three cations were initially assigned equally over the two sites (**Figure 1-1c**), followed by a relaxation of their occupancies until the refinement converged. The degree of lithium ion mixing was negligible so Li^+ was fixed on site 1. The indium cation primarily occupies site 2, with only 2% disordered on site 1. Cobalt, on the other hand, occupies on both sites 1 and 2 (**Figure 6-3** and **Table 6-5**). Thus the olivine phase resembles the parent structure (cation ordered $LiInSiO_4$) but cobalt disorders over the two sites. This is in agreement with the simulation result that shows a tendency towards cobalt disorder in the olivine lattice.

The experimental results clearly show that high cobalt substitution can be achieved in $LiInSiO_4$-olivine. Combined with the results of atomistic scale simulations, it appears that the ability of cobalt to disorder over two cationic sites contributes an additional entropic stability to the compound and therefore, a high degree of substitution can be achieved. The reduction of Co^{3+} to Co^{2+} allows a better match of cation sizes, promoting a high substitution level. At the same time, the fact that Co_2SiO_4 itself can form an olivine structure[222] allows it to produce a solid solution with $LiInSiO_4$ in the final product and results in additional structural stability. On the other hand, cation disorder blocks the most facile 1D Li-ion migration pathway, forcing diffusion to take place along more hindered pathways. Nevertheless, reducing cation diffusion

length by using nano-sized particles would potentially allow reversible Li-ion intercalation, as already seen in a similar situation in triplite-$LiFeSO_4F$.[223]

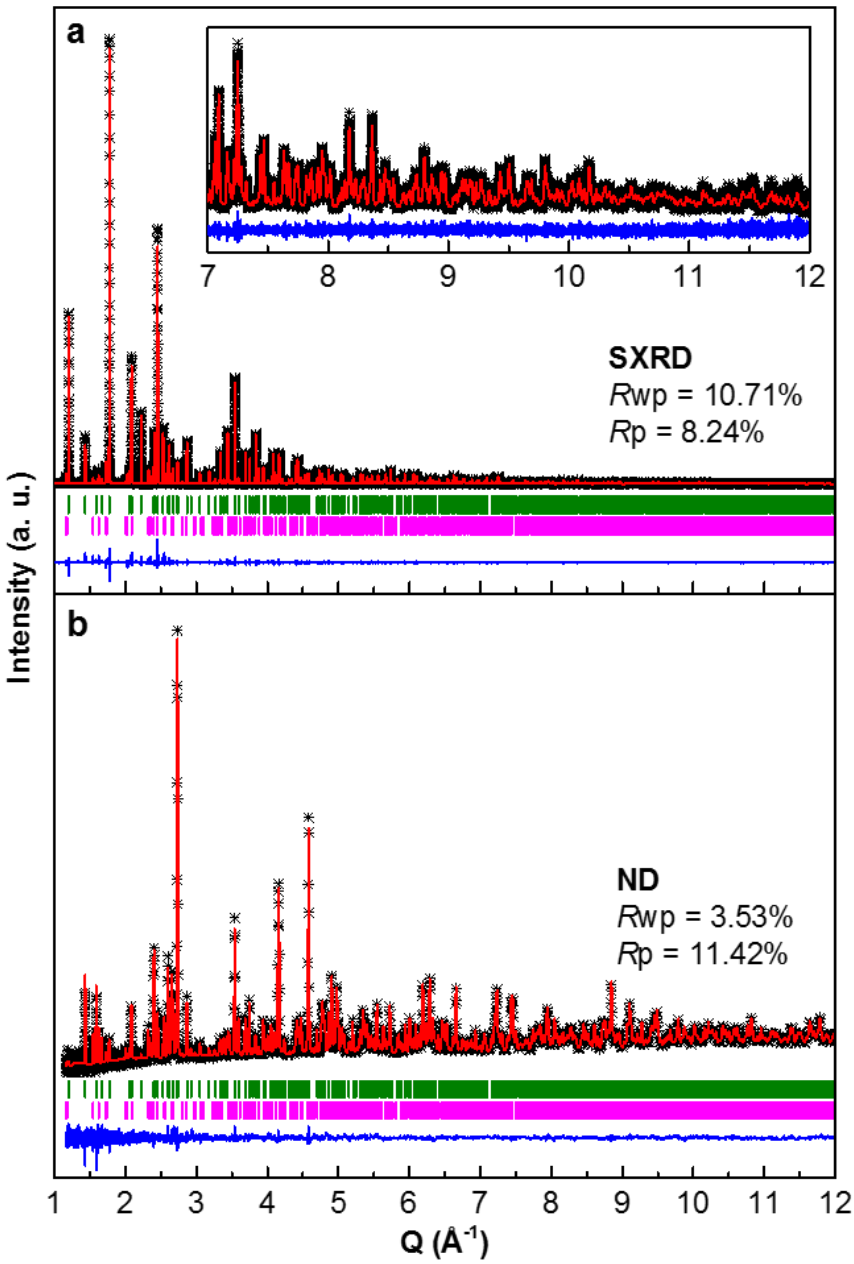

Figure 6-3. Combined Rietveld refinement of (a) synchrotron XRD and (b) time-of-flight neutron diffraction of InCo-11. The experimental data is shown in black crosses, the fitted data is shown in red lines, the difference curve is shown in blue line and the Bragg peak positions of olivine and Li_2CoSiO_4 are shown in green and pink ticks, respectively. The overall χ^2 is 2.173.

Table 6-5. Combined synchrotron XRD time-of-flight neutron diffraction refinement results (measured at 100K, χ^2 = 2.173, *R*wp = 8.45%, *R*p = 8.24%).

Atom	***x***	***y***	***z***	**Occ.**	***U*iso (Å^2)**
Phase 1: $Li_{0.8}In_{0.8}Co_{0.4}SiO_4$ **Space group = *Pbnm*; *a* = 4.82521(2) Å, *b* = 10.46818(3) Å, *c* = 6.02472(2) Å**					
Li1	0	0	0	0.8	0.0067(4)
In1	0	0	0	0.015(1)	0.0067(4)
Co1	0	0	0	0.185(1)	0.0067(4)
In2	0.98428(6)	0.27547(2)	0.25	0.785(1)	0.00331(5)
Co2	0.98428(6)	0.27547(2)	0.25	0.215(1)	0.00331(5)
Si	0.4260(2)	0.08961(7)	0.25	1	0.0013(2)
O1	0.7578(2)	0.0964(1)	0.25	1	0.0038(2)
O2	0.2921(3)	-0.05253(9)	0.25	1	0.0043(2)
O3	0.2765(2)	0.16396(7)	0.0396(1)	1	0.0036(2)
Phase 2: Li_2CoSiO_4 **Space group = *Pbn*2$_1$; *a* = 6.26537(6) Å, *b* = 10.68702(9) Å, *c* = 4.92913(4) Å**					
Li1	-0.0006	0.1618	0.2619	1	0.005
Li2	0.747(5)	0.423(2)	0.253(5)	1	0.005
Co2	0.4915(4)	0.1655(2)	0.259(4)	1	0.005
Si	0.2556(9)	0.4151(4)	0.257(4)	1	0.005
O1	0.256(2)	0.4081(5)	0.592(3)	1	0.005
O2	0.246(2)	0.5578(4)	0.156(4)	1	0.005
O3	0.0384(9)	0.3427(6)	0.161(4)	1	0.005
O4	0.4675(9)	0.3391(6)	0.153(4)	1	0.005

6.4 Conclusions

Atomistic scale simulations on the transition metal (Mn, Fe, and Co) substitutions into the olivine-type $LiScSiO_4$ and $LiInSiO_4$ structures show that among them, cobalt substitution results in the highest trend of cation disorder in the structure. Therefore, cations in $LiIn_{1-x}Co_xSiO_4$ are predicted to be more disordered over site 1 and site 2 in the olivine lattice than for other metals. Experimental attempts show that significant substitution could be obtained only with cobalt, together with the reduction of Co^{3+} to Co^{2+}. This suggest that the additional configurational entropy arising from cation disorder in the structure plays a major role in lowering the free energy of the substituted material. When unfavorable site mixing (owing to size or other effects) dominates, substitution is precluded. This work demonstrates that substitution could be promoted by increasing the entropic parameter as well as matching the ion sizes in the substituted structure, both of which helps to lower the overall free energy.

Chapter 7

Summary and Future Perspectives

This thesis presents the investigation of various positive electrode materials for rechargeable batteries, including sulfides and oxides for Mg batteries, Prussian blue analogues for Mg-Li hybrid batteries, and olivine phase lithium transition metal silicates for Li-ion batteries.

Two titanium sulfides are identified as the second family of Mg insertion positive electrodes after the CPs with improved electrochemical properties. During electrochemical cycling in a Mg full cell, Mg^{2+} can be reversibly de/intercalated into both spinel and layered structures of titanium sulfide. High capacities and good reversibility are obtained for the solid state synthesized micron sized materials. The cycle lives are further extended by decreasing the particle size, either through a mechanical ball milling process or a wet synthesis procedure. The crystal structures show strong influence on the Mg^{2+} diffusion behavior, resulting in the different voltage profiles obtained for the two titanium sulfides. The activation energy of Mg^{2+} migration in the spinel phase, determined by first principles calculation, is comparable to some of the structures allowing facile Li^{+} intercalation at room temperature. As a result, the necessity of cycling Ti_2S_4 against Mg at an elevated temperature suggests that other factors in addition to solid diffusion, such as desolvation at the electrode/electrolyte interphase, must play critical roles on multivalent ion intercalation.

The influence of desolvation is further investigated using birnessite MnO_2 as a sample positive electrode. Facile Mg^{2+} intercalation takes place with the aqueous electrolyte where desolvation energy is low. On the contrary, a conversion mechanism is observed in the nonaqueous system, leaving electrolyte species behind on the surface of MnO_2 during

discharge and indicating a sluggish desolvation process. As Mg^{2+} has twice the charge of monovalent Li^+ or Na^+, its interaction with the other electrolyte species are stronger. Such a factor, which was mostly overlooked in previous research, could well be one of the main reasons for the widely observed poor electrochemical performance of Mg positive electrodes. On the other hand, a bottleneck of Mg^{2+} solid diffusion is identified by a case-study of $Mg_2Mo_3O_8$. Mg^{2+} occupies both the octahedral and tetrahedral sites of the layered structure at the initial state. However, the pathway connecting the two sites contains a highly unstable dumbbell transition state, hindering Mg^{2+} bulk diffusion. Similar quick examination of possible Mg^{2+} pathways in other solid structures can be carried out to evaluate their potential usage as positive electrode materials for Mg batteries.

The Mg-Li hybrid cell is an alternative choice of utilizing a Mg negative electrode while involving facile Li^+ de/intercalation at the positive electrode, so that problems with Mg^{2+} diffusion are completely avoided. As a result of the robust frameworks of Prussian blue analogues, such positive electrodes are stable to high voltages even with a corrosive electrolyte. Operating at an average voltage of 2.3 V, the full cells show great improvement on energy density compared to the previous reported hybrid cells. The rich collection of compounds in the Prussian blue family opens up a wide selection of positive candidates for the hybrid cell. Nevertheless, attention should be paid to the match between the capacity of positive electrode and the salt concentration in electrolyte, since the electrolyte is the only source for Li^+ in the hybrid system.

As many difficulties have been suffered during the discovery of new candidates for Mg positive electrodes, more work should be focused on the identification of the key limitations in order to guide future direction. The two structures of titanium sulfide presented in this thesis

provide a convenient platform to study the crystal structure influence on the solid diffusion of Mg^{2+}, since other factors resulting from different elements are readily ruled out. In addition, the desolvation process has been gradually realized as an important factor during multivalent ion insertion; thus, future research is promoted in the investigation of more detail of such process as well as the coupling between appropriate positive electrodes and electrolytes. The electrolytes, although not discussed in great detail in this thesis, remain as another challenge in the Mg battery field. The search for a non-corrosive, highly anionic stable, low toxic and easily synthesized electrolyte, which at the same time allows facile Mg^{2+} stripping/plating at the negative electrode and desolvation at the positive electrode, is an on-going process parallel to the investigations of positive electrodes. All the components have to be integrated into a full cell in the end to evaluate the overall electrochemical performance and encourage any practical application of rechargeable Mg batteries.

References

1 International Energy Agency, Technology Road Maps, Electric and Plug-ion Hybrid Electric Vehicles. **2011**.

2 Whittingham, M. S. Electrical Energy Storage and Intercalation Chemistry. *Science* **1976**, 192, 1126-1127.

3 Whittingham, M. S. Chalcogenide Battery. US Patent 4009052, **1977**.

4 Whittingham, M. S. The Role of Ternary Phases in Cathode Reactions. *J. Electrochem. Soc.* **1976**, *123*, 315-320.

5 Mizushima, K.; Jones, P. C.; Wiseman, P. J.; Goodenough, J. B. Li_xCoO_2 (0<x 1): a New Cathode Material for Batteries of High Energy Density. *Mat. Res. Bull.* **1980**, *15*, 783-789.

6 Orsini, F.; du Pasquier, A.; Beaudouin, B.; Tarascon, J. M.; Trentin, M.; Langenhuizen, N.; de Beer, E.; Notten, P. In Situ SEM Study of the Interfaces in Plastic Lithium Cells. *J. Power Sources* **1999**, *81-82*, 918-921.

7 Rao, B. M. L.; Francis, R. W.; Christopher, H. A. Lithium-Aluminium Electrodes. *J. Electrochem. Soc.* **1977**, *124*, 1490-1492.

8 Mohri, M.; Yanagisawa, N.; Tajima, Y.; Tanaka, H.; Mitate, T.; Nakajima, S.; Yoshida, M.; Yoshimoto, Y.; Suzuki, T.; Wada, H. Rechargeable Lithium Battery Based on Pyrolytic Carbon as a Negative Electrode. *J. Power Sources* **1989**, *26*, 545-551.

9 Takayuki, Y.; Kato, H.; Anzai, M. Nonaqueous Electrolyte Secondary Battery. US Patent 5054397, **1991**.

10 Lu, Z.; MacNeil, D. D.; Dahn, J. R. Layered $Li[Ni_xCo_{1-2x}Mn_x]O_2$ Cathode Materials for Lithium-Ion Batteries. *Electrochem. Solid-State Lett.* **2001**, *4*, A200-A203.

11 Yabuuchi, N.; Ohzuku, N. Novel Lithium Insertion Material of $LiCo_{1/3}Ni_{1/3}Mn_{1/3}O_2$ for Advanced Lithium-Ion Batteries. *J. Power. Sources* **2003**, *119*, 171-174.

12 Thackeray, M. M.; Johnson, P. J.; de Picciotto, L. A. Electrochemical Extraction of Lithium from $LiMn_2O_4$. *Mat. Res. Bull.* **1984**, *19*, 179-187.

13 Thackeray, M. M. Manganese Oxides for Lithium Batteries. *Prog. Solid St. Chem.* **1997**, *25*, 1-71.

14 Jang, D. H.; Shin, Y. J.; Oh, S. M. Dissolution of Spinel Oxides and Capacity Losses in 4 V $Li/Li_xMn_2O_4$ Cells. *J. Electrochem. Soc.* **1996**, *143*, 2204-2211.

15 Pahdi, A. K.; Nanjundaswamy, K. S.; Masquelier, C.; Okada, S.; Goodenough, J. B. Effect of Structure on the Fe^{3+}/Fe^{2+} Redox Couple in Iron Phosphates. *J. Electrochem. Soc.* **1997**, *144*, 1609-1613.

16 Pahdi, A. K.; Nanjundaswamy, K. S.; Goodenough, J. B. Phospho-Olivines as Positive-Electrode Materials for Rechargeable Lithium Batteries. *J. Electrochem. Soc.* **1997**, *144*, 1188-1194.

17 Legagneur, V.; An, Y.; Mosbah, A.; Portal, R.; Le Gal La Salle, A.; Verbaere, A.; Guyomard, D.; Piffard, Y. $LiMBO_3$ (M = Mn, Fe, Co): Synthesis, Crystal Structure and Lithium Deinsertion/Insertion Properties. *Solid State Ionics* **2001**, *139*, 37-46.

18 Nytén, A.; Abouimrane, A.; Armand, M.; Gustafsson, T.; Thomas, J. O. Electrochemical Performance of Li_2FeSiO_4 as a New Li-Battery Cathode Material. *Electrochem. Commun.* **2005**, *7*, 156-160.

19 Recham, N.; Chotard, J-N.; Dupont, L.; Delacourt, C.; Walker, W.; Armand, M.; Tarascon, J-M. A 3.6 V Lithium-Based Fluorosulphate Insertion Positive Electrode for Lithium-Ion Batteries. *Nature Mater.* **2010**, *9*, 68-74.

20 Barpanda, P.; Ati, M.; Melot, B. C.; Rousse, G.; Chotard, J.-N.; Doublet, M.-L.; Sougrati, M. T.; Corr, S. A.; Jumas, J.-C.; Tarascon, J.-M. A 3.90 V Iron-Based Fluorosulphate Material for Lithium-Ion Batteries Crystallizing in the Triplite Structure. *Nature Mater.* **2011**, *10*, 772-779.

21 Nytén, A.; Kamali, S.; Häggström, L.; Gustafsson, T.; Thomas, J. O. The Lithium Extraction/Insertion Mechanism in Li_2FeSiO_4. *J. Mater. Chem.* **2006**, *16*, 2266-2272.

22 Gong, Z. L.; Li, Y. X.; He, G. N.; Li, J.; Yang, Y. Nanostructured Li_2FeSiO_4 Electrode Material Synthesized through Hydrothermal-Assisted Sol-Gel Process. *Electrochem. Solid-State Lett.* **2008**, *11*, A60-A63.

23 Sirisopanaporn, C.; Masquelier, C.; Bruce, P. G.; Armstrong, A. R.; Dominko, R. Dependence of Li_2FeSiO_4 Electrochemistry on Structure. *J. Am. Chem. Soc.* **2011**, *133*, 1263-1265.

24 Armstrong, A. R.; Kuganathan, N.; Islam, M. S.; Bruce, P. G. Structure and Lithium Transport Pathways in Li_2FeSiO_4 Cathodes for Lithium Batteries. *J. Am. Chem. Soc.* **2011**, *133*, 13031-13035.

25 Saracibar, A.; Van der Ven, A.; Arroyo-de Dompablo, M. E. Crystal Structure, Energetics, and Electrochemistry of Li_2FeSiO_4 Polymorphs from First Principles Calculations. *Chem. Mater.* **2012**, *24*, 495-503.

26 Muldoon, J.; Bucur, C. B.; Gregory, T. Quest for Nonaqueous Multivalent Secondary Batteries: Magnesium and Beyond. *Chem. Rev.* **2014**, *114*, 11683-11720.

27 Aurbach, D.; Cohen, Y.; Moshkovich, M. The Study of Reversible Magnesium Deposition by *In Situ* Scanning Tunneling Microscopy. *Electrochem. Solid-State Lett.* **2001**, *4*, A113-A116.

28 Matsui, M.; Study on Electrochemically Deposited Mg Metal. *J. Power Sources* **2011**, *196*, 7048-7055.

29 Aurbach, D.; Lu, Z.; Schechter, A.; Gofer, Y.; Gizbar, H.; Turgeman, R.; Cohen, Y.; Moshkovich, M.; Levi, E. Prototype Systems for Rechargeable Magnesium Batteries. *Nature* **2000**, *407*, 724-727.

30 Delmas, C.; Cognac-Auradou, H.; Cocciantelli, J. M.; Menetrier, M.; Doumerc, J. P. The $Li_xV_2O_5$ System: An Overview of the Structure Modifications Induced by the Lithium Intercalation. *Solid State Ionics* **1994**, *69*, 257-264.

31 Nov ák, P.; Imhof, R.; Haas, O. Magnesium Insertion Electrodes for Rechargeable Nonaqueous Batteries – A Competitive Alternative to Lithium? *Electrochim. Acta* **1999**, *45*, 351-367.

32 Pereira-Ramos, J.; Messina, R.; Perichon, J. Electrochemical Formation of a Magnesium Vanadium Bronze $Mg_xV_2O_5$ in Sulfone-Based Electrolytes at 150 ℃. *J Electroanal. Chem.* **1987**, *218*, 241-249.

33 Amatucci, G. G.; Badway, F.; Singhal, A.; Beaudoin, B.; Skandan, G.; Bowmer, T.; Plitz, I.; Pereira, N.; Chapman, T.; Jaworski, R. Investigation of Yttrium and Polyvalent Ion Intercalation into Nanocrystalline Vanadium Oxide. *J. Electrochem. Soc.* **2001**, *148*, A940-A950.

34 Gershinsky, G.; Yoo, H. D.; Gofer, Y.; Aurbach, D. Electrochemical and Spectroscopic Analysis of Mg^{2+} Intercalation into Thin Film Electrodes of Layered Oxides: V_2O_5 and MoO_3. *Langmuir* **2013**, *9*, 10964-10972.

35 Le, D. B.; Passerini, S.; Coustier, F.; Guo, J.; Soderstrom, T.; Owens, B. B.; Smyrl, W. H. Intercalation of Polyvalent Cations into V_2O_5 Aerogels. *Chem. Mater.* **1998**, *10*, 682-684.

36 Imamura, D.; Miyayama, M. Characterization of Magnesium Intercalated V_2O_5/Carbon Composites. *Solid State Ionics* **2003**, *161*, 173-180.

37 Imamura, D.; Miyayama, M.; Hibino, M.; Kudo, T. Mg Intercalation Properties into V_2O_5 Gel/Carbon Composites under High-Rate Condition. *J. Electrochem. Soc.* **2003**, *150*, A753-A758.

38 Tepavcevic, S.; Liu, Y.; Zhou, D.; Lai, B.; Maser, J.; Zuo, X.; Chan, H.; Kr_al, P.; Johnson, C. S.; Stamenkovic, V.; Markovic, N. M.; Rajh, T. Nanostructured Layered Cathode for Rechargeable Mg-Ion Batteries. *ACS Nano* **2015**, *9*, 8194-8205.

39 Sa, N.; Kinnibrugh, T. L.; Wang, H.; Gautam, G. S.; Chapman, K. W.; Vaughey, J. T.; Key, B.; Fister, T. T.; Freeland, J. W.; Pro_t, D. L.; Chupas, P. J.; Ceder, G.; Bareno, J. G.; Bloom, I. D.; Burrell, A. K. Structural Evolution of Reversible Mg Insertion into a Bilayer Structure of V_2O_5·nH_2O Xerogel Material. *Chem. Mater.* **2016**, *28*, 2962-2969.

40 Gautam, G. S.; Canepa, P.; Richards, W. D.; Malik, R.; Ceder, G. Role of Structural H_2O in Intercalation Electrodes: The Case of Mg in Nanocrystalline Xerogel-V_2O_5. *Nano Lett.* **2016**, *16*, 2426-2431.

41 Nov ák, P.; Desilvestro, J. Electrochemical Insertion of Magnesium in Metal Oxides and Sulfides from Aprotic Electrolytes. *J. Electrochem. Soc.* **1993**, *140*, 140-144.

42 Yu, L.; Zhang, X. Electrochemical Insertion of Magnesium Ions into V_2O_5 from Aprotic Electrolytes with Varied Water Content. *J. Colloid Interf. Sci.* **2004**, *278*, 160-165.

43 Spahr, M. E.; Nov ák, P; Haas, O.; Nesper, R. Electrochemical Insertion of Lithium, Sodium, and Magnesium in Molybdenum(VI) Oxide. *J. Power Sources* **1995**, *54*, 346-351.

44 Song, J.; Noked, M.; Gillette, E.; Duay, J.; Rubloff, G.; Lee, S. B. Activation of a MnO_2 Cathode by Water-Stimulated Mg^{2+} Insertion for a Magensium Ion Battery. *Phys. Chem. Chem. Phys.* **2015**, *17*, 5256-5264.

45 Kim, C.; Phillips, P. J.; Key, B.; Yi, T.; Nordlund, D.; Yu, Y.-S.; Bayliss, R. D.; Han, S.-D.; He, M.; Zhang, Z.; Burrell, A. K.; Klie, R. F.; Cabana, J. Direct Observation of Reversible Magnesium Ion Intercalation into a Spinel Oxide Host. *Adv. Mater.* **2015**, *27*, 3377-3384.

46 Nam, K. W.; Kim, S.; Lee, S.; Salama, M.; Shterenberg, I.; Gofer, Y.; Kim, J.-S.; Yang, E.; Park, C. S.; Kim, J.-S.; Lee, S.-S.; Chang, W.-S.; Doo, S.-G.; Jo, Y. N.; Jung, Y.; Aurbach, D.; Choi, J. W. The High Performance of Crystal Water Containing Manganese Birnessite Cathodes for Magnesium Batteries. *Nano Lett.* **2015**, *15*, 4071-4079.

47 Sun, X.; Duffort, V.; Mehdi, B. L.; Browning, N. D.; Nazar, L. F. Investigation of the Mechanism of Mg Insertion in Birnessite in Nonaqueous and Aqueous Rechargeable Mg-Ion Batteries. *Chem. Mater.* **2016**, *28*, 534-542.

48 Sa, N.; Wang, H.; Proffit, D. L.; Lipson, A. L.; Key, B.; Liu, M.; Feng, Z.; Fister, T. T.; Ren, Y.; Sun, C.-J.; Vaughey, J. T.; Fenter, P. A.; Persson, K. A.; Burrell, A. K. Is Alpha-V_2O_5 a Cathode Material for Mg Insertion Batteries? *J. Power Sources* **2016**, *323*, 44-50.

49 Arthur, T. S.; Zhang, R.; Ling, C.; Glans, P.-A.; Fan, X.; Guo, J.; Mizuno, F. Understanding the Electrochemical Mechanism of K-αMnO_2 for Magnesium Battery Cathodes. *ACS Appl. Mater. Interfaces* **2014**, *6*, 7004-7008.

50 Levi, E.; Levi, M. D.; Chasid, O.; Aurbach, D. A Review on the Problems of the Solid State Ions Diffusion in Cathodes for Rechargeable Mg Batteries. *J. Electroceram.* **2009**, *22*, 13-19.

51 Yoo, H. D.; Shterenberg, I.; Gofer, Y.; Gershinsky, G.; Pour, N.; Aurbach, D. Mg Rechargeable Batteries: An on-Going Challenge. *Energy Environ. Sci.* **2013**, *6*, 2265-2279.

52 Levi, E.; Lancry, E.; Mitelman, A.; Aurbach, D.; Ceder, G.; Morgan, D.; Isnard O. Phase Diagram of Mg Insertion into Chevrel Phases, $Mg_xMo_6T_8$ (T = S, Se). 1. Crystal Structure of the Sulfides. *Chem. Mater.* **2006**, *18*, 5492-5503.

53 Lancry, E.; Levi, E.; Gofer, Y.; Levi, M.; Salitra, G.; Aurbach, D. Leaching Chemistry and the Performance of the Mo_6S_8 Cathodes in Rechargeable Mg Batteries. *Chem. Mater.* **2004**, *16*, 2832-2838.

54 Levi, M. D.; Lancri, E.; Levi, E.; Gizbar, H.; Gofer, Y.; Aurbach, D. The Effect of the Anionic Framework of Mo_6X_8 Chevrel Phase (X = S, Se) on the Thermodynamics and the Kinetics of the Electrochemical Insertion of Mg^{2+} Ions. *Solid State Ionics* **2005**, *176*, 1695-1699.

55 Levi, E.; Lancry, E.; Mitelman, A.; Aurbach, D.; Isnard, O.; Djurado, D. Phase Diagram of Mg Insertion into Chevrel Phases, $Mg_xMo_6T_8$ (T = S, Se). 2. The Crystal Structure of Triclinic $MgMo_6Se_8$. *Chem. Mater.* **2006**, *18*, 3705-3714.

56 Aurbach, D.; Suresh, G. S.; Levi, E.; Mitelman, A.; Mizrahi, O. Chusid, O.; Brunelli, M. Progress in Rechargeable Magnesium Battery Technology. *Adv. Mater.* **2007**, *19*, 4260-4267.

57 Suresh, G. S.; Levi, M. D.; Aurbach, D. Effect of Chalcogen Substitution in Mixed $Mo_6S_{8-n}Se_n$ (n = 0, 1, 2) Chevrel Phases on the Thermodynamics and Kinetics of Reversible Mg Ions Insertion. *Electrochim. Acta* **2008**, *53*, 3889-3896.

58 Amir, N.; Vestfrid, Y.; Chusid, O.; Gofer, Y.; Aurbach, D. Progress in Nonaqueous Magnesium Electrochemistry. *J. Power Sources* **2007**, *174*, 1234-1240.

59 Duffort, V.; Sun, X.; Nazar, L. F. Screening for Positive Electrodes for Magnesium Batteries: A Protocol for Studies at Elevated Temperatures. *Chem. Commun.* **2016**, *52*, 12458-12461.

60 He, D.; Wu, D.; Gao, J.; Wu, X.; Zeng, X.; Ding, W. Flower-Like CoS with Nanostructures as a New Cathode-Active Material for Rechargeable Magnesium Batteries. *J. Power Sources* **2015**, *294*, 643-649.

61 Liang, Y.; Feng, R.; Yang, S.; Ma, H.; Liang, J.; Chen, J. Rechargeable Mg Batteries with Graphene-Like MoS_2 Cathode andUltrasmall Mg Nanoparticle Anode. *Adv. Mater.* **2011**, *23*, 640-643.

62 Liu, Y.; Jiao, L.; Wu, Q.; Du, J.; Zhao, Y.; Si, Y.; Wang, Y.; Yuan, H. Sandwich-Structured Graphene-Like MoS_2/C Microspheres for Rechargeable Mg Batteries. *J. Mater. Chem. A* **2013**, *1*, 5822-5826.

63 Liu, Y.; Jiao, L.; Wu, Q.; Du, J.; Zhao, Y.; Cao, K.; Liu, H.; Wang, Y.; Yuan, H. Synthesis of rGO-Supported Layered MoS_2 for High-Performance Rechargeable Mg Batteries. *Nanoscale* **2013**, *5*, 9562-9567.

64 Liang, Y.; Yoo, H. D.; Li, Y.; Shuai, J.; Calderon, H. A.; Hernandez, F. C. R.; Grabow, L. C.; Yao, Y. Interlayer-Expanded Molybdenum Disulfide Nanocomposites for Electrochemical Magnesium Storage. *Nano Lett.* **2015**, *15*, 2194-2202.

65 Lu, Z.; Schechter, A.; Moshkovich, M.; Aurbach, D. On the Electrochemical Behavior of Magnesium Electrodes in Polar Aprotic Electrolyte Solutions. *J. Electroanal. Chem.* **1999**, *466*, 203-217.

66 Aurbach, D.; Gofer, Y.; Schechter, A.; Chusid, O.; Gizbar, H.; Cohen, Y.; Moshkovich, M.; Turgeman, R. A Comparison between the Electrochemical Behavior of Reversible Magnesium and Lithium Electrodes. *J. Power Sources* **2001**, *97-98*, 269-273.

67 Gaddum, L. W. French, H. E. The Electrolysis of Grignard Solutions. *J. Am. Chem. Soc.* **1927**, *49*, 1295-1299.

68 Aurbach, D.; Weissman, I.; Gofer, Y.; Levi, E. Nonaqueous Magnesium Electrochmistry andIts Application in Secondary Batteries. *Chem. Rec.* **2003**, *3*, 61-73.

69 Aurbach, D.; Gofer, Y.; Lu, Z.; Schechter, A.; Chusid, O.; Gizbar, H.; Cohen, Y.; Ashkenazi, V.; Moshkovich, M.; Turgeman, R.; Levi, E. A Short Review on the Comparison between Li Battery Systems and Rechargeable Magnesium Battery Technology. *J. Power Sources* **2001**, *97-98*, 28-32.

70 Aurbach, D.; Gizbar, H.; Schechter, A.; Chusid, O.; Gottlieb, H. E.; Gofer, Y.; Goldberg I. Electrolyte Solutions for Rechargeable Magnesium Batteries Based on Organomagnesium Chloroaluminate Complexes. *J. Electrochem. Soc.* **2002**, *149*, A115-A121.

71 Gofer, Y.; Chusid, O.; Gizbar, H.; Viestfrid, Y.; Gottlieb, H. E.; Marks, V.; Aurbach, D. Improved Electrolyte Solutions for Rechargeable Magnesium Batteries. *Electrochem. Solid-State Lett.* **2006**, *9*, A257-A260.

72 Mizrahi, O.; Amir, N.; Pollak, E.; Chusid, O.; Marks, V.; Gottlieb, H.; Larush, L.; Zinigrad, E.; Aurbach, D. Electrolyte Solutions with a Wide Electrochemical Window for Rechargeable Magnesium Batteries. *J. Electrochem. Soc.* **2008**, *155*, A103-A109.

73 Kim, H. S.; Arthur, T. S.; Allred, G. D.; Zajicek, J.; Newman, J. G.; Rodnyansky, A. E.; Oliver, A. G.; Boggess, W. C.; Muldoon, J. Structure and Compatibility of a Magnesium Electrolyte with a Sulphur Cathode. *Nat. Commun.* **2011**, *2*, 427.

74 Doe, R. E.; Han, R.; Hwang, J.; Gmitter, A. J.; Shterenberg, I.; Yoo, H. D.; Pour, N.; Aurbach, D. Novel, Electrolyte Solutions Comprising Fully Inorganic Salts with High Anodic Stability for Rechargeable Magnesium Batteries. *Chem. Commun.* **2014**, *50*, 243-245.

75 See, K. A.; Chapman, K. W.; Zhu, L.; Wiaderek, K. M.; Borkiewicz, O. J.; Barile, C.; J.; Chupas, P. J.; Gewirth, A. A.; The Interplay of Al and Mg Speciation in Advanced Mg Battery Electrolyte Solutions. *J. Am. Chem. Soc.* **2015**, *138*, 328-337.

76 Barile, C. J.; Barile, E. C.; Zavadil, K. R.; Nuzzo, R. G.; Gewirth, A. A. Electrolytic Conditioning of a Magnesium Aluminum Chloride Complex for Reversible Magnesium Deposition. *J. Phys. Chem. C* **2014**, *118*, 27623-27630.

77 Ha, J. H.; Adams, B.; Cho, J.-H.; Duffort, V.; Kim, J. H.; Chung, K. Y.; Cho, B. W.; Nazar, L. F.; Oh, S. H. A Conditioning-Free Magnesium Chloride Complex Electrolyte for Rechargeable Magnesium Batteries. *J. Mater. Chem. A* **2016**, *4*, 7160-7164.

78 Oscar T.; Mohtadi, R.; Arthur, T. S.; Mizuno, F.; Nelson, E. G.; Sevryugina, Y. V.; An Efficient Halogen-Free Electrolyte for Use in Rechargeable Magnesium Batteries. *Angew. Chem. Int. Ed.* **2015**, *54*, 7900-7904.

79 Keyzer, E. N.; Glass, H. F.; Liu, Z.; Bayley, P. M.; Dutton, S. E.; Grey, C. P.; Wright D. S. $Mg(PF_6)_2$-Based Electrolyte Systems: Understanding Electrolyte-Electrode Interactions for the Development of Mg-Ion Batteries. *J. Am. Chem. Soc.* **2016**, *138*, 8682-8685.

80 Schwarz, R.; Pejic, M.; Fischer, P.; Marinaro, M.; Jörissen, L.; Wachtler, M. Magnesocene-Based Electrolytes: A New Class of Electrolytes for Magnesium Batteries. *Angew. Chem. Int. Ed.* **2016**, *55*, 14958-14962.

81 Wan, L. F.; Perdue, B. R.; Apblett, C. A.; Prendergast, D. Mg Desolvation and Intercalation Mechanism at the Mo_6S_8 Chevrel Phase Surface. *Chem. Mater.* **2015**, *27*, 5932-5940.

82 Yagi, S.; Ichitsubo, T.; Shirai, Y.; Yanai, S.; Doi, T.; Murase, K.; Matsubara, E. A Concept of Dual-Salt Polyvalent-Metal Storage Battery. *J. Mater. Chem. A* **2014**, *2*, 1144-1149.

83 Chang, J.; Haasch, R. T.; Kim, J.; Spila, T.; Braun, P. V.; Gewirth, A. A.; Nuzzo, R. G. Synergetic Role of Li^+ During Mg Electrodeposition/Dissolution in Borohydride Diglyme Electrolyte Solution: Voltammetric Stripping Behaviors on a Pt Microelectrode Indicative of Mg-Li Alloying and Facilitated Dissolution. *ACS Appl. Mater. Interfaces* **2015**, *7*, 2494-2502.

84 Cho, J.-H.; Aykol, M.; Kim, S.; Ha, J.-H.; Wolverton, C.; Chung, K. Y.; Kim, K.-B.; Cho, B.-W. Controlling the Intercalation Chemistry to Design High-Performance Dual-Salt Hybrid Rechargeable Batteries. *J. Am. Chem. Soc.*, **2014**, *136*, 16116-16119.

85 Cheng, Y.; Shao, Y.; Zhang, J.-G.; Sprenkle, V. L.; Liu, J.; Li, G. High Performance Batteries Based on Hybrid Magnesium and Lithium Chemistry. *Chem. Commun.* **2014**, *50*, 9644-9646.

86 Gao, T.; Han, F.; Zhu, Y.; Suo, L.; Luo, C.; Xu, K.; Wang, C. Hybrid Mg^{2+}/Li^{+} Battery with Long Cycle Life and High Rate Capability. *Adv. Energy Mater.* **2015**, *5*, 1401507.

87 Yoo, H. D.; Liang, Y.; Li, Y.; Yao, Y. High Areal Capacity Hybrid Magnesium-Lithium-Ion Battery with 99.9% Coulombic Efficiency for Large-Scale Energy Storage. *ACS Appl. Mater. Interfaces*. **2015**, *7*, 7001-7007.

88 Su, S.; Huang, Z.; NuLi, Y.; Tuerxun, F. Yang, J.; Wang, J. A Novel Rechargeable Battery with a Magnesium Anode, a Titanium Dioxide Cathode, and a Magnesium Borohydride/Tetraglyme Electrolyte. *Chem. Commun.* **2015**, *51*, 2641-2644.

89 Wu, N.; Yang, Z.-Z.; Yao, H.-R.; Yin, Y.-X.; Gu, L.; Guo, Y.-G. Improving the Electrochemical Performance of the $Li_4Ti_5O_{12}$ Electrode in a Rechargeable Magnesium Battery by Lithium-Magnesium Co-Intercalation. *Angew. Chem., Int. Ed.* **2015**, *54*, 5757-5761.

90 Zhang, Y.; Xie, J.; Han, Y.; Li, C. Dual-Salt Mg-Based Batteries with Conversion Cathodes. *Adv. Funct. Mater.* **2015**, *25*, 7300-7308.

91 Cheng, Y.; Liu, T.; Shao, Y.; Engelhard, M. H., Liu, J.; Li, G. Electrochemically Stable Cathode Current Collectors for Rechargeable Magnesium Batteries. *J. Mater. Chem. A* **2014**, *2*, 2473-2477.

92 Rietveld, H. M. A Profile Refinement Method for Nuclear and Magnetic Structures. *J. Appl. Cryst.* **1969**, *2*, 65-71.

93 Walton, R. I. Subcritical Solvothermal Synthesis of Condensed Inorganic Materials. *Chem. Soc. Rev.* **2002**, *31*, 230-238.

94 Le Bail, A. Whole Powder Pattern Decomposition Methods and Applications: A Retrospection. *Powder Diffr.* **2005**, *20*, 316-326.

95 Rodr ́guez-Carvajal, J. Recent Advances in Magnetic Structure Determination by Neutron Powder Diffraction. *Physica B* **1993**, *192*, 55-69.

96 Larson, A. C.; Von Dreele, R. B. General Structure Analysis System (GSAS). *Los Alamos National Laboratory Report* **2000**, LAUR 86-748.

97 Toby, B. H. EXPGUI, a Graphical User Interface for GSAS. *J. Appl. Cryst.* **2001**, *34*, 210-213.

98 Ravel, B. Ravel; Newville, M. ATHENA, ARTEMIS, HEPHAESTUS: Data Analysis for X-Ray Absorption Spectroscopy Using IFEFFIT. *J. Synchrotron Rad.* **2005**, *12*, 537-541.

99 Periyapperuma, K.; Tran, T. T.; Trussler, S.; Ioboni, D.; Obrovac, M. N. Conflat Two and Three Electrode Electrochemical Cells. *J. Electrochem. Soc.* **2014**, *161*, A2182-A2187.

100 Blyr, A.; Sigala, C.; Amatucci, G.; Guyomard, D.; Chabre, Y.; Tarascon, J.-M. Self-Discharge of $LiMn_2O_4$/C Li-Ion Cells in Their Discharged State. *J. Electrochem. Soc.* **1998**, *145*, 194-209.

101 Delacourt, C.; Ridgway, P. L.; Srinivasan, V.; Battaglia, V. Measurements and Simulations of Electrochemical Impedance Spectroscopy of a Three-Electrode Coin Cell Design for Li-Ion Cell Testing. *J. Electrochem. Soc.* **2014**, *161*, A1253-A1260.

102 Liu, M.; Rong, Z.; Malik, R.; Canepa, P.; Jain, A.; Ceder, G.; Persson, K. A. Spinel Compounds as Multivalent Battery Cathodes: A Systematic Evaluation Based on *Ab Initio* Calculations. *Energy Environ. Sci.* **2015**, *8*, 964-974.

103 Gautam, G. S.; Canepa, P.; Malik, R.; Liu, M.; Persson K. A.; Ceder, G. First-Principles Evaluation of Multi-Valent Cation Insertion into Orthorhombic V_2O_5. *Chem. Commun.* **2015**, *51*, 13619-13622.

104 Bo, S.-H.; Grey, C. P.; Khalifah, P. G. Defect-Tolerant Diffusion Channels for Mg^{2+} Ions in Ribbon-Type Borates: Structural Insights into Potential Battery Cathodes $MgVBO_4$ and $Mg_xFe_{2-x}B_2O_5$. *Chem. Mater.* **2015**, *27*, 4630-4639.

105 Levi, E.; Gofer, Y.; Aurbach, D. On the Way to Rechargeable Mg Batteries: The Challenge of New Cathode Materials. *Chem. Mater.* **2010**, *22*, 860-868.

106 Schöllhorn, R.; Payer, A. c-TiS_2, a New Modification of Titanium Disulfide with Cubic Structures. *Angew. Chem. Int. Ed. Engl.* **1985**, *24*, 67-68.

107 McKelvy, M. J.; Glaunsinger, W. S. Synthesis and Characterization of Nearly Stoichiometric Titanium Disulfide. *J. Solid State Chem.* **1987**, *66*, 181-188.

108 Sinha, S.; Murphy, D. W. Lithium Intercalation in Cubic TiS_2. *Solid State Ionics* **1986**, *20*, 81-84.

109 James, A. C. W. P.; Goodenough, J. B. Structure and NMR Study of the Lithiated Defect Thiospinels $Li_xCu_{0.07}[Ti_2]S_4$ ($0<x<2$). *J. Solid State Chem.* **1988**, *77*, 356-365.

110 Bruce, P. G.; Saidi, M. Y. Variation of the Preexponential Factor and Activation Energy for Lithium Diffusion in Cubic Titanium Disulfide. *J. Solid State Chem.* 1990, *88*, 411-418.

111 Emly, A.; Van der Ven, A. Mg Intercalation in Layered and Spinel Host Crystal Structures for Mg Batteries. *Inorg. Chem.* **2015**, *54*, 4394-4402.

112 Lightfoot, P.; Krok, F.; Nowinski, J. L; Bruce, P. G. Structure of the Cubic Intercalate Mg_xTiS_2. *J. Mater. Chem.* **1992**, *2*, 139-140.

113 Sun, X.; Bonnick, P.; Duffort, V.; Liu, M.; Rong, Z.; Persson, K. A.; Ceder, G.; Nazar, L. F. A High Capacity Thiospinel Cathode for Mg Batteries. *Energy Environ. Sci.* **2016**, *9*, 2273-2277.

114 Van der Ven, A.; Bhattacharya, J.; Belak, A. A. Understanding Li Diffusion in Li-Intercalation Compounds. *Acc. Chem. Res.* **2013**, *46*, 1216-1225.

115 Benco, L.; Barras, J.-L.; Atanasov, M.; Daul, C. First Principles Calculation of Electrode Material for Lithium Intercalation Batteries: TiS_2 and $LiTi_2S_4$ Cubic Spinel Structures. *J. Solid State Chem.* **1999**, *145*, 503-510.

116 Rouxel, J.; Tournoux, M. Chimie Douce with Solid Precursors, Past and Present. *Solid State Ionics*, **1996**, *84*, 141-149.

117 Jeong, S.; Yoo, D.; Jang, J.; Kim, M.; Cheon, J. Well-Defined Colloidal 2-D Layered Transition-Metal Chalcogenide Nanocrystals via Generalized Synthetic Protocols. *J. Am. Chem. Soc.* **2012**, *134*, 18233-18236.

118 Whittingham, M. S. Preparation of Stoichiometric Titanium Disulfide. US Patent 4007055, **1977**.

119 Patel, S. N.; Balchin, A. A. The Preparation of Titanium Disulphide with Different Stoichiometries, $Ti_{(1+x)}S_2$, and Comparison of Lattice Parameters. *J. Mater. Sci. Lett.* **1984**, *3*, 942-944.

120 Bruce, P. G.; Krok, F.; Nowinski, J.; Gibson, V. C.; Tavakkoli, K. Chemical Intercalation of Magnesium into Solid Hosts. *J. Mater. Chem.* **1991**, *1*, 705-706.

121 Bruce, P. G.; Krok, F.; Lightfoot, P.; Nowinski, J. L. Multivalent Cation Intercalation. *Solid State Ionics* **1992**, *53-56*, 351-355.

122 Dahn, J. R.; McKinnon, W. R.; Haering, R. R. Structure Determination of Li_xTiS_2 by Neutron Diffraction. *Can. J. Phys.* **1980**, *58*, 207-213.

123 Whittingham, M. S.; Thompson, A. H. Intercalation and Lattice Expansion in Titanium Disulfide. *J. Chem. Phys.* **1975**, *62*, 1588.

124 Whittingham, M. S.; Gamble, F. R., Jr. The Lithium Intercalates of the Transition Metal Dichalcogenides. *Mater. Res. Bull.* **1975**, *10*, 363-371.

125 Dahn, J. R.; Py, M. A.; Haering, R. R. In-Situ X-Ray Diffraction Experiments on Lithium Intercalation Compounds. *Can. J. Phys*. **1982**, *60*, 307-313.

126 Suslov, E. A.; Bushkova, O. V.; Sherstobitova, E. A.; Reznitskikh, O. G.; Titov, A. N. Lithium Intercalation into TiS_2 Cathode Material: Phase Equilibria in a Li-TiS_2 System. *Ionics* **2016**, *22*, 503-514.

127 Basu, S.; Worrell, W. L. Fast Ion Transport in Solids; North-Holland: Amsterdam, **1979**.

128 Bruce, P. G.; Saidi, M. Y. Comparison of the Cubic and Layered Polymorphs of Titanium Disulphide. *Electrochim. Acta* **1991**, *36*, 569-575.

129 Rong, Z.; Malik, R.; Canepa, P.; Gautam, G. S.; Liu, M.; Jain, A.; Persson, K.; Ceder, G. Materials Design Rules for Multivalent Ion Mobility in Intercalation Structures. *Chem. Mater*. **2015**, *27*, 6016-6021.

130 Thackeray, M. M.; Johnson, P. J.; de Picciotto, L. A.; Bruce, P. G.; Goodenough, J. B. Electrochemical Extraction of Lithium from $LiMn_2O_4$. *Mater. Res. Bull*. **1984**, *19*, 179-187.

131 Bach, S.; Pereira-Ramos, J. P.; Baffier, N.; Messina, R. Birnessite Manganese Dioxide Synthesized via a Sol-Gel Process: a New Rechargeable Cathodic Material for Lithium Batteries. *Electrochim. Acta* **1991**, *36*, 1595-1603.

132 Bach, S.; Pereira-Ramos, J. P.; Baffier, N. A New MnO_2 Tunnel Related Phase as Host Lattice for Li Intercalation. *Solid State Ionics* **1995**, *80*, 151-158.

133 Feng, Q.; Kanoh, H.; Miyai, Y.; Ooi, K. Hydrothermal Synthesis of Lithium and Sodium Manganese Oxides and Their Metal Ion Extraction/Insertion Reactions. *Chem. Mater*. **1995**, *7*, 1226-1232.

134 Duncan, M. J.; Leroux, F.; Corbett, J. M.; Nazar, L. F. Todorokite as a Li Insertion Cathode. *J. Electrochem. Soc.* **1998**, *145*, 3746-3757.

135 Luo, J.-Y.; Zhang, J.-J.; Xia, Y.-Y. Highly Electrochemical Reaction of Lithium in the Ordered Mesoporous β-MnO_2. *Chem. Mater.* **2006**, *18*, 5618-5623.

136 Caballero, A.; Hernán, L.; Morales, J.; Sánchez, L.; Santos Peña, J.; Aranda, M. A. G. Synthesis and Characterization of High-Temperature Hexagonal P2-$Na_{0.6}MnO_2$ and Its Electrochemical Behaviour as a Cathode in Sodium Cells. *J. Mater. Chem.* **2002**, *12*, 1142-1147.

137 Nam, K. W.; Kim, S.; Yang, E.; Jung, Y.; Levi, E.; Aurbach, D.; Choi, J. W. Critical Role of Crystal Water for a Layered Cathode Material in Sodium Ion Batteries. *Chem. Mater.* **2015**, *27*, 3721-3725.

138 Rasul, S.; Suzuki, S.; Yamaguchi, S.; Miyayama, M. High Capacity Positive Electrodes for Secondary Mg-Ion Batteries. *Electrochim. Acta* **2012**, *82*, 243-249.

139 Zhang, R.; Yu, X.; Nam, K.-W.; Ling, C.; Arthur, T. S.; Song, W.; Knapp, A.; Ehrlich, S. N.; Yang, X.-Q.; Matsui, M. α-MnO_2 as a Cathode Material for Rechargeable Mg Batteries. *Electrochem. Commun.* **2012**, *23*, 110-113.

140 Ling, C.; Mizuno, F. Phase Stability of Post-Spinel Compound AMn_2O_4 (A = Li, Na, or Mg) and Its Application as a Rechargeable Battery Cathode. *Chem. Mater.* **2013**, *25*, 3062-3071.

141 Huie, M. M.; Bock, D. C.; Takeuchi, E. S.; Marschilok, A. C.; Takeuchi, K. J. Cathode Materials for Magnesium and Magnesium-Ion Based Batteries. *Coord. Chem. Rev.* **2015**, *287*, 15-27.

142 Post, J. E.; Veblen, D. R. Crystal Structure Determinations of Synthetic Sodium, Magnesium and Potassium Birnessite Using TEM and the Rietveld Method. *Am. Mineral.* **1990**, *75*, 477-489.

143 Golden, D. C.; Chen, C. C.; Dixon, J. B. Transformation of Birnessite to Buserite, Todorokite, and Manganite under Mild Hydrothermal Treatment. *Clays Clay Miner.* **1987**, *35*, 271-280.

144 Ling, C.; Zhang, R.; Arthur, T. S.; Mizuno, F. How General is the Conversion Reaction in Mg Battery Cathode: A Case Study of the Magnesiation of α-MnO_2. *Chem. Mater.* **2015**, *27*, 5799-5807.

145 Zhang, R.; Arthur, T. S.; Ling, C.; Mizuno, F. Manganese Dioxides as Rechargeable Magnesium Battery Cathode; Synthetic Approach to Understand Magnesiation Process. *J. Power Sources* **2015**, *282*, 630-638.

146 Song, J.; Noked, M.; Gillette, E.; Duay, J.; Rubloff, G.; Lee, S. B. Activation of a MnO_2 Cathode by Water-Stimulated Mg^{2+} Insertion for a Magensium Ion Battery. *Phys. Chem. Chem. Phys.* **2015**, *17*, 5256-5264.

147 Casas-Cabanas, M.; Rodríguez-Carvajal, J.; Palacín, M. R. Faults, a New Program for Refinement of Powder Diffraction Patterns from Layered Structures. *Z. Kristallogr. Suppl.* **2006**, *2006*, 243-248.

148 Armstrong, A. R.; Paterson, A. J.; Dupre, N.; Grey, C. P.; Bruce, P. G. Structural Evolution of Layered $Li_xMn_yO_2$: Combined Neutron, NMR, and Electrochemical Study. *Chem. Mater.* **2007**, *19*, 1016-1023.

149 Ha, S.-Y.; Lee, Y.-W.; Woo, S. W.; Koo, B.; Kim, J.-S.; Cho, J.; Lee, K. T.; Choi, N.-S. Magnesium (II) Bis(trifluoromethane sulfonyl) Imide-Based Electrolytes with Wide Electrochemical Windows for Rechargeable Magnesium Batteries. *ACS Appl. Mater. Interfaces* **2014**, *6*, 4063-4073.

150 Yoo, H. D.; Shterenberg, I.; Gofer, Y.; Doe, R. E.; Fischer, C. C.; Ceder, G.; Aurbach, D. A Magnesium-Activated Carbon Hybrid Capacitor. *J. Electrochem. Soc.* **2014**, *161*, A410-A415.

151 Frackowiak, E.; Be guin, F. Carbon Materials for the Electrochemical Storage of Energy in Capacitors. *Carbon* **2001**, *39*, 937-950.

152 Gupta, R. P.; Sen, S. K. Calculation of Multiplet Structure of Core p-Vacancy Levels. *Phys. Rev. B* **1974**, *10*, 71-77.

153 Nesbitt, H. W.; Banerjee, D. Interpretation of XPS Mn(2p) Spectra of Mn Oxyhydroxides and Constraints on the Mechanism of MnO_2 Precipitation. *Am. Mineral.* **1998**, *83*, 305-315.

154 Biesinger, M. C.; Payne, B. P.; Grosvenor, A. P.; Lau, L. W. M.; Gerson, A. R.; Smart, R., St. C. Resolving Surface Chemical States in XPS Analysis of First Row Transition Metals, Oxides and Hydroxides: Cr, Mn, Fe, Co and Ni. *Appl. Surf. Sci.* **2011**, *257*, 2717-2730.

155 Knipe, S. W.; Mycroft, J. R.; Pratt, A. R.; Nesbitt, H. W.; Bancroft, G. M. X-Ray Photoelectron Spectroscopic Study of Water Adsorption on Iron Sulphide Minerals. *Geochim. Cosmochim. Acta* **1995**, *59*, 1079-1090.

156 Dedryv ère, R.; Leroy, S.; Martinez, H.; Blanchard, F.; Lemordant, D.; Gonbeau, D. XPS Valence Characterization of Lithium Salts as a Tool to Study Electrode/Electrolyte Interfaces of Li-Ion Batteries. *J. Phys. Chem. B* **2006**, *110*, 12986−12992.

157 Lapidus, S. H.; Rajput, N. N.; Qu, X.; Chapman, K. W.; Persson, K. A.; Chupas, P. J. Solvation Structure and Energetics of Electrolytes for Multivalent Energy Storage. *Phys. Chem. Chem. Phys.* **2014**, *16*, 21941-21945.

158 McCarroll, W. H.; Katz, L.; Ward, R. Some Ternary Oxides of Tetravalent Molybdenum. *J. Am. Chem. Soc.* **1957**, *79*, 5410–5414.

159 Cotton, F. A. Metal Atom Clusters in Oxide Systems. *Inorg. Chem.* **1964**, *3*, 1217-1220.

160 Barker, J.; Saidi, M. Y.; Swoyer, J. L. Lithiated Molybdenum Oxide Active Materials. US Patent 6908710 B2, **2005**.

161 Ben-Kamel, K.; Amdouni, N.; Groult, H.; Mauger, A.; Zaghib, K.; Julien, C. M. Structural and Electrochemical Properties of $LiMoO_2$. *J. Power Sources* **2012**, *202*, 314-321.

162 Ma, J.; Zhou, Y.-N.; Gao, Y.; Yu, X.; Kong, Q.; Gu, L.; Wang, Z.; Yang, X.-Q.; Chen, L. Feasibility of Using Li_2MoO_3 in Constructing Li-Rich High Energy Density Cathode Materials. *Chem. Mater.* **2014**, *26*, 3256-3262.

163 Incorvati, J. T.; Wan, L. F.; Key, B.; Zhou, D.; Liao, C.; Fuoco, L.; Holland, M.; Wang, H.; Prendergast, D.; Poeppelmeier, K. R.; Vaughey, J. T. Reversible Magnesium Intercalation into a Layered Oxyfluoride Cathode. *Chem. Mater.* **2016**, *28*, 17-20.

164 Kaveevivitchai, W.; Jacobson, A. J.; High Capacity Rechargeable Magnesium-Ion Batteries Based on a Microporous Molybdenumm-Vanadium Oxide Cathode. *Chem. Mater.* **2016**, *28*, 4593-4601.

165 Wizansky, A. R.; Rauch, P. E.; Disalvo, F. J. Powerful Oxidizing Agents for the Oxidative Deintercalation of Lithium from Transition-Metal Oxides. *J. Sold State Chem.* **1989**, *81*, 203-207.

166 Gautam, G. S.; Sun, X.; Duffort, V.; Nazar, L. F.; Ceder, G. Impact of Intermediate Sites on Bulk Diffusion Barriers: Mg Intercalation in $Mg_2Mo_3O_8$. *J. Mater. Chem. A* **2016**, *4*, 17643-17648.

167 Jain, A.; Ong, S. P.; Hautier, G.; Chen, W.; Richards, W. D.; Dacek, S.; Cholia, S.; Gunter, D.; Skinner, D.; Ceder, G.; Persson, K. A. Commentary: The Materials Project: A materials genome approach to accelerating materials innovation. *APL Mater.* **2013**, *1*, 011002.

168 lek, P. L. G.; Lindsay, W. L. Thermodynamic stability and solubility of molybdenum minerals in soils. *Soil Sci. Soc. Am. J.* **1977**, *41*, 42-46.

169 Staples, L. W. Ilsemannite and Jordisite. *Am. Mineral.* **1951**, *36*, 609-614.

170 Canepa, P.; Jayaraman, S.; Cheng, L.; Rajput, N. N.; Richards, W. D.; Gautam, G. S.; Curtiss, L. A.; Persson, K. A.; Ceder, G. Elucidating the structure of magnesium aluminum chloride complex electrolyte for magnesium-ion batteries. *Energy Environ. Sci.* **2015**, *8*, 3718-3730.

171 Canepa, P.; Gautam, G. S.; Malik, R.; Jayaraman, S.; Rong, Z.; Zavadil, K. R.; Persson, K.; Ceder, G. Understanding the initial stages of reversible Mg deposition and stripping in inorganic nonaqueous electrolytes. *Chem. Mater.* **2015**, *27*, 3317-3325.

172 Kumar, A.; Yusuf, S. M. Structural and Magnetic Properties of $Fe[Fe(CN)_6]$ $4H_2O$. *Phys. Rev. B* **2005**, *71*, 054414.

173 Imanishi, N.; Morikawa, T.; Kondo, J.; Yamane, R.; Takeda, Y.; Yamamoto, O.; Sakaebe, H.; Tabuchi, M. Lithium Intercalation Behavior of Iron Cyanometallates. *J. Power Sources* **1999**, *81-82* 530-534.

174 Asakura, D.; Li, C. H.; Mizuno, Y.; Okubo, M.; Zhou, H.; Talham, D. R. Bimetallic Cyanide-Bridged Coordination Polymers as Lithium Ion Cathode Materials: Core@Shell Nanoparticles with Enhanced Cyclability. *J. Am. Chem. Soc.* **2013**, *135* 2793-2799.

175 Shen, L.; Wang, Z.; Chen, L. Prussian Blues as a Cathode Material for Lithium Ion Batteries. *Chem. Eur. J.* **2014**, *20*, 12559-12562.

176 Wang, L.; Lu, Y.; Liu, J.; Xu, M.; Cheng, J.; Zhang, D.; Goodenough, J. B. A Superior Low-Cost Cathode for a Na-Ion Battery. *Angew. Chem. Int. Ed.* **2013**, *52*, 1964-1967.

177 Wu, X.; Deng, W.; Qian, J.; Cao, Y.; Ai, X.; Yang, H. Single-Crystal $FeFe(CN)_6$ Nanoparticles: A High Capacity and High Rate Cathode for Na-Ion Batteries. *J. Mater. Chem. A* **2013**, *1*, 10130-10134.

178 You, Y.; Wu, X.-L.; Yin, Y.-X.; Guo, Y.-G. High-Quality Prussian Blue Crystals as Superior Cathode Materials for Room-Temperature Sodium-Ion Batteries. *Energy Environ. Sci.* **2014**, *7*, 1643-1647.

179 Lee, H.-W.; Wang, R. Y.; Pasta, M.; Lee, S. W.; Liu, N.; Cui, Y. Manganese Hexacyanomanganate Open Framework as a High-Capacity Positive Electrode Material for Sodium-Ion Batteries. *Nat. Comm.* **2014**, *5*, 5280.

180 Wang, L.; Song, J.; Qiao, R.; Wray, L. A.; Hossain, M. A.; Chuang, Y.-D.; Yang, W.; Lu, Y.; Evans, D.; Lee, J.-J.; Vail, S.; Zhao, X.; Nishijima, M.; Kakimoto, S.; Goodenough, J. B.

Rhombohedral Prussian White as Cathode for Rechargeable Sodium-Ion Batteries. *J. Am. Soc. Chem.* **2015**, *137*, 2548-2554.

181 Song, J.; Wang, L.; Lu, Y.; Liu, J.; Guo, B.; Xiao, P.; Lee, J.-J.; Yang, X.-Q.; Henkelman, G.; Goodenough, J. B. Removal of Interstitial H_2O in Hexacyanometallates for a Superior Cathode of a Sodium-Ion Battery. *J. Am. Chem. Soc.* **2015**, *137*, 2658-2664.

182 Li, W.-J.; Chou, S.-L.; Wang, J.-Z.; Kang, Y.-M.; Wang, J.-L.; Liu, Y.; Gu, Q.-F.; Liu, H.-K.; Dou, S.-X. Facile Methode to Syntheisze Na-Enriched $Na_{1+x}FeFe(CN)_6$ Frameworks as Cathode with Superior Electrochemical Performance for Sodium-Ion Batteries. *Chem. Mater.* **2015**, *27*, 1997-2003.

183 Lipson, A. L.; Pan, B.; Lapidus, S. H.; Liao, C.; Vaughey, J. T.; Ingram, B. J. Rechargeable Ca-Ion Batteries: A New Energy Storage System. *Chem. Mater*. **2015**, *27*, 8442-8447.

184 Wang, R. Y.; Wessells, C. D.; Huggins, R. A.; Cui, Y. Highly Reversible Open Framework Nanoscale Electrodes for Divalent Ion Batteries. *Nano Lett.* **2013**, *13*, 5748-5752.

185 Li, Z.; Xiang, K.; Xing, W.; Carter, W. C.; Chiang, Y.-M. Reversible Aluminum-Ion Intercalation in Prussian Blue Analogs and Demonstration of a High-Power Aluminum-Ion Asymmetric Capacitor. *Adv. Energy Mater.* **2015**, *5*, 1401410.

186 Herren, F.; Fischer, P.; Ludi, A.; Hälg, W. Neutron Diffraction Study of Prussian Blue, $Fe_4[Fe(CN)_6]_3 \cdot xH_2O$. Location of Water Molecules and Long-Range Magnetic Order. *Inorg. Chem.* **1980**, *19*, 956-959.

187 Childers, J.; Crumbliss, A.; Lugg, P.; Palmer, R.; Morosoff, N.; Patel, D. Spectral Characterization of Redox-Active Prussian Blue on Metallated Plasma Polymer Surface Modified Carbon Electrodes Using Photothermal Detection. *J. Phys. Colloq.* **1983**, *44*, 285-290.

188 Crumbliss, A. L.; Lugg, P. S.; Childers, J. W.; Palmer, R. A. Fourier Transform Infrared Photothermal Spectroscopic Characterization of Prussian Blue Surface Modified Electrodes. Countercation Effects. *J Phys. Chem.* **1985**, *89*, 482-488.

189 Kunimatsu, K.; Shigematsu, Y.; Uosaki, K.; Kita, H. Study of the $Fe(CN)_6^{3-}/Fe(CN)_6^{4-}$ Redox System on Pt by EMIRS. Part I. Infrared Spectra of the Intermediates in the Charge Transfer. *J. Electroanal. Chem.* **1989**, *262*, 195-209.

190 Novakovski, V. M.; Sorokina, A. N. Model Study of Chloride Pitting in 18-8 Stainless Steel. *Corros. Sci.* **1966**, *6*, 227-233.

191 McCafferty, E. Sequence of Steps in the Pitting of Aluminum by Chloride Ions. *Corros. Sci.* **2003**, *45*, 1421-1438.

192 Muldoon, J.; Bucur, C. B.; Oliver, A. G.; Zajicek, J.; Allred, G. D.; Boggess, W. C. Corrosion of Magnesium Electrolytes: Chlorides – the Culprit. *Energy Environ. Sci.* **2013**, *6*, 482-487.

193 Pramudita, J. C.; Schmid, S.; Godfrey, T.; Whittle, T.; Alam, M.; Hanley, T.; Brand, H. E. A.; Sharma, N. Sodium Uptake in Cell Construction and Subsequent *in Operando* Electrode Behaviour of Prussian Blue Analogues, $Fe[Fe(CN)_6]_{1-x} \cdot yH_2O$ and $FeCo(CN)_6$. *Phys. Chem. Chem. Phys.* **2014**, *16*, 24178-24187.

194 Aines, R. D.; Rossman, G. R. Water in Minerals? A Peak in the Infrared. *J. Geophys. Res.* **1984**, *89*, 4059-4071.

195 Ellis, B. L.; Lee, K. T.; Nazar, L. F. Positive Electrode Materials for Li-Ion and Li-Batteries. *Chem. Mater.* **2010**, *22*, 691-714.

196 Gong, Z.; Yang, Y. Recent Advances in the Research of Polyanion-Type Cathode Materials for Li-Ion Batteries. *Energy Environ. Sci.* **2011**, *4*, 3223-3242.

197 Cheng, F.; Liang, J.; Tao, Z. Chen, J. Functional Materials for Rechargeable Batteries. *Adv. Mater.* **2011**, *23*, 1695-1715.

198 Morgan, D.; Van der Ven, A.; Ceder, G. Li Conductivity in Li_xMPO_4 (M = Mn, Fe, Co, Ni) Olivine Materials. *Electrochem. Solid-State Lett.* **2004**, *7*, A30-A32.

199 Islam, M. S.; Driscoll, D. J.; Fisher, C. A. J.; Slater, P. R. Atomic-Scale Investigation of Defects, Dopants, and Lithium Transport in the $LiFePO_4$ Olivine-Type Battery Material. *Chem. Mater.* **2005**, *17*, 5085-5092.

200 Nishimura, S.-I.; Kobayashi, G.; Ohoyama, K.; Kanno, R.; Yashima, M.; Yamada, A. Experimental Visualization of Lithium Diffusion in Li_xFePO_4. *Nature Mater.* **2008**, *7*, 707-711.

201 Huang, H.; Yin, S.-C.; Nazar, L. F. Approaching Theoretical Capacity of $LiFePO_4$ at Room Temperature at High Rates. *Electrochem. Solid-State Lett.* **2001**, *4*, A170-A172.

202 Kang, B.; Ceder, G. Battery Materials for Ultrafast Charging and Discharing. *Nature* **2009**, *458*, 190-193.

203 Wu, X.-L.; Jiang, L.-Y.; Cao, F.-F.; Guo, Y.-G.; Wan, L.-J. $LiFePO_4$ Nanoparticles Embedded in a Nanoporous Carbon Matrix: Superior Cathode Material for Electrochemical Energy-Storage Devices. *Adv. Mater.* **2009**, *21*, 2710-2714.

204 Saracibar, A.; Van der Ven, A.; Arroyo-de Dompablo, M. E. Crystal Structure, Energetics, and Electrochemistry of Li_2FeSiO_4 Polymorphs from First Principles Calculations. *Chem. Mater.* **2012**, *24*, 495-503.

205 Redfern, S. A. T.; Artioli, G.; Rinaldi, R.; Henderson, C. M. B.; Knight, K. S.; Wood, B. J. Octahedral Cation Ordering in Olivine at High Temperature. II: An in Situ Neutron Powder Diffraction Study on Synthetic $MgFeSiO_4$ (Fa50). *Phys. Chem. Miner.* **2000**, *27*, 630-637.

206 Fujion, K.; Sasaki, S.; Takéuchi; Y. Sadanaga, R. X-Ray Determination of Electron Distribution in Forsterite, Fayalite and Tephroite. *Acta Cryst.* **1981**, *B37*, 513-518.

207 Hazen, R. M.; Downs, R. T.; Finger, L. W. High-Pressure Crystal Chemistry of $LiScSiO_4$: An Olivine with Nearly Isotropic Compreesion. *Am. Mineral.* **1996**, *81*, 327-334.

208 Redhammer, G.J.; Roth, G. $LiInSiO_4$: A New Monovalent-Trivalent Olivine. *Acta Crystallogr. Sect. C-Cryst. Struct. Commun.* **2003**, *C59*, i38-i40.

209 Zhou, F.; Cococcioni, M.; Kang, K.; Ceder, G. The Li Intercalation Potential of $LiMPO_4$ and $LiMSiO_4$ Olivines with M = Fe, Mn, Co, Ni. *Electrochem. Commun.* **2004**, *6*, 1144-1148.

210 Arroyo-de Dompablo, M. E., Gallardo-Amores, J. M.; Garc á-Mart ínez, J.; Mor án, E.; Tarascon, J.-M.; Armand, M. Is It Possible to Prepare Olivine-Type $LiFeSiO_4$? A Joint Computational and Experimental Investigation. *Solid State Ionics* **2008**, *179*, 1758-1762.

211 Recham, N.; Casas-Cabanas, M.; Cabana, J.; Grey, C. P.; Jumas, J.-C.; Dupont, L.; Armand, M.; Tarascon, J.-M. Formation of a Complete Solid Solution between the Triphylite and Fayalite Olivine Structures. *Chem. Mater.* **2008**, *20*, 6798-6809.

212 Bush, T. S.; Catlow, C. R. A.; Chadwick, A. V.; Cole, M.; Geatches, R. M.; Greaves, G. N.; Tomlinson, S. M. Studies of Cation Dopant Sites in Metal Oxides by EXAFS and Computer-Simulation Techniques. *J. Mater. Chem.* **1992**, *2*, 309-316.

213 Fisher, C.A.; Hart Prieto, M.V., Islam, M.S. Lithium Battery Materials $LiMPO_4$ (M = Mn, Fe, Co, and Ni): Insights into Defect Association, Transport Mechanisms, and Doping Behavior. *Chem. Mater.* **2008**, *20*, 5907-5915.

214 Dick, B. G.; Overhauser, A. W. Theory of the Dielectric Constants of Alkali Halide Crystals. *Phys. Rev.* **1958**, *112*, 90-103.

215 Gale, J. D.; Rohl, A. L. The General Utility Lattice Program (GULP). *Mol. Simul.* **2003**, *29*, 291-341.

216 Fisher, C. A. J.; Islam, M. S. Defect, Protons and Conductivity in Brownmillerite-Structured $Ba_2In_2O_5$. *Solid State Ionics* **1999**, *118*, 355-363.

217 Minervini, L.; Zacate, M.O.; Grimes, R.W. Defect Cluster Formation in M_2O_3-Doped CeO_2. *Solid State Ionics* **1999**, *116*, 339-349.

218 Sierka, M.; Sauer, J. Structure and Reactivity of a Silica and Zeolite Catalysts by a Combined Quantum Mechanics–Shell-Model Potential Approach Based on DFT. *Faraday Discuss.* **1997**, *106*, 41-62.

219 Sanders, M. J.; Leslie, M. J.; Catlow. C. R. A. Interatomic Potentials for SiO_2. *J. Chem. Soc. Chem. Com.* **1984**, 1271-1273.

220 Woodley, S. M.; Catlow, C.R.A.; Piszora,P.; Stempin, K.; Wolska, E. Computer Modeling Study of the Lithium Ion Distribution in Quaternary Li-Mn-Fe-O Spinels. *J. Solid State Chem.* **2000**, *153*, 310-316.

221 Braithwaite, J. S.; Catlow, C.R.A.; Harding, J. H.; Gale J. D. A Computational Study of the High Voltage $Li_xCo_yMn_{4-y}O_8$ Cathode Material. *Phys. Chem. Chem. Phys.* **2000**, *2*, 3841-3846.

222 Tamada, O; Fujino, K.; Sasaki, S. Structures and Electron Distribution of α-Co_2SiO_4 and α-Ni_2SiO_4 (Olivine Structure). *Acta. Cryst.* **1983**, *B39*, 692-697.

223 Tripathi, R.; Popov, G.; Sun, X.; Ryan, D. H.; Nazar, L. F. Ultra-Rapid Microwave Synthesis of Triplite $LiFeSO_4F$. *J. Mater. Chem. A* **2013**, *1*, 2990-2994.